

LOW COGGING TORQUE PMSM DRIVES WITH RECTANGULAR CURRENT CONTROL

Teză destinată obținerii
titlului științific de doctor inginer
la
Universitatea "Politehnica" din Timișoara
în domeniul INGINERIE ELECTRICĂ
de către

Ing. Alin Nicușor Știrban

Conducător științific:
Referenți științifici:

prof.univ.dr.ing. Ion Boldea
prof.univ.dr.ing. Mircea Rădulescu
prof.univ.dr.ing. Loránd Szabó
prof.univ.dr.ing. Dorin Popovici

Ziua susținerii tezei: 15.10.2010

Seriile Teze de doctorat ale UPT sunt:

- | | |
|------------------------|---|
| 1. Automatică | 7. Inginerie Electronică și Telecomunicații |
| 2. Chimie | 8. Inginerie Industrială |
| 3. Energetică | 9. Inginerie Mecanică |
| 4. Ingineria Chimică | 10. Știința Calculatoarelor |
| 5. Inginerie Civilă | 11. Știința și Ingineria Materialelor |
| 6. Inginerie Electrică | |

Universitatea „Politehnica” din Timișoara a inițiat seriile de mai sus în scopul diseminării expertizei, cunoștințelor și rezultatelor cercetărilor întreprinse în cadrul școlii doctorale a universității. Seriile conțin, potrivit H.B.Ex.S Nr. 14 / 14.07.2006, tezele de doctorat susținute în universitate începând cu 1 octombrie 2006.

Copyright © Editura Politehnica – Timișoara, 2010

Această publicație este supusă prevederilor legii dreptului de autor. Multiplicarea acestei publicații, în mod integral sau în parte, traducerea, tipărirea, reutilizarea ilustrațiilor, expunerea, radiodifuzarea, reproducerea pe microfilme sau în orice altă formă este permisă numai cu respectarea prevederilor Legii române a dreptului de autor în vigoare și permisiunea pentru utilizare obținută în scris din partea Universității „Politehnica” din Timișoara. Toate încălcările acestor drepturi vor fi penalizate potrivit Legii române a drepturilor de autor.

România, 300159 Timișoara, Bd. Republicii 9,
tel. 0256 403823, fax. 0256 403221
e-mail: editura@edipol.upt.ro

PREFACE

This thesis represents an approach to the design and control of permanent magnet synchronous motors fed with rectangular current. The present thesis includes the electromagnetic design for a (6+6) slots/ 8 poles 3 phase brushless DC actuator with interior permanent magnets, a comparison between FEM calculated and measured parameters, presents an accurate and efficient dynamic circuit model for brushless DC motor drives, and proposes a new sensorless control method for BLDC motor drive system, with accurate position and speed estimation.

*This thesis is dedicated to the memory of my mother,
for her endless love, support and encouragement*

Acknowledgements

I wish to express my gratitude to my supervisor Prof. Ion Boldea from University "Politehnica" of Timisoara, Faculty of Electrical and Power Engineering. His guidance, support and encouragement made this work possible. I would like to thank Ph.D. Eng. Dorin Iles, former head of the R&D department at EBM-Papst, Germany, for his support and for the fruitful discussions during and after my two months Ph.D. internship in Germany.

I wish to thank all of those who contributed to my engineering education and also to my colleagues from Intelligent Motion Control Laboratory at Faculty of Electrical and Power Engineering, Timisoara. Assoc. Prof. Lucian Tutelea, Ph.D. Eng. Liviu Iepure and Ph.D. Eng. Robert Antal deserve my special gratitude. Many thanks also to Prof. Gheorghe Daniel Andreescu from Faculty of Automation and Computers, University "Politehnica" of Timisoara, Romania.

Most of all, I want to thank my family and my girlfriend, Ana, for their understanding, encouragement and support.

Timișoara, September, 2010

Alin Nicușor Știrban

Știrban, Alin Nicușor

Low cogging torque tooth wound PMSM drives with rectangular current control

Teze de doctorat ale UPT, Seria 6, Nr. 19, Editura Politehnica, 2010, 192 pagini, 143 figuri, 14 tabele.

ISSN: 1842-7022

ISBN: 978-606-554-182-5

Keywords: interior permanent magnet brushless DC motor (IPMBLDC), concentrated (non-overlapped) windings, cogging torque, parameter measurement, finite element method, sensorless control, starting method.

Abstract

The present thesis investigates an interior permanent magnet synchronous motor with 8 rotor poles and nonuniform (6+6) stator slots and concentrated windings fed with trapezoidal currents.

The electromagnetic design of the proposed solution was done algorithmically and it was validated using Finite Element Method (FEM). FEM-analysis offers direct results for torque, back-EMF and inductances. Whenever possible, FEM-calculated characteristics are compared with experimentally obtained ones, in order to validate the FEM-computations for this type of machine. The BLDC model developed in this thesis takes into account the phase commutation phenomenon, the real waveforms of back-EMF and inductances, based on FEM calculations.

For the sensorless control of brushless DC PM motor drive, this thesis introduces and investigates a FEM assisted position and speed observer, based on the line-to-line PM flux linkage estimation. Even if the proposed observer relies on the fundamental model of the machine, a safe starting strategy under heavy load torque, called I-f control, is used, with seamless transition to the proposed sensorless control.

Table of Contents

Preface	3
Acknowledgements	4
Abstract	4
Table of contents	5
Motivation	9
Objectives of the thesis	10
Outline of the thesis	11
Nomenclature	12
Chapter 1 Brushless permanent magnet machines and their control	15
Abstract	15
1.1. Introduction	15
1.2. Brushless permanent magnet machine types and topologies	16
1.3. Brushless permanent magnet motor drives	20
1.3.1. Sinusoidal PMSM drives	21
1.3.2. Brushless permanent magnet DC drives	21
1.4. Magnetic materials for brushless PM machines	22
1.4.1. Permanent magnet materials	22
1.4.2. Iron core materials	25
1.5. Operation principle of brushless DC motor	26
1.6. BLDC control techniques	32
1.7. Applications	36
1.8. Overview and conclusions	40
References	41
Chapter 2 (6+6) slot/8 pole synchronous machine: analytical model of interior permanent magnet rotor	44
Abstract	44
2.1. Introduction	44
2.2. PMSM with concentrated windings	46
2.3. PMSM with concentrated windings and nonuniform slots	49
2.4. Preliminary design methodology of an IPMSM with concentrated windings and an irregular distribution of stator slots	51
2.4.1. Global topology selection	51
2.4.2. Materials selection	52
2.4.2.1. Iron core laminations	52
2.4.2.2. The permanent magnets	54

6 Table of contents

2.4.3. Design theme.....	55
2.4.4. Electric and magnetic loadings	56
2.4.5. Choosing a few dimensioning factors.....	57
2.4.5. A few technological constraints	57
2.4.6. Dimensioning methodology.....	57
2.5. Weights and costs of active materials	71
2.6. Thermal verification	72
2.7. Conclusion.....	73
References.....	73
Chapter 3 FE analysis versus experimental results: fields, torque, and parameters	75
Abstract	75
3.1. Introduction.....	75
3.2. FE analysis of concentrated coils and nonuniform slots (6+6/8)	
IPMSM with trapezoidal current control.....	77
3.2.1. The FE software.....	77
3.2.2. The FE model	77
3.2.3. Field distribution	79
3.2.3.1. No-load field distribution	79
3.2.3.2. Field distribution under load.....	83
3.2.4. No-load phase flux linkage and back-EMF	86
3.2.5. Cogging torque computation.....	88
3.2.6. Load torque	89
3.2.7. Reduction of torque ripple	94
3.2.8. Computation of inductances.....	96
3.3. Experimental analysis of concentrated coils and nonuniform slots (6+6/8) IPMBLDC	102
3.3.1. Phase resistance measurement	103
3.3.2. Phase self and line-to-line inductance measurement.....	103
3.3.3. Standstill torque measurement	105
3.3.4. Phase back-EMF measurement.....	107
3.3.5. Cogging torque measurement.....	109
3.3.6. Friction and iron loss torque versus speed	111
3.3.7. Rated torque-speed characteristic	111
3.4. FEM preprocessor for PMSM	112
3.5. Conclusion.....	114
References.....	115
Chapter 4 Dynamic circuit model with FEM extracted parameters.....	117
Abstract	117
4.1. Introduction.....	117
4.2. Mathematical model of BLDC motor drive system	118

4.3. Commutation of BLDC motors	121
4.3.1. Bipolar excitation, two phases on	121
4.3.2. Bipolar excitation, three phases on	122
4.3.3. Unipolar excitation	122
4.4. Voltage Source Inverter for bipolar-driven BLDC motor	124
4.5. Modeling and implementation of BLDC motor drive system	127
4.5.1. BLDC motor model block.....	128
4.5.2. Inductance block.....	130
4.5.3. Voltage Source Inverter	130
4.5.4. Speed and current controller blocks	131
4.6. Simulation results and discussions	133
4.7. Conclusion.....	139
References.....	140
Chapter 5 Observers for sensorless control of BLDC PM motor drive, with experiments.....	143
Abstract	143
5.1. Introduction.....	143
5.2. Commutation strategy and FEM assisted position observer	144
5.3. Speed observers.....	147
5.4. Simulation results.....	149
5.5. Experimental results	153
5.6. Conclusions	161
References.....	161
Chapter 6 Sensorless control implementation and performance, with experiments.....	163
Abstract	163
6.1. Introduction.....	163
6.2. I-F control starting method	164
6.3. Transition strategies	164
6.3.1. Transition from I-f control to FEM assisted position and speed observer.....	164
6.3.2. Transition from FEM assisted position and speed observer to I-f control	165
6.4. Simulation results.....	166
6.5. Experimental results	168
6.5.1. Constant speed operation.....	169
6.5.2. Dynamics.....	170
6.5.3. Transition from I-F control to FEM assisted position and speed observer BLDC PM motion-sensorless control	172
6.5.4. Transition from FEM assisted position and speed observer BLDC PM motion-sensorless control to I-F control	174

8 Table of contents

6.6. Conclusion.....	175
References.....	175
Chapter 7 The experimental test platform	177
Abstract	177
7.1. Laboratory setup for Chapter 3	177
7.1.1. BLDC motor	177
7.1.2. Laboratory precise dynamometer	178
7.2. Laboratory setup for Chapters 5 and 6.....	180
7.2.1. dSpace DS1103	181
7.2.2. Position sensor	181
7.3. Software	182
7.4. Conclusion.....	184
References.....	184
Chapter 8 Conclusion and Contributions	185
8.1. Conclusion.....	185
8.2. Original contributions	186
8.3. Future work.....	187
Author’s papers related to the Ph.D. thesis	188
Author’s CV.....	189

Motivation

In the 20th century, the squirrel cage induction motors have been the most popular electric motors, due to its rugged construction. Improvements in the field of power electronics, digital signal processors and control technology have added more features to these motor drives to make them more prevalent in industrial installations. However squirrel cage induction motors suffer from poor power factor and efficiency as compared to synchronous motors. On the other hand, synchronous motors and DC commutator motors have limitations such as speed, noise problems, wear and EMI due to the use of commutator and brushes. These limitations have led to the development of brushless permanent magnet synchronous motors which have PM excitation on the rotor.

The advantages of BLDC motors and their rapidly decreasing cost, have led to their widespread application in many variable-speed drives. Their high power density makes them ideal candidates for applications such as robotic actuators, computer disk drives, and office equipment. With their high efficiency, high power factor, and maintenance-free operation, domestic appliances and heating, ventilating, and air conditioning (HVAC) equipments are now increasingly employing BLDC motors in preference to DC and induction motors. They are also being developed for automotive applications such as electric power steering, power accessories, and active suspension, in addition to vehicle propulsion.

For PM motors rated up to 10 kW the cost of the encoder is below 10% of the motor manufacturing cost and depends on the motor rating and encoder type. Operation without electromechanical sensors and associated cabling not only improves the reliability but also simplifies the installation of the system.

The target of this thesis is to study in detail one type of PMSM with IPM, easy to manufacture, with trapezoidal back-EMF, and very low cogging torque. The thesis also presents a new sensorless control solution for BLDC motor drives, with accurate position and speed estimation, which can also be applied in servo drives.

Objectives of the thesis

The major objectives of the thesis are:

- to offer a comprehensive overview of brushless permanent magnet synchronous machines and their control, focusing on BLDC machines;
- the implementation of the electromagnetic design for a fractional slot concentrated winding permanent magnet synchronous machine case study: an interior permanent magnet synchronous motor with 8 rotor poles and nonuniform (6+6) stator slots, with very low cogging torque ($<1\% \cdot T_{eb}$), fed with trapezoidal currents;
- a comparison between FEM calculated and measured torque, back-EMF and inductances for a (6+6) slots/ 8 poles 3 phase brushless DC actuator with interior permanent magnets.
- to reduce the total torque pulsations at rated torque the skewing technique is applied ($<10\% \cdot T_{eb}$);
- to develop a dynamic circuit model for BLDC motor, using FEM extracted parameters (using "curve fitting" method), under Matlab/Simulink environment;
- to propose a new sensorless control method for BLDC motor drive system, with accurate position and speed estimation, which can be applied also in servo drives;
- using a safe starting strategy under heavy load torque, called *I-f* control, with seamless transition to the proposed method;
- digital simulations and experimental validations using advanced laboratory equipments are expected;

Outline of the thesis

The thesis is organized in 8 chapters following the above presented objectives:

The **first** chapter offers a comprehensive overview of brushless permanent magnet synchronous machines and their control, focusing on BLDC machines. The basics of brushless DC motor operation are presented. Finally, an overview of control methods and application areas for BLDC PM motors are highlighted.

The **second** chapter presents a synthesis of fractional slot concentrated winding permanent magnet synchronous machines. The determination of the machines with concentrated windings and irregular distribution of slots is depicted here. The final part of this chapter presents the implementation of the electromagnetic design for a fractional slot concentrated winding permanent magnet synchronous machine case study: an interior permanent magnet synchronous motor with 8 rotor poles and nonuniform (6+6) stator slots, fed with trapezoidal currents.

Chapter **three** presents a comparison between FEM calculated and measured torque, back-EMF and inductances for a (6+6) slots/ 8 poles 3 phase brushless DC actuator with interior permanent magnets. Methods for reducing the total torque pulsations are presented and applied. The tests carried out within the measurement procedure have the purpose to deliver machine parameters necessary for further system simulations and control tasks. Whenever possible, FEM-calculated characteristics are compared with experimentally obtained ones, in order to validate the FEM computations for this type of machine.

Chapter **four** presents an accurate and efficient model of brushless DC motor drives considering the phase commutation phenomenon. The developed model of BLDC motor, with real back-EMF waveform and adjustable inductance component (to account for the dependence of inductances with rotor position – for interior permanent magnet rotor) is verified through numerical simulations, showing its practical effectiveness.

Chapter **five** proposes and investigates a FEM assisted position and speed observer for brushless DC PM motor drive sensorless control, based on the line-to-line PM flux linkage estimation. For performance applications, the position between commutation points is obtained by comparing the estimated line-to-line PM flux with a look-up table, which contains the position versus FEM calculated line-to-line PM flux. A simulation model and experimental results are shown, demonstrating the reliability of FEM assisted position and speed observer for BLDC PM motor.

Chapter **six** presents the implementation and performances of the brushless DC (BLDC) PM motor drive sensorless control with the FEM offline assisted position and speed observer, based on the line-to-line PM flux linkage estimation, presented in detail in Chapter five. Even if the proposed observer relies on the fundamental model of the machine, a safe starting strategy under heavy load torque, called I-f control, is used, with seamless transition to the proposed sensorless control. The I-f starting method allows low-speed sensorless control, without knowing the initial position, and without machine parameters identification.

In chapter **seven** the test platforms (from EBM - Papst, Germany and UPT, Romania) used for the experimental work are described.

Chapter **eight** summarizes the work and the conclusions, original contributions and future perspectives are presented.

NOMENCLATURE

Symbols

A	Area	m^2
a	Number of parallel current paths	-
B	Magnetic flux density	T
$B_{g,PM}$	Air-gap flux density due to permanent magnet	T
B_r	Remanence or remanent magnetic flux density	T
B_m	Damping constant	$Nm/(rad/s)$
b	Width	m
b_m	Width of magnet	m
$\cos\varphi$	Power factor	-
D	Diameter	m
e_a, e_b, e_c	Back-EMF of stator phases a, b, and c	V
f	Frequency	Hz
f_{sw}	Switching frequency	Hz
g	Air-gap length, radial	m
H	Magnetic field intensity	A/m
H_c	Coercivity or coercive field strength	A/m
h	Height	m
i_a, i_b, i_c	Currents of stator phases a, b, and c	A
i_{dc}	DC current	A
J	Inertia of the motor shaft and the load system	$kg \cdot m^2$
k_{sf}	Slot-copper-filling factor	-
L_{aa}, L_{bb}, L_{cc}	Self inductance of stator phases a, b, and c	H
L_{ab}, L_{bc}, L_{ca}	Mutual inductance between stator phases a and b, b and c, and c and a, respectively	H
l_{stack}	Stack length	m
m	Mass	kg
m	Number of phases	-
m_{Cu}	Weight of copper	kg
m_{PM}	Weight of permanent magnets	kg
m_{rFe}	Weight of iron, rotor yoke	kg
m_{sFeY}	Weight of iron, stator yoke	kg
m_{sFeth}	Weight of iron, stator teeth	kg
m_{sFe}	Weight of stator core	kg
N_1	Number of turns per phase	-
N_s	Number of stator slots	-
n	Mechanical speed	rpm
P_{Cu}	Copper losses	W
P_{Eddy}	Eddy current losses of the magnets	W
P_{Fe}	Iron losses	W
P_h	Total losses	W
P_{in}	Input power	W
P_n	Rated power	W
q_1	Number slots per pole per phase	-
ρ_1	Number of pole pairs	-
R_s	Resistance of stator phase	Ω

T_{cogg}	Cogging torque	$N\cdot m$
T_{comm}	Commutation torque	$N\cdot m$
T_e	Electromagnetic torque	$N\cdot m$
T_L	Load torque	$N\cdot m$
T_{rel}	Reluctance torque	$N\cdot m$
t	Time	s
ΔT_{p-p}	Peak-to-peak torque ripple % of average torque	%
V_{a0}, V_{b0}, V_{c0}	Voltages of stator phases a, b, and c	V
V_{n0}	Voltage between motor and inverter neutral point	V
V_{ab}, V_{bc}, V_{ca}	Line-to-line voltage between stator phases a and b, b and c, and c and a, respectively	V
V_{DC}	DC bus voltage	V
w	Width	m

Greek letters

η	Efficiency	%
λ	Permeance factor	-
λ_{PM}	Flux linkage due to permanent magnet	Wb
$\Phi_{g,PM}$	Air-gap flux created by permanent magnets	Wb
σ	Conductivity	S/m
μ	Permeability	H/m
μ_r	Relative permeability	-
μ_0	Permeability of air (vacuum, $4\cdot\pi\cdot 10^{-7}$)	H/m
T_p	Pole pitch	m
T_s	Slot pitch	m
ω_e	Electrical angular speed	rad/s
ω_m	Mechanical angular speed	rad/s
θ_e	Electrical rotor angle coordinate (position)	rad
θ_m	Mechanical rotor angle coordinate (position)	rad
ψ	Flux linkage	Wb
ψ_a, ψ_b, ψ_c	Total flux linkage of stator phases a, b, and c	Wb

Abbreviations

2D	Two-dimensional;
AC	Alternating current;
Alnico	Aluminum Nickel Cobalt – alloy;
BLAC	Brushless AC (machine);
BLDC	Brushless DC (machine);
CCW	Counter-clockwise;
CP	Commutation Point;
DC	Direct current;
DSP	Digital signal processor;
EMF	Electromotive force;
EV	Electric vehicle;
FE	Finite elements;
FEA	Finite elements analysis;
FEM	Finite elements method;
GCD	Greatest common divisor;
HEV	Hybrid electric vehicle;

14 NOMENCLATURE

LCM	Least common multiple;
LPF	Low-pass filter;
MMF	Magneto-motive force;
NdFeB	Neodymium Iron Boron – alloy;
IPMSM	Interior permanent magnet synchronous motor;
IPMBLDCM	Interior permanent magnet brushless d.c. motor;
IM	Induction machine;
PI	Proportional-Integral controller;
PM	Permanent magnet;
PLL	Phase-locked loop;
PWM	Pulse width modulation;
PMSM	Permanent magnet synchronous motor;
RMS	Root mean square;
SM	Synchronous machine;
SmCo	Samarium Cobalt – alloy

Indices/Subscripts

a, b, c	Indices for stator phases a, b, and c;
d	Direct;
q	Quadrature;
e	Electrical quantity;
m	Mechanical quantity;
s	Stator quantity;
σ	Leakage;
n	Rated;
max	Maximum;
y	Yoke;
th	Teeth;

Superscripts

*	Reference quantity;
^	Estimated quantity;

Chapter 1

Brushless permanent magnet machines and their control

Abstract

This chapter offers a comprehensive overview of brushless permanent magnet synchronous machines and their control, focusing on BLDC machines. First, a brief introduction to brushless PM machines is presented. In sections 2 and 3, a classification of brushless PM motors and drives is offered. Section 4 offers an introduction to material used for brushless PM machines. The basics of brushless DC motor operation are presented in section 5. Finally, an overview of control methods and application areas for brushless DC PM motors are highlighted.

1.1. Introduction

Synchronous motors (SMs) are in general three-phase AC fed in the stator, and DC (or PM) excited in the rotor. The rotor tends to align itself with the rotating field produced by the stator. The rotor magnetization is produced by the permanent magnets in the rotor or by external magnetization (e.g. a DC supply feeding the field winding). These motor types are called permanent magnet synchronous motors (PMSMs) and separately excited synchronous motors (SM), respectively.

The use of permanent magnets excitation in electrical machines brings the following advantages [1]:

- higher torque or output power per unit volume than using electromagnetic excitation,
- simplification of construction and maintenance,
- lower cost for some types of machines,
- faster dynamic performance than motors with electromagnetic excitation (higher magnetic flux density in the air-gap),
- improved efficiency because the copper losses are reduced; also the iron losses are reduced.

The main drawbacks of the permanent magnet excitation are [2]:

- high cost of the permanent magnets with very good quality,
- demagnetization at high temperature—accordingly the machine design and cooling should take this fact into account,
- increased constructive effort for permanent magnet fixture on/in rotor,
- additional effort for field weakening control.

The history of permanent magnets motors has been dependent on the development of the magnet materials [3]. The PM excitation in electrical machines was for the first time used in the early 19th century, but the use of very poor quality

PM materials (steel or tungsten steel) soon discouraged their use in favor of electromagnetic excitation systems. In 1932, the invention of Alnico revived the PM excitation systems. Their application has been limited to small and fractional horsepower DC commutator machines.

In the 20th century, the cage induction motors have been the most popular electric motors, due to their robust construction. Improvements in the field of power electronics and control technology have increased their application to electrical drives. The disadvantages of cage induction motors are their small air-gap, and lower efficiency and power factor as compared to synchronous motors. These limitations have led to the development of brushless PM motors which have PM excitation on the rotor [1, 4].

The development of the rare earth PMs, made possible to manufacture also large PM synchronous motors, making the use of brushless PM motors an attractive option. Rare earth PMs can not only improve the steady state performance of the machine but also the power density (high power-to-volume ratio), dynamic performance, and quality. As the magnet materials have been further developed and their market prices decreased, the use of these motors has been growing. However, in the last decades the increasing interest in brushless motors has also been caused by continuous technology development in power semiconductors, microprocessors/logic ICs, adjustable speed drivers (ASDs) control schemes. The improvements in the control of brushless PM motors were due to the introduction of advanced control theory and its applicability with powerful microprocessors. This led to a much easier and more cost effective control of brushless motors, with the possibility of operating the motor over a wide speed range and still maintaining a good efficiency.

The advancements in geometries and design innovations have made possible the use of brushless PM motors in many domestic, commercial and industrial applications. Brushless PM machines are suitable for position control in machine tools, robotics and high precision servos, speed control and torque control in various industrial drives and process control applications, due to their excellent dynamic capability, reduced losses and high torque/weight ratio.

Brushless PM motors have found applications in diverse fields, such as domestic appliances, automobiles, transportation, aerospace equipment, power tools, toys, vision and sound equipment and healthcare equipment ranging from microwatts to megawatts.

1.2. Brushless permanent magnet machine types and topologies

A “brushless” motor is a motor in which all components associated with sliding contacts are eliminated. These components include brushes, commutators, slip-rings required in a conventional DC motor or synchronous AC motor for connection to the rotor windings. In general, there can be recognized three main categories of brushless permanent magnet electrical machines [1, 5]:

- brushless DC machines (BLDC),
- brushless AC machines (BLAC),
- special brushless machines.

Brushless DC machines are derived directly from the classical DC machine by replacing the commutator and brushes with an electronic power supply. The motor is often designed to have a trapezoidal back-EMF waveform and the current waveforms are square (trapezoidal), with alternating polarity. Only two phase windings (for wye-connection) conduct the current at the same time, and the

1.2. Brushless permanent magnet machine types and topologies 17

switching pattern is synchronized with the rotor angular position (electronic commutation). Fig. 1.1 shows a typical example. Permanent magnets (mounted on the rotor surface) are generally used for excitation.

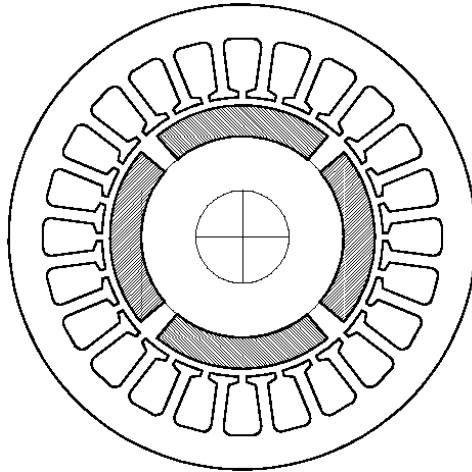


Fig. 1.1. Brushless permanent-magnet motor. This nonsalient-pole motor can be either "brushless DC" or "brushless AC".

Brushless AC machines are similar to brushless DC machines, but the back-EMF waveform is designed to be sinusoidal and the current waveform is also controlled to be sinusoidal. They are used in servo systems where smooth torque control is required. Resolvers are often used for shaft position feedback. In some cases the permanent magnets are mounted inside the rotor, as shown in Fig. 1.2. This tends to introduce **saliency** and a reluctance torque component. The saliency can also be helpful when the motor is to operate at constant power over a wide speed range — as, for example, in drives for electric vehicles.

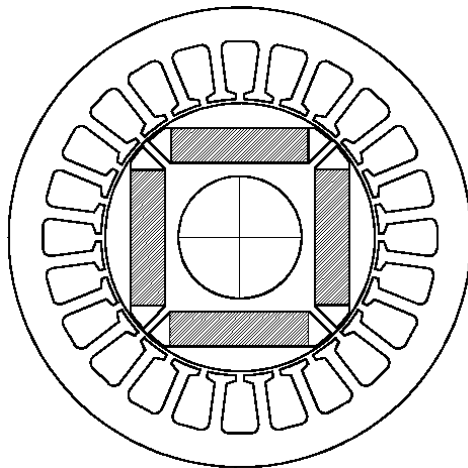


Fig. 1.2. Interior-permanent-magnet brushless AC motor.

Special brushless machines not derived from classical DC or AC machines. This category covers a huge range of different designs, including a wide variety of blower motors (Fig. 1.3 – the exterior-rotor motor has a tapered air-gap to ensure self-starting from any rotor position), timing motors, and others. Often the manufacturing volumes of these motors are in millions.

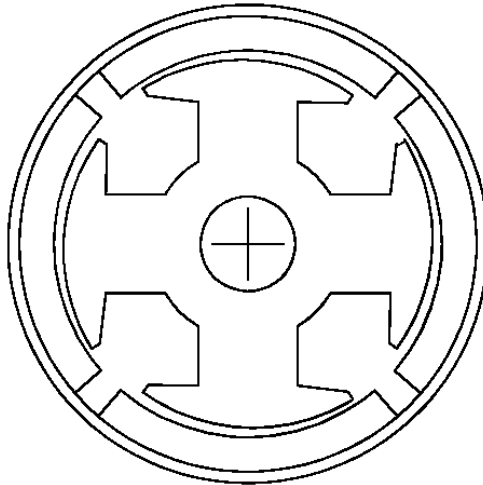


Fig. 1.3. Single-phase permanent-magnet motor.

Brushless permanent magnet DC and AC synchronous motors designs are practically the same: with a polyphase stator and PMs located on/in the rotor.

The armature current of brushless permanent magnet AC and DC motors is not transmitted through brushes, which have wear limitations and require maintenance. Another advantage of the brushless motor is the fact that the power losses occur mainly in the stator, where the heat can be easily transferred through ribbed frame or, in larger machines, water cooling systems can be used. Consequently the power density can be increased in comparison with a DC commutator motor. Considerable improvements in dynamics can be achieved because the air-gap magnetic flux density is high, the rotor has a lower inertia, and there are no speed-dependent current limitations. Thus, the volume of a brushless PM motor can be reduced by 40 to 50% while still keeping the same rating as that of a PM commutator motor [1].

The brushless permanent magnet AC and DC (moving magnet rotor) are designed as [1-11]:

- motors with conventional slotted stators,
- motors with slotsless (surface-wound) stators,
- cylindrical type:
 - surface magnet rotor (Fig. 1.4a, 1.4b, 1.4c),
 - inset magnet rotor (Fig. 1.4d),
 - interior magnet rotor (Fig. 1.4e, 1.4f, 1.4g),
 - rotor with buried magnets symmetrically distributed (Fig. 1.4h),
 - rotor with buried magnets asymmetrically distributed according to German patent 1173178 assigned to Siemens, also called *Siemosyn* (Fig. 1.4i).

1.2. Brushless permanent magnet machine types and topologies 19

- disk type, also called axial flux permanent magnet (AFPM):
 - single-sided (Fig. 1.5a),
 - double-sided (Fig. 1.5b, 1.5c),
 - with internal rotor (Fig. 1.5b),
 - with internal stator (armature) (Fig.1.5c),
 - multi-stack (Fig. 1.5d).

The stator (armature) winding of brushless PM motors can be made of coils distributed in slots, concentrated non-overlapping coils or slotless coils.

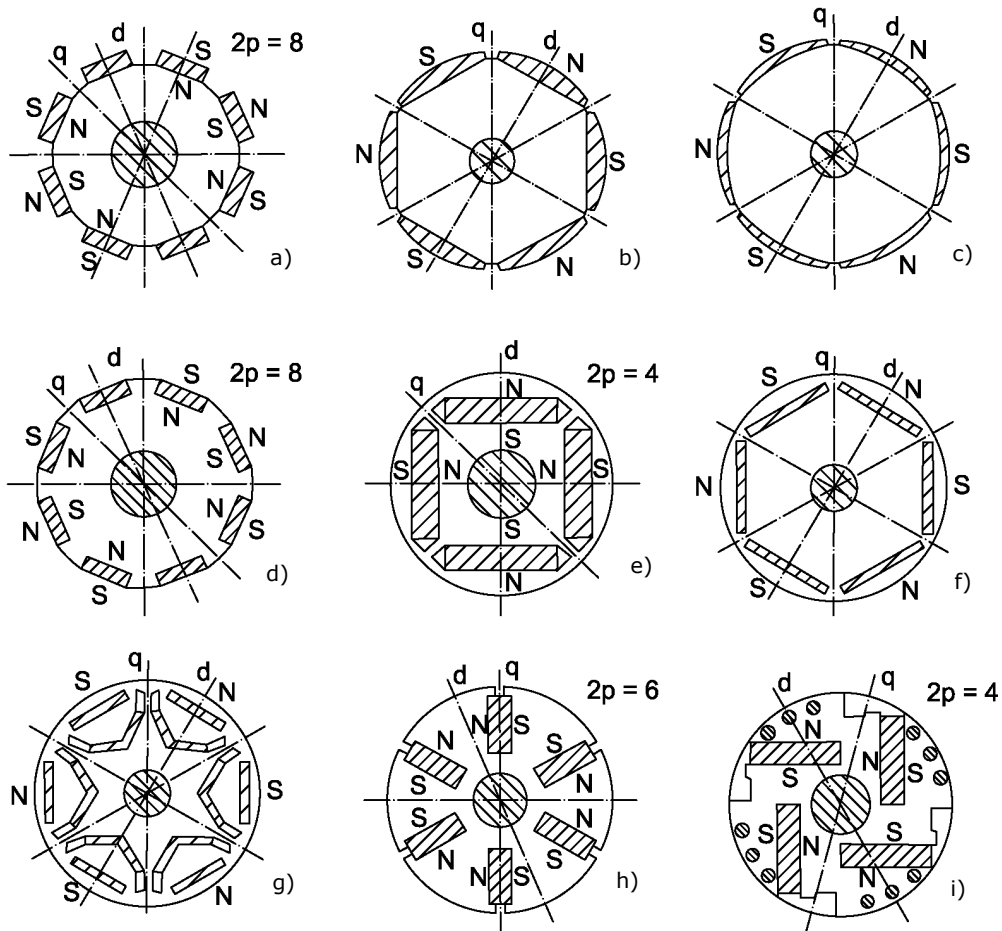


Fig. 1.4. Rotor configurations for PM synchronous motors: a) uniform thickness surface-magnet rotor, b) bread loaf magnets, c) decentred magnets, d) inset-magnet rotor, e) and f) interior single-layer magnets, g) interior double layer magnets (folded magnets), h) rotor with buried (spoke) magnets symmetrically distributed, i) rotor with buried magnets asymmetrically distributed [1].

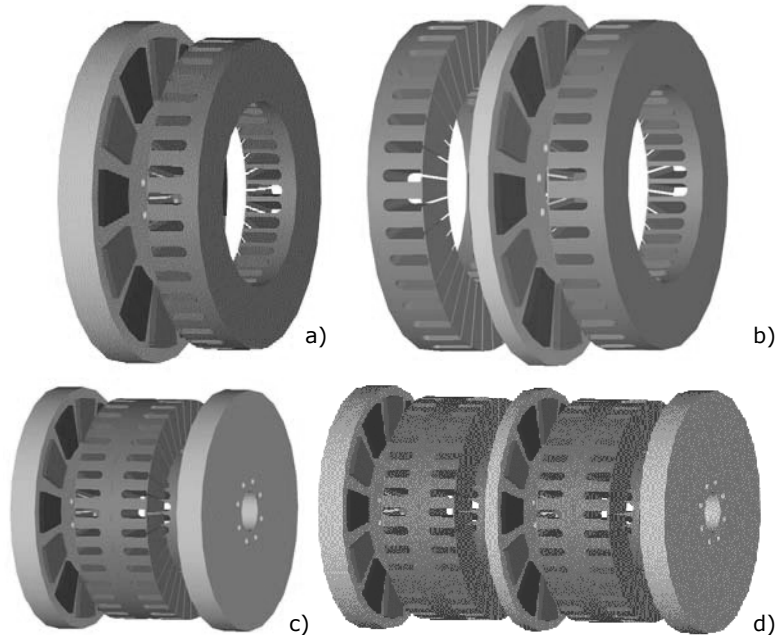


Fig. 1.5 AFPM motor configurations: a) single-sided, b) double-sided with internal rotor, c) double-sided with external rotor, d) multi stack [12].

1.3. Brushless permanent magnet motor drives

Basically, all electromechanical drives can be divided into constant-speed drives, servo drives and variable-speed drives [1].

A **constant-speed drive** implies a synchronous motor alone, which keeps the speed constant without an electronic converter, and feedback or any other motor when there is less restriction on the speed variation tolerance.

A **servo system** is a drive with speed or position feedback for precise control where the response time and the accuracy with which the motor follows the speed and position commands are extremely important.

In a **variable-speed drive** the accuracy and the response time with which the motor follows the speed and position commands are not important, but the requirement is to change the speed over a wide range.

We may distinguish three ways to classify brushless PMSM drives: with respect to current waveform, voltage frequency correlation, motion sensor presence.

From the point of view of current waveform, we may distinguish:

- sinusoidally excited motors – Fig. 1.6a,
- square wave (trapezoidally excited) motors – Fig. 1.6b.

From the point of view of motion sensor presence, there are:

- drives with motion sensors,
- drives without motion sensors (sensorless).

Finally, sinusoidal current drives may be:

- scalar (V/f) control – a damper cage in the rotor is required,
- vector control (current or current and voltage),
- direct torque and flux control (DTFC).

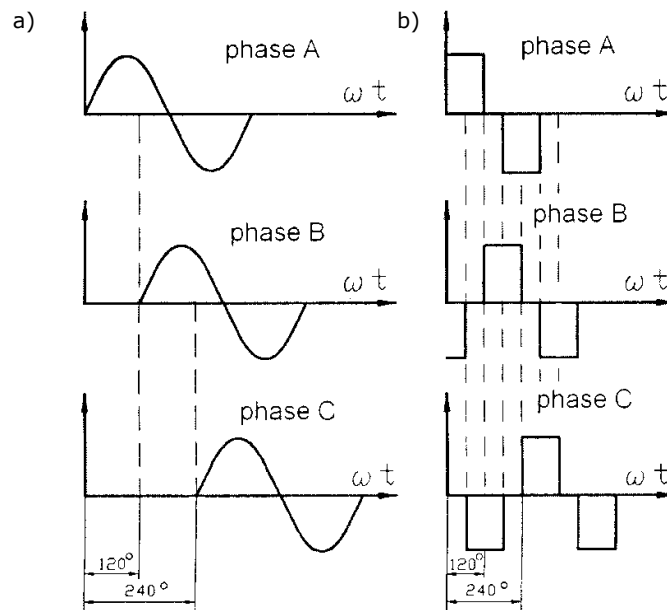


Fig. 1.6. Basic armature waveforms for three phase brushless PM motors: a) sinusoidally excited, b) square wave.

1.3.1. Sinusoidal PMSM drives

Sinusoidally excited motors are fed with three phase sinusoidal waveforms in order to get optimal torque quality (Fig. 1.6a) and operate on the principle of a rotating magnetic field. They are called sinwave motors or PM synchronous motors. All phase windings conduct at a time. In most cases overlapped windings are employed in the stator. For the rotor mostly skewed surface permanent magnets are used in order to induce a sinusoidal back-EMF. Complex, cost-intensive high-resolution rotor position sensors like encoders or resolvers are mandatory for the sinusoidal current control. Also at least two current sensors are necessary to impose the shape of the phase currents.

This sinusoidal PMSM drive is the only proper technology for high performance applications due to the low torque ripple.

1.3.2. Brushless permanent magnet DC drives

Square wave motors are also fed with three-phase waveforms by 120° one from another, but these waveforms are rectangular or trapezoidal (Fig. 1.6b). Such a shape is produced when the armature current (MMF) is precisely synchronized with the rotor instantaneous position and frequency (speed). The most direct and popular method of providing the required rotor position information is to use an

absolute angular position sensor mounted on the rotor shaft. Only two phase windings out of three conduct current simultaneously. Such a control scheme or electronic commutation is functionally equivalent to the mechanical commutation in DC motors. This explains why motors with square wave motors are called brushless DC motors. An alternative name used in power electronics and motion control is self-controlled synchronization.

The basic elements of a brushless DC motor drive are [1]: PM motor, inverter, line-side converter, shaft position sensor (encoder, resolver, Hall elements), gate signal generator, current detector, and controller (e.g., microprocessor or computer with DSP board). A simplified block diagram is shown in Fig. 1.7.

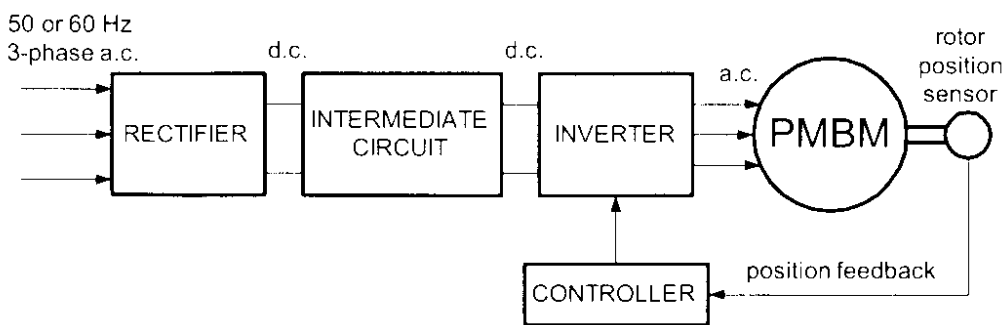


Fig. 1.7. Brushless DC motor drive [1].

1.4. Magnetic materials for brushless PM machines

1.4.1. Permanent magnet materials

There are three classes of PMs used for electric motors [1, 13-22]:

- Alnicos (Al, Ni, Co, Fe);
- Ceramics (ferrites), e.g. barium ferrite $\text{BaO} \cdot 6\text{Fe}_2\text{O}_3$ and strontium ferrite $\text{SrO} \cdot 6\text{Fe}_2\text{O}_3$;
- Rare-earth materials, i.e., samarium-cobalt SmCo and neodymium-iron-boron NdFeB.

Alnico

The main advantages of Alnico are its high magnetic remanent flux density, low temperature coefficients and high maximum service temperature (520°C). These advantages allow a high air-gap magnetic flux density at high magnet temperature. Its major drawbacks are low coercive force H_c and extremely nonlinear demagnetization curve (Fig. 1.8). Therefore, it is very easy not only to magnetize but also to demagnetize Alnico. Alnico has been used in PM DC commutator motors of disk type with relatively large air-gaps. This results in a negligible armature reaction magnetic flux acting on the PMs. Sometimes, Alnico PMs are protected from the armature flux, and consequently from demagnetization, using additional mild steel pole shoes. Alnicos dominated the PM motor market in the range from a few watts to 150 kW, between the mid 1940s and the late 1960s, when ferrites became the most widely used materials [1].

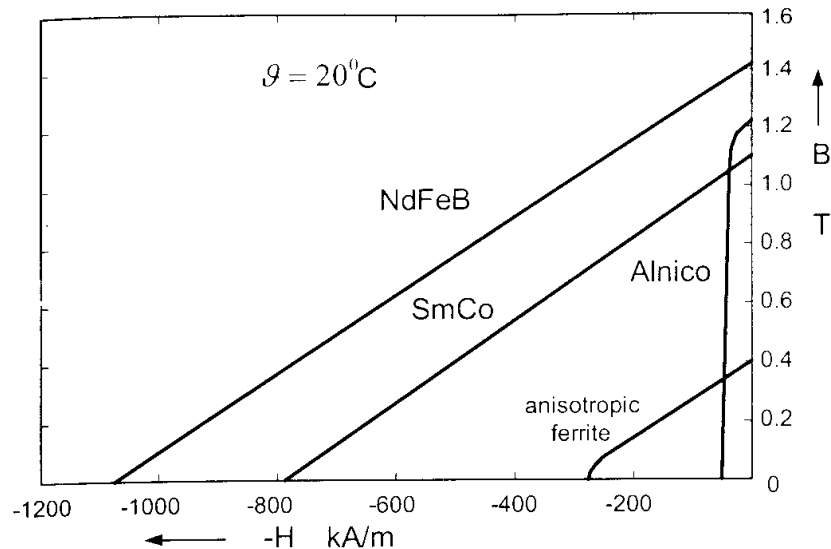


Fig. 1.8. Demagnetization curves for different permanent magnets at room temperature [1].

Ferrites

The development of barium and strontium ferrites started in the 1950s. A ferrite has remarkably higher coercive force and energy product $(BH)_{\max}$ than earlier materials. The main advantages of ferrites are their low cost and very high electric resistance (no eddy-current losses in the PM volume). Ferrite magnets are most economical in fractional horsepower motors and may show an economic advantage over Alnico up to about 7.5 kW [1]. Barium ferrite PMs (Fig. 1.9) are commonly used in small DC motors for automobiles and electric toys. Also larger machines with ferrite magnets are constructed, but, due to the relatively low remanence B_r (Fig. 1.8), it has been difficult to reach a sufficiently high air-gap flux density for high performance machines.

Rare-earth permanent magnets

The development of rare-earth magnets was the next milestone in advances of permanent magnetism. These offered high remanence and high coercive force resulting in a significantly higher available energy density $(BH)_{\max}$ than ferrites can achieve. These properties and the large reversible demagnetization range (high intrinsic coercive force H_{ci}) made these materials to be the superior choice for high performance machines. The first generation of these new alloys based on the composition SmCo_5 and invented in the 1960s has been commercially produced since the early 1970s. SmCo_5 has the advantage of high remanent flux density, high coercive force, high energy product, linear demagnetization curve, and low temperature coefficient (Fig. 1.8). The high price of the raw materials has prohibited a large scale use.

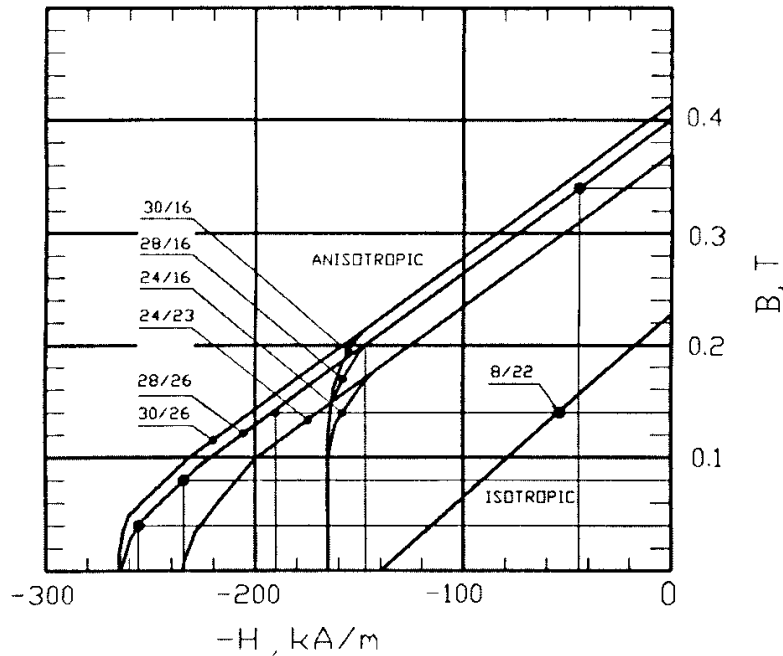


Fig. 1.9. Demagnetization curves of *Hardferrite* barium ferrites manufactured by Magnetfabrik Schramberg GmbH & Co., Germany [1].

Major efforts were made to find a magnet material with as good properties but constituted of cheaper raw materials. This research led to the neodymium-iron-boron NdFeB magnets, introduced in 1983 by Sumitomo Special Metals, Japan [1]. Although cheaper than SmCo and of even higher energy density, NdFeB is not always superior, due to its lower thermal stability, caused by lower Curie temperature, and its reactivity, which leads for instance to corrosion problems. In contrary to ferrites the conductivity of rare-earth alloys can yield eddy current losses. Some of these problems can be overcome by embedding the rare-earth powders in a matrix, for instance in resin or, for flexible magnets, rubber (also used with ferrite powder). Fig. 1.10 illustrates the advances of permanent magnet materials. NdFeB magnets have great potential for considerably improving the performance-to-cost ratio for many applications. For this reason they will have a major impact on the development an application of PM apparatus in the future.

A problem of NdFeB magnets is their reactivity. This leads to corrosion and subsequently loss of magnetic properties. Therefore this magnets are often coated, (nickel, aluminum chromate or polymer coatings), increasing the costs of the magnets. An alternative is to ensure complete sealing in the motor production process. This can be achieved for example by embedding the magnets entirely in resin.

In most properties, SmCo magnets are superior to NdFeB magnets. Only the maximum energy product at room temperature is higher for NdFeB. However, the high price of SmCo normally limits its use in commercial drives. For special applications the increased price can be justified in high performance servo drives. Fig. 1.11 illustrates the demagnetization flux density-magnetic field strength BH curves of the NdFeB magnets at different temperatures.

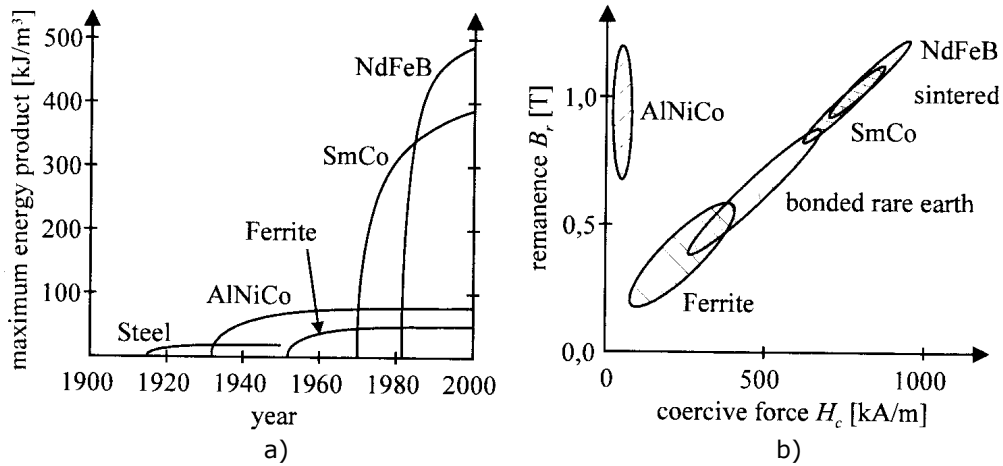


Fig. 1.10. Development of magnet materials energy product a), and comparison in terms of remanence and coercivity at room temperature b) [21].

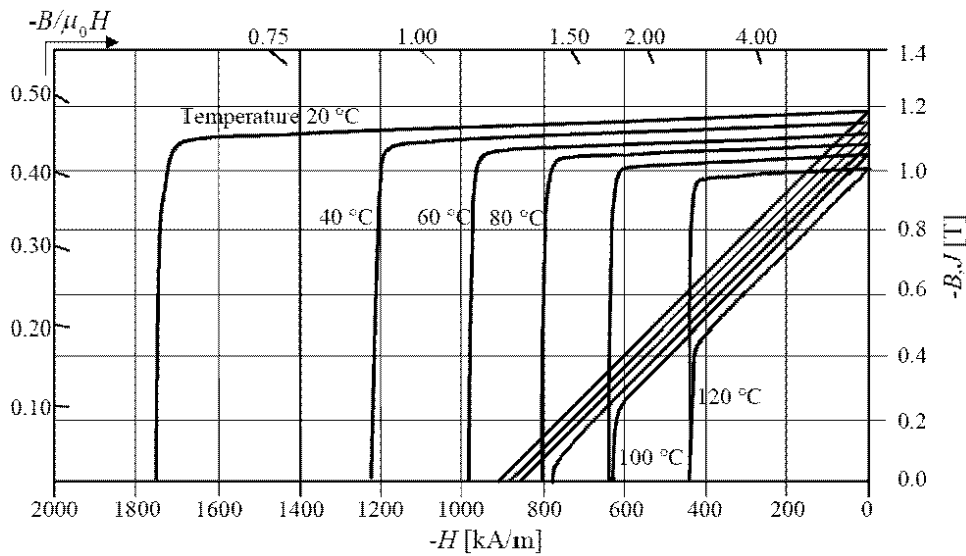


Fig. 1.11. BH and JH curves of NdFeB magnets in the second quadrant. An increase of 100 °C in the temperature, decreases the remanence flux density by almost 20 %. Also the so-called knee-point, where the polarization J is lost and the irreversible demagnetization starts to take place, occurs at lower demagnetizing field strengths H as the temperature increases [22].

1.4.2. Iron core materials

Classical soft magnetic materials – cold rolled magnetic lamination (CRML) steel – are still widely used in most electric motors as the primary flux-carrying path. For up to 150 Hz maximum switching frequency, general silicon-laminated cores made of 0.5 mm (0.65 mm for increased productivity) unoriented grain laminations are used. For fundamental frequencies above 150 Hz, thinner

laminations (0.2 mm or less) are used, to reduce the eddy current losses. The magnetization curves for a few typical soft magnetic materials are presented in Fig. 1.12.

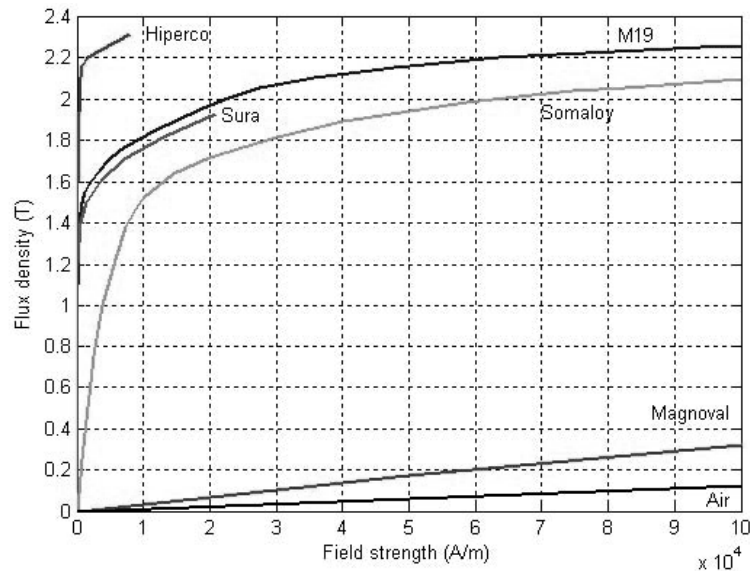


Fig. 1.12. Magnetization curves for typical soft magnetic materials [23].

An important characteristic of the soft magnetic materials is the dependency of the core losses versus flux density amplitude and frequency. The core losses are divided into eddy current and hysteresis losses. M19 and SURA are two widely used trade names for silicon laminations. Hiperco50 is a trade name for a high saturation flux density laminated material, with up to 50% cobalt and moderate losses at frequencies below 500 Hz. Thin laminations such as SURA007 (0.18 mm) have shown acceptable losses at 2500 Hz [23]. Magnoval is a sintered material with low relative magnetic permeability ($\mu_r = (3-5) \cdot \mu_0$) used for slot wedges to decrease PM flux density pulsations, and cogging and total torque pulsations, at the cost of higher leakage and synchronous inductances. Magnoval is also good for increasing the machine inductance in high-frequency machines, reducing the current ripple.

1.5. Operation principle of brushless DC motor

For a brushless DC motor, the air-gap flux density waveform is essentially a square wave, but fringing causes the corners to be somewhat rounded [24]. As the rotor rotates, the waveform of the voltage induced in each phase with respect to time is an exact replica of the air-gap flux density waveform with respect to rotor position. Because of fringing, the back-EMF waveform takes on a trapezoidal shape. The shape of the back-EMF waveform distinguishes the BLDC motor from the permanent magnet synchronous motor (PMSM), which has a sinusoidal back-EMF waveform. This has given rise to the terminology “trapezoidal motor” and “sinusoidal motor” for describing these two permanent magnet AC (PMAC) machines.

A 3-phase brushless DC motor is generally designed so that the flat top of the phase back-EMF waveform is just over 120° wide [5, 24-30]. Then each phase is supplied with a current waveform consisting of blocks of constant current, 120° wide. During each 120° period, the electromagnetic power conversion is $e_a \cdot i_a = T_e \cdot \omega_m$, where T_e is the electromagnetic torque. If the EMF and current waveforms are sufficiently flat during this period, and the speed is essentially constant, T_e is also constant.

Fig. 1.13 shows the ideal waveforms for a brushless DC motor (BLDC). Due to the fact that the PM produces a square wave air-gap flux distribution (Fig. 1.13a), the stator MMF is supposed to be rectangular. Consequently, the PM flux linkage in the stator winding $\lambda_{aPM}(\theta_m)$ varies linearly with rotor position (Fig. 1.13b). Finally the phase EMF e_a is rectangular with respect to rotor position (Fig. 1.13c).

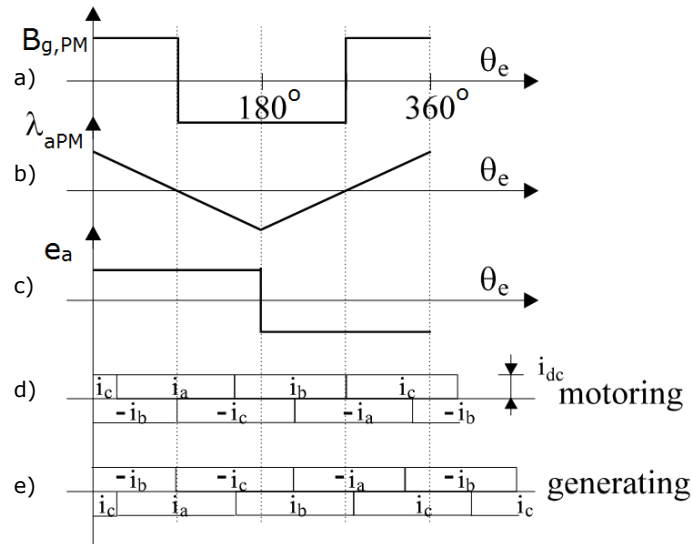


Fig. 1.13. Ideal waveforms for BLDC ($\theta_e = p \cdot \theta_m$): a) PM air-gap flux density, b) PM flux per phase a, c) EMF in phase a, d) ideal currents for motoring, e) ideal currents for generating [27].

For motoring (and zero advance angle) the phase currents are in phase with the EMFs (Fig. 1.13d). On the other hand, for an advancing angle equal with π , the electromagnetic power becomes negative and regenerative braking mode is obtained (Fig. 1.13e) [27].

By Faraday's Law the phase EMF is

$$e_a = -\frac{d\lambda_{aPM}(\theta_m)}{dt} = -\frac{d\lambda_{aPM}(\theta_m)}{d\theta_m} \cdot \frac{d\theta_m}{dt} = -\frac{d\lambda_{aPM}(\theta_m)}{d\theta_m} \cdot \omega_m \quad (1.1)$$

where ω_m is the angular velocity in mechanical rad/s and θ_m is the rotor position in mechanical radians. As long as the flux linkage is varying linearly with rotor position, the induced EMF is constant. When the flux-linkage reaches a maximum, it starts to decrease at the same absolute rate, and the EMF changes polarity. The result is a squarewave generated EMF, e_a .

The EMF can be calculated from the air-gap flux distribution. If $B_{g,PM}$ is the average flux-density over one pole-pitch, the air-gap flux $\Phi_{g,PM}$ is given by

$$\Phi_{g,PM} = \int_0^{\pi/p_1} B(\theta) \cdot r \cdot d\theta \cdot l_{stack} = B_{g,PM} \cdot \frac{\pi \cdot D \cdot l_{stack}}{2 \cdot p_1} \quad (1.2)$$

where r is the stator bore radius, D is the stator bore diameter ($= 2r$), l_{stack} is the stack length, and p_1 is the number of pole-pairs.

The maximum flux linkage per phase is $\lambda_{PM} = N_1 \cdot \Phi_{g,PM}$, and then the linear variation of phase flux linkage λ_{aPM} with rotor position θ_m is

$$\lambda_{aPM}(\theta_m) = \left(1 - \frac{p_1 \cdot \theta_m}{\pi/2}\right) \cdot \lambda_{PM} \quad (1.3)$$

were N_1 turns in series per phase.

From (1.1-1.3) the peak phase EMF is

$$e_a = \omega_m \cdot \frac{2 \cdot p_1}{\pi} \cdot \lambda_{PM} \quad (1.4)$$

Fig. 1.14 shows the commonly used bridge circuit for a 3-phase brushless permanent-magnet motor. For "squarewave" operation (Fig. 1.13), it has two phases conducting at any time. If the motor is wye-connected they carry the same current I in series, and the line-line EMF during each 60° interval is

$$e_{LL} = 2 \cdot e_a = k_E \cdot \omega_m \quad (1.5)$$

where k_E is the *back-EMF constant* in Vs/rad:

$$k_E = \frac{4 \cdot p_1 \cdot \lambda_{PM}}{\pi} \quad (1.6)$$

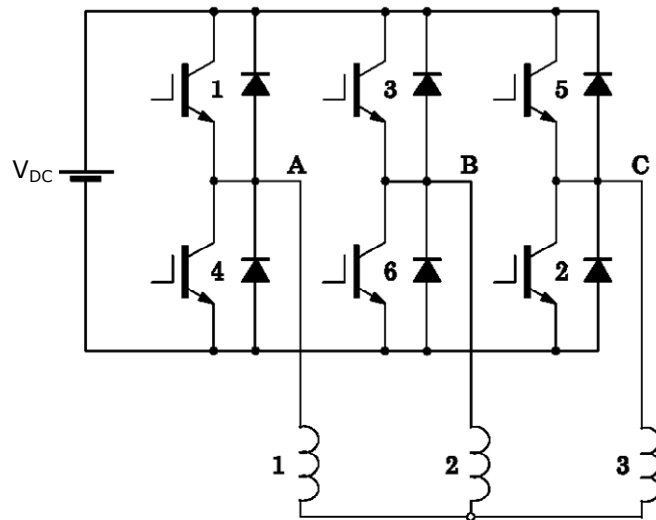


Fig. 1.14. Drive circuit for wye-connected brushless DC motor.

The electromagnetic power is $e_{LL} \cdot I$ and the electromagnetic torque is $T_e = e_{LL} \cdot I / \omega_m$. This can be written

$$T_e = k_T \cdot I \quad (1.7)$$

where $k_T = k_E$ is the *torque constant* in Nm/A. When driven this way with "two phases on", the motor behaves very similar to a permanent magnet DC commutator motor. It is because of this similarity in control characteristics that the trapezoidal PMAC motor is widely known as the BLDC motor, although this term is a misnomer as it is actually a synchronous AC motor. But it is also not a rotating field machine in the AC sense, because the armature MMF rotates in discrete steps of 60° electrical as opposed to a smooth rotation in other AC machines.

The torque is produced in blocks 60° wide, and there are 6 such blocks every electrical cycle. See Fig. 1.16.

The electronic power supply is called the drive. In low-power drives, MOSFETs are popular because they are easy to control, and they can be switched at high frequency. This makes it possible to regulate the current by chopping with low acoustic noise. MOSFETs are ideal for low-voltage drives because of their low on-state voltage drop. At higher powers and voltages, IGBTs are used.

Current and EMF waveforms are shown in Figs. 1.13 and 1.16 for the wye-connected motor, and in Fig. 1.17 for the delta-connected motor, whose drive circuit is shown in Fig. 1.15. The line current waveforms are identical for the two connections, as is the commutation table for the transistors (Table 1.1).

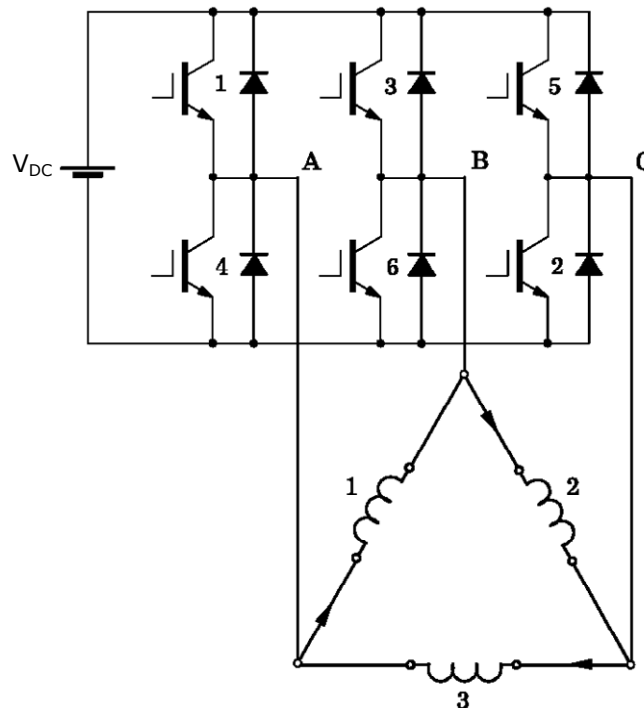


Fig. 1.15. Drive circuit for delta-connected brushless DC motor.

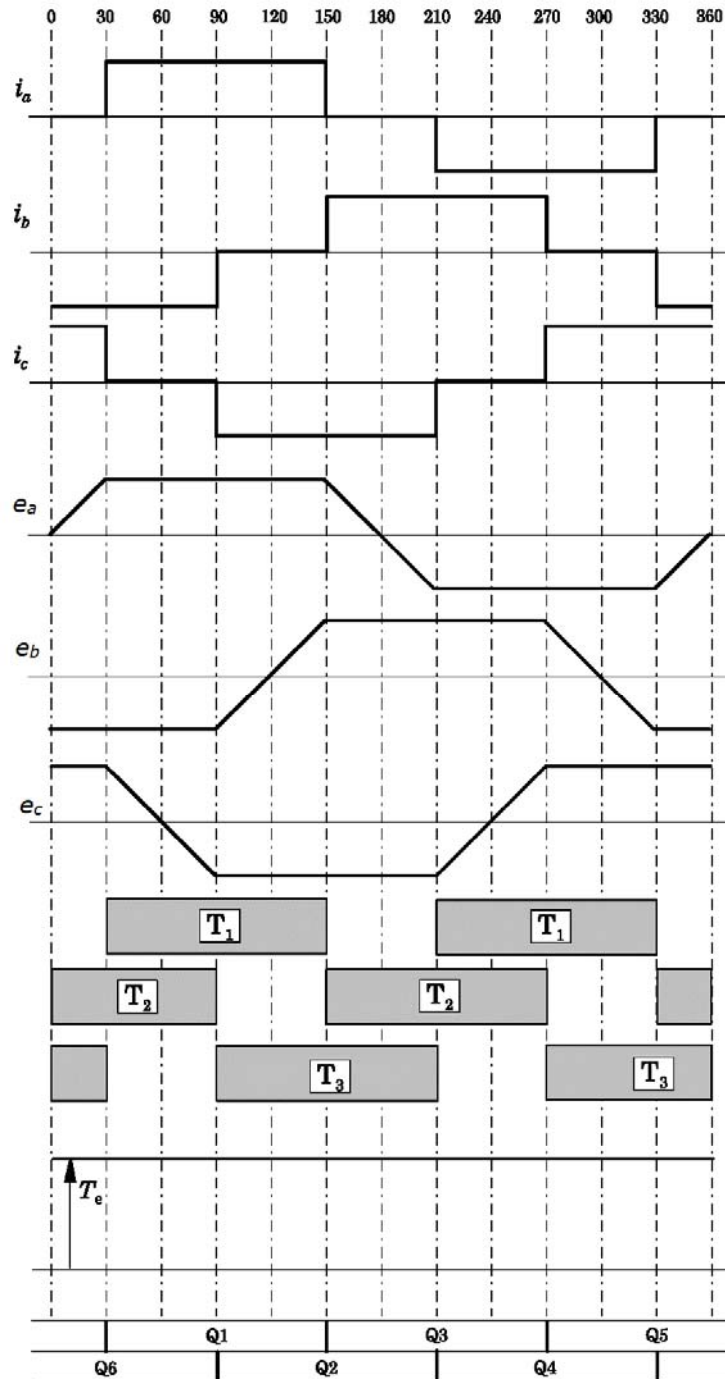


Fig. 1.16. Ideal waveforms of line currents i_a, i_b, i_c , phase EMFs e_a, e_b, e_c , phase torques T_1, T_2, T_3 , and total electromagnetic torque T_e in wye-connected brushless DC motor drive.

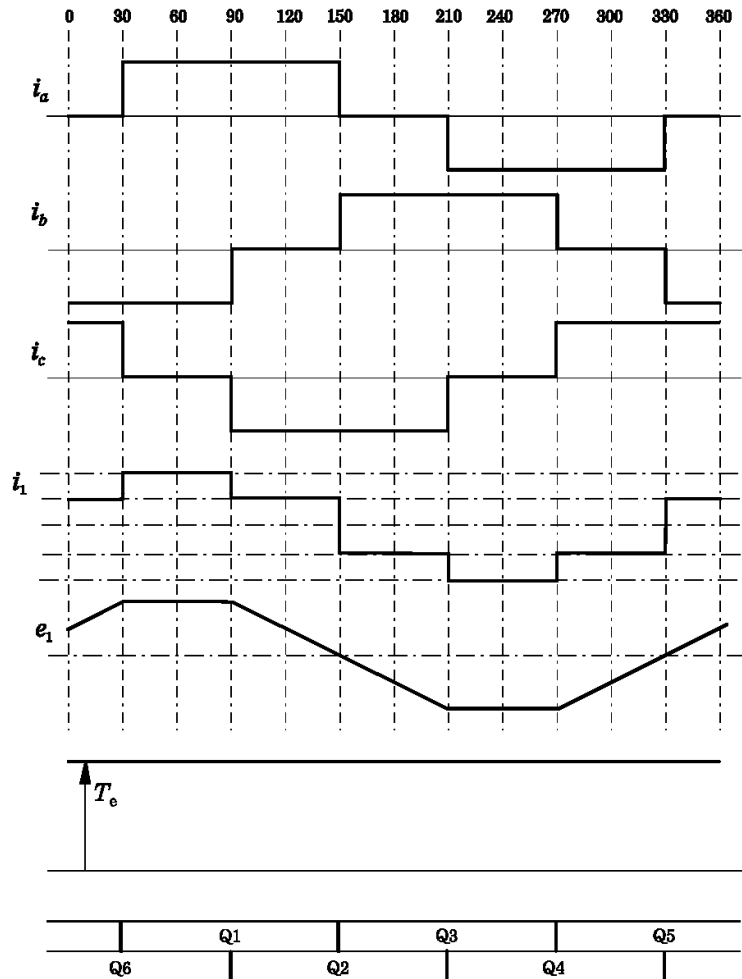


Fig. 1.17. Ideal waveforms of line currents i_a , i_b , i_c , phase current i_1 , phase EMF e_1 and total electromagnetic torque T_e in delta-connected brushless DC motor drive.

Table 1.1. Commutation table for Brushless DC Motor Drive: 120° squarewave line currents

Rotor position [°elec.]	Line			Phase leg A		Phase leg B		Phase leg C	
	A	B	C	Q1	Q4	Q3	Q6	Q5	Q2
330-30	0	-1	+1	0	0	0	1	1	0
30-90	+1	-1	0	1	0	0	1	0	0
90-150	+1	0	-1	1	0	0	0	0	1
150-210	0	+1	-1	0	0	1	0	0	1
210-270	-1	+1	0	0	1	1	0	0	0
270-330	-1	0	+1	0	1	0	0	1	0

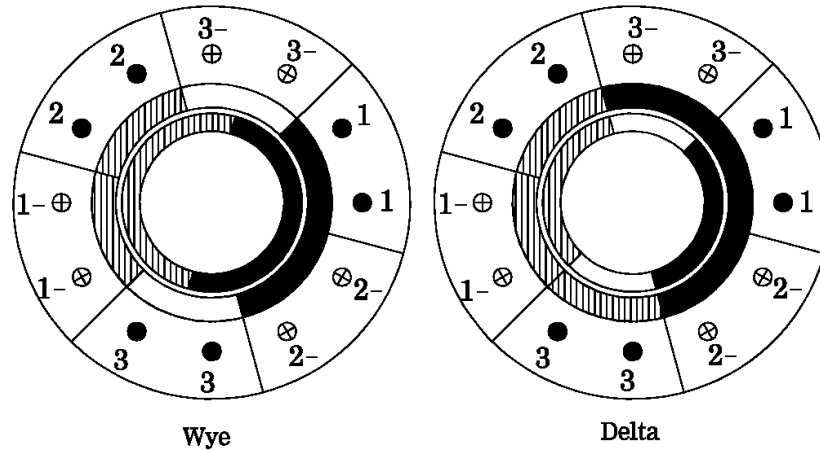


Fig. 1.18. Interaction of arc magnets and ampere-conductor "phasebelts" in wye- and delta-connected brushless DC motors [5].

Fig. 1.18 shows the interaction of the "phasebelts" of ampere-conductors with the magnet arcs in wye- and delta-connected motors. In the wye-connected motor, the magnet arc is 180° . With two phases conducting, the positive and negative "phasebelts" produce belts of ampere-conductors 120° wide. Therefore the motor can rotate 60° with no change in the overlap between each magnet and the belt of ampere-conductors nearest to it. This ensures constant torque over a 60° angle. At the end of each 60° period, the current is commutated from one phase into the next. In Fig. 1.18, phase 2 will be the next to turn off, and phase 3 will be the next to turn on, if the rotor is rotating counter-clockwise (CCW).

In the delta-connected motor, three phases are conducting at any time, giving 180° belts of ampere-conductors. To ensure that the overlap is constant for 60° , the magnet arc is reduced to 120° [5]. Clearly, in the delta-connected motor the phase windings have to withstand higher voltages than when the phases are wye-connected. Now, to reduce the leakage in 180° span magnets and account for fringing in 120° span magnets, as a compromise 150° span magnets are used [26].

1.6. BLDC control techniques

In general, a brushless DC motor drive system contains the BLDC motor, the PWM inverter, the speed and current controller, the current sensors and the position (speed) sensors (or estimators, for sensorless control).

The stator excitation for BLDC motors needs to be synchronized with rotor speed and position to produce constant torque. The controller performs the role of the mechanical commutator in the case of a DC machine, because of which the BLDC motor is also called the electronically commutated motor (ECM). The rotor position needs to be detected at every 60° electrical interval for the commutation. The most common method of sensing the rotor position is by means of a Hall effect position sensor. Rotor position sensing of three-phase BLDC motors requires three Hall switches spaced 120° electrical apart, mounted on the stator frame. The digital signals from the Hall sensors are then decoded to obtain the three-phase switching sequence for the inverter. In the block diagram of a BLDC motor drive shown in Fig. 1.19, this function is performed by the controller, which also processes the signal

from the DC link current sensor. Based on these two inputs, gating signals are provided to the six inverter switches.

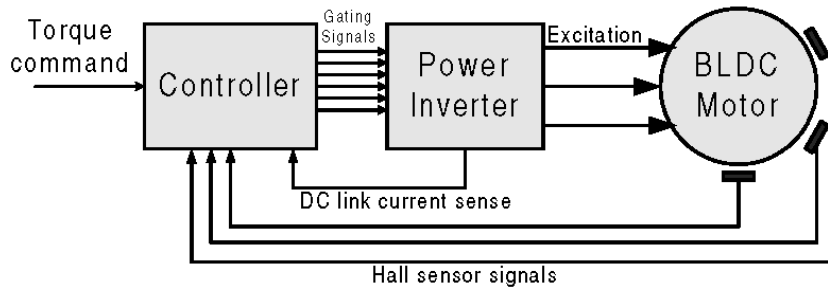


Fig. 1.19. BLDC motor drive schematic [24].

High-resolution optical encoders or resolvers can also be used to provide position feedback for applications in which their cost is justified by the improved performance. For applications requiring speed or position control, the speed and position control loops can be built around the inner current control loop. The possibility to operate with just three Hall sensors gives the BLDC PM motor an edge over its sinusoidal counterpart in low-cost applications. It should be mentioned that PMSM motors are also sometimes operated with rectangular currents, to minimize the cost of the position sensor, although the output torque waveform is far from ideal because of the mismatch between the motor and the inverter [24].

Motion sensorless control methods

There are several reasons to eliminate the use of electromechanical position sensors:

- the mechanical sensor is easily affected by temperature, humidity and vibration, which limits its applied range,
- the mechanical sensor increases the rotary inertia of the rotor shaft, as well as the dimension of the electric motor,
- reliability improvement of the system,
- cost reduction of electromechanical drives,
- in motors rated below 1 W the power consumption by position sensors can substantially reduce the motor efficiency,
- in compact applications, it may not be possible to mount position sensors.

For PM motors rated up to 10 kW the cost of the encoder is below 10% of the motor manufacturing cost and depends on the motor rating and encoder type. Operation without electromechanical sensors and associated cabling not only improves the reliability but also simplifies the installation of the system.

As compared to the sensorless control methods for PM synchronous motors with sinusoidal EMF waveforms, where all three phases are excited at any time, the sensorless approach is different for BLDC motors with trapezoidal EMF waveforms where only two out of three phases are simultaneously excited. The most commonly used sensorless control methods for BLDC are based on the back-EMF detection in an unexcited phase winding.

The basic idea of position sensorless control methods is to eliminate the position sensors (usually three Hall sensors). To accomplish this task, additional

circuitry and computational efforts are required to estimate the commutation instances of the brushless PM DC motor from the voltage and current signals which can easily be sensed. Therefore, sensorless techniques demand high performance processors with large memory and program codes for computation and estimation, as compared to sensor-based drive systems.

The position sensorless approach has many advantages, e.g. minimum installation cost, minimum space requirement, no environmental restrictions (e.g. high pressure and temperature environment in HVAC compressors), EMI free position information, reduced controller cost etc.

BLDC motor control schemes that eliminate the use of shaft position sensors have been intensively researched for the last two decades [31-40]. The main methods reported in the literature can be grouped as: back-EMF sensing, back-EMF integration, flux linkage based technique, freewheeling diode conduction, inductance variation sensing. Closed-loop observer based methods to address position sensing in PM machines and sensorless schemes for PM synchronous motors can be extended to brushless DC motors in the same fashion or with some modifications [4].

1) Back-EMF sensing techniques [37]

Switching instants for the inverter can be obtained by detecting the zero crossing of the phase back-EMF from the unexcited phase and introducing a speed-dependent time delay. Since back-EMF is zero at standstill and proportional to speed, the terminal voltage sensing method is not possible at low speeds, so a different algorithm has to be used for starting and low speed. Also, the estimated commutation points that are shifted by 30° from zero crossing of back-EMFs have position errors in transient state and at high speeds, because of the speed-dependent phase shifts introduced by the capacitors in the low-pass filters. With back-EMF sensing method, an operating speed range is typically around 1000–6000 RPM [33]. The zero-crossing points of the back-EMF in each phase may be an attractive feature to use for sensing, because these points are independent of speed and occur at rotor positions where the phase winding is not excited. There are several commercially available integrated circuits that use the back-EMF sensing technique for sensorless control. The availability of fast digital signal processor (DSP) controllers has enabled the implementation of many computationally intensive algorithms for rotor position sensing.

Another method that has a reduced operating speed range uses phase-locked loop circuitry. This method provides switching signals similar to Hall sensor outputs by using a phase-locked loop to lock on to the back-EMF of the inactive phase in every 60° interval.

The third harmonic back-EMF sensing method [38] provides a wider speed range than the terminal voltage-sensing method. The third harmonic component is obtained by summing the terminal voltages. This voltage signal does not necessitate much filtering. To obtain switching instants, the filtered third harmonic voltage signal can be integrated to find the third harmonic flux linkage. The third harmonic flux linkage lags the third harmonic of the phase back-EMF voltages by 30° . The zero crossings of the third harmonic of the flux linkage correspond to the commutation instants of the BLDC motor. To acquire correct commutation instants, sensing the positive or negative going zero-crossing of the back-EMF is essential [32].

The third harmonic method provides a wider speed range (100-6000 rpm) than the zero-crossing method, and does not introduce as much phase delay as the voltage-sensing method.

Starting techniques for sensorless schemes are generally open loop or rely on bringing the rotor to an initial known position. Open-loop starting is accomplished by providing a slowly rotating stator field that gradually increases in magnitude or frequency until the rotor starts rotating. However, the direction of rotation cannot be controlled using this method. This disadvantage can be overcome by the "align and go" starting method, in which the rotor is aligned to the specified position by energizing any two phases of the stator, and then the rotor is accelerated to the desired speed according to the given commutation sequences. The "align and go" method suffers demagnetization of permanent magnets due to large instantaneous peak currents at starting.

2) Back-EMF integration technique [33]

In this method, position information is extracted by integrating the back-EMF of the unexcited phase. Integration starts when the open phase's back-EMF crosses zero. A threshold is set to stop the integration that corresponds to a commutation instant. This method also has a problem at low speeds because of the error accumulation problem. As the back-EMF is assumed to vary linearly from positive to negative (trapezoidal back-EMF), and this linear slope is assumed speed-insensitive, the threshold voltage is kept constant throughout the speed range. Current advance can be implemented by changing the threshold. Once the integrated value reaches the threshold voltage, a reset signal is asserted to zero the integrator output. To prevent the integrator from starting to integrate again, the reset signal is kept on long enough to insure that the integrator does not start until the residual current in the open phase passes a zero-crossing. This type of control algorithm has been implemented commercially. The integration technique is less sensitive to switching noise, automatically adjusts to speed changes, but the low speed operation is poor because of the error accumulation problem [32].

3) Flux-linkage based technique [4, 32-34]

In this method, the flux linkage is calculated using measured voltages and currents. The fundamental idea is that the phase flux linkage can be estimated continuously by integrating the voltage after subtracting the resistive voltage drop from the phase voltage. The open-loop integration is prone to errors caused by drift, which can be reduced if the pure integrator is replaced by a low pass filter or an alternative integrator structure. From the initial position, machine parameters, and the flux linkages' relationship to rotor position, the rotor position can be estimated. In most electrical machines, it is not practical to measure the phase voltages directly, because of isolation related issues; therefore, applied phase voltage is estimated from DC supply voltage of the solid-state converter [4]. This method also has significant estimation error in low speed. Improper error of parameters and sampled current is reason for accumulation error at low speeds, in which the voltage equation is integrated in a relatively large period of time.

4) Freewheeling diode conduction [39]

This method uses indirect sensing of the zero crossing of the phase back-EMF to obtain the switching instants of the BLDC motor. In the 120° conducting wye-connected BLDC motor, one of the phases is always open-circuited. For a short period after opening the phase, there remains phase current flowing, via a freewheeling diode. This open phase current becomes zero in the middle of the commutation interval, which corresponds to the point where back-EMF of the open phase crosses zero. The biggest disadvantage of this method is the requirement of six additional isolated power supplies for the comparator circuitry, to detect current flowing in each freewheeling diode.

By this technique, 45-2300 rpm sensorless operation has been achieved. This technique outperforms the previously mentioned back-EMF methods at low-speeds.

5) Inductance variation sensing [40]

The fundamental concept behind the inductance variation is the rate of current change in the motor, which depends on the inductance of the winding. The inductance variation can be sensed after injecting a current pulse in the armature windings [40]. This scheme is particularly useful at zero speed, when there is no back-EMF. This method is suitable for the IPM (Interior Permanent Magnet) BLDC motor with high performance material, such as the NdFeB magnet. In order to get various inductance profiles, a large current pulse is required. Therefore, the application of inductance variation sensing methods may be useful to address the problem of starting, including identification of the rotor position before full excitation of the machine. Initial rotor position identification is particularly important in applications such as traction, where any reverse motion is not acceptable.

Despite implementation difficulties, several methods of position sensing from inductance variation have been applied for sensorless operation. Low frequency excitation pulse results in large current amplitudes, which facilitate easy detection, but can cause audible noise from the motor, whereas high frequency avoids audible noise, but reduces current amplitudes. Therefore, choosing an appropriate modulation frequency and modifying the machine rotor can further improve rotor position sensing using this method.

1.7. Applications

The advantages of BLDC motors and their rapidly decreasing cost, have led to their widespread application in many variable-speed drives [2, 26, 41-45]. Their high power density makes them ideal candidates for applications such as robotic actuators, computer disk drives, and office equipment. With their high efficiency, high power factor, and maintenance-free operation, domestic appliances and heating, ventilating, and air conditioning (HVAC) equipments are now increasingly employing BLDC motors in preference to DC and induction motors. They are also being developed for automotive applications such as electric power steering, power accessories, and active suspension, in addition to vehicle propulsion.

Fig. 1.20 gives a comparison of the different machine technologies, considering automotive applications [2]. Though all machine types have advantages, for high performance automotive applications, the brushless DC motor represents one of the best candidates.

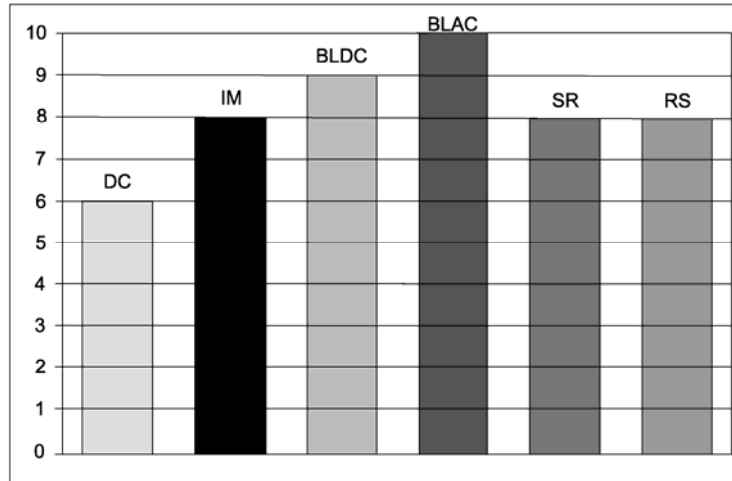


Fig. 1.20. Competing machine technologies for automotive applications: DC (brushed DC), IM (induction), BLDC (brushless DC), BLAC (brushless AC), SR (switched-reluctance), RS (reluctance synchronous) machines.

Classic electric motors are preferred for motion control, in general and household appliances, in particular. The most common motors for household appliances are single phase AC induction motors, including split phase, capacitor start, capacitor run types and universal motors. These motors operate at constant speed directly from AC mains, irrespective of efficiency; however, consumers now demand appliances with low energy consumption, improved performance, reduced acoustic noise, and many more convenience features. Therefore, household appliances are expected to be one of the largest end product market for brushless DC motors over the next few years. The major household appliances include fans, blowers, washing machines, room air-conditioners, refrigerators, vacuum cleaners, food processors, etc.

Electric and hybrid electric vehicles

Recently, there has been growing research interest for use of brushless DC motors in electric vehicles (EVs) and hybrid electric vehicles (HEVs), due to environmental concerns of vehicular emissions. An electric drive is one of the main parts of an EV/HEV and requires multidisciplinary power electronic technologies, including motors, converter topologies, switching devices, microprocessors/DSPs, and control strategies. The brushless DC motor is more suitable for EVs/HEVs and low power applications, due to high power density, less volume, high torque, high efficiency, overload capacity power, easy control, simple hardware and software, and low maintenance. It is very difficult to identify a unique drive solution for all kinds of electric vehicles (i.e. bikes, cars, vans, trucks, etc.). For many applications, the motor should have shape flexibility, compactness, robustness, high efficiency and high torque.

Fig. 1.21 shows a single rotor lamination of Toyota Prius PM brushless motor. The rotor with interior PMs has been selected because it provides wider torque-speed range under the size and weight restrictions, than other rotor configurations.

Electric motors for hybrid cars are typically rated from 30 to 75 kW. Water cooling permits weight reductions of 20% and size reductions of 30% as compared to forced-air motor cooling, while the power consumption of cooling system drops by 75% [1]. The use of a single water cooling system for the motor and solid state converter offers further size reductions.

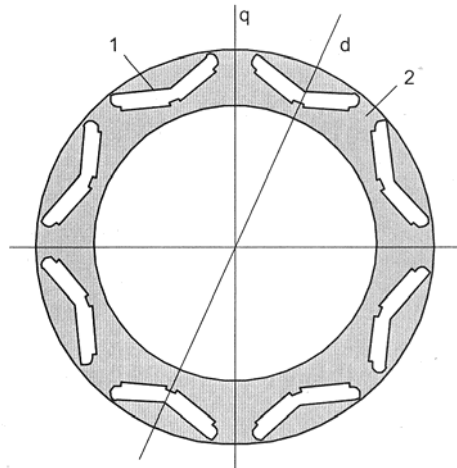


Fig. 1.21. Rotor punching of Toyota Prius electric motor: 1 – groove for PM, 2- ferromagnetic bridge between PMs.

Variable-speed cooling fans

Computers, instruments and office equipments use cooling fans with simple PM brushless DC motors that have inner salient pole stator and outer rotor ring magnet, as shown in Fig. 1.22. The rotor is equipped with fan blades.

Usually the fan is supplied from a low voltage DC source (12, 24, 42, or 115 V), making easy to control the fan electronically. The simplest method of controlling the DC brushless motor is on/off switching with a single transistor. More sophisticated methods for fan control are digital interface integrated circuits (ICs), equipped with remote temperature sensors [1].

Computer hard disk drive

Brushless DC motors have been used in various high-speed applications such as the hard disk drive (HDD - see Fig. 1.23) of computers, which run at very high speed to reduce the access time of the data written on the surface of a rotating disk [18, 44-45]. In order to run the motor at high speed, back-EMF constant is designed to be small, to reduce the voltage drop due to back-EMF. But, it results in small starting torque, therefore a long transient period. It is one of the drawbacks of a brushless DC motor in high-speed applications. Therefore a combination of unipolar and bipolar drives has been used, which utilizes the advantage of the large starting torque of a bipolar drive and the high operating speed of a unipolar drive. A DSP/FPGA based controller can be used to drive the brushless DC motor with the bipolar or unipolar method, and to switch from one method to the other at any speed.

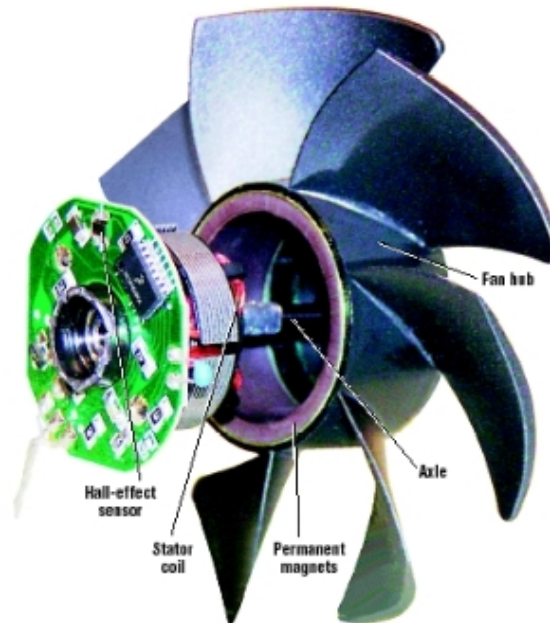


Fig. 1.22. PM brushless motor fan: two-phase inner stator with four concentrated coils, outer rotor with ring-shaped PM. Control electronics is mounted on the stator.



Fig. 1.23. An example of hard disk drive. The disk drive spindle motors are brushless DC motor with outer rotors designs.

CD players

Spindle drives are most often done with PM brushless motors connected to the disk platforms (Fig. 1.24). In most cases, CD spindle electromechanical drives use pancake brushless DC motors with many stator poles, so that the motor can run at low and very stable speeds. Brushless DC motors (shown in Fig. 1.23) can be found in CD players, video cassette players, and other consumer electronics drive systems [44-45].



Fig. 1.24. Pancake PM brushless motor with 12 concentrated stator coils and outer rotor with ring-shaped PM. The stator is integrated with control electronics.

Many other applications of PMBLDC motors have been reported, such as tread mills, washers, dexterous robotic hands, wheelchairs, compressors of household air conditioners, automotive HVACs and commercial freezers, fans [43], pumps and space mission tools.

1.8. Overview and conclusions

An overview of brushless permanent magnet synchronous machines and their control, focusing on BLDC machines, was presented.

A brief introduction to brushless PM machines was offered, highlighting the advantages of permanent magnet excitations over the conventional electrically excitations for synchronous machines. The higher efficiency and torque density of these machines are their main merits.

A classification of brushless permanent magnet motors types and drives was offered.

A review of permanent magnet materials and iron core materials used for brushless PM machines was presented.

The operation principle of brushless DC motor was presented, giving the ideal waveforms for the wye- and delta-connected BLDC motor drive.

BLDC motors are preferred for numerous applications; however, most of them require sensorless control of these motors. The operation of brushless DC motors requires rotor-position sensing for controlling the winding currents. The sensorless control would need estimation of rotor position from the voltage and current signals, which are easily sensed. A review of sensorless control methods for brushless DC motors was presented.

The main application areas of brushless DC motor were highlighted, with illustrated examples.

References

- [1] J.F. Gieras, "Permanent Magnet Motor Technology, Design and Applications", 3rd ed., CRC Press, Taylor and Francis Group, Boca Raton, FL, 2010.
- [2] D. Iles, "Automotive Permanent Magnet Actuation Technologies", PhD Thesis, Timisoara, 2005.
- [3] P. Campbell, "Permanent Magnet Materials and Their Application", Cambridge University Press, New York, 1996.
- [4] B. Singh and S. Singh, "State of the Art on Permanent Magnet Brushless DC Motor Drives", *Journal of Power Electronics*, Vol. 9, pp. 1-17, January 2009.
- [5] T.J.E. Miller, "SPEED's Electric Motors", Glasgow, 2002.
- [6] J.R. Hendershot and T.J.E. Miller, "Design of Brushless Permanent-Magnet Motors", Oxford University Press, New York, 1995.
- [7] B. Singh, B.P. Singh, S. Dwivedi, "A State of Art on Different Configurations of Permanent Magnet Brushless Machines", *IE (I) Journal – EL*, Vol. 78, pp. 63-73, June 2006.
- [8] B. Singh, "Recent Advancements in Permanent Magnet Brushless DC Motors", *Sadhana*, Vol. 22, Part 6, pp. 837-853, December 1997.
- [9] P. Salminen, "Fractional Slot Permanent Magnet Synchronous Motors for Low Speed Applications", PhD Thesis, Lappeenranta, Finland, 2004.
- [10] W.H. Yeadon and A.W. Yeadon, "Handbook of Small Electric Motors", McGraw-Hill, New York, 2001.
- [11] I. Şerban, M. Ferdowsi, E.G. Strangas, "Electrical Machines", Chapter 8 in "Systems, Controls, Embedded Systems, Energy, and Machines", 3rd ed., R.C. Dorf, CRC Press, Taylor and Francis, Boca Raton, FL, 2006.
- [12] S.K. Challa, "Comparative Study of Axial Flux Permanent Magnet Brushless DC Motor Operating with the Winding Connected in Single-Phase and Two-Phase System", Louisiana, 2006.
- [13] R. Krishnan, "Permanent Magnet Synchronous and Brushless DC Motor Drives", CRC Press, Taylor and Francis Group, Boca Raton, FL, 2010.
- [14] B.D. Cullity and C.D. Graham, "Introduction to Magnetic Materials", 2nd ed., John Wiley and Sons Inc., Hoboken, New Jersey, 2009.

- [15] M. Eshani, Y. Gao, A. Emadi, "Modern Electric, Hybrid Electric, and Fuel Cell Vehicles", 2nd ed., CRC Press, Taylor and Francis Group, Boca Raton, FL, 2010.
- [16] C.A. Gross, "Electric Machines", CRC Press, Taylor and Francis Group, Boca Raton, FL, 2007.
- [17] H.-W. Lee, "Advanced Control for Power Density Minimization of The Brushless DC Generator", PhD Thesis, Texas, 2003.
- [18] A.E. Fitzgerald, C. Kingsley, Jr., S.D. Umans, "Electric Machinery", 5th ed., McGraw-Hill Inc., 1990.
- [19] MAGCRAFT Advanced Magnetic Materials, "Permanent Magnetic Selection and Design Handbook".
- [20] DEXTER Magnetic Technologies, "Permanent Magnet Catalog".
- [21] E. Nipp, "Permanent Magnet Motor Drives with switched Stator Windings", PhD thesis, Stockholm, 1999.
- [22] J. Puranen, "Induction Motor Versus Permanent Magnet Synchronous Motor in Motion Control Applications: A Comparative Study", PhD Thesis, Lappeenranta, Finland, 2006.
- [23] I. Boldea and L.N. Tutelea, "Electric Machines: Steady State, Transients, and Design with MATLAB", CRC Press, Taylor and Francis Group, Boca Raton, FL, 2010.
- [24] H.A. Toliyat and T. Gopalarathnam, "AC Machines Controlled as DC Machines (Brushless DC Machines/Electronics)", Chapter 10 in "The Power Electronics Handbook", J.D. Irwin, CRC Press LLC, Boca Raton, FL, 2002.
- [25] D.C. Hanselman, "Brushless Permanent-Magnet Motor Design", McGraw-Hill Inc., 1994.
- [26] S.A. Nasar, I. Boldea, L.E. Unnewehr, "Permanent Magnet, Reluctance, and Self-Synchronous Motors", CRC Press, Boca Raton, FL, 1993.
- [27] I. Boldea and S.A. Nasar, "Electric Drives", 2nd ed., CRC Press, Taylor and Francis Group, Boca Raton, FL, 2006.
- [28] B.K. Bose, "Modern Power Electronics and AC Drives", Prentice Hall, 2002.
- [29] S.B. Ozturk, "Modelling, Simulation and Analysis of Low-Cost Direct Torque Control of PMSM Using Hall-Effect Sensors", Master Thesis, Texas, 2005.
- [30] R.M. Crowder, "Electric Drives and Their Controls", Oxford University Press, New York, 1998.
- [31] P. Pillay and P. Freere, "Literature Survey of Permanent Magnet AC Motors and Drives", *IEEE IAS Annual Meeting Conference Record*, Vol. 1, pp. 74-84, October 1989.
- [32] J.P. Johnson, M. Ehsani, Y. Güzelgünler, "Review of Sensorless Methods for Brushless DC", in *Conference Record IEEE-IAS Annual Meeting*, Vol. 1, pp. 143-150, 1999.
- [33] T.-H. Kim and M. Ehsani, "Sensorless Control of the BLDC Motors From Near-Zero to High Speeds", *IEEE Trans. on Power Electronics*, Vol. 19, No. 6, pp. 1635-1645, November 2004.

-
- [34] T.-H. Kim, H. W. Lee, M. Ehsani, "State of the Art and Future Trends in Position Sensorless Brushless DC Motor/Generator Drives", in *Proc. IEEE Industrial Electronics Society Conf.*, pp. 1718-1725, 2005.
- [35] N. Muruganatham and S. Palani, "Sensorless Methods for Brushless DC Motor With Trapezoidal Back-EMF – A Survey", *International Journal of Applied Engineering Research*, Vol. 4, 2009.
- [36] D. Montesinos, S. Galceran, F. Blaabjerg, A. Sudria, O. Gomis, "Sensorless Control of PM Synchronous Motors and Brushless DC Motors - An Overview and Evaluation", in *Proc. European Conf. Power Electronics and Applications*, pp. 1-10, 2005.
- [37] J. Shao, "Direct Back EMF Detection Method for Sensorless Brushless DC (BLDC) Motor Drives", Master Thesis, Blacksburg, Virginia, 2003.
- [38] J. X. Shen, Z. Q. Zhu, D. Howe, "Sensorless Flux-Weakening Control of Permanent Magnet Brushless Machines Using Third-Harmonic Back-EMF", in *Proc. IEEE IEMDC*, Vol. 2, pp.1229-1235, 2003.
- [39] S. Ogasawara and H. Akagi, "An Approach to Position Sensorless Drive for Brushless DC Motors," *IEEE Trans. Industrial Applications*, Vol. 27, pp. 928-933, Sept./Oct. 1991.
- [40] G.H. Jang, J.H. Park, J.H. Chang, "Position Detection and Start-up Algorithm of A Rotor in A Sensorless BLDC Motor Utilizing Inductance Variation", *IEE Proc – Elec. Power Applications*, Vol. 149, No. 2, pp. 137-142, March 2002.
- [41] O. Wallmark, "Control of Permanent-Magnet Synchronous Machines in Automotive Applications", PhD Thesis, Göteborg, Sweden, 2006.
- [42] Z. Wu, J. Wang, J. Ying, J. Zeng, "Sensorless Brushless DC Motor Drive for Air-Conditioner Compressor", in *Proc. Fifth Int. Conf. Electrical Machines and Systems*, Vol. 2, pp. 968-971, 2001.
- [43] A. Lelkes, and M. Bufe, "BLDC Motor for Fan Application with Automatically Optimized Commutation Angle", in *Proc. IEEE PESC*, Vol. 3, pp. 2277-2281, 2004.
- [44] T. Kenjo and S. Nagamori, "Permanent-Magnet and Brushless DC Motors", Oxford University Press, New York, 1985.
- [45] T. Kenjo, "Electric Motors and Their Controls", Oxford University Press, New York, 1991.

Chapter 2

(6+6) Slot/8 Pole Synchronous Machine: Analytical Model of Interior Permanent Magnet Rotor

Abstract

This chapter presents a synthesis of fractional slot concentrated winding permanent magnet synchronous machines. The determination of the machines with concentrated windings and irregular distribution of slots is depicted here.

The final part of this chapter presents the implementation of the electromagnetic design for a fractional slot concentrated winding permanent magnet synchronous machine case study: an interior permanent magnet synchronous motor with 8 rotor poles and nonuniform (6+6) stator slots and concentrated windings fed with trapezoidal currents.

2.1. Introduction

The winding configurations most commonly used for three-phase PM brushless machines, can be classified as follows [1]:

- overlapping, which can be either distributed (Fig. 2.1a, $q = 2$) or concentrated (Fig. 2.1b, $q = 1$),
- nonoverlapping, i.e., concentrated, which can be either double-layer (with all teeth wound, Fig. 2.1c) or single-layer (with alternate teeth wound, Fig. 2.1d).

Fig. 2.2a and b shows actual prototypes of both types of nonoverlapping (fractional slot concentrated) windings [2].

Since a distributed overlapping winding generally results in a more sinusoidal magneto-motive force (MMF) distribution and back-EMF waveform, it is used extensively in PM brushless ac (BLAC) machines.

On the other hand, fractional slot concentrated winding synchronous permanent magnet machines have been gaining interest over the last few years [1-17]. This is mainly due to the several advantages that this type of windings provides. These include high-power density, high efficiency, short end turns, high slot fill factor particularly when coupled with segmented stator structures, low cogging torque, flux-weakening capability, and fault tolerance. Table 2.1 summarizes the key differences between distributed windings and fractional slot concentrated windings [1].

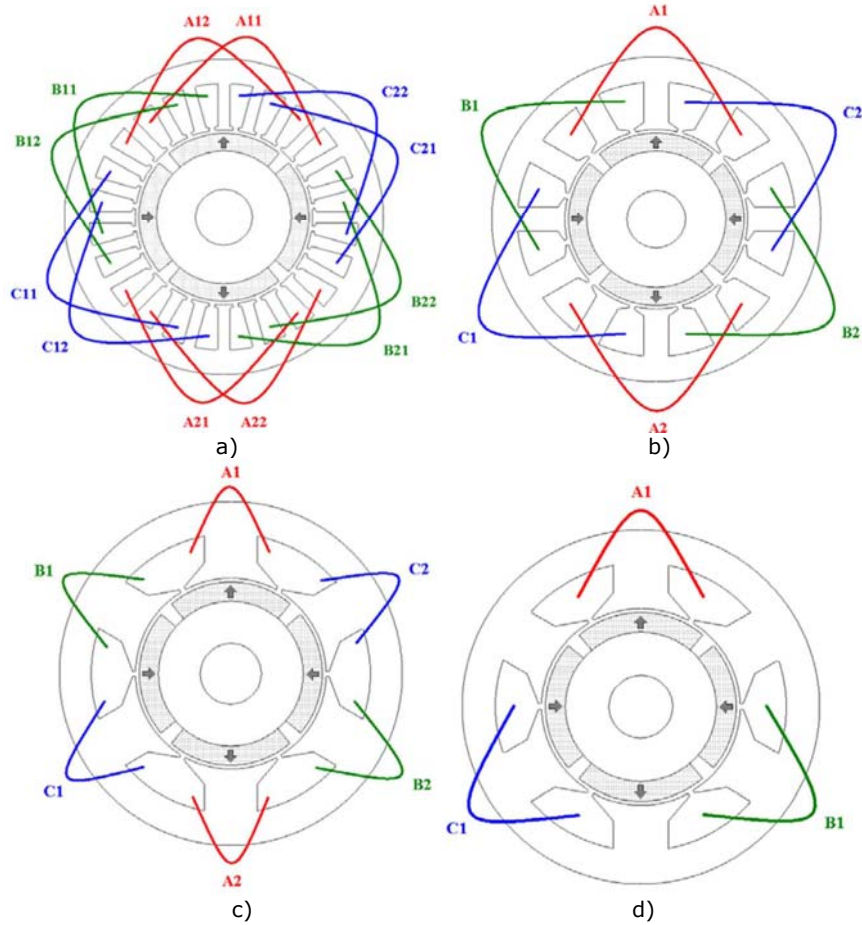


Fig. 2.1. Typical stator winding configurations (four poles) [1]: a) 24 slots, overlapping (distributed), b) 12 slots, overlapping (concentrated), c) 6 slots, nonoverlapping, double-layer (all teeth wound), d) 6 slots, nonoverlapping, single-layer (alternate teeth wound).

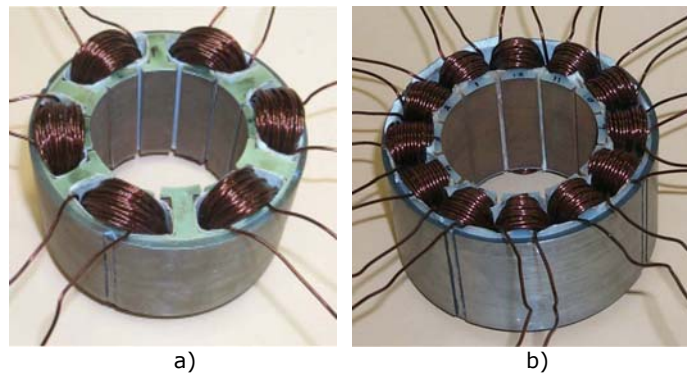


Fig. 2.2. Stators of 12-slot/10-pole motors: a) design with single-layer winding, b) design with double-layer winding [2].

Table 2.1. Comparison of distributed and concentrated windings [1]

	Distributed Windings	Concentrated Windings
Typical copper slot fill factor	35%-45%	50%-65% (if coupled with segmented stator structures)
Stator structure	Continuous laminations	Continuous laminations or segmented structures
End turns	Long overlapping	Short non-overlapping
Torque-producing stator space harmonic component	Fundamental	In most cases (except for 0.5 slot/pole/phase) a higher order harmonic

Concentrated windings are often used in small BLDC motors as well as in AC servomotors, due to their short end windings and simple structure, suitable for high volume automated manufacturing [3, 4]. They are not yet frequently used in larger electrical machines, where efficiency and smooth torque production are more important. This can change if the traditional drawbacks of the winding type, i.e. high torque ripple and low fundamental winding factor, can be improved.

In low speed applications it is often a good choice to set a high pole number [5]. It has the advantage that the iron weight per rated torque is low due to the rather low flux per pole. A high pole number with conventional winding ($q \geq 1$) structures also involves a high slot number, which increases the costs and, in the worst case, leads to a low filling factor since the amount of insulation material compared to the slot area is high. Instead the fractional slot winding ($q < 1$) solution does not require many slots although the pole number is high, as a result both the iron and the copper mass can be reduced. Compared to the conventional windings ($q \geq 1$) with the same slot number, it can be shown that the length of the end winding is less than one third in concentrated fractional wound motors. This offers a remarkable potential to reduce the machine copper losses. If the copper weight can be reduced, also the material costs, correspondingly, will decrease, because the raw material cost of copper is about 6 times the cost of iron. Some fractional slot motors offer relatively low fundamental winding factors and create harmonics and sub-harmonics, causing extra heating, additional losses and vibration.

2.2. PMSM with concentrated windings

The use of windings concentrated around the teeth, offer obvious advantages for the electric machines with radial air-gap. With concentrated windings, the volume of copper used in the end-windings can be reduced significantly, particularly if the axial length of the machine is small. There is minimization of both copper volume and Joule losses, reduction in the manufacturing cost, and improvement in the output characteristics for these machines, when compared to more traditional structures with one slot/pole/phase. This winding structure is also easier to realize than a lap winding and the number of coils is reduced. However, the use of these machines is still limited to applications of sub-fractional power (lower than 50 W), such as motors for electric fans or computer peripherals [6].

In the case of the three-phase machines, the concentrated winding is too often associated and restricted to a winding with a short pitch of 120° electric, i.e., to a winding with reduced performances, compared to the traditional structures. But there is a significant number of three-phase structures which can support a concentrated winding if the number of poles is increased. These structures present a fractional number of slots per pole and per phase. The main difficulty for the study of these machines lies in the determination of their winding and in particular the order of the phases under each pole.

The various combinations of slots and poles which allow the realization of a balanced winding can be determined by this relation in the case of the three-phase machines

$$\frac{N_s}{[\text{GCD}(N_s, 2 \cdot p_1)]} = 3 \cdot k \quad (2.1)$$

where N_s is the number of slots, p_1 the number of pairs of poles and k an integer number. (GCD: Greatest Common Divisor).

The number of slots per pole and per phase is defined by

$$S_{pp} = \frac{N_s}{2 \cdot p_1 \cdot m} \quad (2.2)$$

where m is the number of phase.

The three-phase machines which can be equipped with concentrated windings have a number of slots per pole and per phase less than or equal to 0.5. Table 2.2 gives a list of the various structures where it is possible to obtain a balanced concentrated winding [6, 7]. In this table, the winding coefficient of the fundamental component is used to characterize the performances of each structure. This coefficient is defined as the ratio between the flux embraced by each turn and the flux produced by the excitation MMF. Its value is less or equal to unity. The performance of the machine is directly related to the value of this ratio for a sinusoidal current supply and also for a rectangular current supply. In the case of a traditional machine with one slot/pole/phase, the winding coefficient of the fundamental component is equal to 1 in the case of an armature where the slots are not skewed. The same coefficient is reduced to 0.955 when the slots are skewed.

In Table 2.2 [6], the winding coefficient lies between brackets when it is possible to artificially increase the winding pitch by using the tooth tips like horns of traditional pole pieces used in DC or synchronous machines to collect and concentrate the air-gap flux. This situation occurs when the number of slots per pole and per phase is lower than $1/3$.

The structures which can use a concentrated winding with only one layer are also identified in Table 2.2 (underlined characters). In these machines, the reduced number of coils equal to greatly simplify the realization and the assembly.

The stator MMFs with $N_s \neq 2 \cdot p_1$ have rather large winding factors for $2 \cdot p_1$ periods (Table 2.2), but they also have sub- and super-harmonics, which may be included in the differential leakage inductance [8].

Table 2.2. Winding factors of concentrated windings [6]

N_s Slots	$2 \cdot p_1$ - Poles											
	2	4	6	8	10	12	14	16	18	20	22	24
3	1/2 0.866	1/4 0.866		1/8 (0.866)	1/10 (0.866)	1/14 (0.866)	1/16 (0.866)	1/20 (0.866)	1/22 (0.866)			
6		1/2 0.866		1/4 (0.866)	1/5 (0.866)	1/7 (0.866)	1/8 (0.866)	1/10 (0.866)	1/11 (0.866)			
9			1/2 0.866	3/8 0.945	3/10 0.945	3/12 (0.866)	3/14 (0.945)	3/16 (0.945)	3/20 (0.945)	3/22 (0.945)		
12				1/2 0.866	2/5 0.966	2/7 (0.966)	1/4 (0.966)	1/5 (0.866)	2/11 (0.966)			
15					1/2 0.866	5/14 0.866	5/16 0.866	1/4 (0.866)	5/22 (0.951)			
18						1/2 0.866	3/7 0.945	3/8 0.945	3/10 0.945	3/11 (0.902)	1/4 (0.866)	
21							1/2 0.866	7/16 0.932	7/20 0.953			
24								1/2 0.866	2/5 0.966	4/11 0.957		

The machines with a number of slots/pole/phase equal to are structures with concentrated windings and a short pitch of 120° electrical. Their performances are relatively low in the case of a supply with sinusoidal currents. The winding coefficient of the fundamental component is only equal to 0.866.

In the case of a rectangular current supply and with a smooth rotor using surface-mounted permanent magnets, the no-load back-EMF generated in the windings does not present a flat portion with a sufficient width [6]. The torque ripple is then important when the motor is loaded. This kind of machine can be used only for low power applications where there is no particular constraint on the torque ripple.

The machines with a number of slots/pole/phase between $1/2$ and $1/3$, generally present higher performances. The machine with 12 slots and ten poles is particularly interesting: it can support a concentrated winding with one layer and its torque ripple is low [6]. Moreover, these structures present also a no-load cogging torque of low amplitude taking into account the high relative value of its frequency. It has been demonstrated that the number of periods of this no-load cogging torque can be derived from the least common multiple of N_s and $2 \cdot p_1$; the larger the LCM the smaller the cogging torque.

$$N = LCM(N_s, 2 \cdot p_1) \quad (2.3)$$

To reduce the no-load cogging torque, it is possible to skew the slots with an angle equal to a fraction of the slot pitch. The skewing angle can be derived from

$$\alpha = \frac{2\pi}{3} \quad (2.4)$$

In the case of the machines with a number of slots/pole/phase lower than $1/3$, it is possible to adjust the width of the tooth tips to a value close to the dimension of the pole pitch to increase the magnetic flux embraced by the winding.

The structures with a number of slots/pole/phase between $1/3$ and $1/4$ are the most interesting and the value of their winding coefficient is high. The structure with 12 slots and 14 poles is using a winding with one layer and its static electromagnetic couple is more sinusoidal than in the preceding structure [6]. This structure is more suitable for a supply with sinusoidal currents.

The torque developed by the structures with a number of slots/pole/phase equal to $1/4$ or lower is more sinusoidal but decreased. In the case of a rectangular current supply, it is then preferable to use stators with an irregular distribution of slots which present higher performances.

2.3. PMSM with concentrated windings and nonuniform slots

These machines can be derived from machines with a number of poles higher than two [6, 9]. The arrangement of the stator coils must be modified to eliminate the tangle of the end-windings and to concentrate the winding. The total quantities of iron and copper used in the machine must be preserved to respect the constraints of saturation and to preserve the performances of the original machine [6].

A permanent magnet machine with 24 slots and 8 poles is chosen for the conceptual derivation of a machine with concentrated coils and nonuniform slots. In

the first step, the coils, which prevent the concentration of windings, are removed. It is necessary to remove the same number of coils in each phase to keep a balanced winding. Next, the arrangement of the stator slots is modified by an association of the teeth which are localized on each side of the empty slots [6]. For the case in print, the conceptual derivation of a machine with concentrated coils and nonuniform slots is unfolded in Fig. 2.3.

The original widths of the teeth are preserved to observe the constraints of same magnetic saturation. With this method, the remaining slots can be increased to preserve the total quantity of copper used in the slots of the original machine. During the final step, the space between the tips under the main teeth is filled to obtain a true polar horn. This way the machine with 24 slots and 8 poles can be modified to obtain a machine with six coils, eight poles, six main teeth, and six auxiliary teeth. Because the teeth do not have the same width, it is possible to define this structure as a machine with concentrated coils and nonuniform slots.

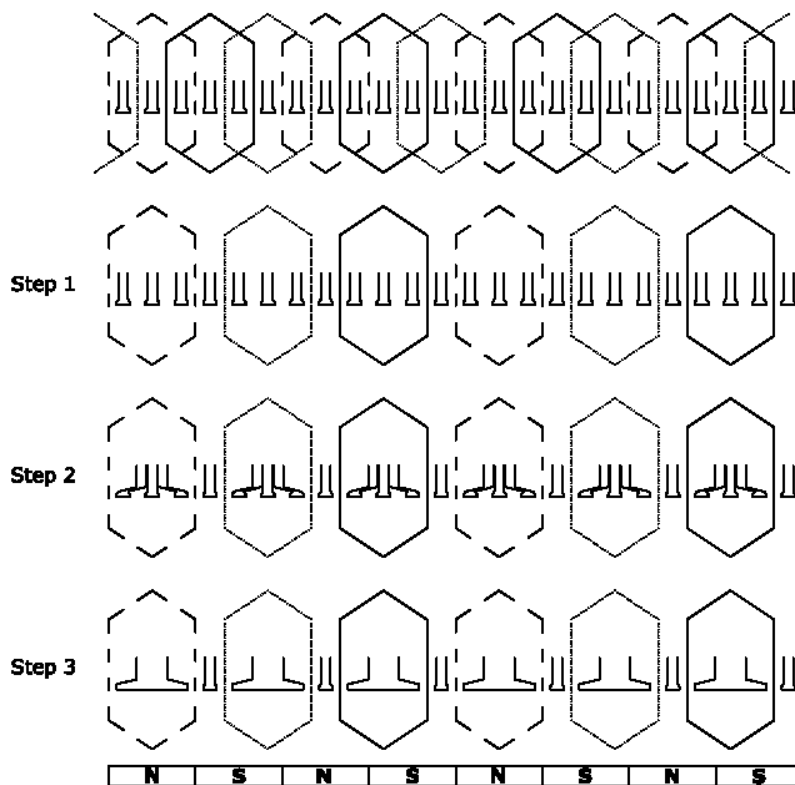


Fig. 2.3. Derivation of a machine with concentrated coils and nonuniform slots from an initial machine with 24 slots and 8 poles.

2.4. Preliminary design methodology of an IPMSM with concentrated windings and an irregular distribution of stator slots

2.4.1. Global topology selection

The requirements of the motor used in a direct drive system are high torque-to-weight ratio and high efficiency. A motor type that fulfills this specification is the PMSM, since it has the highest torque density and efficiency. A suitable winding and rotor must be chosen.

In PMSM the currents carried by the stator winding system and the rotor field excited by permanent magnets, are interacting during the energy conversion to produce torque. This interaction produces also a centrifugal force, which can cause the separation of PM at high speeds. This can be avoided in the case of interior permanent magnet synchronous motors since the PM are inserted in the interior of rotor core.

The decision to choose IPMSM for the automotive applications was made taking into account the major advantages of this electric machine type regarding following application aspects [10, 11]:

- safety (the robustness of the rotor can be combined with robust non-overlapped concentrated stator windings),
- reliability (brushless motor technology),
- technical performance parameters (high torque density, high dynamics, wide speed range due good field-weakening capability),
- manufacturing technology (easy to manufacture due to simple motor topology in the absence of any kind of skewing),
- cost (lowest cost of the permanent magnets due to their simple shape).
- pole flux maximization, while keeping a minimal level of cogging torque simultaneously.

A (6+6) slots/8 poles IPMSM with concentrated windings and an irregular distribution of stator slots is the solution preferred in this thesis.

The quality of this topology can be expressed as follows

– cogging torque factor

$$k_{T_cog} = LCM(N_s, 2 \cdot p_1) = LCM(12, 8) = 24 \quad (2.5)$$

– winding factor

$$\begin{aligned} k_{w1} = k_{p1} &= \sin\left(\frac{\pi}{2} \cdot \frac{y}{y_d}\right) = \sin\left(\frac{\pi}{2} \cdot \frac{2 \cdot \pi / N_s}{2 \cdot \pi / 2 \cdot p_1}\right) \\ &= \sin\left(\frac{\pi}{2} \cdot \frac{2 \cdot \pi}{2 \cdot \pi} \cdot \frac{12}{8}\right) = \sin\left(\frac{\pi}{3}\right) = 0.866 \end{aligned} \quad (2.6)$$

– topological quality factor (with a weighting coefficient of 0.5 for the cogging torque and 0.5 for the winding factor) [10]

$$k_{T_50/50} = w_1 \cdot k_{T_cog} + w_2 \cdot k_{w1} = 0.5 \cdot 24 + 0.5 \cdot 0.866 = 12.433 \quad (2.7)$$

The topological quality factor of the chosen solution is rather not extremely high, but this configuration assures, due a low number of active components (coils and permanent magnets), a low material and manufacturing cost.

2.4.2. Materials selection

In the following the selection of the materials for the active parts will be presented.

2.4.2.1. Iron core laminations

The material for the stator and rotor cores was chosen to be laminated non-oriented silicon M800-50A electric steel [12, 13]. For the rotor of the PMSM also a massive iron core could be chosen. The inner parts provided by the stamping process of the stator laminations can be used economically for the rotor core. Table 2.3 presents the main material properties of the iron core laminations.

Table 2.3. Material properties for iron core laminations

Parameter	Symbol	Value	Unit
Composition	v	99,95	[%] Fe
Initial relative permeability at $B=0.02$ [T]	$\mu_{r,i}$	1084	[-]
Maximum relative permeability	$\mu_{r,max}$	4032	[-]
Saturation induction	B_{sat}	1.7	[T]
Mass density	ρ_{Fe}	7800	kg/m ³

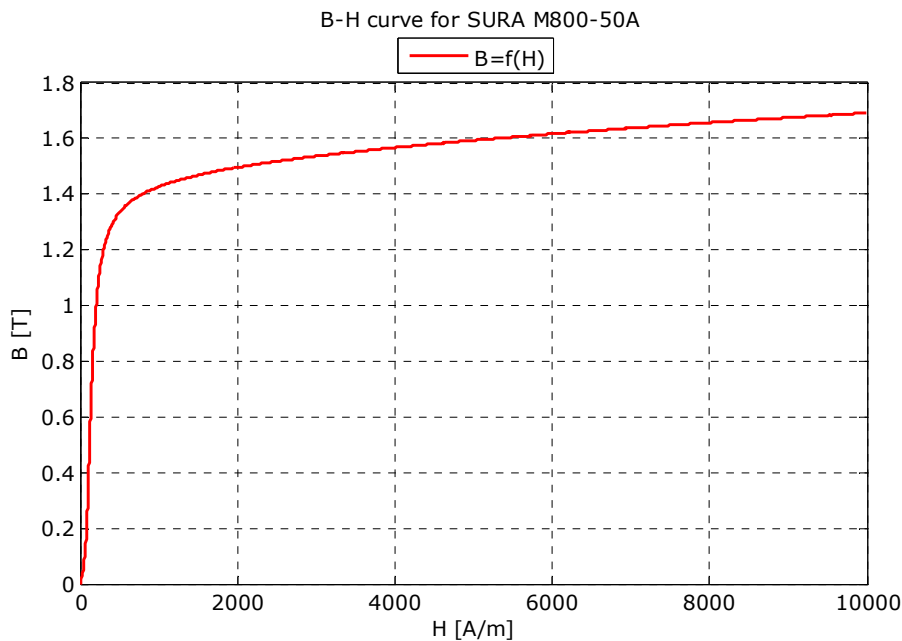


Fig. 2.4. DC magnetization curve.

The DC magnetization curve is shown in Fig. 2.4. The variation of the specific total losses versus frequency at 1.5 T (peak), and versus peak flux density at 50 Hz is presented in Fig. 2.5, and Fig. 2.6 respectively.

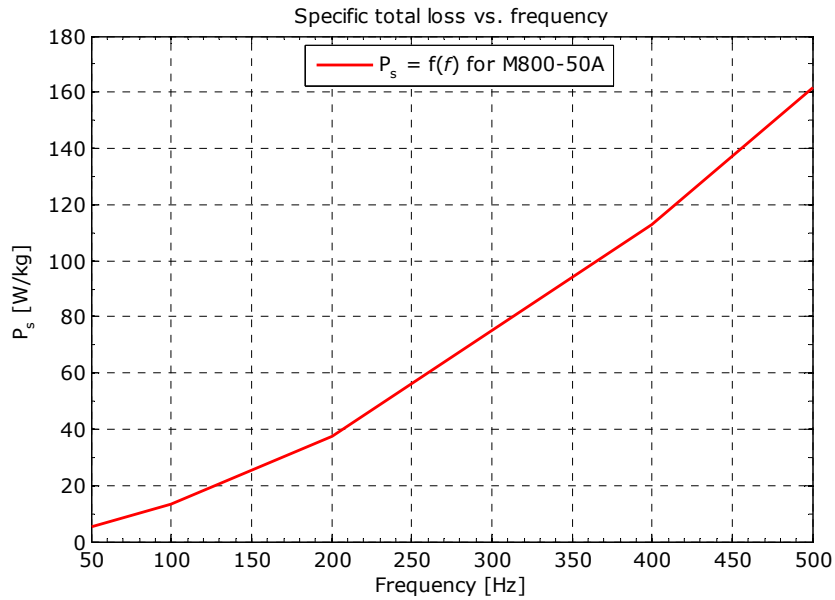


Fig. 2.5. Specific total losses versus frequency at 1.5 T (peak).

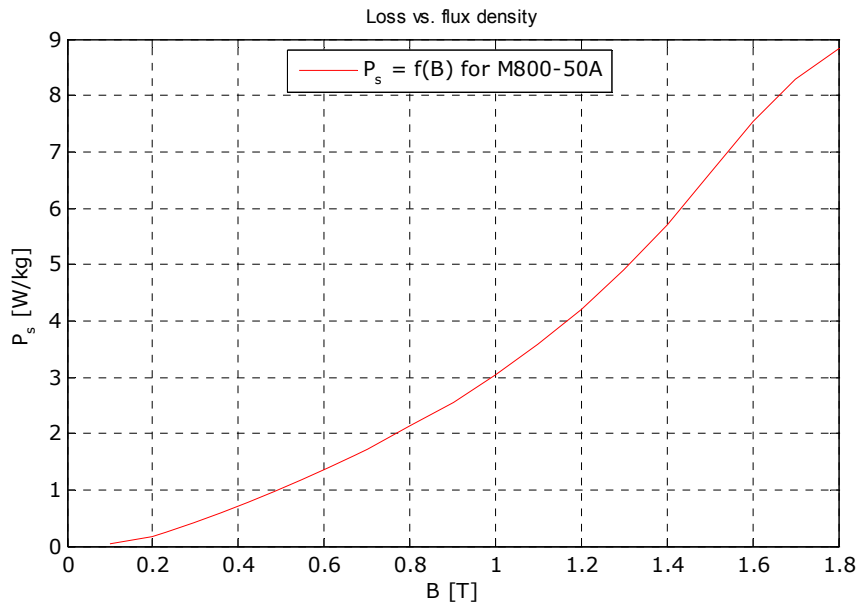


Fig. 2.6. Specific total losses versus peak flux density at 50 Hz.

2.4.2.2. The permanent magnets

For the actual high-performance application high-energy permanent magnet material is required. As Neodymium-Iron-Boron (NdFeB) magnets fulfill the technical requirements and have an acceptable price they will be chosen for the actual design. Table 2.4 presents the main material properties [14] of magnetic material.

Table 2.4. Material properties for NdFeB

Parameter	Symbol	Value	Unit
Remanent induction	B_r	1.2	T
Intrinsic coercivity	H_{cJ}	$810 \cdot 10^3$	A/m
Recoil permeability	μ_r	1.05	-
Maximal energy product	$B \cdot H_{max}$	220	kJ/m^3
Magnetizing force	H_{magn}	$2300 \cdot 10^3$	A/m
Temperature coefficient of the remanent induction	α_{Br}	-0.001	$1/^\circ\text{C}$
Temperature coefficient of the intrinsic coercivity	α_{HcJ}	-0.0006	$1/^\circ\text{C}$
Curie temperature	T_{Curie}	310	$^\circ\text{C}$
Mass density	ρ_{PM}	7400	kg/m^3

The demagnetization curve of the magnetic material at 20°C is shown in Fig. 2.7.

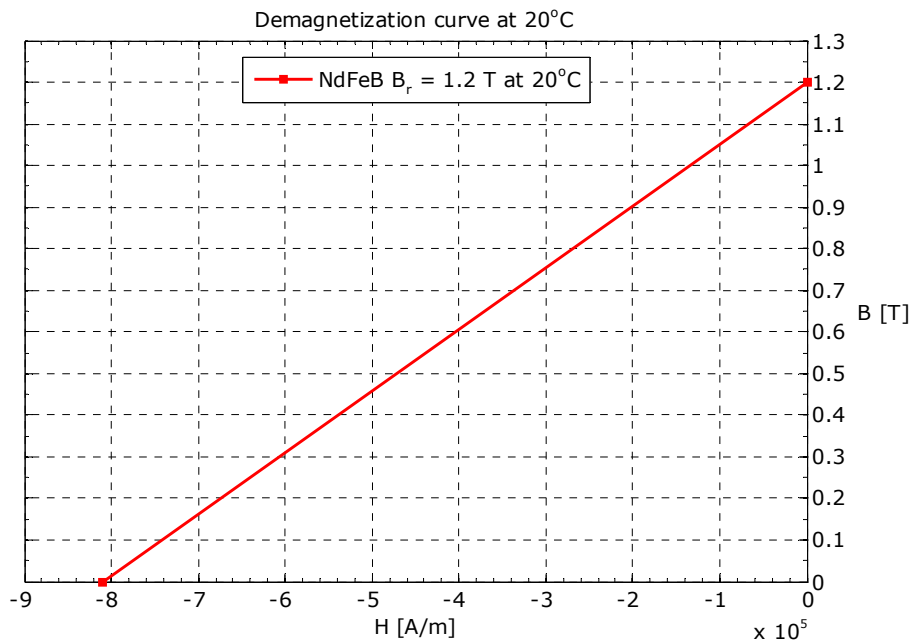


Fig. 2.7. Demagnetization curve at 20°C .

2.4.3. Design theme

General specifications of a variable speed interior PM synchronous machine:

- Base power, $P_b = 120 \text{ W}$,
- Base speed, $n_b = 1000 \text{ rpm}$,
- Maximum speed, $n_{max} = 2000 \text{ rpm}$,
- Power at maximum speed: P_b ,
- DC voltage, $V_{DC} = 12 \text{ V}$,
- Number of poles, $2 \cdot p_1 = 8$,
- Number of phases, $m = 3$,
- Supply: PWM inverter, rectangular current control,
- Maximum voltage, V_{phmax} , as in Fig. 2.11, and base voltage, V_b .
- Star connection of stator phases,
- Very low cogging torque, $T_{cogg} < 1.5\% \cdot T_{ebr}$,
- Number of slots per pole per phase, $q_1 = 0.5$.

Additional specifications related to duty cycle, motor-cooling system, constraints related to volume, efficiency at base power, and cost of active materials in the rotor may be added.

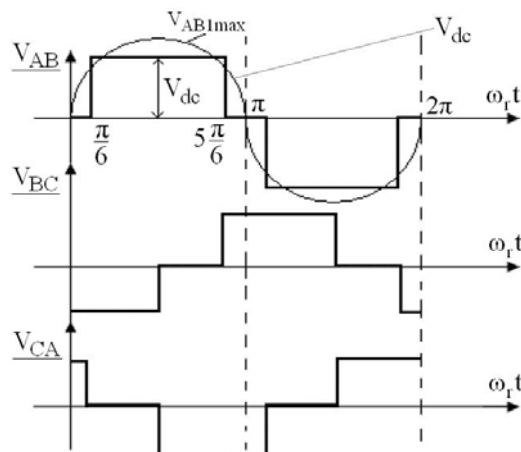


Fig. 2.11. Ideal line voltages for six-pulse PWM inverter operation [8].

Maximum phase voltage:

According to Fig. 2.11, the fundamental V_{phmax} for the maximum phase voltage is (using Fourier decomposition):

$$(V_{phmax})_{RMS} = \frac{V_{line,max}}{\sqrt{6}} = \frac{1}{\sqrt{6}} \frac{4}{\pi} \sin\left(\frac{\pi}{3}\right) V_{DC} = \frac{\sqrt{2}}{\pi} V_{DC} = \frac{\sqrt{2}}{\pi} \cdot 12 = 5.402 \text{ V (RMS)} \quad (2.8)$$

The base voltage, V_b , is chosen so that an acceptable rectangular current control is still achieved

$$(V_b)_{\text{RMS}} = 0.4 \cdot (V_{ph\text{max}})_{\text{RMS}} = 0.4 \cdot 5.402 = 2.16 \text{ V} \quad (2.9)$$

2.4.4. Electric and magnetic loadings

The first stage in general design of electric machines consists in choosing the electric and magnetic loadings. For PMSMs, these loadings are described as follows [8, 10, 15-25]:

- The specific tangential force, f_{tsp} , concept may be preferred when high torque density is target in the design. It is measured in N/cm^2 and varies from $0.1\text{N}/\text{cm}^2$ in micro-motors to $10\text{N}/\text{cm}^2$ in larger torque density.
- PM air-gap flux density: B_{ag} (T), varies from 0.2T in micro-motors to 1T in large torque density design. Together B_{ag} and f_{tsp} determine the volume of the machine for given base torque (T_{eb}).
- Stator tooth flux density: B_{st} (T) determine the magnetic saturation degree in the machine; it varies from 1.2T to 1.8T in general, for silicon laminated stator cores. As the machine magnetic air-gap (which includes the surface PM thickness) is large the teeth magnetic saturation influence is rather small and thus B_{st} may be chosen rather large; in contrast, if B_{st} is large (and the fundamental frequency f_b is large) the core losses would be large. Smaller values of B_{st} lead to wider teeth and thus thinner slots, that is larger design current densities and consequently, larger copper losses. To prevent this, deeper slots are adapted, but then the machine's external diameter (and volume) is increased. Moreover the copper losses may not decrease notably by deepening the slot as the average diameter (and length) of end connection of coils increases.
- The stator yoke flux density B_{ys} (T) is again chosen as a compromise between magnetic saturation level and core losses limitations. Small values of B_{ys} may lead to a larger machine size and weight, especially if the number of poles is small ($2p_1 = 2, 4$).
- Current density j_{co} (A/mm^2) determines the copper losses and the copper volume. Corroborated thin and deep slots that have small values of j_{co} ($2 - 3.5\text{A}/\text{mm}^2$) may lead to high leakage inductance, and machine volume (and weight). On the other hand, high j_{co} values ($> 8\text{A}/\text{mm}^2$) in general not only imply forced cooling but also lead to lower efficiency, while reducing the machine volume.
- Rotor yoke flux density B_{yr} (T) is imported in machine with a large number of poles (and large diameter) when the PMs are not any more placed directly on the shaft.

2.4.5. Choosing a few dimensioning factors

- Machine shape factor λ : the ratio between the axial (stack) length of the machine, l_{stack} , and the stator interior diameter, D_{is} ($\lambda = l_{stack}/D_{is}$, usual between 0.3 and 3).
- Stator winding current path count a_1 , is always a divisor of number of poles for two layers winding and of the number of pole pairs for single layers windings. To avoid circulation current between current paths, due to inherent machine symmetry imperfection, $a_1 = 1$ whenever possible, with the exception of low voltage large current (automotive) applications.
- Elementary conductors in parallel: for large currents (or fundamental frequency) the coil turns are made of multiple elementary conductors in parallel with same degree of transposition to reduce skin effects.
- The minimum value of slot opening b_{os} is limited by the possibility to introduce the coils, turn by turn, in the slot and by the increase of slot leakage inductance and PM flux fringing. Its maximum value is limited by the PM flux reduction, cogging torque increase and torque ripple.

2.4.5. A few technological constraints

- The laminated core filling factor, $k_{stk} = 0.8 - 0.95$, is the ratio of laminations height to total laminated core length (laminations insulation coating means $k_{stk} < 1$).
- Slot copper filling factor, $k_{sf} = 0.33 - 0.7$; lower values corresponds to semiclosed slots with coils introduced turn by turn in the slot while larger values corresponds to open slot and pre-made coils made of rectangular cross section conductors.
- Minimum air-gap from mechanical considerations in super high speed machines is increased to reduce PM eddy currents losses due to stator MMF space harmonic.
- The straight turn end connection that exits the slot.
- Difference between PM, l_{PM} , and stator stack length, l_{stack} , in order to avoid axial forces on the bearings.
- Minimum shaft diameter, based on the maximum envisaged torque.

2.4.6. Dimensioning methodology

Based on the general aspects regarding the sizing of electric machines this paragraph will present the selection of the key design quantities, and the dimensioning procedure for the actual case study IPMSM.

With known specification data and key design quantities the dimensioning process can be defined algorithmically [8, 10]. The different geometrical dimensions are presented in Fig. 2.8 for the whole motor, Fig. 2.9 for the rotor with interior permanent magnets, and Fig. 2.10 for the stator.

The dimensioning steps are as follows:

Step 1. Interior stator diameter, D_{is} :

The sizing of the machine uses an equation based on the electromagnetic torque, T_{eb} , and the tangential specific force, f_{tsp} (in N/cm²).

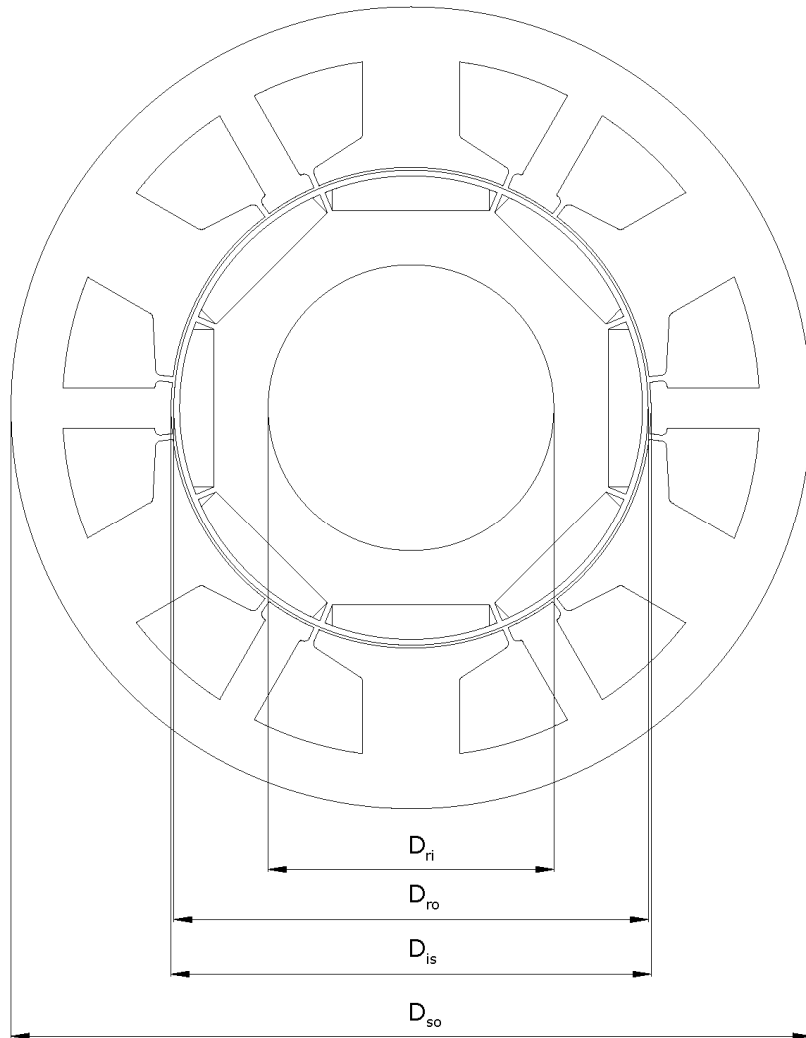


Fig. 2.8. Cross-section of an interior permanent magnet synchronous motor with irregular distribution of stator slots with dimensions.

The base electromagnetic torque, T_{eb} , provided from $n_b = 0$ rpm to $n_b = 1000$ rpm, is

$$T_{eb} \approx \frac{P_b}{2 \cdot \pi \cdot n_b} = \frac{120}{2 \cdot \pi \cdot 1000/60} = 1.146 \text{ Nm} \quad (2.10)$$

The ratio of the stator stack length, l_{stack} , to the stator interior diameter, D_{is} , is

$$\lambda = \frac{l_{stack}}{D_{is}} = 0.3 - 3 \quad (2.11)$$

$$T_{eb} = \frac{D_{is}}{2} \cdot f_{tsp} \cdot \pi \cdot D_{is} \cdot \frac{l_{stack}}{D_{is}} \cdot D_{is} \quad (2.12)$$

For $\lambda = 0.48$ and $f_{tsp} = 2 \text{ N/cm}^2$:

$$D_{is} = \sqrt[3]{\frac{2 \cdot T_{eb}}{\lambda \cdot \pi \cdot f_{tsp}}} = \sqrt[3]{\frac{2 \cdot 1.146}{0.48 \cdot \pi \cdot 2 \cdot 10^4}} = 4.2 \cdot 10^{-2} \text{ m} = 42 \text{ mm} \quad (2.13)$$

Step 2. Stator stack length, l_{stack} , and rotor length, l_{rotor} :

$$l_{stack} = \lambda \cdot D_{is} = 0.48 \cdot 42 = 20 \text{ mm} \quad (2.14)$$

$$l_{rotor} = 1.05 \cdot l_{stack} = 1.05 \cdot 20 = 21 \text{ mm} \quad (2.15)$$

Step 3. Height of the magnetic pole piece, h_{PM} :

$$h_{PM} \geq 4 \cdot g \quad (2.16)$$

where: g – air-gap.

With $g = 0.25 \text{ mm}$, yields $h_{PM} \geq 1 \text{ mm}$. We choose $h_{PM} = 3 \text{ mm}$.

Step 4. PM air-gap flux density, B_{gPM} :

$$B_{gPM} = \frac{B_r}{1 + k_{fringe}} \cdot \frac{h_{PM}}{h_{PM} + h_{bridge} + g} \quad (2.17)$$

where the fringing factor $k_{fringe} = 0.1 - 0.2$, and the height of the rotor bridge (Fig. 2.10) $h_{bridge} = 0.50 \text{ mm}$.

From Equation (2.17) yields

$$B_{gPM} = \frac{1.2}{1 + 0.2} \cdot \frac{3}{3 + 0.50 + 0.25} = 0.8 \text{ T}$$

The temperature dependency and the curvature of the air-gap are not considered in the Equation (2.17). A more accurate equation considering that the air-gap is curved is presented in [21].

Step 5. Maximum air-gap pole flux, Φ_{PMmax} :

$$\Phi_{PMmax} = B_{g_av} \cdot \tau_{PM} \cdot l_{stack} \quad (2.18)$$

where the pole pitch, τ_{PM} , is

$$\tau_{PM} = \frac{\pi \cdot D_{is}}{2 \cdot p_1} = \frac{\pi \cdot 42 \cdot 10^{-3}}{8} = 16.5 \cdot 10^{-3} \text{ m} = 16.5 \text{ mm} \quad (2.19)$$

B_{g_av} is the average value of the air-gap flux density, and is defined

$$B_{g_av} = k_{av} \cdot B_{gPM} \quad (2.20)$$

The coefficient k_{av} is the ratio of the average-to-maximum value of the normal component of the air-gap magnetic flux density. If the magnetic field distribution is sinusoidal, $k_{av} = 2/\pi$. In the case of PM brushless DC motors, the air-gap flux density is essentially a square wave, but fringing causes the corners to be somewhat rounded, so in this case the coefficient k_{av} is between the value

corresponding to sinusoidal distribution of magnetic field $2/\pi$ (0.6366) and the value corresponding to the ideal rectangular distribution of magnetic field, i.e., 1.

With $k_{av} = 0.95$, the average value of the air-gap flux density is

$$B_{g_av} = 0.95 \cdot 0.8 = 0.76 \text{ T}$$

Maximum air-gap pole flux yields

$$\Phi_{PM\max} = 0.76 \cdot 16.5 \cdot 10^{-3} \cdot 20 \cdot 10^{-3} = 2.51 \cdot 10^{-4} \text{ Wb}$$

Let us consider that the total PM flux linkage in the stator, 2 coils per phase in parallel, varies linearly with the rotor position, with the maximum of λ_{PM} :

$$\lambda_{PM\max} = \Phi_{PM\max} \cdot N_1 \quad (2.21)$$

$$\lambda_{PM}(\theta_e) = \left(1 - \frac{2 \cdot \theta_e}{\pi}\right) \cdot \lambda_{PM\max}; \quad \theta_e = p_1 \cdot \theta_m \quad (2.22)$$

where

θ_m is the mechanical angle (in radians),

θ_e is the electrical angle (in radians).

The maximum PM flux linkage in one phase is given by Equation 2.21:

$$\lambda_{PM\max} = 2.51 \cdot 10^{-4} \cdot N_1 \quad (2.23)$$

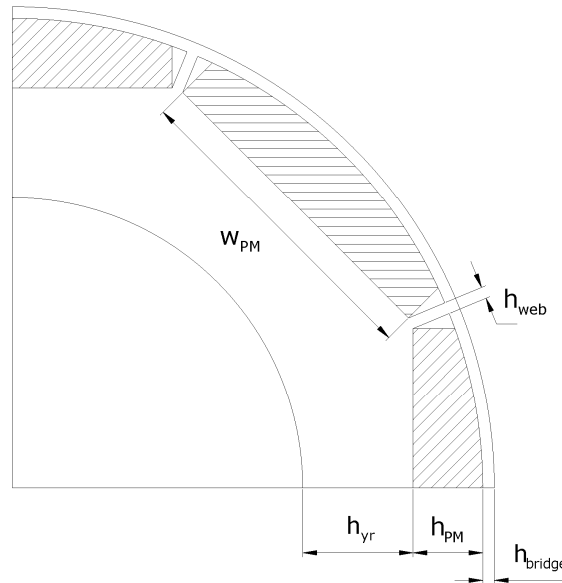


Fig. 2.9. Rotor geometry.

Step 6. Rotor outer diameter, D_{ro} :

$$D_{ro} = D_{is} - 2 \cdot g = 42 - 2 \cdot 0.25 = 41.5 \text{ mm} \quad (2.24)$$

Step 7. Width of the magnetic pole piece, w_{PM} :

$$w_{PM} = \frac{D_{ro} - 2 \cdot h_{bridge} - 2 \cdot h_{PM}}{\tan\left(\frac{1}{2}\left(\pi - \frac{\pi}{p_1}\right)\right)} \cdot \frac{h_{web}}{\sin\left(\frac{1}{2}\left(\pi - \frac{\pi}{p_1}\right)\right)} \quad (2.25)$$

where the height of the rotor web (Fig. 2.10) $h_{web} = 0.50$ mm.

From Equation (2.25) yields

$$w_{PM} = \frac{41.5 - 2 \cdot 0.5 - 2 \cdot 3}{\tan\left(\frac{1}{2}\left(\pi - \frac{\pi}{4}\right)\right)} \cdot \frac{0.5}{\cos\left(\frac{1}{2}\left(\pi - \frac{\pi}{4}\right)\right)} = 13.75 \text{ mm}$$

Step 8. Number of turns per phase multiplied by phase current, $N_1 \cdot I_b$:

The developed electromagnetic torque is

$$T_{eb} = \frac{2 \cdot e_a \cdot I_b}{\omega_m} \quad (2.26)$$

where

e_a is the phase back-EMF,

ω_m is the mechanical angular speed in rad/s.

The phase back-EMF is

$$e_a = -\frac{d\lambda_{PM}(\theta_m)}{dt} = -\frac{d\lambda_{PM}(\theta_m)}{d\theta_m} \cdot \frac{d\theta_m}{dt} = -\frac{d\lambda_{PM}(\theta_m)}{d\theta_m} = \frac{2 \cdot p_1}{\pi} \cdot \lambda_{PM \max} \cdot \omega_m \quad (2.27)$$

With the expression of the phase back-EMF, the torque can be written

$$T_{eb} = \frac{4 \cdot p_1}{\pi} \cdot \lambda_{PM \max} \cdot I_b \quad (2.28)$$

So, from Equations 2.23 and 2.28:

$$N_1 \cdot I_b = \frac{T_{eb}}{\frac{4 \cdot p_1}{\pi} \cdot \Phi_{PM \max}} = \frac{1.146}{\frac{4 \cdot 4}{\pi} \cdot 2.51 \times 10^{-4}} = 896.48 \text{ A turns} \quad (2.29)$$

Step 9. Slot area, A_{slot} :

There is one coil in each slot, and thus the active area of stator slot, A_{slot} , is

$$A_{slot} = \frac{N_1 \cdot I_b}{a_1 \cdot k_{sf} \cdot j_{co}} = \frac{896.48}{2 \cdot 0.55 \cdot 15 \cdot 10^6} = 54.33 \cdot 10^{-6} \text{ m}^2 = 54.33 \text{ mm}^2 \quad (2.30)$$

where number of parallel current paths $a_1 = 2$, slot filling factor $k_{sf} = 0.55$ and current density $j_{co} = 15 \text{ A/mm}^2$.

Step 10. Number of stator slots, N_s :

$$N_s = q_1 \cdot m \cdot 2 \cdot p_1 = 0.5 \cdot 3 \cdot 8 = 12 \quad (2.31)$$

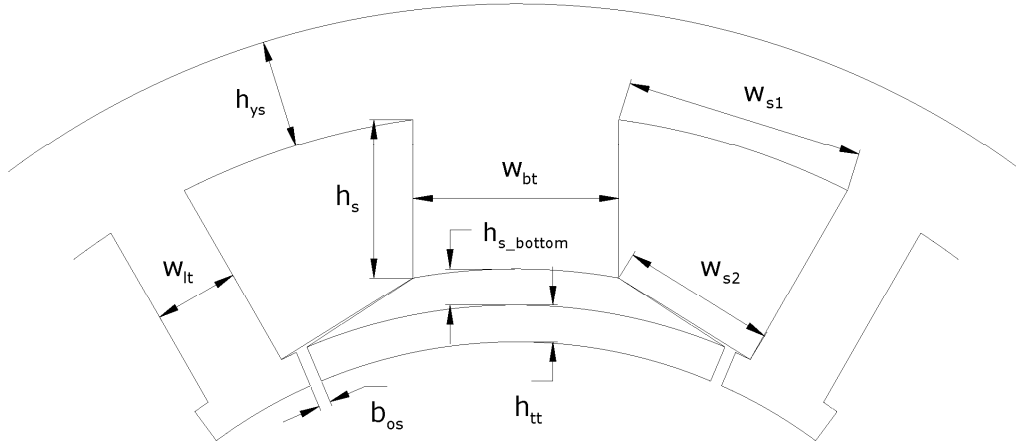


Fig. 2.10. Stator slot geometry.

Step 11. Slot opening, b_{os} :

$$b_{os} = 0.5 \text{ mm (small)} \quad (2.32)$$

Step 12. Stator big tooth width, w_{bt} :

The stator big tooth pitch, τ_{bt} , is chosen equal to the PM span on the rotor, τ_{PM} , to reduce the cogging torque.

$$\tau_{bt} = \frac{\pi \cdot D_{is}}{2 \cdot p_1} = 16.5 \text{ mm} \quad (2.33)$$

$$w_{bt} = \tau_{bt} \cdot \frac{B_{g-av}}{B_{sbt}} = 16.5 \cdot 10^{-3} \cdot \frac{0.76}{1.5} = 8.36 \cdot 10^{-3} \approx 8.5 \cdot 10^{-3} \text{ m} = 8.5 \text{ mm} \quad (2.34)$$

where the flux density in the stator big teeth, $B_{sbt} = 1.5 \text{ T}$.

Step 13. Stator little tooth width, w_{lt} :

Stator little tooth pitch, τ_{lt} is

$$\begin{aligned} \tau_{lt} &= \frac{\pi \cdot D_{is}}{N_s/2} - \tau_{bt} - D_{is} \cdot 2 \cdot \text{asin} \left(\frac{b_{os}}{D_{is}} \right) = \\ &= \frac{2 \cdot \pi \cdot 42 \cdot 10^{-3}}{12} - 16.5 \cdot 10^{-3} - 42 \cdot 10^{-3} \cdot 2 \cdot \text{asin} \left(\frac{0.5}{42} \right) = 4.5 \cdot 10^{-3} \text{ m} = 4.5 \text{ mm} \end{aligned} \quad (2.35)$$

$$w_{lt} = \tau_{lt} \cdot \frac{B_{g-av}}{B_{slt}} = 4.5 \cdot 10^{-3} \cdot \frac{0.76}{1} = 3.42 \cdot 10^{-3} \approx 3.5 \cdot 10^{-3} \text{ mm} = 3.5 \text{ mm} \quad (2.36)$$

where the flux density in the stator little teeth, $B_{slt} = 1 \text{ T}$.

Step 14. Slot height, h_s , and mean slot width, b_s :

The bottom width of the slot, w_{s2} , is

$$\begin{aligned} w_{s2} &= \frac{\pi \cdot (D_{is} + 2 \cdot (h_{tt} + h_{s_bottom}))}{N_s} - \frac{w_{bt} + w_{lt}}{2} \\ &= \frac{\pi \cdot (42 + 2 \cdot (1.5 + 1.5))}{12} - \frac{8.5 + 3.5}{2} = 6.56 \text{ mm} \end{aligned} \quad (2.37)$$

where the tooth tip height $h_{tt} = 1.5$ mm and height of the slot bottom $h_{s_bottom} = 1.5$ mm.

Knowing the active slot area, A_{slot} , the slot height is

$$h_s = \frac{-w_{s2} + \sqrt{w_{s2}^2 + 2 \cdot A_{slot} \cdot \left(\tan\left(\frac{\alpha_{bt}}{2}\right) + \tan\left(\frac{\alpha_{lt}}{2}\right) \right)}}{\tan\left(\frac{\alpha_{bt}}{2}\right) + \tan\left(\frac{\alpha_{lt}}{2}\right)} \quad (2.38)$$

where α_{bt} and α_{lt} are determined with the next expressions:

$$\alpha_{bt} = \frac{2 \cdot \tau_{bt}}{D_{is}} + 2 \cdot \text{asin}\left(\frac{b_{os}}{D_{is}}\right) = \frac{2 \cdot 16.5}{42} + 2 \cdot \text{asin}\left(\frac{0.5}{42}\right) = 46.38^\circ \quad (2.39)$$

$$\alpha_{lt} = \frac{2 \cdot \tau_{lt}}{D_{is}} + 2 \cdot \text{asin}\left(\frac{b_{os}}{D_{is}}\right) = \frac{2 \cdot 4.5}{42} + 2 \cdot \text{asin}\left(\frac{0.5}{42}\right) = 13.62^\circ \quad (2.40)$$

$$h_s = \frac{-6.56 + \sqrt{6.56^2 + 2 \cdot 54.33 \cdot \left(\tan\left(\frac{46.38^\circ}{2}\right) + \tan\left(\frac{13.62^\circ}{2}\right) \right)}}{\tan\left(\frac{46.38^\circ}{2}\right) + \tan\left(\frac{13.62^\circ}{2}\right)} = 6.5 \text{ mm}$$

Now the upper width of the slot, w_{s1} , and the mean slot width, w_s , are

$$\begin{aligned} w_{s1} &= \frac{\pi \cdot (D_{is} + 2 \cdot (h_{tt} + h_{s_bottom} + h_s))}{N_s} - \frac{w_{bt} + w_{lt}}{2} \\ &= \frac{\pi \cdot (42 + 2 \cdot (1.5 + 1.5 + 6.5))}{12} - \frac{8.5 + 3.5}{2} = 9.97 \text{ mm} \end{aligned} \quad (2.41)$$

$$w_s = \frac{w_{s1} + w_{s2}}{2} = \frac{9.97 + 6.56}{2} = 8.265 \text{ mm} \quad (2.42)$$

Step 15. Tooth height or slot depth, h_{ts} :

$$h_{ts} = h_s + h_{tt} + h_{s_bottom} = 6.5 + 1.5 + 1.5 = 9.5 \text{ mm} \quad (2.43)$$

Step 16. Stator yoke height, h_{ys} :

$$h_{ys} = \frac{\pi \cdot D_{is} \cdot B_{g_av}}{N_s \cdot 2 \cdot B_{ys}} = \frac{\pi \cdot 42 \cdot 10^{-3} \cdot 0.76}{12 \cdot 2.1} = 4.2 \cdot 10^{-3} \text{ m} \cong 4.5 \cdot 10^{-3} \text{ m} = 4.5 \text{ mm} \quad (2.44)$$

where the flux density in the stator yoke, $B_{ys} = 1$ T.

Step 17. Stator outer diameter, D_{so} :

$$D_{so} = D_{is} + 2 \cdot (h_{ts} + h_{ys}) = 42 + 2 \cdot (9.5 + 4.5) = 70 \text{ mm} \quad (2.45)$$

Step 18. Rotor yoke height, h_{yr} :

$$h_{yr} = \frac{\pi \cdot D_{is} \cdot B_{g-av}}{2 \cdot p_1 \cdot 2 \cdot B_{yr}} = \frac{\pi \cdot 42 \cdot 10^{-3} \cdot 0.76}{8 \cdot 2 \cdot 1.35} \cong 4.75 \cdot 10^{-3} \text{ m} = 4.75 \text{ mm} \quad (2.46)$$

where the flux density in the rotor yoke, $B_{yr} = 1.35$ T.

Step 19. Interior rotor diameter, D_{ri} :

$$D_{ri} = D_{ro} - 2 \cdot (h_{bridge} + h_{PM} + h_{yr}) = 41.5 - 2 \cdot (0.5 + 3 + 4.75) = 25 \text{ mm} \quad (2.47)$$

Step 20. Number of turns per phase, N_1 :

The frequency at base speed is

$$f_b = \frac{n_b \cdot p_1}{60} = \frac{1000 \cdot 4}{60} = 66.67 \text{ Hz} \quad (2.48)$$

The phase back-EMF e_1 at base speed is

$$e_1 = \frac{2}{\pi} \cdot \lambda_{PM \max} \cdot \omega_{1b} = \frac{2}{\pi} \cdot 2.51 \cdot 10^{-4} \cdot N_1 \cdot 2 \cdot \pi \cdot 66.67 = 0.06694 \cdot N_1 \quad (2.49)$$

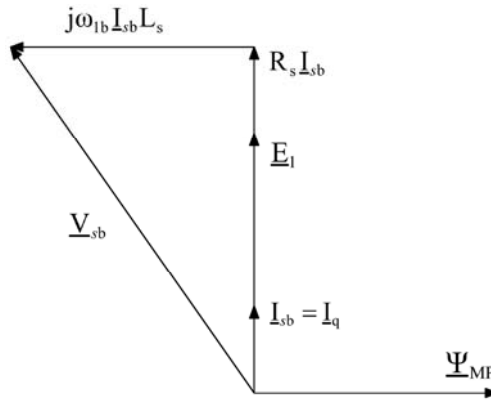


Fig. 2.11. The phasor diagram at base speed (pure I_q control, $I_d = 0$).

Considering the total current in axis q [$I_d = 0$], the number of turns per phase can be calculated, for base speed and torque (Fig. 2.11).

$$V_b = \sqrt{(e_1 + R_s \cdot I_b)^2 + (\omega_{1b} \cdot L_s \cdot I_b)^2} = 2.16 \text{ V} \quad (2.50)$$

The phase resistance, R_s , is

$$R_s = \rho_{co} \cdot \frac{l_{turn} \cdot N_1^2}{a_1 \cdot (N_1 \cdot I_b / (a_1 \cdot j_{co}))} \quad (2.51)$$

The turn length, l_{turn} , is

$$\begin{aligned} l_{turn} &= 2 \cdot \left(l_{stack} + \frac{\pi}{2} \cdot (D_{is} + h_{ts}) \cdot \sin\left(\frac{\alpha_{bt}}{2}\right) \right) = 2 \cdot \left(20 + \frac{\pi}{2} \cdot (42 + 9.5) \cdot \sin\left(\frac{46.38^\circ}{2}\right) \right) \\ &= 103.7 \text{ mm} = 0.104 \text{ m} \end{aligned} \quad (2.52)$$

With the turn length from Equation 2.52 and copper electric resistivity $\rho_{co} = 2.3 \cdot 10^{-8} \text{ } \Omega\text{m}$ at 100°C , the phase resistance is

$$R_s = 2.3 \cdot 10^{-8} \cdot \frac{0.104 \cdot N_1^2}{2.896.48} \cdot (2.15 \cdot 10^6) = 4 \cdot 10^{-5} \cdot N_1^2 \quad (2.53)$$

The phase inductance comprises the main inductance L_m , the leakage inductance L_{sl} , and the coupling inductance L_{12} :

$$\begin{aligned} L_m &= 2 \cdot N_1^2 \cdot \mu_0 \cdot \frac{\tau_{bt} \cdot l_{stack}}{(h_{PM} + g)} \cdot \frac{1}{a_1} \\ &= \frac{2 \cdot 4 \cdot \pi \cdot 10^{-7} \cdot 16.5 \cdot 10^{-3} \cdot 20 \cdot 10^{-3}}{(3 + 0.25) \cdot 10^{-3} \cdot 2} \cdot N_1^2 = 1.276 \cdot 10^{-7} \cdot N_1^2 \end{aligned} \quad (2.54)$$

The phase mutual inductance, L_{12} :

$$L_{12} \approx -\frac{L_m}{3} \quad (2.55)$$

The leakage inductance is calculated using geometrical slot- and end-connection permeances, λ_{ss} and λ_{s0} .

$$\lambda_{ss} = \frac{h_s}{3 \cdot w_{s2}} \cdot k_t + \frac{2 \cdot h_{s_bottom}}{w_{s2} + b_{os}} + \frac{h_{tt}}{b_{os}} \quad (2.56)$$

where [16]

$$k_t = 3 \cdot \frac{4 \cdot t^2 - t^4 \cdot (3 - 4 \cdot \ln t) - 1}{4 \cdot (t^2 - 1)^2 \cdot (t - 1)}; \quad t = \frac{w_{s1}}{w_{s2}} \quad (2.57)$$

$$t = \frac{8.265}{6.56} = 1.26$$

$$k_t = 3 \cdot \frac{4 \cdot 1.26^2 - 1.26^4 \cdot (3 - 4 \cdot \ln(1.26)) - 1}{4 \cdot (1.26^2 - 1)^2 \cdot (1.26 - 1)} = 0.9944$$

$$\lambda_{ss} = \frac{6.5}{3 \cdot 6.56} \cdot 0.9944 + \frac{2 \cdot 1.5}{6.56 + 0.5} + \frac{1.5}{0.5} = 3.7534$$

The analytical computation of the geometrical end-connection permeance, λ_{s0} , is done with the next expression [15]

$$\lambda_{s0} = \frac{p_1 \cdot q_1 \cdot D_{end}}{16 \cdot l_{stack}} \cdot \ln \left(\frac{D_{end}^2 \cdot \pi}{2 \cdot h_{ts} \cdot (w_{s1} + w_{s2})} \right) \quad (2.58)$$

where D_{end} is the diameter of the end-connection

$$D_{end} = (D_{is} + h_{ts}) \cdot \sin \left(\frac{\alpha_{bt}}{2} \right) = (42 + 9.5) \cdot \sin \left(\frac{46.38^\circ}{2} \right) = 20.28 \text{ mm} \quad (2.59)$$

$$\lambda_{s0} = \frac{4 \cdot 0.5 \cdot 20.28}{16 \cdot 20} \cdot \ln \left(\frac{20.28^2 \cdot \pi}{2 \cdot 9.5 \cdot (8.265 + 6.56)} \right) = 0.1931$$

Finally, the leakage inductance, L_{sl} , per phase is

$$\begin{aligned} L_{sl} &= 2 \cdot \mu_0 \cdot \frac{(\lambda_{ss} + \lambda_{s0})}{p_1 \cdot a_1 \cdot q_1} \cdot l_{stack} \cdot N_1^2 \\ &= 2 \cdot 4 \cdot \pi \cdot 10^{-7} \cdot \frac{(3.7534 + 0.1931)}{4 \cdot 2 \cdot 0.5} \cdot 20 \cdot 10^{-3} \cdot N_1^2 = 0.496 \cdot 10^{-7} \cdot N_1^2 \end{aligned} \quad (2.60)$$

The synchronous inductance L_s is

$$\begin{aligned} L_s &= L_m - L_{12} + L_{sl} = \frac{4}{3} \cdot L_m + L_{sl} \\ &= \left(\frac{4}{3} \cdot 1.276 + 0.496 \right) \cdot 10^{-7} \cdot N_1^2 = 2.197 \cdot 10^{-7} \cdot N_1^2 \end{aligned} \quad (2.61)$$

$$\begin{aligned} V_b &= \sqrt{(e_1 + R_s \cdot I_b)^2 + (\omega_{1b} \cdot L_s \cdot I_b)^2} \\ &= \sqrt{(0.06694 \cdot N_1 + 4 \cdot 10^{-5} \cdot N_1^2 \cdot I_b)^2 + (2 \cdot \pi \cdot 66.67 \cdot 2.197 \cdot 10^{-7} \cdot N_1^2 \cdot I_b)^2} \\ &= N_1 \cdot \sqrt{0.1028^2 + 0.0825^2} = 0.132 \cdot N_1 \end{aligned} \quad (2.62)$$

So the number of turns, N_1 , is

$$N_1 = 16.34 \text{ turns/coil} \cong 16 \text{ turns/coil} \quad (2.63)$$

Step 21. From Equation 2.53 the phase resistance, R_s , is

$$R_s = 4 \cdot 10^{-5} \cdot N_1^2 = 4 \cdot 10^{-5} \cdot 16^2 = 10.24 \text{ m}\Omega \quad (2.64)$$

Step 22. From Equation 2.61 the synchronous inductance, L_s , is

$$L_s = 2.197 \cdot 10^{-7} \cdot N_1^2 = 2.197 \cdot 10^{-7} \cdot 16^2 = 56.24 \text{ }\mu\text{H} \quad (2.65)$$

Step 23. From Equation 2.49 the phase back-EMF, e_1 , at base speed is

$$e_1 = 0.06694 \cdot N_1 = 0.06694 \cdot 16 = 1.071 \text{ V} \quad (2.66)$$

Step 24. The phase base current, I_b

$$I_b = \frac{(N_1 \cdot I_b)}{N_1} = \frac{896.48}{16} = 56.03 \text{ A} \quad (2.67)$$

Step 25. The copper losses, P_{co} , for base torque in the three-phase armature winding due to a 120° square wave current are:

$$P_{co} = 2 \cdot R_s \cdot I_b^2 = 2 \cdot 10.24 \cdot 10^{-3} \cdot 56.03^2 = 64.3 \text{ W} \quad (2.68)$$

Step 26. The mechanical losses are known as a function of the angular speed:

$$P_{mech} = f(\omega_m) \quad (2.69)$$

We chose the mechanical losses as

$$P_{mech} = 0.5\% \cdot P_b = 0.5\% \cdot 120 = 0.6 \text{ W} \quad (2.70)$$

Step 27. The iron losses in the stator teeth, P_{Fet} :

Based on available core-loss data, we may calculate hysteresis and eddy current losses [8]:

$$p_{hbt} = \frac{1}{\gamma_{Fe}} \cdot k_h \cdot f_b^{efh} \cdot B_{sbt}^{eBh} \quad (2.71)$$

$$p_{hlt} = \frac{1}{\gamma_{Fe}} \cdot k_h \cdot f_b^{efh} \cdot B_{slt}^{eBh} \quad (2.72)$$

$$p_{ebt} = \frac{\pi^2}{6 \cdot \rho_{Fe} \cdot \gamma_{Fe}} \cdot f_b^{efe} \cdot B_{sbt}^{eBe} \cdot d^{ed} \quad (2.73)$$

$$p_{elt} = \frac{\pi^2}{6 \cdot \rho_{Fe} \cdot \gamma_{Fe}} \cdot f_b^{efe} \cdot B_{slt}^{eBe} \cdot d^{ed} \quad (2.74)$$

$$p_{Febt} = p_{hbt} + p_{ebt} \quad (2.75)$$

$$p_{Felt} = p_{hlt} + p_{elt} \quad (2.76)$$

where

$\gamma_{Fe} = 7.8 \cdot 10^3 \text{ kg/m}^3$, is the iron density,

$k_h = 1$, is a multiplier constant for hysteresis losses,

$f_b = 66.67 \text{ Hz}$, is the base frequency,

B_{sbt} , B_{slt} are the flux densities in the stator big teeth, and stator little teeth respectively.

$efh = 1.1$, is the frequency exponent for hysteresis losses,

$eBh = 1.8$, is the flux density exponent for hysteresis losses,

$\rho_{Fe} = 61.9 \cdot 10^{-9} \text{ } \Omega \cdot \text{m}$ at 20°C, is the electrical resistivity of iron,

$d = 0.50 \text{ mm}$, is the lamination thickness,

$efe = 2$, is the frequency exponent for eddy current losses,

$eBe = 2$, is the flux density exponent for eddy current losses,

$ed = 2$, is the lamination thickness exponent.

Substituting the above values in Equations (2.71)-(2.76), we obtain

$$\begin{aligned}\rho_{\text{hbt}} &= \frac{1}{7.8 \cdot 10^3} \cdot 1 \cdot (66.67)^{1.1} \cdot (1.5)^{1.8} = 0.027 \text{ W/kg} \\ \rho_{\text{hlt}} &= \frac{1}{7.8 \cdot 10^3} \cdot 1 \cdot (66.67)^{1.1} \cdot 1^{1.8} = 0.013 \text{ W/kg} \\ \rho_{\text{ebt}} &= \frac{\pi^2}{6.61.9 \cdot 10^{-9} \cdot 7.8 \cdot 10^3} \cdot (66.67)^2 \cdot (1.5)^2 \cdot (0.5 \cdot 10^{-3})^2 = 8.518 \text{ W/kg} \\ \rho_{\text{ebt}} &= \frac{\pi^2}{6.61.9 \cdot 10^{-9} \cdot 7.8 \cdot 10^3} \cdot (66.67)^2 \cdot 1^2 \cdot (0.5 \cdot 10^{-3})^2 = 3.786 \text{ W/kg} \\ \rho_{\text{Febt}} &= 0.027 + 8.518 = 8.545 \text{ W/kg} \\ \rho_{\text{Felt}} &= 0.013 + 3.786 = 3.799 \text{ W/kg}\end{aligned}$$

The iron losses in the stator teeth are

$$P_{\text{Fet}} = \rho_{\text{Febt}} \cdot m_{\text{sbth}} + \rho_{\text{Felt}} \cdot m_{\text{slth}} \quad (2.77)$$

The stator big teeth and the stator little teeth weights, m_{slth} and m_{sbth} , are:

$$m_{\text{sbth}} = \frac{N_s}{2} \cdot w_{\text{bt}} \cdot h_{\text{ts}} \cdot l_{\text{stack}} \cdot k_{\text{stk}} \cdot \gamma_{\text{Fe}} = \frac{12}{2} \cdot 8.5 \cdot 9.5 \cdot 20 \cdot 10^{-9} \cdot 0.93 \cdot 7.8 \cdot 10^3 = 0.07 \text{ kg} \quad (2.78)$$

$$m_{\text{slth}} = \frac{N_s}{2} \cdot w_{\text{lt}} \cdot h_{\text{ts}} \cdot l_{\text{stack}} \cdot k_{\text{stk}} \cdot \gamma_{\text{Fe}} = \frac{12}{2} \cdot 3.5 \cdot 9.5 \cdot 20 \cdot 10^{-9} \cdot 0.93 \cdot 7.8 \cdot 10^3 = 0.029 \text{ kg} \quad (2.79)$$

where k_{stk} is the stacking factor and it vary from 0.5 to 0.95 approaching to unity as the lamination thickness increase.

$$P_{\text{Fet}} = 8.545 \cdot 0.07 + 3.799 \cdot 0.029 = 0.708 \text{ W}$$

Step 28. The iron losses in the stator yoke, P_{Fey} :

$$\rho_{\text{hy}} = \frac{1}{\gamma_{\text{Fe}}} \cdot k_h \cdot f_b^{\text{eff}} \cdot B_{\text{ys}}^{\text{eBh}} = \frac{1}{7.8 \cdot 10^3} \cdot 1 \cdot (66.67)^{1.1} \cdot 1^{1.8} = 0.013 \text{ W/kg} \quad (2.80)$$

$$\rho_{\text{ey}} = \frac{\pi^2}{6 \cdot \rho_{\text{Fe}} \cdot \gamma_{\text{Fe}}} \cdot f_b^{\text{efe}} \cdot B_{\text{ys}}^{\text{eBe}} \cdot d^{\text{ed}} \quad (2.81)$$

$$= \frac{\pi^2}{6.61.9 \cdot 10^{-9} \cdot 7.8 \cdot 10^3} \cdot (66.67)^2 \cdot 1^2 \cdot (0.5 \cdot 10^{-3})^2 = 3.786 \text{ W/kg}$$

$$\rho_{\text{Fey}} = \rho_{\text{hy}} + \rho_{\text{ey}} = 0.013 + 3.786 = 3.799 \text{ W/kg} \quad (2.81)$$

$$P_{\text{Fey}} = \rho_{\text{Fey}} \cdot m_{\text{sy}} \quad (2.83)$$

The stator yoke weight, m_{sy} , is:

$$\begin{aligned}m_{\text{sy}} &= \pi \cdot \left(D_{\text{so}}^2 - (D_{\text{so}} - 2 \cdot h_{\text{ys}})^2 \right) / 4 \cdot l_{\text{stack}} \cdot k_{\text{stk}} \cdot \gamma_{\text{Fe}} \\ &= \pi \cdot \left(70^2 - (70 - 2 \cdot 4.5)^2 \right) / 4 \cdot 20 \cdot 10^{-9} \cdot 0.93 \cdot 7.8 \cdot 10^3 = 0.134 \text{ kg}\end{aligned} \quad (2.84)$$

$$P_{\text{Fey}} = 3.799 \cdot 0.134 = 0.51 \text{ W}$$

Step 29. The total iron losses, P_{Fe} :

– is the sum of the teeth and the stator yoke losses

$$P_{Fe} = P_{Fet} + P_{Fey} = 0.708 + 0.51 = 1.218 \text{ W} \quad (2.85)$$

Step 30. The total losses, P_{loss} :

– is the sum of the copper, iron and mechanical losses

$$P_{loss} = P_{co} + P_{Fe} + P_{mech} = 64.3 + 1.218 + 0.6 = 66.118 \text{ W} \quad (2.86)$$

Step 31. The efficiency of the machine at base power and speed is

$$\eta = \frac{P_b}{P_b + P_{loss}} = \frac{120}{120 + 66.118} = 0.645 \quad (2.87)$$

The design solution of the IPMSM is shown in Fig. 2.12., the dimensions and properties are listed in Table 2.5 and the machine parameters are presented in Table 2.6.

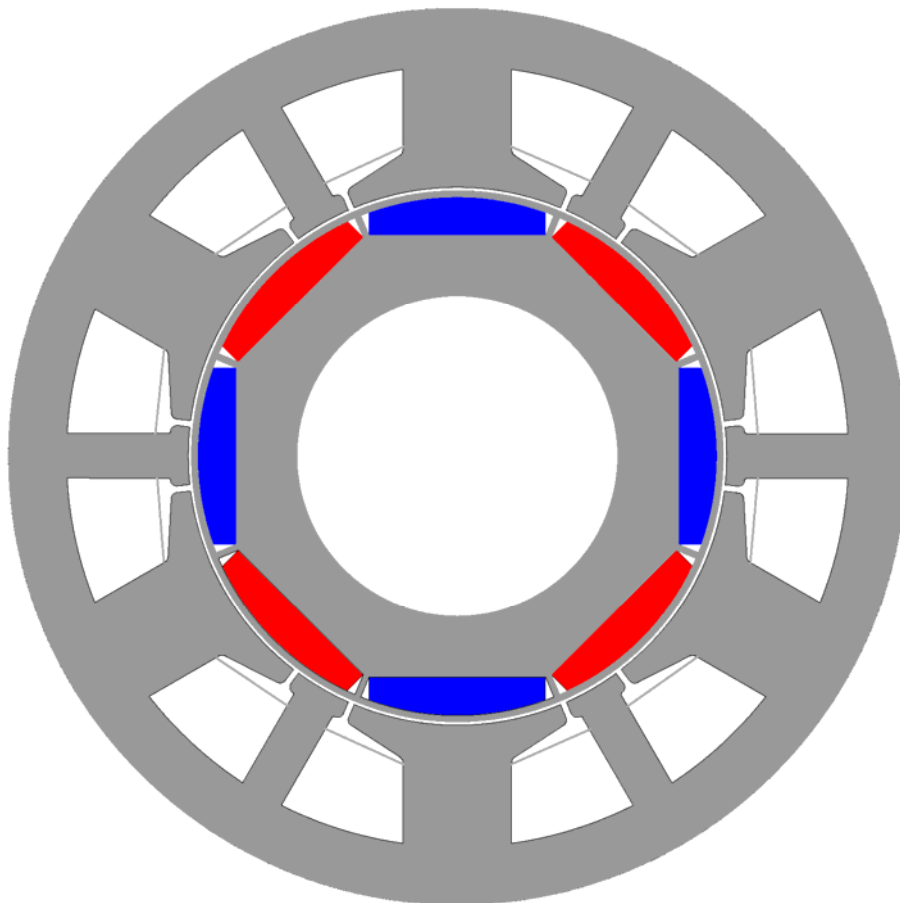


Fig. 2.12. Motor cross-section.

Table 2.5. Dimensions and properties of the dimensioned IPMSM

Parameter	Value	Measure unit
Topology		
number of phases (m)	3	-
number of stator slots	12	-
number of rotor poles	8	-
Geometry		
stator outer diameter	70	mm
stator inner diameter	42	mm
air-gap	0.25	mm
stator big tooth width	8.5	mm
stator little tooth width	3.5	mm
stator yoke height	4.5	mm
rotor yoke height	4.75	mm
stack length	20	mm
magnet width	13.75	mm
magnet height	3	mm
slot opening	0.5	mm
tooth tip height	1.5	mm
height of the slot bottom	1.5	mm
slot depth	9.5	mm
rotor bridge and wedge width	0.5	mm
Winding		
no. slots/pole/phase	0.5	-
no. turns per phase	16	-
no. of parallel current paths	2	-
slot fill factor	0.55	-
no. coils/phase	2	-
Materials		
core material	M800-50A	-
magnet type	NdFeB(1.2T)	-

Table 2.6. Machine parameters (analytical calculation)

Parameter	Symbol	Value	Measure unit
Phase resistance (100°C operating temperature)	R_s	10.24	m Ω
Phase leakage inductance	L_s	56.24	μ H
Phase base current	I_b	56.03	A
Phase base voltage (rms)	V_b	2.16	V
Base output power	P_b	120	W
Rated efficiency	η	64.5	%
Rated copper losses	P_{co}	64.3	W
Rated iron losses in stator teeth	P_{Fet}	0.708	W
Rated iron losses in stator yoke	P_{Fey}	0.51	W
Rated total iron losses	P_{Fe}	1.218	W
Rated friction losses (bearing, windage)	P_{mech}	0.6	W

2.5. Weights and costs of active materials

The weight of windings:

$$m_{Co} = N_s \cdot \frac{I_{turn}}{2} \cdot A_{slot} \cdot k_{sf} \cdot \gamma_{Co} = 12 \cdot \frac{0.104}{2} \cdot 54.33 \cdot 10^{-6} \cdot 0.55 \cdot 8.93 \cdot 10^3 = 0.167 \text{ kg} \quad (2.88)$$

where $\gamma_{Co} = 8.93 \cdot 10^3 \text{ kg/m}^3$, is the copper density.

The PM weight:

$$m_{PM} = 2 \cdot p_1 \cdot A_{PM} \cdot I_{rotor} \cdot \gamma_{PM} \quad (2.89)$$

where $\gamma_{PM} = 7.4 \cdot 10^3 \text{ kg/m}^3$, is the permanent magnet density, and A_{PM} is one magnet pole piece area:

$$A_{PM} = \left(h_{PM} - \left(\frac{D_{ro}}{2} - h_{bridge} \right) \cdot \left(1 - \cos \left(\frac{\alpha_{PM}}{2} \right) \right) \right) \cdot W_{PM} + \left(\frac{D_{ro}}{2} - h_{bridge} \right)^2 \cdot \left(\frac{\alpha_{PM}}{2} - \sin \left(\frac{\alpha_{PM}}{2} \right) \cdot \cos \left(\frac{\alpha_{PM}}{2} \right) \right) \quad (2.90)$$

$$\alpha_{PM} = 2 \cdot \text{asin} \left(\frac{W_{PM}}{D_{ro} - 2 \cdot h_{bridge}} \right) = 2 \cdot \text{asin} \left(\frac{13.75}{41.5 - 2 \cdot 0.5} \right) = 0.693 \text{ rad} \quad (2.91)$$

$$\begin{aligned} A_{PM} &= \left(3 - \left(\frac{41.5}{2} - 0.5 \right) \cdot \left(1 - \cos \left(\frac{0.693}{2} \right) \right) \right) \cdot 13.75 \cdot 10^{-6} \\ &+ \left(\frac{41.5}{2} - 0.5 \right)^2 \cdot \left(\frac{0.693}{2} - \sin \left(\frac{0.693}{2} \right) \cdot \cos \left(\frac{0.693}{2} \right) \right) \cdot 10^{-6} \\ &= 3.563 \cdot 10^{-5} \text{ m}^2 \\ m_{PM} &= 2 \cdot 4 \cdot 3.563 \cdot 10^{-5} \cdot 21 \cdot 10^{-3} \cdot 7.4 \cdot 10^3 = 0.0443 \text{ kg} \end{aligned}$$

The rotor yoke weight:

$$\begin{aligned} m_{rFe} &= \left(\pi \cdot \frac{(D_{ro}^2 - D_{ri}^2)}{4} - 2 \cdot p_1 \cdot A_{PM} \right) \cdot I_{rotor} \cdot k_{stk} \cdot \gamma_{Fe} \\ &= \left(\pi \cdot \frac{((41.5)^2 - 25^2)}{4} \cdot 10^{-6} - 2 \cdot 4 \cdot 3.563 \cdot 10^{-5} \right) \cdot 21 \cdot 10^{-3} \cdot 0.93 \cdot 7.8 \cdot 10^3 = \\ &= 0.088 \text{ kg} \end{aligned} \quad (2.92)$$

The stator teeth weight:

$$\begin{aligned} m_{sbth} &= \frac{N_s}{2} \cdot w_{bt} \cdot h_{ts} \cdot I_{stack} \cdot k_{stk} \cdot \gamma_{Fe} = \frac{12}{2} \cdot 8.5 \cdot 9.5 \cdot 20 \cdot 10^{-9} \cdot 0.93 \cdot 7.8 \cdot 10^3 = 0.07 \text{ kg} \\ m_{slth} &= \frac{N_s}{2} \cdot w_{lt} \cdot h_{ts} \cdot I_{stack} \cdot k_{stk} \cdot \gamma_{Fe} = \frac{12}{2} \cdot 3.5 \cdot 9.5 \cdot 20 \cdot 10^{-9} \cdot 0.93 \cdot 7.8 \cdot 10^3 = 0.029 \text{ kg} \\ m_{sth} &= m_{sbth} + m_{slth} = 0.07 + 0.029 = 0.1 \text{ kg} \end{aligned} \quad (2.93)$$

The stator yoke weight:

$$\begin{aligned} m_{sy} &= \pi \cdot \left(D_{so}^2 - (D_{so} - 2 \cdot h_{ys})^2 \right) / 4 \cdot l_{stack} \cdot k_{stk} \cdot \gamma_{Fe} \\ &= \pi \cdot \left(70^2 - (70 - 2 \cdot 4.5)^2 \right) / 4 \cdot 20 \cdot 10^{-9} \cdot 0.93 \cdot 7.8 \cdot 10^3 = 0.134 \text{ kg} \end{aligned} \quad (2.94)$$

The stator core weight:

$$m_{sFe} = m_{sy} + m_{sth} = 0.134 + 0.1 = 0.234 \text{ kg} \quad (2.95)$$

The total weight of the active materials becomes

$$m_{tot} = m_{rFe} + m_{PM} + m_{sFe} + m_{co} = 0.088 + 0.0443 + 0.234 + 0.167 = 0.533 \text{ kg} \quad (2.96)$$

As the laminations are stamped from squares, their weight, m_{Fe} , is in fact

$$m_{uFe} = D_{so}^2 \cdot l_{stack} \cdot k_{stk} \cdot \gamma_{Fe} = 70^2 \cdot 20 \cdot 10^{-9} \cdot 0.93 \cdot 7.8 \cdot 10^3 = 0.711 \text{ kg} \quad (2.97)$$

The costs of the active materials can be written as

$$\begin{aligned} C_{mat} &= m_{uFe} \cdot C_{lam} + m_{PM} \cdot C_{PM} + m_{co} \cdot C_{co} \\ &= 0.711 \cdot 5 + 0.0402 \cdot 50 + 0.167 \cdot 10 = 7.24 \text{ USD} \end{aligned} \quad (2.98)$$

where $C_{lam} = 5$ USD/kg, $C_{co} = 10$ USD/kg and $C_{PM} = 50$ USD/kg are the specific prices for the laminations, copper and permanent magnets respectively [8].

2.6. Thermal verification

To roughly verify the winding over temperature of the machine, first the total frame area, A_{frame} , for heat transfer is calculated:

$$A_{frame} = \pi \cdot D_{so} \cdot l_{frame} \cdot k_f + \frac{\pi}{2} \cdot D_{so}^2 \quad (2.99)$$

where $k_f = 3$ is the cooling surface increase ratio due to fins [8] and l_{frame} is:

$$l_{frame} = l_{stack} + D_{end} = 20 + 20.28 = 40.28 \text{ mm} \quad (2.100)$$

$$A_{frame} = \pi \cdot 70 \cdot 40.28 \cdot 10^{-6} \cdot 3 + \frac{\pi}{2} \cdot 70^2 \cdot 10^{-6} = 0.03427 \text{ m}^2$$

The adding an equivalent heat transfer coefficient, α_t (in W/m²°C), from 14 (for unventilated frames) to 100 (for water-cooled frame jackets), the winding over temperature, T_w , is

$$T_w = \frac{P_{co} + P_{Fe}}{\alpha_t \cdot A_{frame}} = \frac{64.3 + 1.217}{14.2 \cdot 0.03427} = 134.63 \text{ °C} \quad (2.101)$$

For a maximum winding temperature of 155°C (class F) the thermal calculation is verified.

If the over temperature is high, the machine design is redone from start, with a smaller f_{tsp} and / or longer λ (longer stack length).

2.7. Conclusion

A synthesis of fractional slot concentrated winding permanent magnet synchronous machines was presented, emphasizing the PMSM structures with concentrated windings and irregular distribution of stator slots.

A permanent magnet machine with 24 slots and 8 poles is chosen for the conceptual derivation of a machine with concentrated coils and nonuniform slots

This chapter also presents the electromagnetic design for a fractional slot concentrated winding permanent magnet synchronous machine case study: an interior permanent magnet synchronous motor with 8 rotor poles and nonuniform (6+6) stator slots and concentrated windings fed with trapezoidal currents.

Next chapters from this thesis will focus on the motor topology introduced and designed here.

References

- [1] A.M. El-Rafaie, "Fractional-Slot Concentrated-Windings Synchronous Permanent Magnet Machines: Opportunities and Challenges", *IEEE Trans. on Industrial Electronics*, Vol. 57, No. 1, pp. 107-121, January 2010.
- [2] D. Ishak, Z.Q. Zhu, D. Howe, "Comparison of PM Brushless Motors, Having Either All Teeth or Alternate Teeth Wound", *IEEE Trans. on Energy Conversion*, Vol. 21, No. 1, pp. 95-103, March 2006.
- [3] F. Magnussen and C. Sadarangani, "Winding Factors and Joule Losses in Permanent Magnet Machines with Concentrated Windings", *IEEE International Electrical Machines and Drives Conference 2003, IEMDC'03*, Madison, WI, Vol. 1, pp. 333-339, June 2003.
- [4] F. Magnussen and H. Lendenmann, "Parasitic Effects in PM Machines with Concentrated Windings", *Industry Applications Conference, 40th IAS Annual Meeting, Conference Record of the 2005*, Vol. 2, pp. 1044-1049, 2005.
- [5] P. Salminen, "Fractional Slot Permanent Magnet Synchronous Motors for Low Speed Applications", PhD Thesis, Lappeenranta, Finland, 2004.
- [6] J. Cros and P. Viarouge, "Synthesis of high performance PM Motors with Concentrated Windings", *IEEE Trans. on Energy Conversion*, Vol. 17, No. 2, pp. 248-253, June 2002.
- [7] F. Libert and J. Soulard, "Investigation on Pole-Slot Combinations for Permanent-Magnet Machines with Concentrated Windings", *International Conference Electrical Machines (ICEM 04)*, Cracow, Poland, September 2004.
- [8] I. Boldea and L.N. Tutelea, "Electric Machines: Steady State, Transients, and Design with MATLAB", CRC Press, Taylor and Francis Group, Boca Raton, FL, 2010.
- [9] S.P. Cheng and C.C. Hwang, "Design of High-Performance Spindle Motors With Single-Layer Concentrated Windings and Unequal Tooth Widths", *IEEE Trans. on Magnetics*, Vol. 43, No. 2, pp. 802-804, February 2007.

- [10] D. Iles, "Automotive Permanent Magnet Actuation Technologies", PhD Thesis, Timisoara, 2005.
- [11] J.J. Germishuizen and M.J. Kamper, "IPM Traction Machine With Single Layer Non-Overlapping Concentrated Windings", *IEEE Trans. on Industry Applications*, Vol. 45, No. 4, pp. 1387-1394, July/August 2009.
- [12] Power Core M800-50A NGO Electrical Steel Application Note, ThyssenGrupp Steel, pp. 1-9, 2009.
- [13] Typical Data for SURA[®] M800-50A, Cogent Surahammars Bruks AB, 2008.
- [14] DEXTER Magnetic Technologies, "Permanent Magnet Catalog".
- [15] D.C. Hanselman, "Brushless Permanent-Magnet Motor Design", McGraw-Hill Inc., 1994.
- [16] J.F. Gieras, "Permanent Magnet Motor Technology, Design and Applications", 3rd ed., CRC Press, Taylor and Francis Group, Boca Raton, FL, 2010.
- [17] T.J.E. Miller, "SPEED's Electric Motors", Glasgow, 2002.
- [18] J.R. Hendershot and T.J.E. Miller, "Design of Brushless Permanent-Magnet Motors", Oxford University Press, Oxford, U.K., 1995.
- [19] W. Ouyang, D. Zarko, T.A. Lipo, "Permanent Magnet Machine Design Practice and Optimization", *Industry Applications Conference, 41st IAS Annual Meeting, Conference Record of the 2006 IEEE*, Tampa, FL, Vol. 4, pp. 1905-1911, 2006.
- [20] C.B. Rasmusen, "Modeling and Simulation of Surface Mounted PM Motors", PhD Thesis, Institute of Energy Technology, Aalborg University, Aalborg, Denmark, 1996.
- [21] S. Meier, "Theoretical Design of Surface-Mounted Permanent Magnet Motors with Field-Weakening Capability", Master Thesis, Royal Institute of Technology, Stockholm, 2002.
- [22] M. Markovic and Y. Perriard, "An Analytical Formula for The Back-EMF of A Slotted BLDC Motor", *IEEE International Electrical Machines and Drives Conference 2007, IEMDC '07*, Vol. 2, pp. 1534-1539, 2007.
- [23] E.V. Kazmin, E.A. Lomonova, J.J.H. Paulides, "Brushless Traction PM Machines Using Commercial Drive Technology, Part I: Design Methodology and Motor Design", *International Conference on Electrical Machines and Systems, ICEMS*, pp. 3801-3809, 2008.
- [24] E.V. Kazmin, E.A. Lomonova, J.J.H. Paulides, "Brushless Traction PM Machines Using Commercial Drive Technology, Part II: Comparative Study of the Motor Configurations", *International Conference on Electrical Machines and Systems, ICEMS*, pp. 3772-3780, 2008.
- [25] F. Meier and J. Soulard, "PMSMs with Non-Overlapping Concentrated Windings: Design Guidelines and Model References", *EVER*, Monaco, March 2009.

Chapter 3

FE analysis versus experimental results: fields, torque, and parameters

Abstract

This chapter presents a comparison between FEM calculated and measured torque, back-EMF and inductances for an (6+6) slots/ 8 poles 3 phase brushless DC actuator with interior permanent magnets. Dimensioning procedure of the proposed topology was presented in the previous chapter and here is validated using a 2D Finite Element Method (FEM). A numerical calculation of the magnetic field distribution of the brushless DC actuator is carried out determining all relevant characteristics of the motor: field distribution at no-load and at load, back-EMF at no-load, cogging torque (torque at zero current), load torque pulsations, reluctance torque pulsations, torque-rotor angular position characteristics for different trapezoidal-current shapes, torque-rotor angular position characteristics for different current amplitudes, and saturated synchronous inductances.

The tests carried out within the measurement procedure have the purpose to deliver machine parameters necessary for further system simulations and control tasks. Whenever possible, FEM-calculated characteristics are compared with experimentally obtained ones, in order to validate the FEM computations for this type of machine.

3.1. Introduction

The technical advantages of permanent magnet synchronous motors (PMSM) with trapezoidal shape back-EMF, also called permanent magnet brushless DC motors (PMBLDCM), have determined in the last years the extension of their area of application in a wide range of industrial fields such as automotive applications, home appliance and industrial robots.

This electric machine type has many performance advantages in comparison with the conventional electrically excited synchronous machine, such as: no copper losses in the rotor (and also reduced iron losses), reduced size and weight design due the permanent magnet excitation [1], low noise and maintenance, high efficiency, improved reliability and very good control characteristics in a wide speed range. However, the permanent magnet excitation has some drawbacks: high cost of the permanent magnets, demagnetization at high temperature, increased constructive effort for permanent magnet fixture on/in rotor, additional effort for field weakening control.

In PMSM the currents carried by the stator winding system and the rotor field excited by permanent magnets, are interacting during the energy conversion to produce torque. This interaction produces also a centrifugal force, which can cause the separation of PM at high speeds [2]. This can be avoided in the case of interior

permanent magnet synchronous (IPMSMs), since extra benefits are added to those of surface permanent magnet synchronous machines (SPMSMs), like higher torque output capabilities due to the reluctance torque, robust structure by embedded permanent magnets in the interior of rotor core. Not surprisingly, a vast amount of attention has been given to these motors in a variety of automotive applications [1-12].

A major drawback of IPMSM is that produces significantly level of cogging torque, generated by the interaction between the magnetized permanent magnets and the air-gap permeance harmonics. One main issue becomes critical in IPMSM with trapezoidal current control, the reduction of cogging torque that may cause vibration and acoustic noise.

Accurate estimation of machine parameters is very important for the development of high performance drive systems, for system simulations and controller design. In order to obtain accurate results from mathematical machine models embedded in system simulations and controller, their accurate parameters are needed. It is obvious that the exact determination of the machine parameters is the main task, as they are imposing the accuracy with which all the characteristics of the permanent magnet synchronous machine under consideration will be derived.

Several methods for estimating the synchronous machine parameters have been presented so far in the literature [13-19]. Although the IPMSM is a type of synchronous machine, many of conventional test methods for synchronous machines are not applicable to IPMSM. The identification method presented in [15] accurately predicts the machine parameters even in a machine with large harmonics (IPM or reluctance machine), but it is well known that in the case of permanent magnets embedded inside the rotor iron, calculations based on classical dq theory can be unreliable, mainly because of the variation of parameters due to saturation [17].

This chapter presents a comparison between FEM-calculated and measured torque, back-EMF and inductances for a three-phase interior permanent magnet brushless DC motor with 8 rotor poles and (6+6) nonuniform stator slots and concentrated windings, considered as a proper candidate for an automotive actuator application. This configuration is chosen because it has by default flat back-EMF shape, being proper for block commutated motors, has less coils than a traditional 12 slots motor and it seems possible with this specific configuration to directly minimize the cogging torque without skewing the slots.

In the first part of the chapter a numerical calculation of the magnetic field distribution, using a 2D Finite Element Method (FEM), was carried. FEM is used to validate and to analyze the topology, determining all relevant characteristics of the machine: field distribution at no-load and at load, back-EMF at no-load, cogging torque (zero current), load torque pulsations, reluctance torque pulsations, torque-rotor angular position characteristics for different trapezoidal-current shapes, torque-rotor angular position characteristics for different current amplitudes, and saturated synchronous inductances.

In the second part of the chapter measurement procedures were described and the measurement results are presented and discussed. Whenever possible, calculated characteristics are compared with experimentally obtained ones, in order to validate the FEM-computations for this type of machine.

3.2. FE analysis of concentrated coils and nonuniform slots (6+6/8) IPMSM with trapezoidal current control

3.2.1. The FE software

Finite element analysis is a very useful tool for predicting and estimating the effect of different design parameters on motor performance [13]. Different software packages related to FEA exist in use. The results in this section were computed using Finite Element Method Magnetics software, FEMM, Ver. 4.2 [20].

FEMM is a suite of programs for solving low frequency electromagnetic problems on two-dimensional planar and axisymmetric or planar domains. The program addresses linear/nonlinear magnetostatic problems, linear/nonlinear time harmonic magnetic problems, linear electrostatic problems, and steady-state heat flow problems [20].

FEMM has three parts:

- **Interactive shell (femm.exe)** – is a Multiple Document Interface pre-processor and a post-processor. It contains a CAD-like interface for laying out the geometry of the problem to be solved and for defining material properties and boundary conditions. Autocad DXF files can be imported to facilitate the analysis of existing geometries. The program allows the user to inspect the field at arbitrary points, as well as evaluate a number of different integrals and plot various quantities of interest along user-defined contours.
- **triangle.exe**. Triangle splits the solution region into a large number of triangles, a vital part of the finite element process.
- **Solvers (fkern.exe** for magnetics, **belasolv** for electrostatics, **hsolv** for heat flow problems, and **csolv** for current flow problems). Each solver takes a set of data files that describe problem and solves the relevant partial differential equations to obtain values for the desired field throughout the solution domain.

A very important feature for FEMM software is the Lua scripting language, which is integrated into the interactive shell. Lua can both build and analyze a geometry and evaluate the post-processing results, simplifying the creation of various sorts of “batch” runs. All edit boxes in the user interface are parsed by Lua, allowing equations or mathematical expressions to be entered into any edit box instead of a numerical value.

3.2.2. The FE model

Using FEMM, the modeling includes following steps:

- **Problem definition** (Problem Type, Length Units, Frequency, Depth, Solver Precision and Minimum Angle).
- **Geometry definition**. This can be done by user, using the CAD-like features of the software or by importing it as DXF-file.
- **Boundary definition** – an adequate number of boundary conditions has to be defined by the user, to guarantee a unique solution.
- **Materials property definition** – is used to specify the properties to be associated with each geometrical closed region. These properties have to do with the material that the block is composed of, as well as some attributes about how the material is put together (laminated).

- **Winding system definition** – allows the user to apply constraints on the current flowing in one or more blocks
- **Mesh generation** – automatic or manual.
- **FEM application**
- **Postprocessor** – is used to view solutions generated by the solver, to extract the results and to analyze them.

FE-analysis of the topology can offer direct results for:

- field distribution at no-load and at load,
- back-EMF at no-load,
- cogging torque (zero current)
- load torque pulsations,
- reluctance torque pulsations,
- torque-rotor angular position characteristics for different trapezoidal-current shapes,
- torque-rotor angular position characteristics for different current amplitudes,
- saturated synchronous inductances.

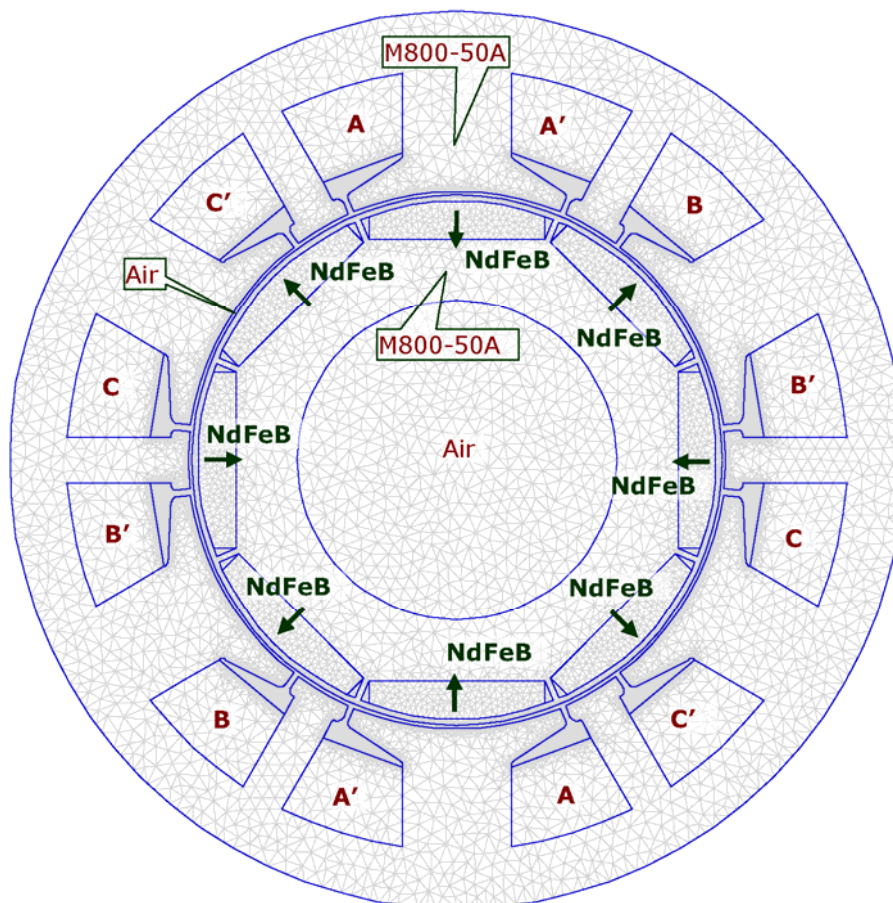


Fig. 3.1. Finite elements mesh and material definition.

The numerical calculation of the magnetic field distribution for the topology designed in Chapter 2 can be solved two dimensionally by observing the parallel plane symmetry [21].

Analysis and calculations using FEM were done for a reduced number of elements (59131 elements, 29686 nodes) for the mesh of the complete machine model, as can be seen in Fig. 3.1. This is enough for an accurate FE-modeling of a machine with these dimensions (Chapter 2, Table 2.5).

The winding definition is presented in Fig. 3.1. This distribution corresponds to a winding scheme of the 12-slots/8-poles machine with a single-layer concentrated winding with star-parallel phase connection as shown in Fig. 3.2.

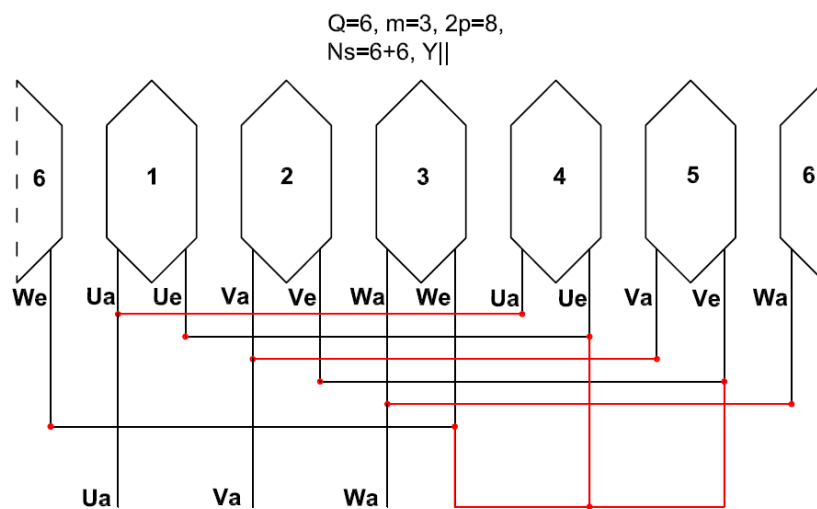


Fig. 3.2. Winding layout of (6+6) slots/ 8 poles machine.

3.2.3. Field distribution

The first step in a FE-analysis is the field distribution at no-load and at load. This gives the possibility to get first information about the design quality [1]. Mainly the "harmony" of the field distribution and the saturation level can be assessed.

3.2.3.1. No-load field distribution

The no-load field distribution, saturation level, and the air-gap flux density were calculated for two rotor positions. Fig. 3.3, Fig. 3.4, and Fig. 3.5 present the results for the d-axis aligned with phase "a" (d-axis aligned with the tooth corresponding to phase "a"). Fig. 3.6, Fig. 3.7, and Fig. 3.8 present the results for the q-axis aligned with phase "a" (q-axis aligned with the tooth corresponding to phase "a").

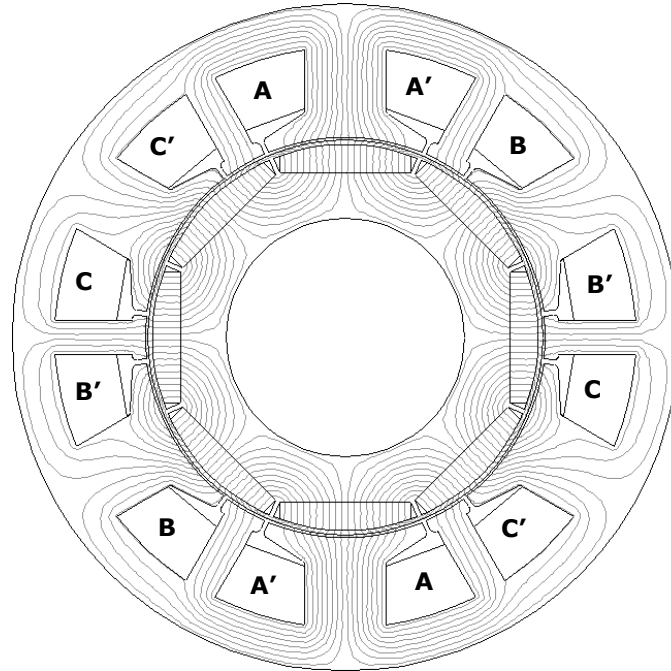


Fig. 3.3. Field distribution (no-load, d-axis aligned with the tooth corresponding to phase "a").

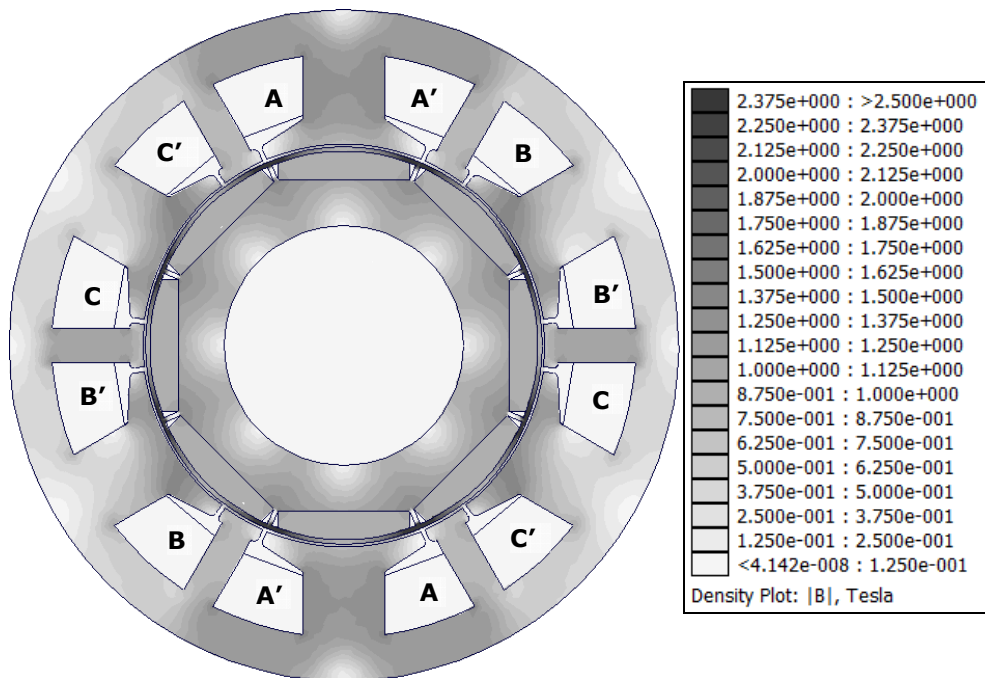


Fig. 3.4. Flux density distribution (no-load, d-axis aligned with the tooth corresponding to phase "a").

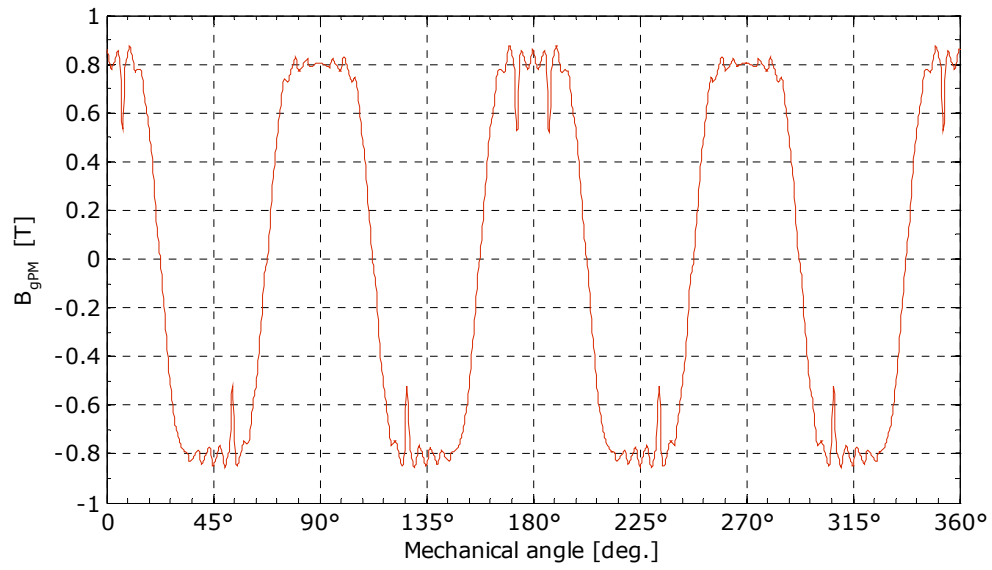


Fig. 3.5. Air-gap flux density (no-load, d-axis aligned with the tooth corresponding to phase "a").

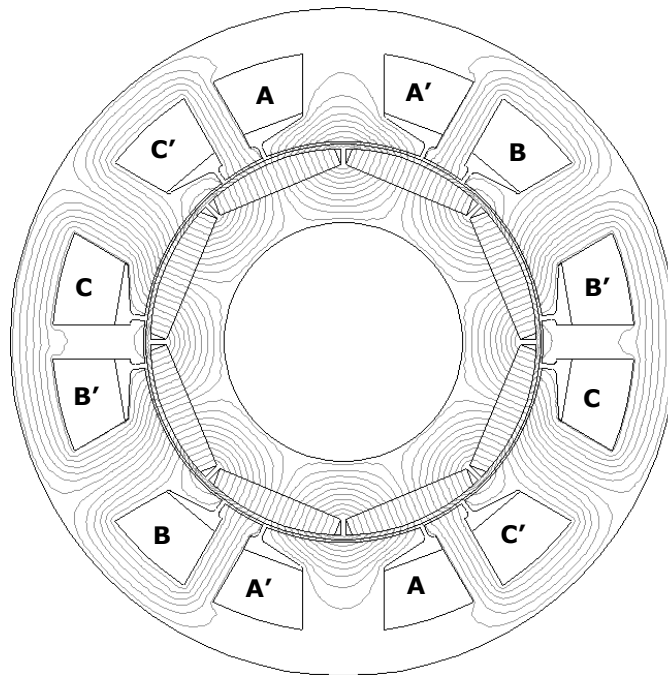


Fig. 3.6. Field distribution (no-load, q-axis aligned with the tooth corresponding to phase "a").

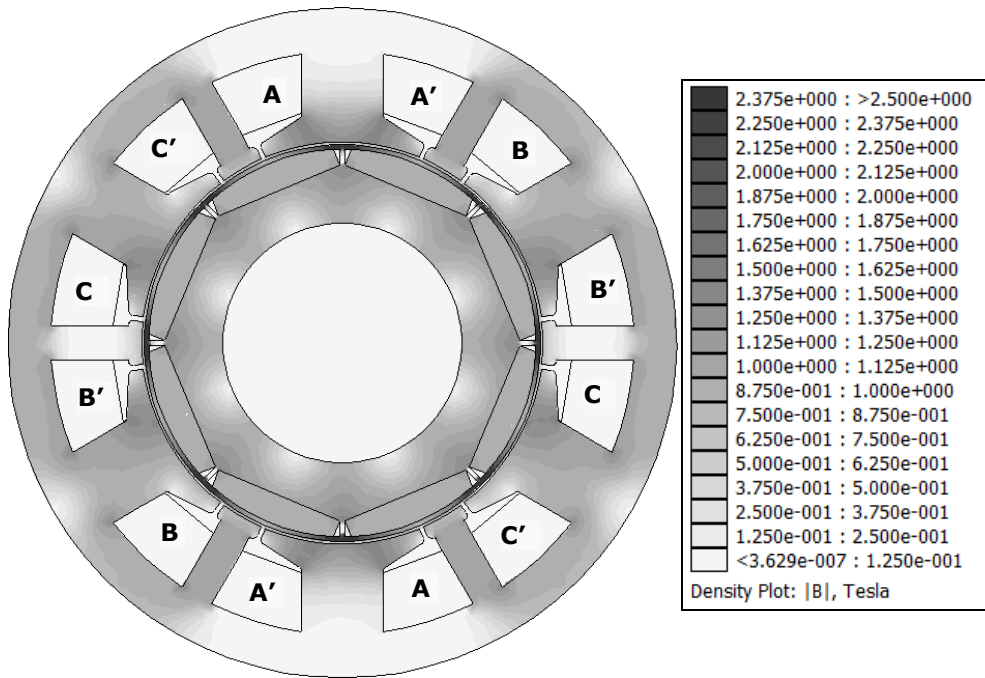


Fig. 3.7. Flux density distribution (no-load, q-axis aligned with the tooth corresponding to phase "a").

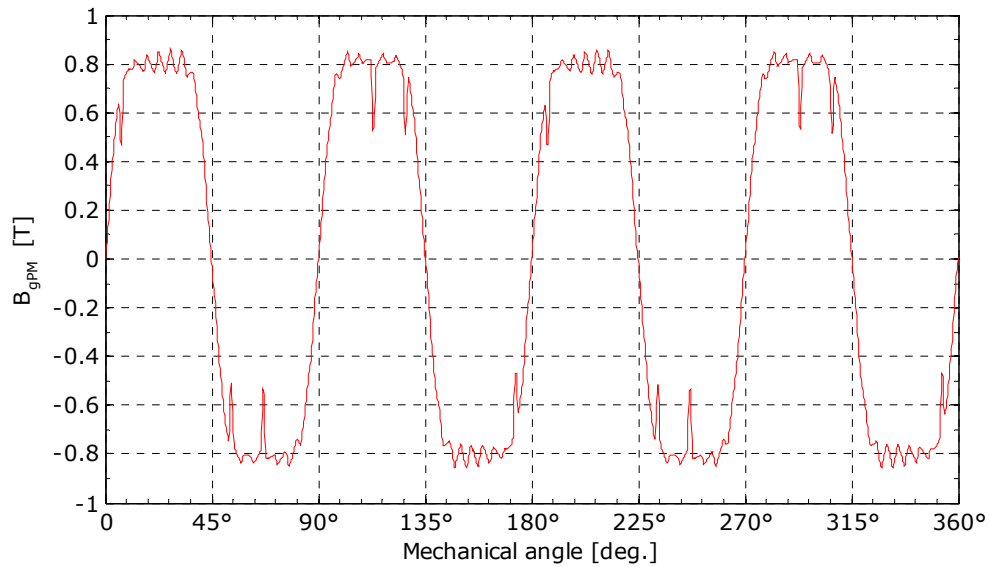


Fig. 3.8. Air-gap flux density (no-load, q-axis aligned with the tooth corresponding to phase "a").

A good field distribution confirms the design and, at the same time, the correctness of the FE modeling and computation. The very high saliency of the

tangential iron bridges in the rotor, at the tipper magnets shoulders can be observed. This saliency is mandatory for a good design in order to reduce the leakage [1]. The rest of the magnetic circuit presents (at no-load) flux densities below 1.2 T. This situation will change under load, when high currents will disturb the field distribution (armature reaction).

3.2.3.2. Field distribution under load

The field distribution for the loaded motor is presented now. The considered load point is: base electromagnetic torque $T_{eb} = 1.14$ Nm, phase base current $I_b = 56$ A peak.

In order to see better the changes in the field distribution in the load case, the results are presented in comparison to the results for the no-load situation. Fig. 3.9 presents the comparison between field distribution at load and at no-load. Fig. 3.10 shows the comparison between flux density distributions in both cases. Fig. 3.11 highlights the higher saturated regions (above 1.0 T) for load versus no-load.

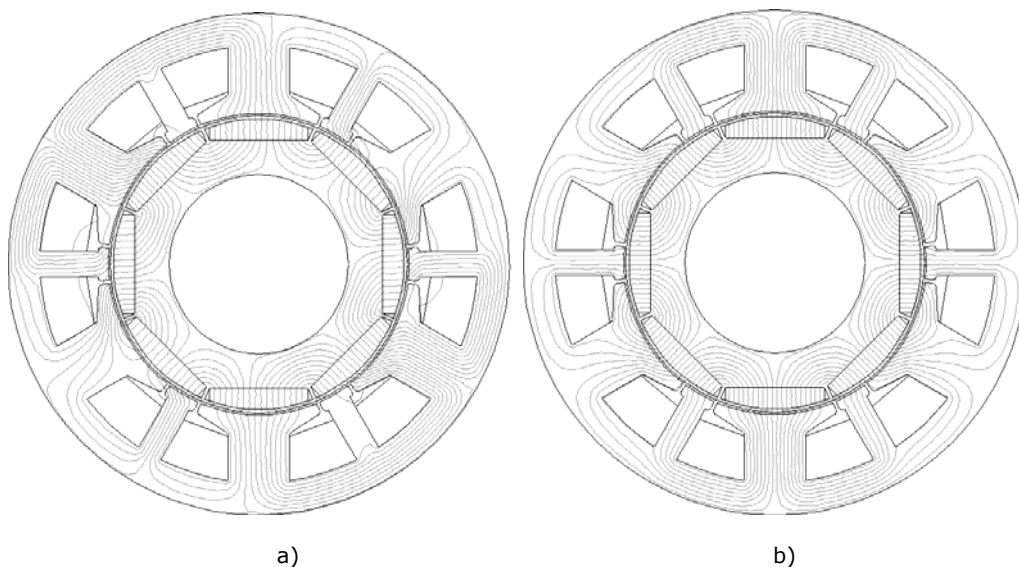


Fig. 3.9. Field distribution: a) under load, b) no-load.

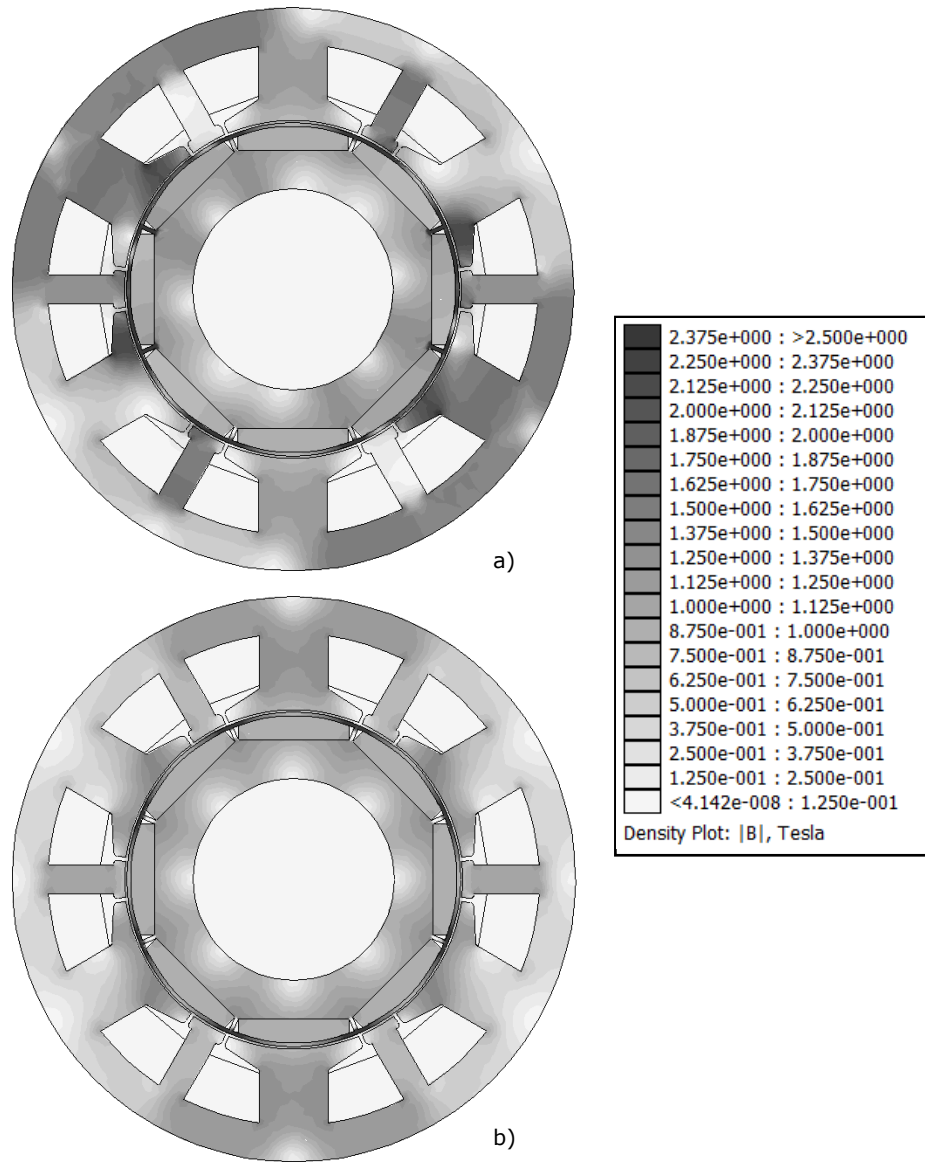


Fig. 3.10. Flux density distribution: a) under load, b) no-load.

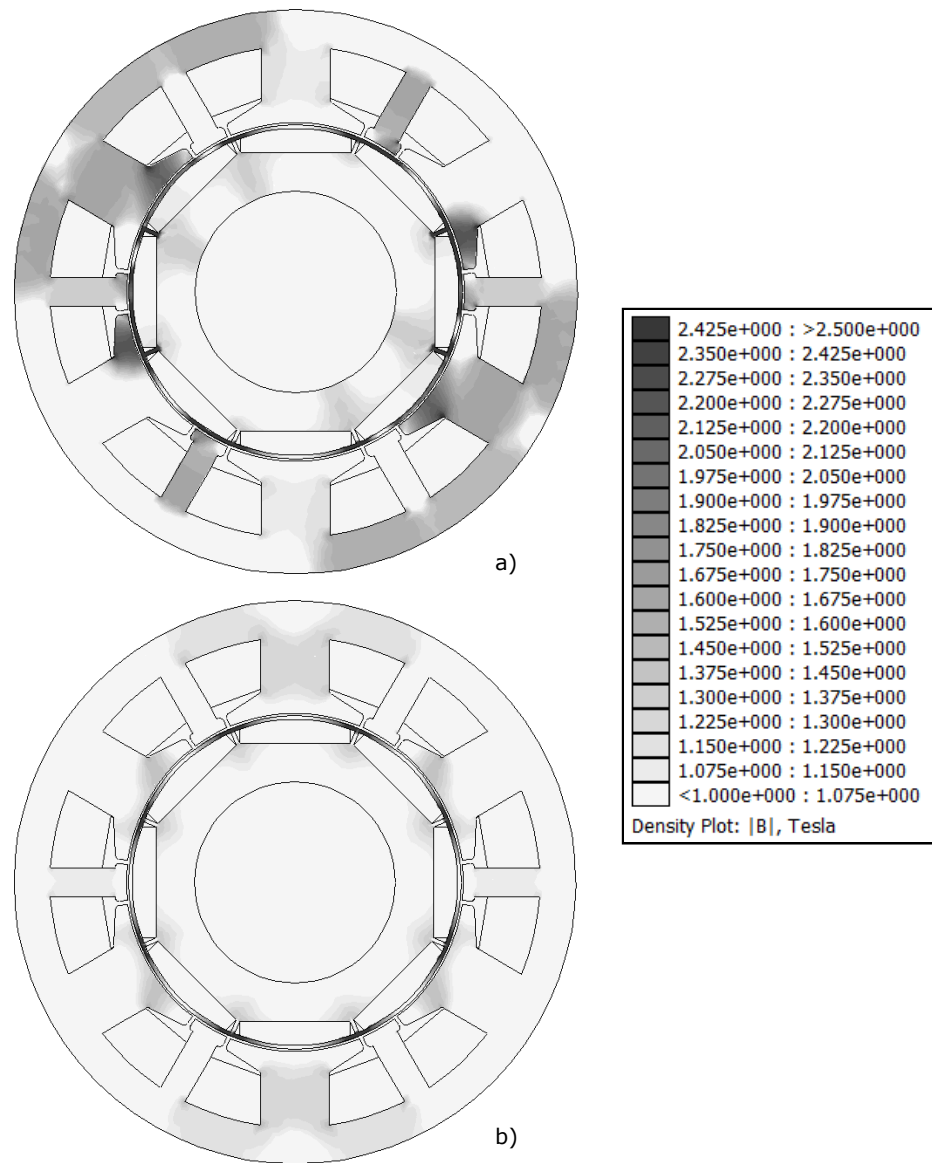


Fig. 3.11. Higher saturated regions (above 1 T) for: a) load, b) no-load.

3.2.4. No-load phase flux linkage and back-EMF

The no-load flux linkage is calculated for different rotor. In FEMM the total flux in a bulk flux path can be determined using the line integral of the normal component of the flux density, B_n , along a specified contour. This integral is performed by evaluating a large number of points at evenly spaced along the contour and integrating using a simple trapezoidal-type integration scheme [20].

$$\Phi = I_{stack} \cdot \int_{\Gamma} B_n \cdot dl \quad (3.1)$$

For the machine topology analyzed in this chapter, three contours have to be specified, one for each phase (see Fig. 3.12).

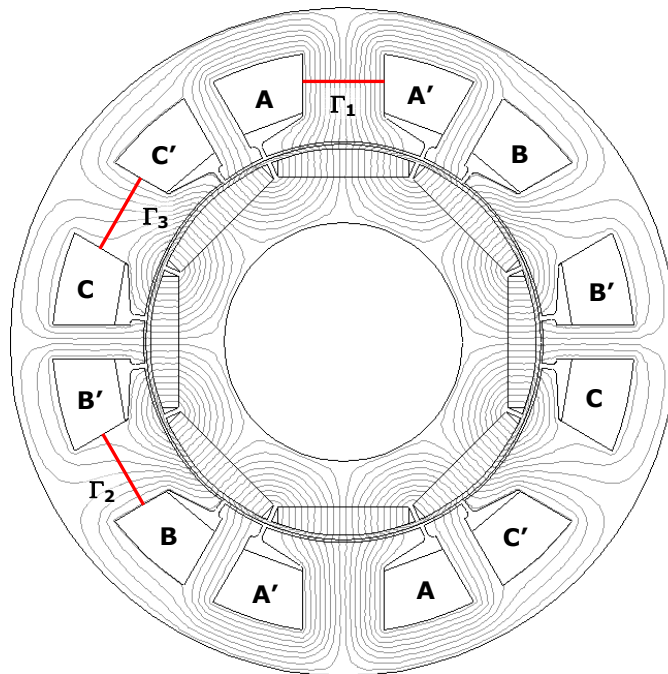


Fig. 3.12. Contours definition for no-load flux linkage computation.

Fig. 3.13 shows the FEM-calculated no-load phase flux linkages. The back-EMF was calculated using Faraday's Law

$$e_a = -\frac{d\lambda_{aPM}(\theta_m)}{dt} = -\frac{d\lambda_{aPM}(\theta_m)}{d\theta_m} \cdot \frac{d\theta_m}{dt} = -\frac{d\Phi_{aPM}(\theta_m)}{d\theta_m} \cdot N_1 \cdot \frac{d\theta_m}{dt} = k_E \cdot \omega_m \quad (3.2)$$

where ω_m is the angular velocity of the rotor in mechanical rad/s, θ_m is the rotor position in mechanical radians and k_E is the back-EMF constant in Vs/rad

$$k_E = -\frac{d\Phi_{aPM}(\theta_m)}{d\theta_m} \cdot N_1 \quad (3.3)$$

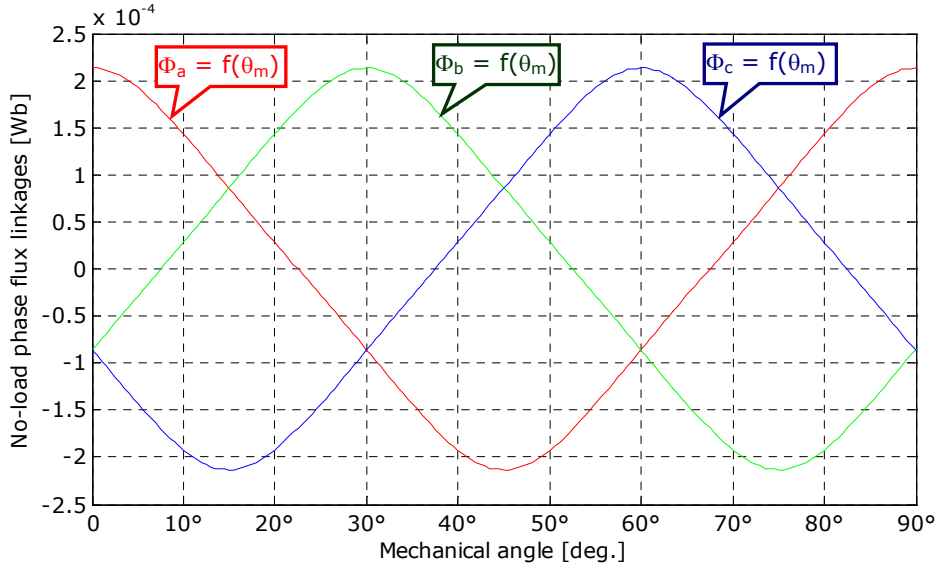


Fig. 3.13. FEM-calculated no-load phase flux linkages.

In Fig. 3.14 the phase back-EMF constant k_E is shown.

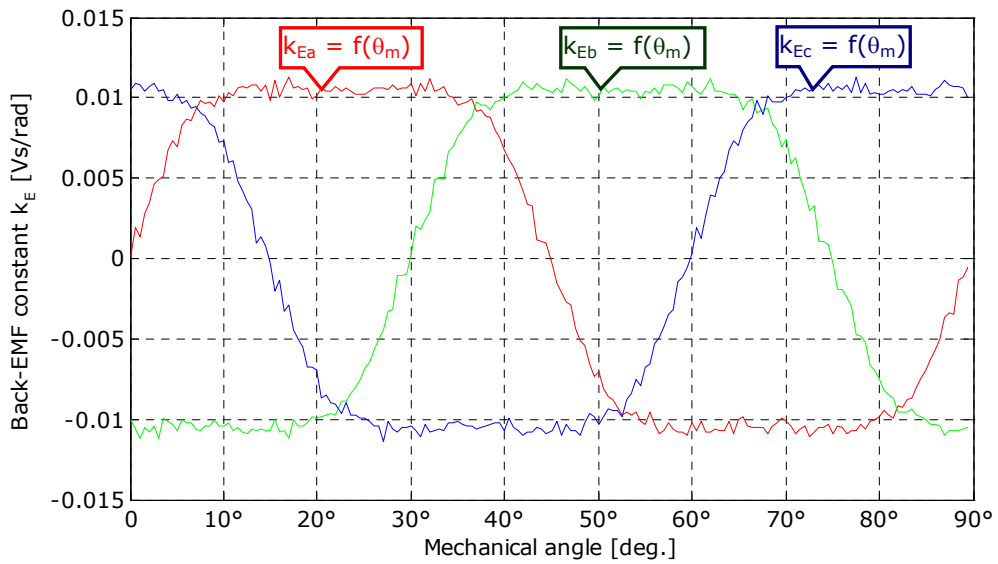


Fig. 3.14. FEM-calculated phase back-EMF constant k_E versus rotor angular mechanical position.

In Fig. 3.15, the phase back-EMFs at no-load and base speed, $n_b = 1000$ rpm, are shown.

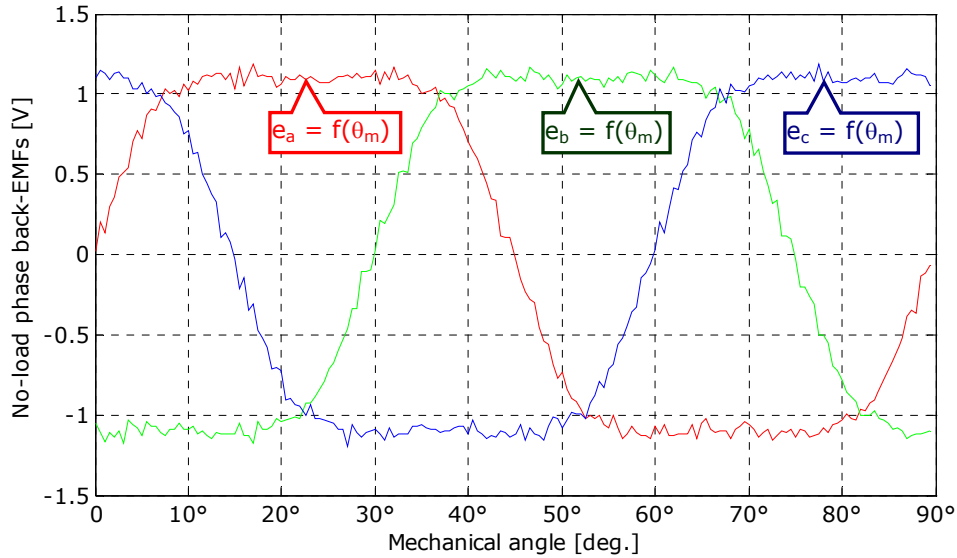


Fig. 3.15. FEM-calculated no-load phase back-EMFs at base speed.

The extended trapezoidal shape of back-EMFs, suitable for trapezoidal (block) current control is visible [9].

3.2.5. Cogging torque computation

The FEM-calculated cogging torque (zero current) versus rotor position was obtained by calculating the torque developed by the rotor with permanent magnets, in different positions, for zero current, using the Weighted Stress Tensor delivered by FEMM software. The Weighted Stress Tensor block is a volume integral version of Maxwell's stress tensor that automatically picks a collection of paths for the integration that yield good torque results. The results are typically more accurate than the Maxwell Stress Tensor line integral, since in some sense, all possible contours are averaged to yield the Weighted Stress Tensor torque result [20].

The cogging torque computation was done for a natural period of cogging torque, given by

$$T_{T_cogg} = \frac{360^{\circ\text{mech}}}{\text{LCM}(N_s, 2 \cdot p_1)} = \frac{360^{\circ}}{\text{LCM}(12, 8)} = \frac{360^{\circ}}{24} = 15^{\circ\text{mech}} \quad (3.4)$$

The variation of the calculated cogging torque versus rotor angular position in one natural period is presented in Fig. 3.16.

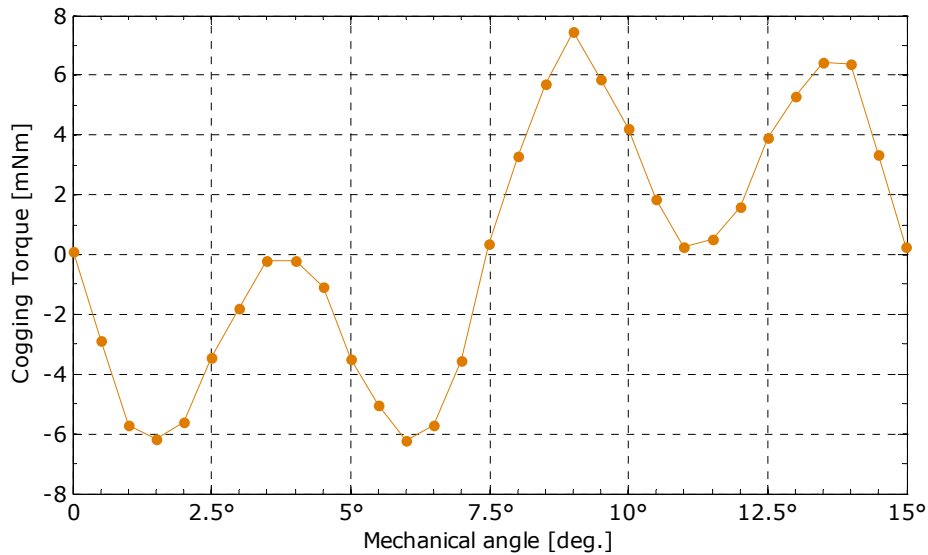


Fig. 3.16. FEM-calculated cogging torque.

For this topology, the minimization of cogging torque was done directly without skewing the slots [10]. The condition referring to the maximum cogging torque required in the specifications of the chosen prototype was met

$$T_{\max_cogg} = 7.46 \text{ [mNm]} < 0.7\% \cdot T_{eb} = 0.007 \cdot 1.14 = 8 \text{ [mNm]} \quad (3.5)$$

However, it can be observed, that the period is smaller; actually the 3-rd harmonic of the cogging torque becomes very high.

3.2.6. Load torque

In the following, the results of several FE-calculations for load torque will be presented. The extended trapezoidal shape of back-EMF (Fig. 3.15) makes this motor suitable for block (trapezoidal) current control.

Fig. 3.17 presents the ideal phase base current waveforms used for the control of BLDC. In practice, the armature current waveform is distorted and differs from the rectangular shape. It can be approximated by a trapezoidal waveform [22] (Fig. 3.17 - dash lines).

Fig. 3.18 presents the FEM-calculation of load torque for full load ideal rectangular current (with solid line) and for full load practical (trapezoidal) current (with dash line).

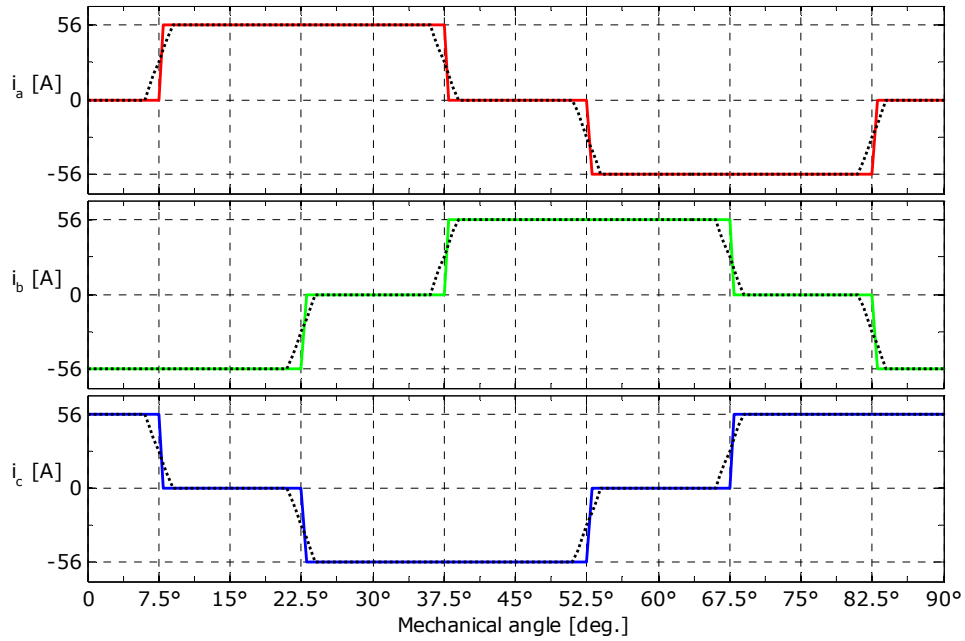


Fig. 3.17. Ideal (solid lines) and practical (dash lines) waveforms of the phase base current.

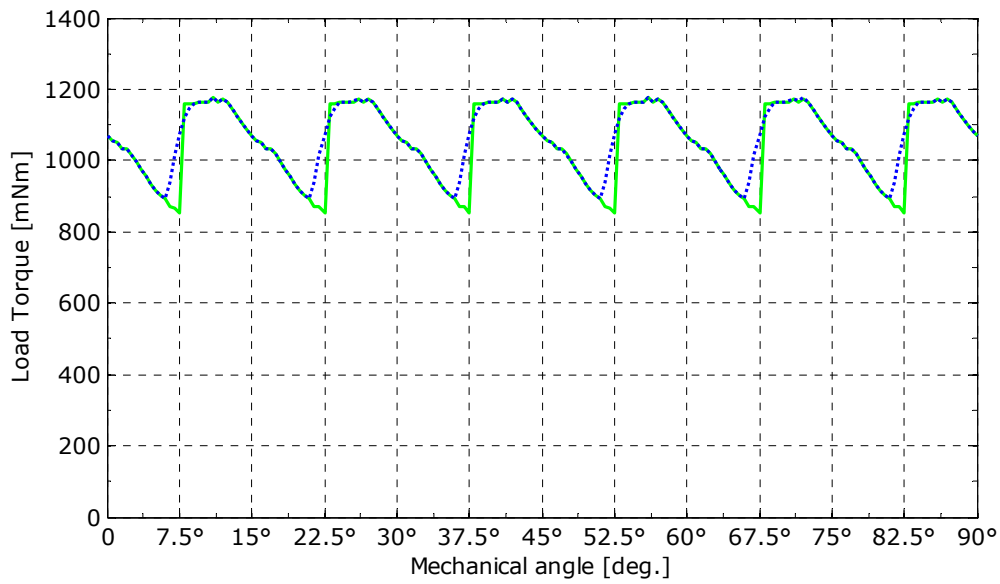


Fig. 3.18. Load torque versus rotor position at full load rectangular current (ideal and practical – 56 A peak).

Fig. 3.19 presents a comparison of the load torque: for full load trapezoidal currents with intervals in which current is zero (Fig. 3.17), and for full load

trapezoidal current waveform without intervals in which currents is zero (Fig. 3.20), respectively.

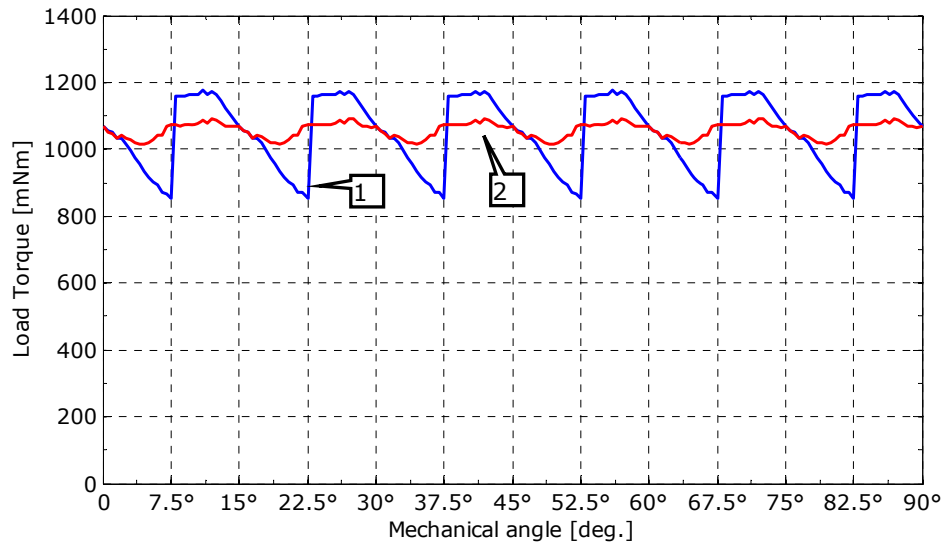


Fig. 3.19. Load torque versus rotor position for two different types of current waveforms:
 1 – Load torque for current waveform with intervals in which current is zero (Fig. 3.17)
 2 – Load torque for current waveform without intervals in which currents is zero (Fig. 3.20)

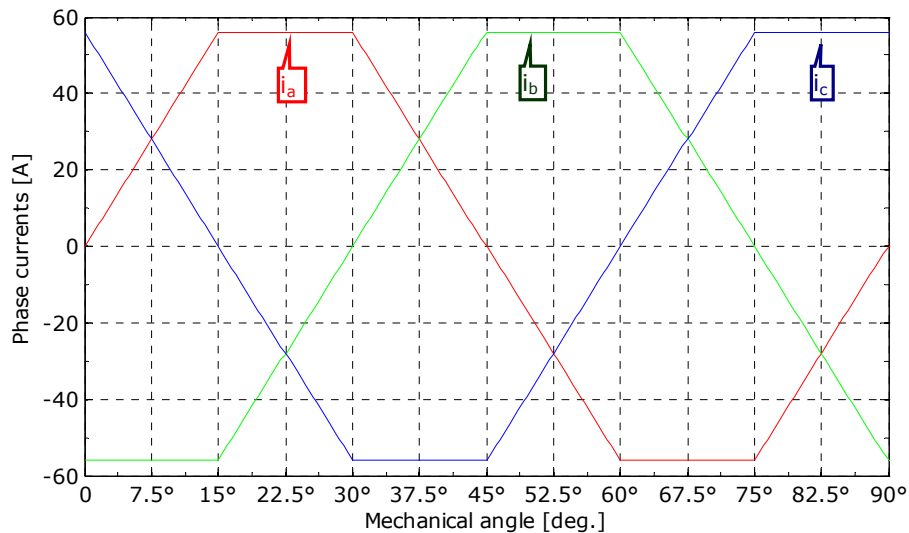


Fig. 3.20. Trapezoidal current waveform without intervals in which current is zero.

It is obvious from Fig. 3.19, that the total torque has a reduced ripple in the case of full load trapezoidal current waveform without intervals in which current is zero, compared to the total torque for full load trapezoidal current waveform with intervals in which current is zero.

Fig. 3.21 presents the total torque versus rotor angular position for four different phase current amplitudes.

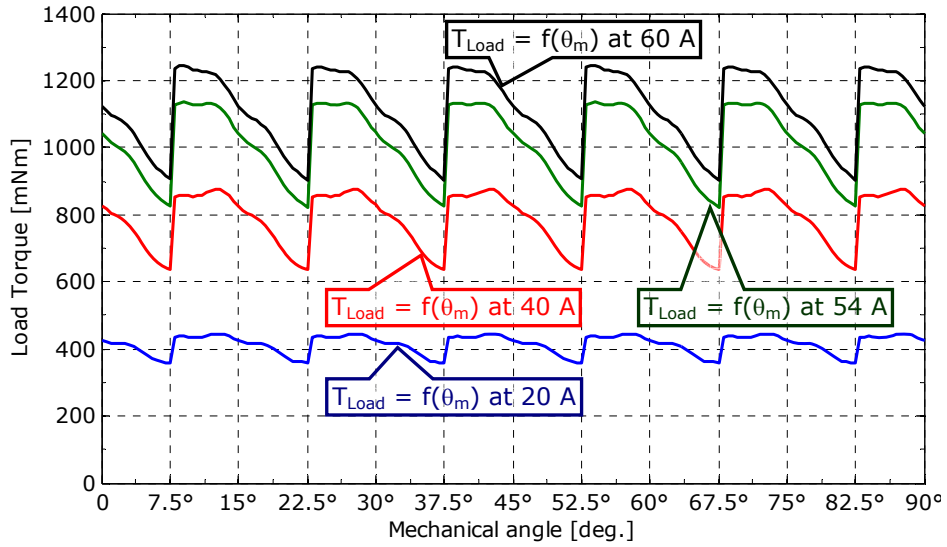


Fig. 3.21. Total torque vs. rotor angular position for four different phase current amplitudes.

Fig. 3.21 proves that the magnetic saturation magnifies the torque pulsations (in per unit) at full (rated) current.

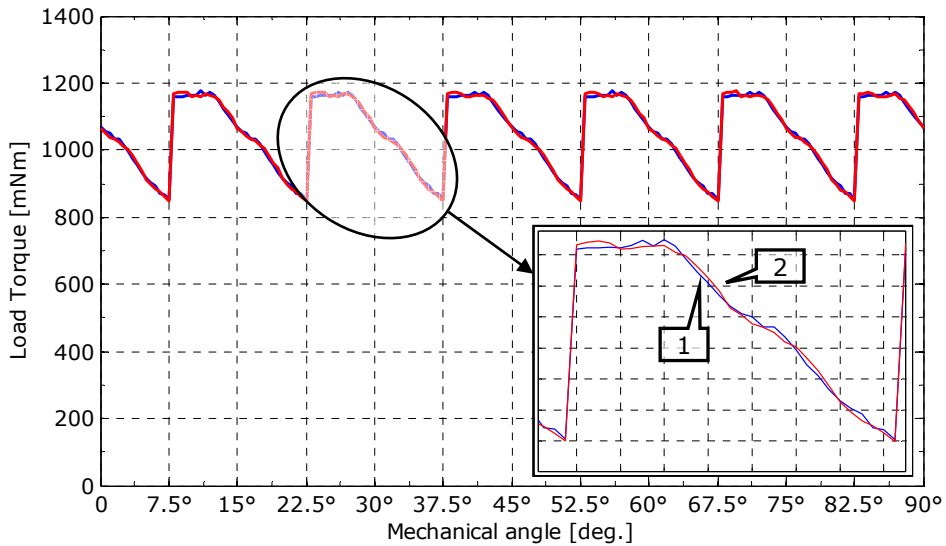


Fig. 3.22. Torque versus rotor angular position with rotor no eccentricity (1) and with 20% eccentricity (2).

From Fig. 3.22 it is obvious that the eccentricity of the rotor doesn't have a big influence regarding the shape of the load torque versus rotor angular position.

$$eccentricity = \frac{g_{max} - g_{min}}{g_{max} + g_{min}} \cdot 100 \quad (3.6)$$

where g is the air-gap length in radial direction.

Fig. 3.23 compares total torque, for full load (56 A peak), versus rotor angular position with reluctance torque (the case when the rotor has air instead of magnets) versus rotor angular position, for full load.

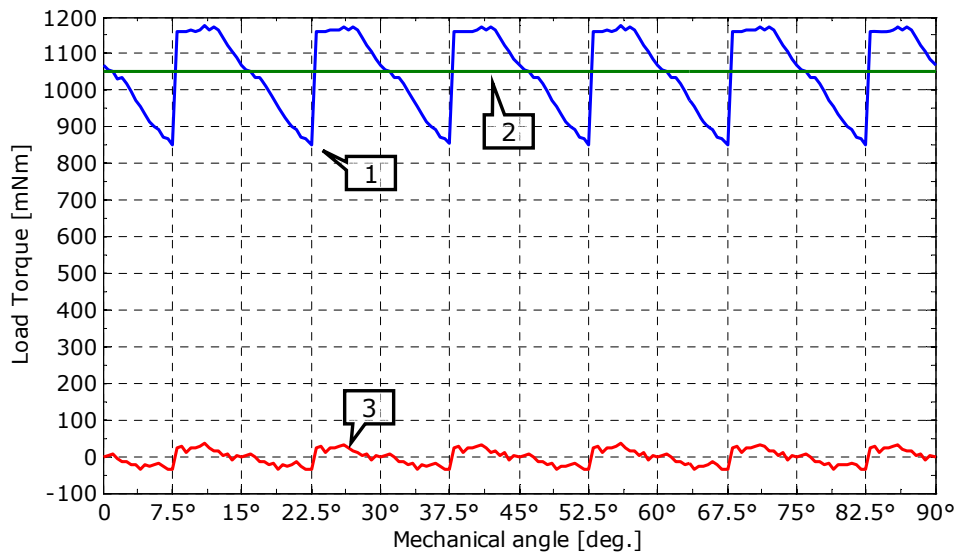


Fig. 3.23. Total torque (with magnets) (1), average torque (2) and reluctance torque (without magnets) (3) versus rotor angular position.

From Fig. 3.23, it seems that one major cause of the total torque ripple is the reluctance torque, taking into account that the level of cogging torque represents 0.7% from total torque. So in order to reduce the total torque ripple we have to reduce the reluctance torque.

Fig. 3.24 presents a comparison between the total torque for rated current and the commutation torque, which is obtained from the total torque minus average torque (see Fig. 3.23, signal 2), cogging torque, and reluctance torque. This figure emphasizes the idea that the total torque ripple will be reduced by decreasing the reluctance torque.

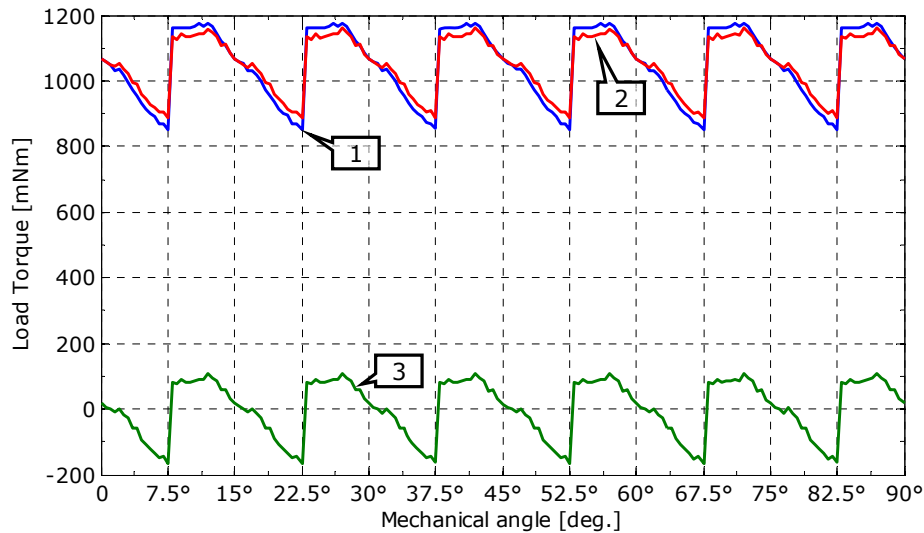


Fig. 3.24. Total torque (1), total torque minus cogging torque and reluctance torque, and commutation torque (3) versus rotor angular position.

3.2.7. Reduction of torque ripple

The main sources of torque ripple coming from the machine are [22, 23]:

- cogging effect – interaction between the rotor magnetic flux and variable permeance of the air-gap due to the stator slot geometry; this effect produces the *cogging torque*,
- distortion of sinusoidal or trapezoidal back-EMF waveform which produce the *field harmonic electromagnetic torque* [22],
- unequal permeances of the air-gap in the d and q axis produces the *reluctance torque*.

The causes of torque pulsation coming from the supply are:

- current harmonics from PWM,
- phase current commutation,
- DC-link voltage pulsation and inverter dead-time.

The torque ripple can be reduced both by proper motor design and motor control. Torque ripple reduction techniques by motor design include [22]:

a) Elimination of slots

Since the cogging torque is produced by the interaction between the PM field and the variable permeance of the air-gap due to the stator slot geometry, a slotless winding can totally eliminate the cogging torque. One major drawback of slotless PM brushless motors is the use of more PM material than in slotted motors.

b) Skewed slots

Normally, the stator slot skew can reduce the cogging torque practically to zero value. However, the stator slot skew reduces the EMF which deteriorates the motor performance. Skewed slots are less effective in the case of rotor eccentricity.

c) Shaping stator slots

The methods of reducing the cogging torque by shaping the stator slots include: bifurcated slots, empty (dummy slots), closed slots, teeth with different width of the active surface.

d) Selection of the number of stator slots

The cogging torque is significantly affected by the least common multiple $LCM(N_s, 2 \cdot p_1)$ of the slot number N_s and pole number $2 \cdot p_1$; the larger the LCM the smaller the cogging torque. Similarly, the cogging torque increases as the greatest common divisor $GCD(N_s, 2 \cdot p_1)$ of the slot number and pole number increases.

e) Shaping PMs

PMs thinner at the edges than in the center can reduce both the cogging and commutation torque ripple. This method together with bifurcated stator slots can reduce the cogging torque as effectively as skewed slots with much less reduction of the EMF.

f) Skewing PMs

Skewed PMs reduce the cogging torque in a similar way to skewed stator slots [23, 24]. Fabrication of twisted magnets for small rotor diameters and small number of poles is rather difficult. Bread loaf-shaped PMs are equivalent to skewed PMs.

g) Shifted PM segments

Sometimes it is more convenient to divide the magnet axially into 2 to 6 shorter segments, than designing one long magnet per pole. These segments are then shifted one from each other by equal or unequal distances. Fabrication of short, straight PM segments is much easier than long, twisted magnets.

For the topology analyzed in this chapter it was applied this torque ripple reduction method using 2 axial segments. The segments are then shifted one from each other with 7.5 mechanical degrees. The torque developed by the 1st segment, the torque developed by the 2nd segment, total developed torque, average torque (for no skew) and average torque (for the case when the shifted PM segments method is applied) versus rotor angular position are shown in Fig. 3.25. The total torque pulsation is 7.7% from average torque ($\Delta T_{p-p} = (T_{\max} - T_{\min}) / (2 \cdot T_{av})$).

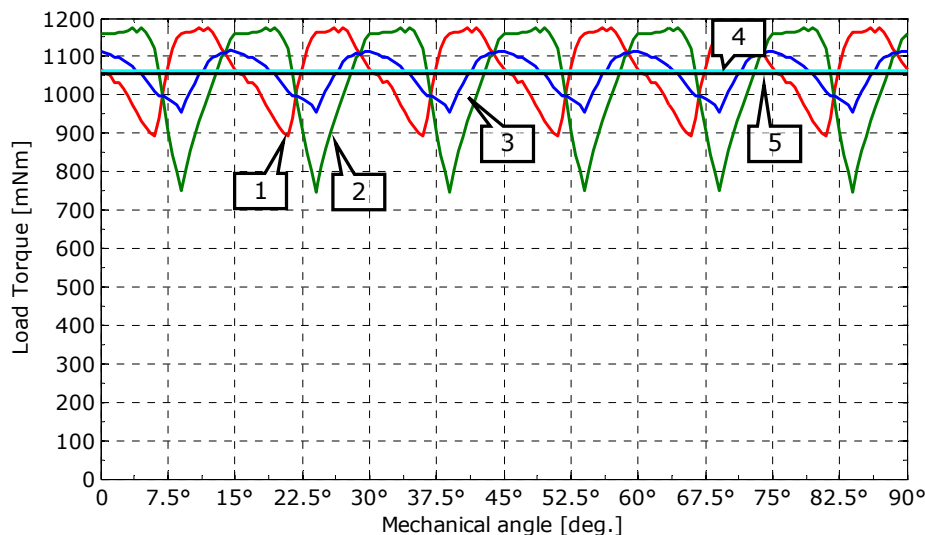


Fig. 3.25. The torque developed by the 1st segment (1), the torque developed by the 2nd segment (2), total developed torque (3), average torque (for no skew) (4) and average torque (for the case with the PMs divided in 2 segments of equal length, shifted with 7.5 mechanical degrees) (5) versus rotor angular position.

i) Selection of magnet width

Properly selected PM width with respect to the stator slot pitch is a good method to reduce the cogging torque. Cogging torque minimization require wider PM pole shoe than the multiple of slot pitch [22].

j) Magnetization of PMs

There is a choice between parallel, radial and direction-dependent magnetization types.

k) Notches in the rotor

The rotor pole face designed using several notches is a reduction method for the cogging torque, reluctance torque and total torque pulsations [24, 25]. Ref. [19] proves the presence of notches on the rotor pole face has a dramatic effect in a reduction of cogging torque, but it does not reduce the reluctance torque and the total torque pulsations.

3.2.8. Computation of inductances

It is a very important task to calculate, as accurately as possible, the values of the inductances of the IPMSM. In general, the inductance is calculated as a ratio of the flux linkage and the current:

$$L = \frac{\Psi}{I} \quad (3.7)$$

The calculations of the inductances can be done using one of following methods [1]:

- frozen permeability method,
- current perturbation method.

In the present section the current perturbation method was used. The normal inductances were calculated as ratio of the flux and current, and the transient inductances were calculated as ratio of the flux-difference and current-difference.

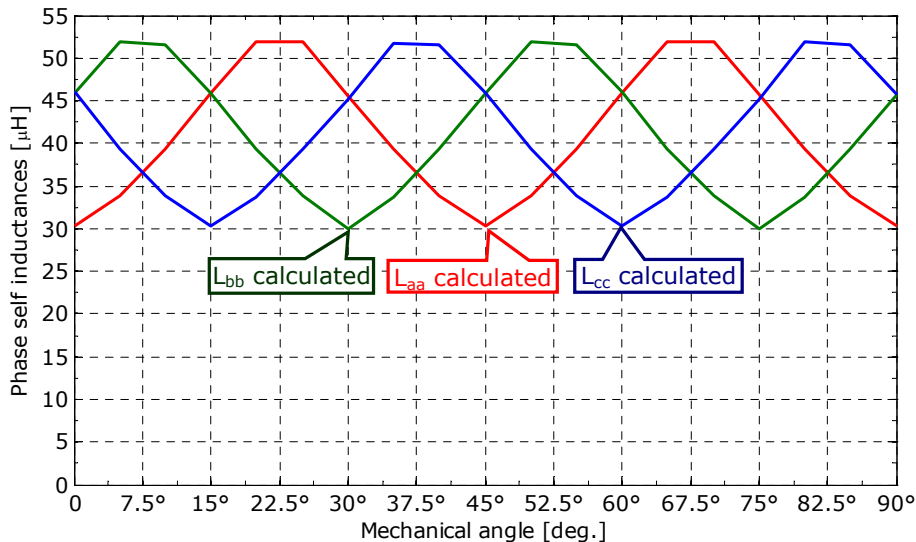


Fig. 3.26. Phase self FEM-calculated inductances for 28.3 mA.

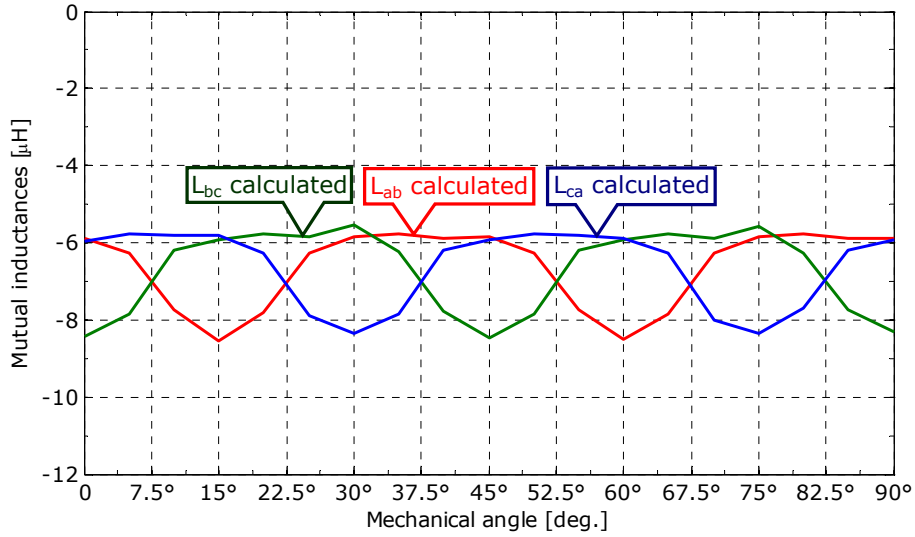


Fig. 3.27. Mutual FEM-calculated inductances for 28.3 mA.

The self and mutual inductances computation was done independently for each phase by imposing only the current for the respective phase, while the other two phase currents were kept at zero. To obtain the useful flux and mutual fluxes, for each phase, from the fluxes, calculated at different positions, we subtract the fluxes produced by the permanent magnets in each phase (no-load flux linkage).

Fig. 3.26 and Fig. 3.27 present the self and mutual calculated inductances, for a current amplitude of 28.3 mA.

To complete the transition from the FEM model to the circuit model necessary for the investigation of machine transients and control, in presence of magnetic saturation for our IPMSM (to consider reluctance torque presence) we are curve fitting results from FEM to analytical expressions for inductances.

For the normal inductances, one obtains the next analytical expressions (shown in Fig. 3.28, Fig. 3.29, and Fig. 3.30) with the values of polynomial coefficients p_{aa} , p_{ba} , p_{ca} , listed in Table 3.1

$$L_{aa}(\theta_e, i_a) = \frac{\Psi_{aa}(\theta_e, i_a)}{i_a} \quad (3.8)$$

$$= \left(p_{aa0}(i_a) + 2 \cdot \sum_{k=1}^3 [p_{aa1k}(i_a) \cdot \cos(k \cdot \theta_e) - p_{aa2k}(i_a) \cdot \sin(k \cdot \theta_e)] \right) \cdot 10^{-6}$$

$$L_{ba}(\theta_e, i_a) = \frac{\Psi_{ba}(\theta_e, i_a)}{i_a} \quad (3.9)$$

$$= \left(p_{ba0}(i_a) + 2 \cdot \sum_{k=1}^3 [p_{ba1k}(i_a) \cdot \cos(k \cdot \theta_e) - p_{ba2k}(i_a) \cdot \sin(k \cdot \theta_e)] \right) \cdot 10^{-6}$$

$$L_{ca}(\theta_e, i_a) = \frac{\Psi_{ca}(\theta_e, i_a)}{i_a} \tag{3.10}$$

$$= \left(p_{ca0}(i_a) + 2 \cdot \sum_{k=1}^3 [p_{ca1k}(i_a) \cdot \cos(k \cdot \theta_e) - p_{ca2k}(i_a) \cdot \sin(k \cdot \theta_e)] \right) \cdot 10^{-6}$$

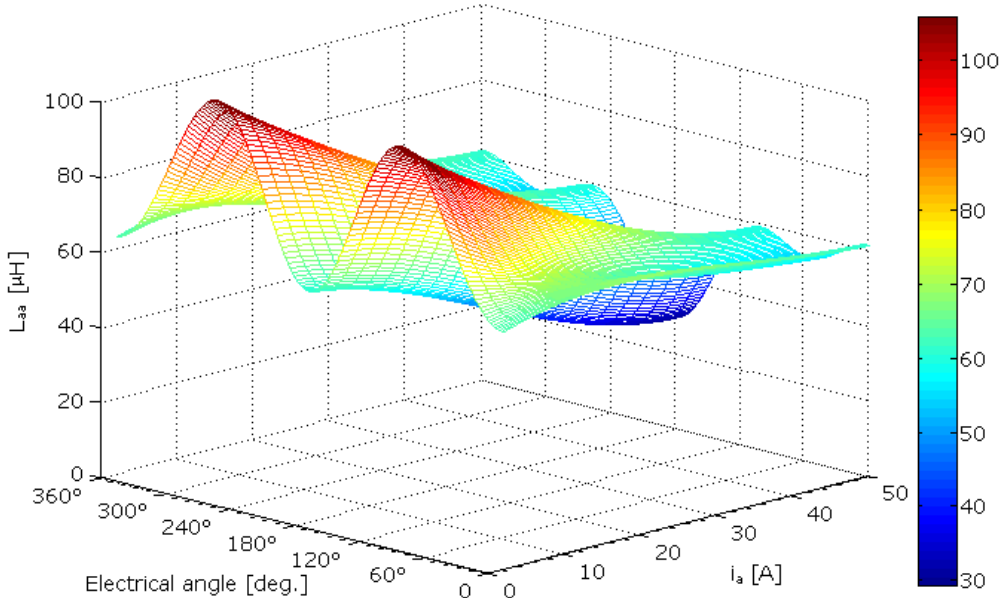


Fig. 3.28. Self inductance of phase A.

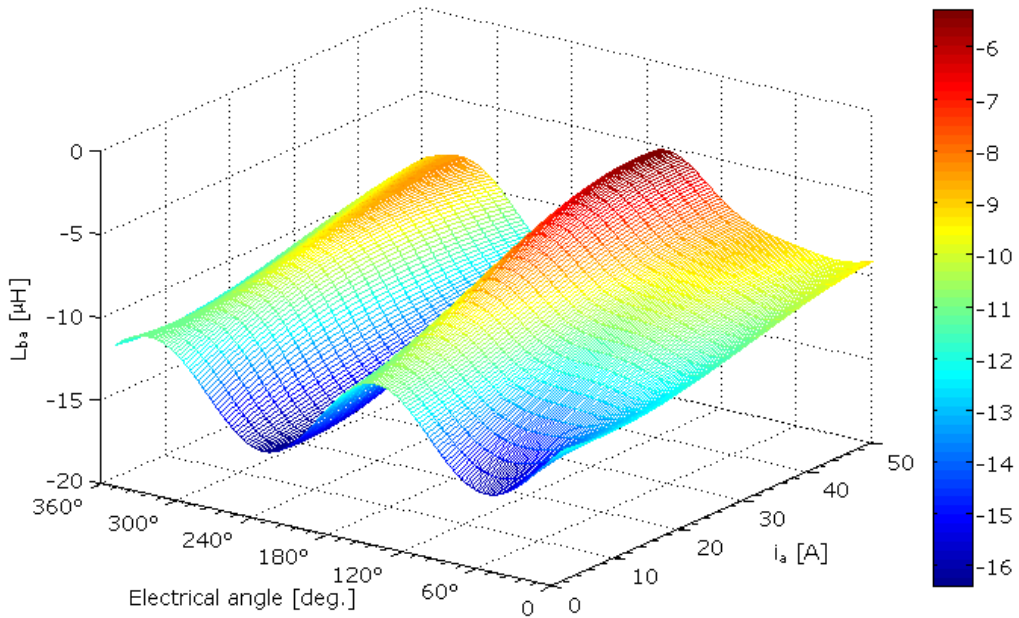


Fig. 3.29. The mutual inductance between phase B and A.

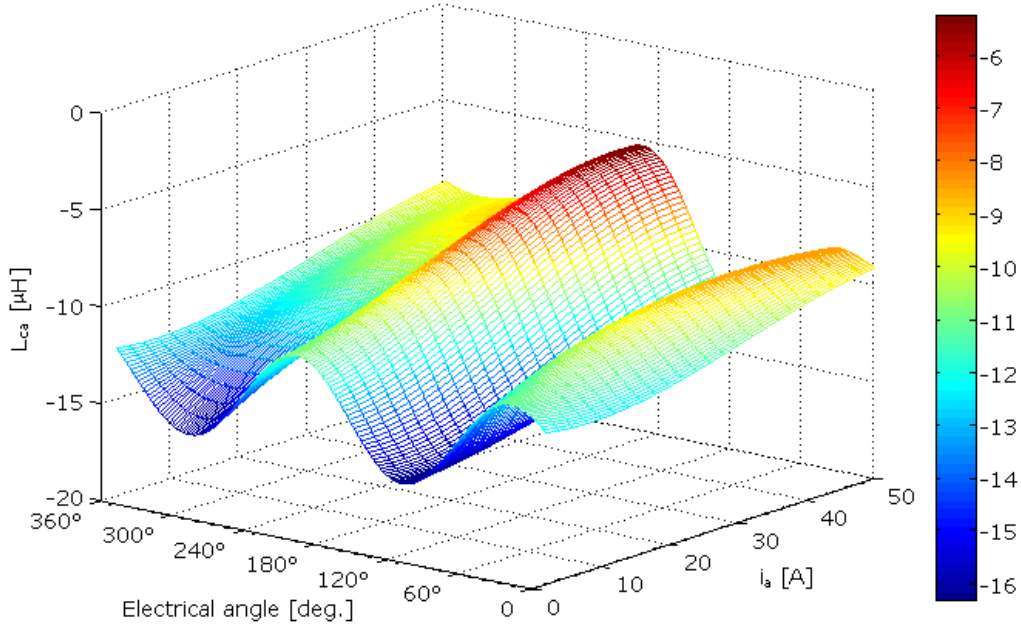


Fig. 3.30. The mutual inductance between phase C and A.

For the transient inductances, one obtains the next analytical expressions (shown in Fig. 3.31, Fig. 3.32, and Fig. 3.33) with the values of polynomial coefficients p_{aat} , p_{bat} , p_{cat} , listed in Table 3.1:

$$\begin{aligned}
 L_{aat}(\theta_e, i_a) &= \frac{\partial \Psi_{aa}(\theta_e, i_a)}{\partial i_a} \\
 &= \left(p_{aat0}(i_a) + 2 \cdot \sum_{k=1}^3 [p_{aat1k}(i_a) \cdot \cos(k \cdot \theta_e) - p_{aat2k}(i_a) \cdot \sin(k \cdot \theta_e)] \right) \cdot 10^{-6}
 \end{aligned} \tag{3.11}$$

$$\begin{aligned}
 L_{bat}(\theta_e, i_a) &= \frac{\partial \Psi_{ba}(\theta_e, i_a)}{\partial i_a} \\
 &= \left(p_{bat0}(i_a) + 2 \cdot \sum_{k=1}^3 [p_{bat1k}(i_a) \cdot \cos(k \cdot \theta_e) - p_{bat2k}(i_a) \cdot \sin(k \cdot \theta_e)] \right) \cdot 10^{-6}
 \end{aligned} \tag{3.12}$$

$$\begin{aligned}
 L_{cat}(\theta_e, i_a) &= \frac{\partial \Psi_{ca}(\theta_e, i_a)}{\partial i_a} \\
 &= \left(p_{cat0}(i_a) + 2 \cdot \sum_{k=1}^3 [p_{cat1k}(i_a) \cdot \cos(k \cdot \theta_e) - p_{cat2k}(i_a) \cdot \sin(k \cdot \theta_e)] \right) \cdot 10^{-6}
 \end{aligned} \tag{3.13}$$

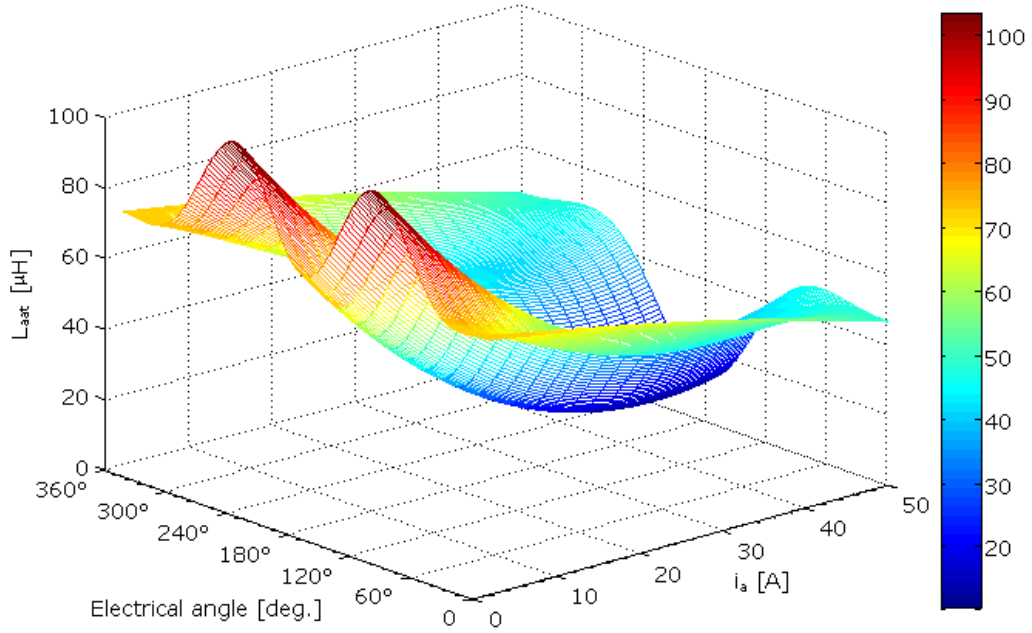


Fig. 3.31. Self transient inductance of phase A.

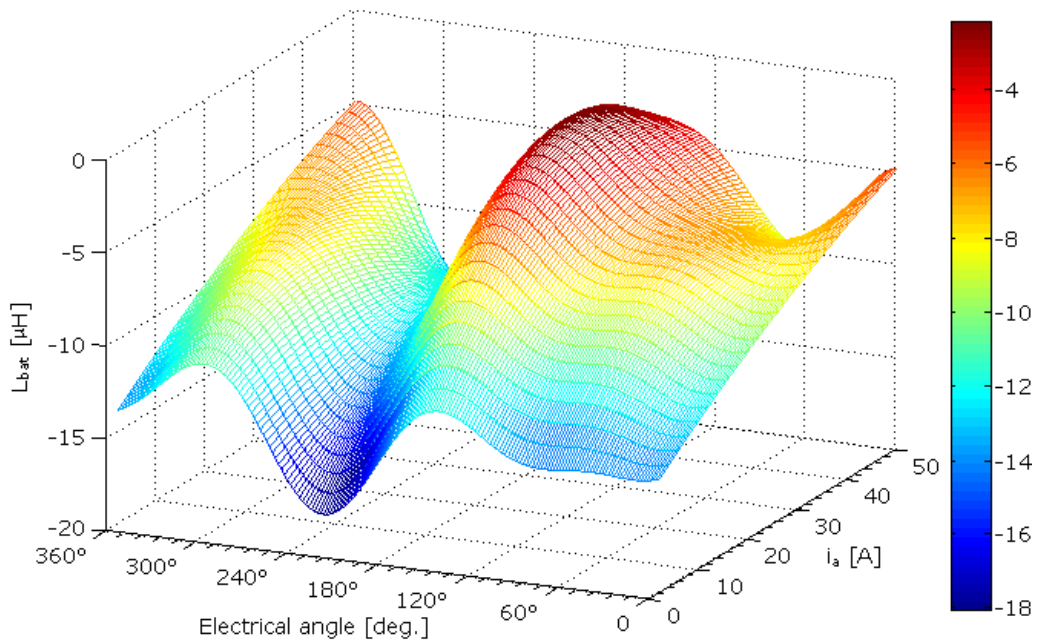


Fig. 3.32. The mutual transient inductance between phase B and A.

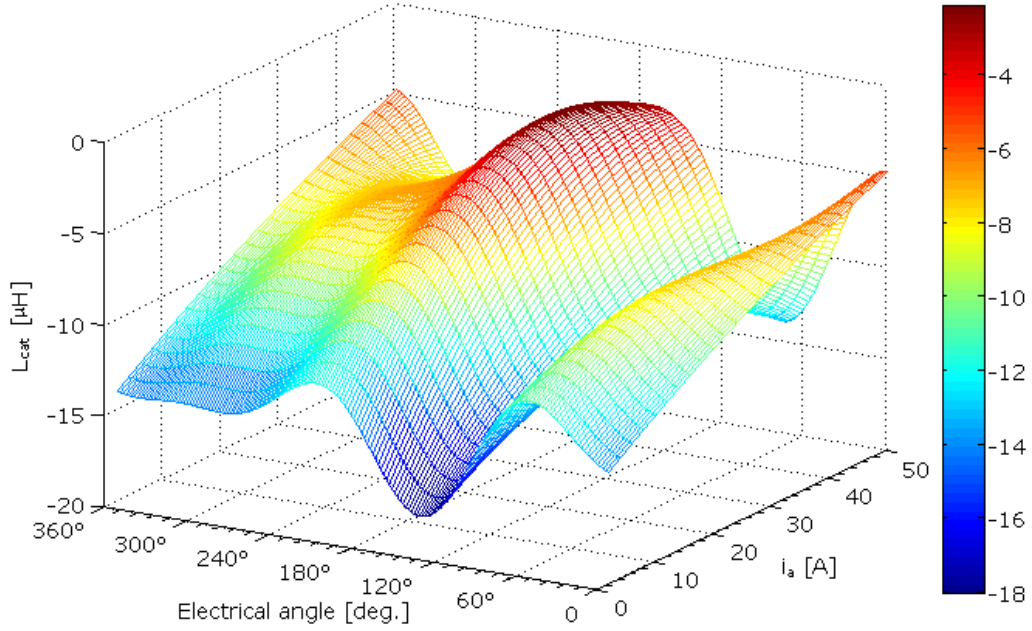


Fig. 3.33. The mutual transient inductance between phase C and A.

Table 3.1. Polynomial coefficients for inductances' analytical expressions

	$\cdot i_a^3$	$\cdot i_a^2$	$\cdot i_a^1$	$\cdot i_a^0$
ρ_{aa0}	$2.0 \cdot 10^{-4}$	-0.008	-0.7714	85.263
ρ_{aa1k}	$-1.412 \cdot 10^{-4}$	0.011	-0.0907	-0.4052
	$1.022 \cdot 10^{-4}$	-0.0132	0.5809	-11.961
	$1.041 \cdot 10^{-4}$	-0.0108	0.3288	0.422
ρ_{aa2k}	$8.02 \cdot 10^{-7}$	$-5.406 \cdot 10^{-5}$	$4.5508 \cdot 10^{-4}$	0.0213
	$-4.31 \cdot 10^{-7}$	$4.35 \cdot 10^{-5}$	-0.0012	0.0036
	$2.57 \cdot 10^{-7}$	$-1.762 \cdot 10^{-5}$	$5.951 \cdot 10^{-5}$	0.0124
ρ_{ba0}	$-4.408 \cdot 10^{-5}$	0.0023	0.0901	-13.733
ρ_{ba1k}	$1.461 \cdot 10^{-5}$	-0.0013	0.0202	-0.0091
	$-2.074 \cdot 10^{-5}$	0.0022	-0.0592	0.8
	$-6.849 \cdot 10^{-6}$	0.0012	-0.0528	0.0739
ρ_{ba2k}	$-5.428 \cdot 10^{-7}$	$2.85 \cdot 10^{-4}$	-0.0275	-0.04
	$-1.525 \cdot 10^{-7}$	$-6.54 \cdot 10^{-5}$	-0.0058	1.12
	$-1.203 \cdot 10^{-5}$	0.0011	-0.024	-0.001
ρ_{ca0}	$-4.381 \cdot 10^{-5}$	0.0023	0.0901	-13.746
ρ_{ca1k}	$-1.464 \cdot 10^{-5}$	-0.0013	0.0203	-0.0315
	$-1.977 \cdot 10^{-5}$	0.0021	-0.0579	0.8154
	$-7.303 \cdot 10^{-6}$	0.0013	-0.0537	0.0762
ρ_{ca2k}	$6.226 \cdot 10^{-7}$	$-3.152 \cdot 10^{-4}$	0.0295	$-9.25 \cdot 10^{-4}$
	$-2.57 \cdot 10^{-7}$	$1.137 \cdot 10^{-4}$	0.004	-1.1025
	$1.158 \cdot 10^{-5}$	-0.0011	0.0234	-0.0024

Table 3.1. Continued

	$\cdot i_a^3$	$\cdot i_a^2$	$\cdot i_a^1$	$\cdot i_a^0$
p_{aat0}	-	0.0297	-2.5072	89.1053
p_{aat1k}	-	-0.0087	0.7	-5.2
	-	-0.0064	-0.368	-6.823
	-	-0.0016	0.0137	3.908
p_{aat2k}	-	$5.888 \cdot 10^{-5}$	-0.0032	0.0394
	-	$5.153 \cdot 10^{-6}$	$1.4 \cdot 10^{-4}$	-0.0097
	-	$1.156 \cdot 10^{-5}$	$-8.73 \cdot 10^{-4}$	0.0147
p_{bat0}	-	-0.0049	0.3885	-14.528
p_{bat1k}	-	$5.303 \cdot 10^{-4}$	-0.06	0.575
	-	$-4.627 \cdot 10^{-5}$	0.0386	-0.2
	-	0.0014	-0.05	-0.3
p_{bat2k}	-	$6.7 \cdot 10^{-4}$	-0.0501	-0.0734
	-	$-1.885 \cdot 10^{-4}$	-0.0134	1.1436
	-	$-3.313 \cdot 10^{-4}$	0.0335	-0.4767
p_{cat0}	-	-0.0049	0.3868	-14.5307
p_{cat1k}	-	$5.565 \cdot 10^{-4}$	-0.0597	0.5623
	-	$-7.446 \cdot 10^{-6}$	0.0364	-0.1641
	-	0.0013	-0.0477	-0.323
p_{cat2k}	-	$-6.95 \cdot 10^{-4}$	0.0516	0.0567
	-	$2 \cdot 10^{-4}$	0.0131	-1.1478
	-	$3.03 \cdot 10^{-4}$	-0.0318	0.4604

3.3. Experimental analysis of concentrated coils and nonuniform slots (6+6/8) IPMBLDC

The measurement procedure consists of several tests. These tests were chosen in order to allow the estimation of machine parameters in a wide area of variation. A first classification would subdivide them in standstill or locked-rotor, and running tests. Whenever possible, the experimental characteristics are compared with FEM-calculated characteristics, in order to validate the FEM accuracy in determining the BLDC parameters.

Fig. 3.34 shows the stator with concentrated winding and the rotor with permanent magnets of the built prototype before assembling. The main dimensions and material properties of the prototype are the same as for the machine topology analyzed with FEM from the previous section (the dimensions are listed in detail in Chapter 2, Table 2.5).



Fig. 3.34. Stator and rotor before assembling.

3.3.1. Phase resistance measurement

The phase resistance must be determined initially because it is needed for some of the parameter estimation methods. Resistances can be measured using a precision ohmmeter, RLC-bridge, or multimeter. Using a precision ohmmeter, the phase resistance R_{ph} and line-to-line motor resistance R_{LL} obtained values are shown in Table 3.2.

Table 3.2. Resistance measurement results at 20 °C

R_{ph}			Difference in comparison with mean value.		
[mΩ]					
A	B	C	%		
10.7	11.3	11	-2.73	2.73	0.00
11.00					
R_{LL}			Difference in comparison with mean value.		
[mΩ]					
AB	BC	CA	%		
22	22.2	21.7	0.15	1.06	-1.21
21.97					

This prototype presents a small asymmetry, 2.73%, of the phase resistances. The line-to-line resistances have an asymmetry of 1.21 %. However, these values were obtained for a prototype manufactured under laboratory conditions. For the industrial practice a phase resistance asymmetry of up to 3% is satisfactory [1].

For further parameter estimation the mean values of the phase and line-to-line resistances will be used.

3.3.2. Phase self and line-to-line inductance measurement

The easiest method to measure an inductance is to use an RLC-bridge. The measurement of the phase and line-to-line inductances in dependence with rotor position was carried out using a special rotor positioning device. The measurement was done using a frequency of 50 Hz for the injected current. However, the

inductances measured with this method are unsaturated values, as the injected current was very small (40 mA peak).

The relation between the self, mutual and line-to-line inductances is for the Y-phase connection:

$$L_{LL_ab}(\theta_m) = L_{aa}(\theta_m) + L_{bb}(\theta_m) - 2 \cdot L_{ab}(\theta_m) \quad (3.14)$$

After measuring the phase self and line-to-line inductances, the mutual inductances for the Y-phase connection can be calculated with the formula:

$$L_{ab}(\theta_m) = \frac{L_{aa}(\theta_m) + L_{bb}(\theta_m) - L_{LL_ab}(\theta_m)}{2} \quad (3.15)$$

The results of the measurements phase self inductances, line-to-line inductances and the calculated values of the mutual inductances are depicted in Table 3.3.

Table 3.3. Measured inductances using a RLC-bridge (50 Hz, 40 mApeak) and calculated mutual inductances.

θ_m [deg.]	Phase self inductances			Line-to-line inductances			Phase mutual inductances		
	L_{aa} [μ H]	L_{bb} [μ H]	L_{cc} [μ H]	L_{LL_ab} [μ H]	L_{LL_bc} [μ H]	L_{LL_ca} [μ H]	L_{ab} [μ H]	L_{bc} [μ H]	L_{ca} [μ H]
0	43.81	58.53	52.28	113.51	127.30	105.82	-5.585	-8.245	-4.865
5	51.43	58.24	45.08	123.84	116.80	105.63	-7.085	-6.74	-4.56
10	52.98	58.00	44.08	122.51	118.16	105.96	-6.645	-6.92	-4.45
15	56.20	57.40	39.26	130.21	106.49	104.70	-8.305	-4.915	-4.62
20	57.74	53.62	41.28	127.68	103.43	110.89	-8.16	-4.265	-5.935
25	58.07	46.62	49.06	116.51	104.27	122.30	-5.91	-4.295	-7.585
30	57.08	39.87	54.62	107.07	103.57	129.52	-5.06	-4.54	-8.91
35	54.20	42.20	57.01	104.82	110.80	128.38	-4.21	-5.795	-8.585
40	47.65	51.14	56.80	107.06	122.08	118.58	-4.135	-7.07	-7.065
45	41.87	57.02	55.52	107.68	130.35	108.88	-4.395	-8.905	-5.745
50	43.66	58.70	52.31	113.7	128.02	105.50	-5.67	-8.505	-4.765
55	51.06	58.22	45.38	123.43	117.36	106.23	-7.075	-6.88	-4.895
60	56.02	56.31	39.22	129.05	106.02	105.51	-8.36	-5.245	-5.135
65	57.78	52.79	41.76	126.24	103.27	110.64	-7.835	-4.36	-5.55
70	57.68	45.71	49.18	116.69	103.33	121.06	-6.65	-4.22	-7.10
75	56.89	39.72	54.50	105.64	103.46	128.66	-4.515	-4.62	-8.635
80	53.60	43.07	57.00	105.02	110.49	127.72	-4.175	-5.21	-8.56
85	47.30	51.16	57.17	107.11	123.17	116.82	-4.325	-7.42	-6.175
90	41.45	57.18	55.54	107.80	130.54	107.72	-4.585	-8.91	-5.365

Fig. 3.35 and Fig. 3.36 present phase self and mutual measured inductances, respectively, in comparison with FEM-calculated ones, from the previous section. The calculated inductances are up to 30 % smaller than measured ones because a 2D FEM was used, and thus the end-turn leakage inductances were not taken into account. The end coil-connections inductance should be computed analytically or from a separate finite element method [21]. The inductances variation with rotor position is clearly validated by experiments. The magnetic "saliency" is to be expected, given the stator slot openings and the IPM structure of the rotor.

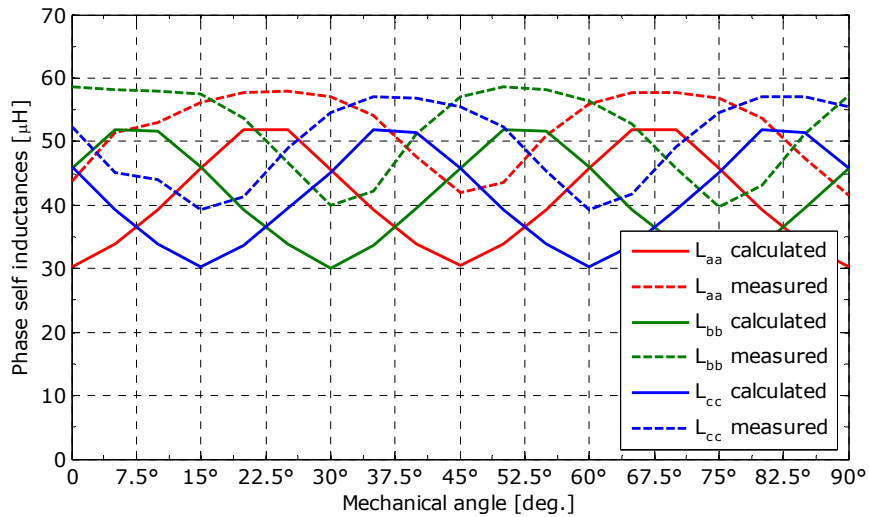


Fig. 3.35. Phase self inductances measured with RLC-bridge (50 Hz, 40 mApeak) in comparison with FEM-calculated ones.

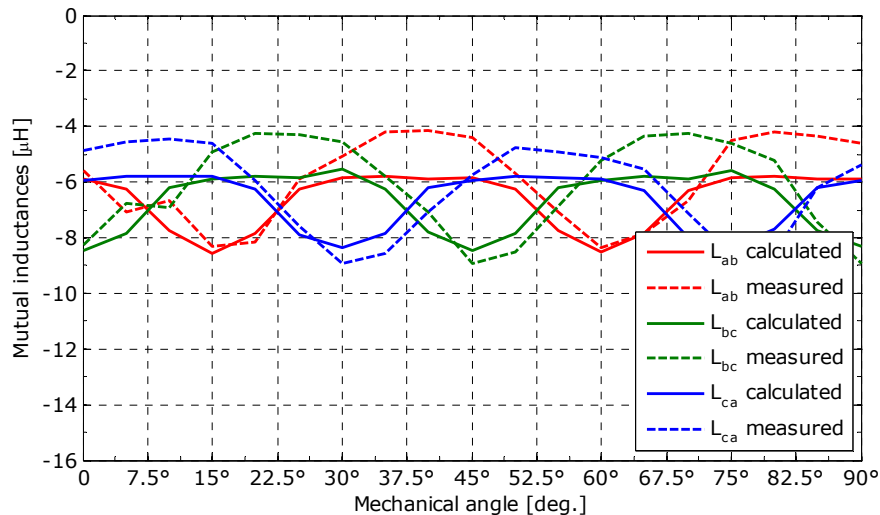


Fig. 3.36. Mutual inductances measured with RLC-bridge (50 Hz, 40 mApeak) in comparison with FEM-calculated ones.

3.3.3. Standstill torque measurement

In the following the standstill shaft output torque will be measured. As the speed is zero, the iron core losses and the mechanical losses are also zero. As this test requires the sampling of the torque for different rotor positions a rotor positioning device was used. The motor phases were fed at zero speed with rectangular currents controlled by a dSpace system.

Fig. 3.37 presents the variation of the measured torque with rotor position for four values of the current amplitude, in comparison with FEM-calculated load torque for the same values of the current amplitude. The calculated torque exceeds

by 7.5 % the measured torque for higher imposed currents. The main reason for this discrepancy may be the flux linkage reduction produced by the temperature rise of the permanent magnets in the measured prototype.

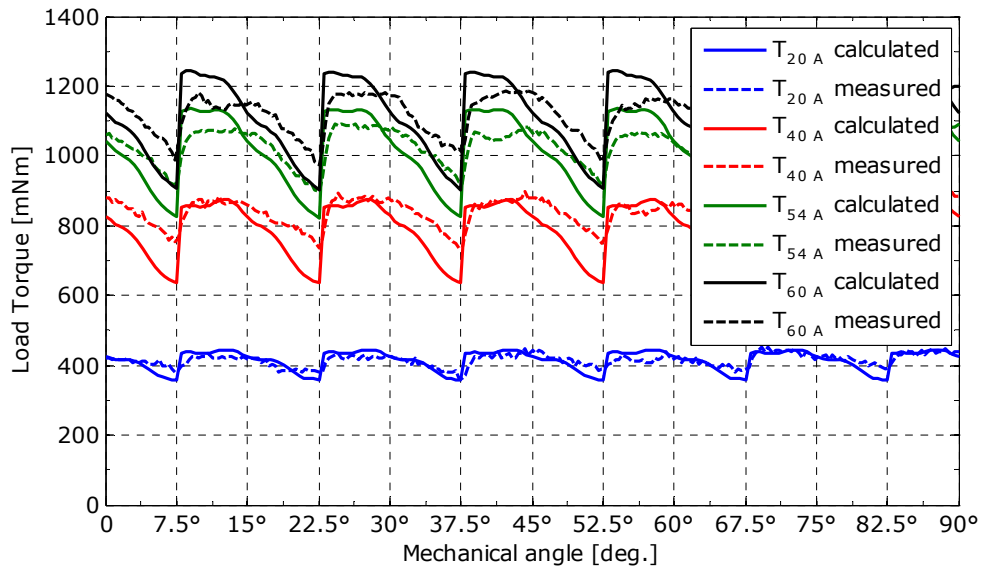


Fig. 3.37. Measured and FEM-calculated torque vs. rotor position for four different phase current amplitudes.

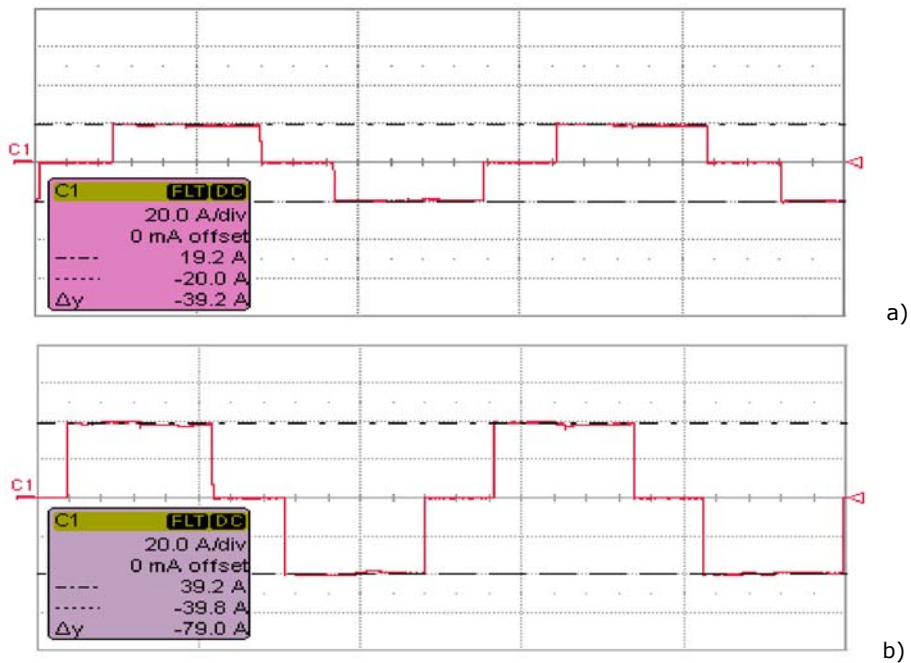


Fig. 3.38. Measured phase current at: a) 20 A amplitude, b) 40 A amplitude.

Though the cogging torque is small, full torque pulsations with trapezoidal current persist (Fig. 3.37) both due to rotor saliency and magnetic saturation.

Fig. 3.38a and Fig. 3.38b present the phase current waveform, for 20 A, 40 A amplitude, respectively, measured during standstill torque measurements.

3.3.4. Phase back-EMF measurement

The measurements were done running the machine as generator with open phases. The phase voltage signals were recorded using a Labview platform especially dedicated to test electric machines (Fig. 3.39). Fig. 3.40 shows the phase back-EMFs versus rotor angular position.

The calculation of the phase back-EMF constant can be done directly by using the measured back-EMF and the speed

$$k_{E-ph} = \frac{E_{ph-peak}}{\omega_m} = \frac{E_{ph-peak}}{2 \cdot \pi \cdot f_m} = \frac{E_{ph-peak}}{2 \cdot \pi \cdot \frac{n}{60}} = \frac{0.814}{2 \cdot \pi \cdot \frac{750}{60}} = 0.01036 \text{ [Vs/rad]} \quad (3.16)$$

Also the amplitude of the permanent magnet phase flux linkage can be calculated.

$$\lambda_{PM-ph-peak} = \frac{k_{E-ph-peak}}{p_1} = \frac{0.01036}{4} = 2.6 \cdot 10^{-3} \text{ [Wb]} \quad (3.17)$$

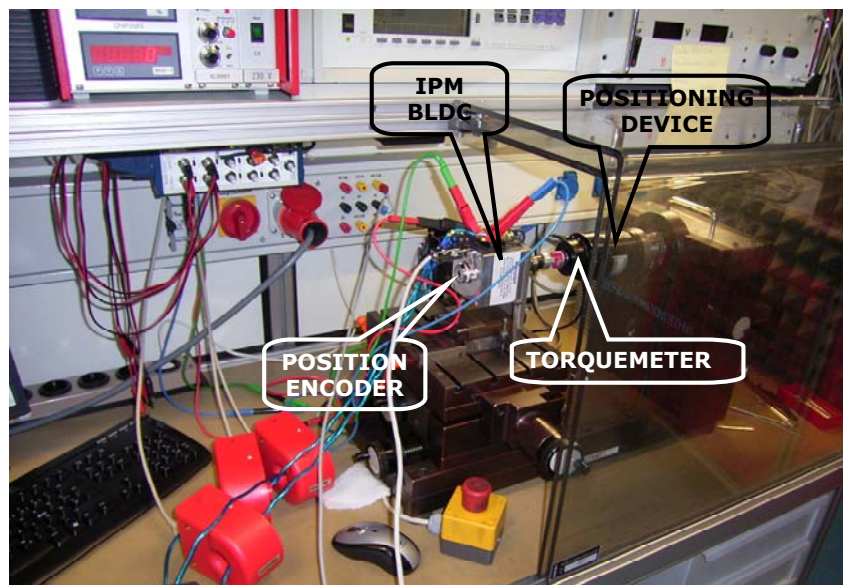


Fig. 3.39. (continued).



Fig. 3.39. The setup used to measure the back-EMF.

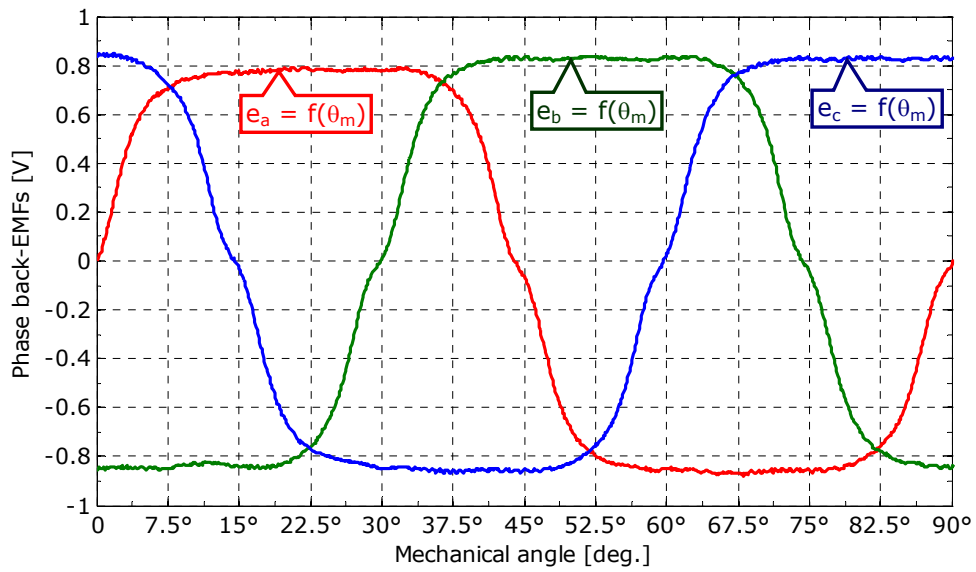


Fig. 3.40. Shape of the phase back-EMFs (back-EMF vs. rotor angular position at 750 rpm).

Fig. 3.41 presents the comparison between the measured and FEM-calculated back-EMF constant k_{E_phr} proving a good agreement between FEM calculations and measurements.

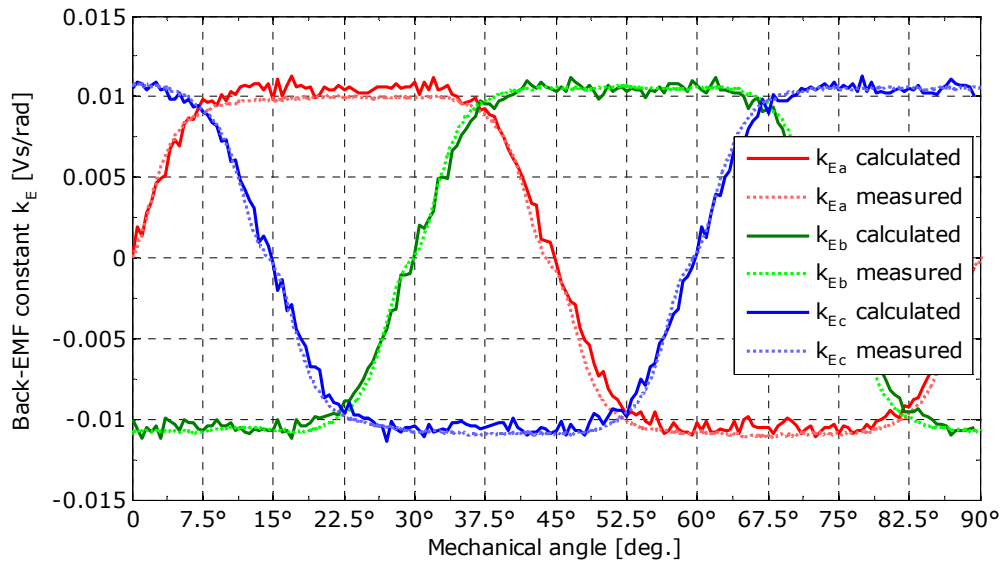


Fig. 3.41. Measured and FEM-calculated back-EMF constant $k_{E_{ph}}$ vs. rotor angular position.

The difference between the measured and the calculated back-EMF can have the following causes [1]:

- the FE-calculation was done in 2D and the flux linkage in the dimension was not taken into account,
- the prototype has different geometric dimensions and materials magnetic properties in comparison with the FE-model – tolerances, lower permeability for iron core, lower magnetic flux density for permanent magnets,
- the winding distribution in the slot could be different in the prototype and FE-model (assumed uniform).

3.3.5. Cogging torque measurement

Given the crucial importance of cogging torque in some automotive applications its measurement becomes mandatory. The measuring setup is similar to the one used for measuring the back-EMF, with the exception that the rotor of the motor with zero stator current is turned slowly (10.5 rpm) from an external drive and the cogging torque is measured by a torque meter.

The measured cogging torque versus rotor angular position is shown in Fig. 3.42. The measured torque in these conditions includes the friction and iron loss torque. The latter was considered equal to the offset torque in the measurements, because this torque does not contain substantial pulsations [1], and was finally eliminated, to segregate the cogging torque (Fig. 3.43).

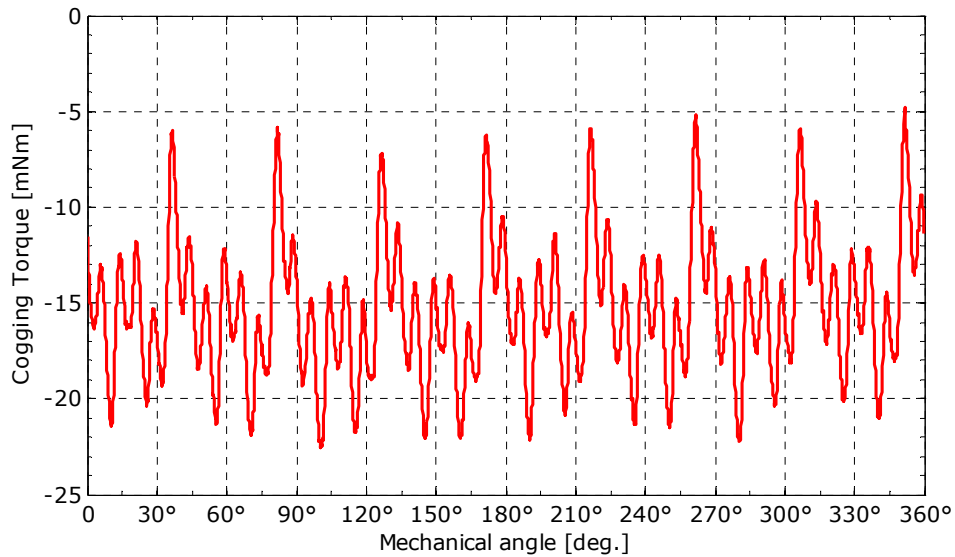


Fig. 3.42. Measured cogging torque vs. rotor mechanical position.

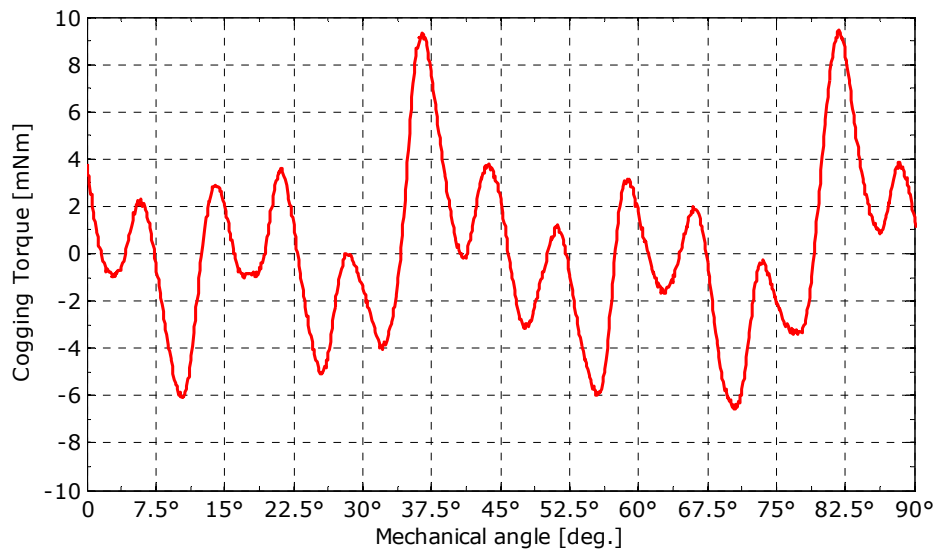


Fig. 3.43. Measured cogging torque vs. rotor mechanical position.

The difference between the FEM-calculated cogging torque (Fig. 3.16) and the measured one, without offset, (Fig. 3.43) can be attributed to some factors as in the case of the back-EMF computation:

- the prototype has different geometric dimensions and materials magnetic properties in comparison with the FE-model – tolerances, lower permeability for iron core, lower magnetic flux density for permanent magnets,

- the FE-calculation was done in 2D and the flux linkage in the dimension was not taken into account,
- numerical errors in the FE-computation,
- torque measurement error.

3.3.6. Friction and iron loss torque versus speed

The sum of the friction and iron loss torque (at no-load) can be determined using the same measurement setup as the one for the measurement of the cogging torque, with the difference that the speed has to be varied between standstill and the maximum operational speed for the drive.

Fig. 3.44 presents the thus measured friction and iron loss torque (at no-load) versus speed.

In order to separate the two torque components a measurement of the friction loss torque versus speed must be carried out. This would be possible only if the permanent magnets were removed from the rotor [1].

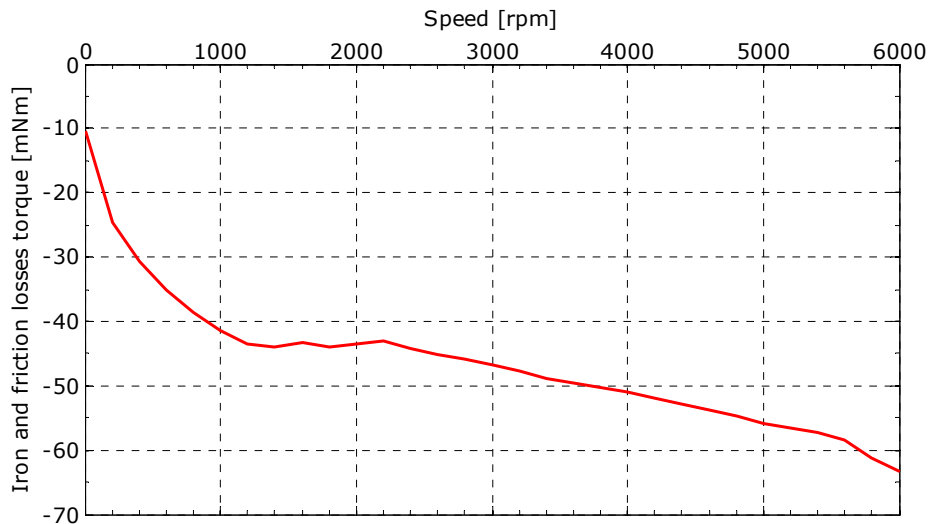


Fig. 3.44. Measured iron and friction losses torque vs. speed.

3.3.7. Rated torque-speed characteristic

The measurement of the rated torque-speed characteristic was carried out on the test bench using a block current control for the motor under test. Only the current controller was employed in order to reduce the errors in the measurements.

The speed was imposed by the load machine controlled using a separate controller. The measured torque-speed characteristic is presented in Fig. 3.45.

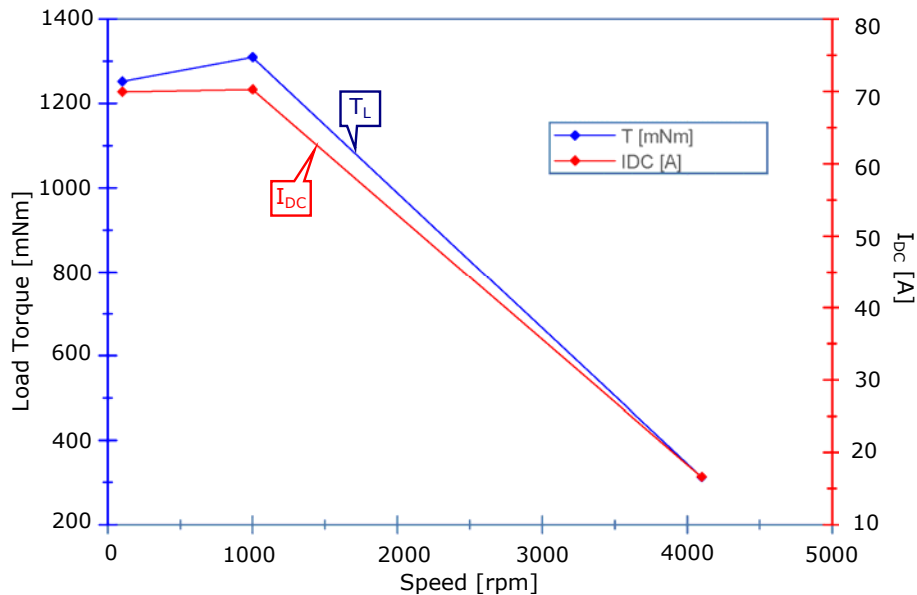


Fig. 3.45. Measured torque and phase current vs. speed curve (maximal DC current 70.27 Apeak).

3.4. FEM preprocessor for PMSM

Using the Matlab graphical user interface (GUI), a FEA preprocessor for different PMSM topologies has been implemented. At the moment this preprocessor is implemented only for FEMG as FEM solver, but it can be extended to other FEM existing solvers.

Fig. 3.46 illustrates the main page menu used to select the PMSM topology and main input data: number of phases (m), number of poles (n_p) and number of stator slots (n_s). The PMSM configurations implemented in the software are:

- 1) Stator configurations:
 - Symmetric stator,
 - Asymmetric stator.
- 2) Rotor configurations:
 - Interior bread loaf PM,
 - Surface PM,
 - Exterior bread loaf PM,
 - Interior parallelepipedic PM,
 - Interior parallelepipedic PM with pole cap.

Fig. 3.47 shows the dimensions selection page for a case of PMSM: asymmetric stator and interior bread loaf PM rotor. For every topology other geometrical dimensions are available for modification.

Fig. 3.48 presents the FEM dialog page, which includes the material selection, selection of the PM's magnetization, winding definition, a few control specifications (current shape, current amplitude and advance angle) and the menu for the postprocessor stage: field distribution, cogging torque, back-EMF, and load torque. Other postprocessor options can be added: iron loss calculation, inductances, efficiency, etc.

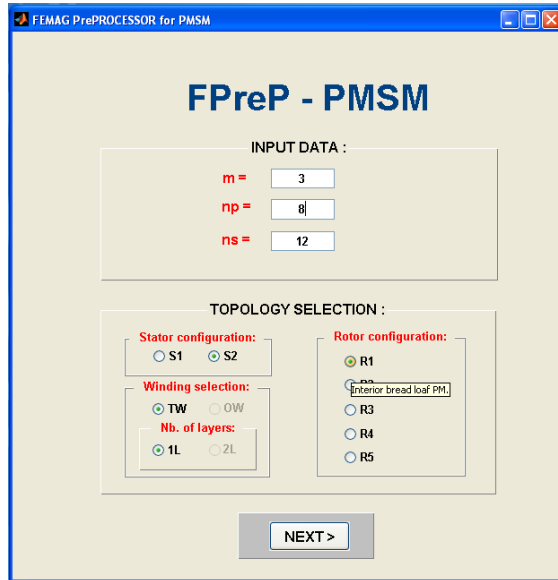


Fig. 3.46. FEM preprocessor for PMSM – main page.

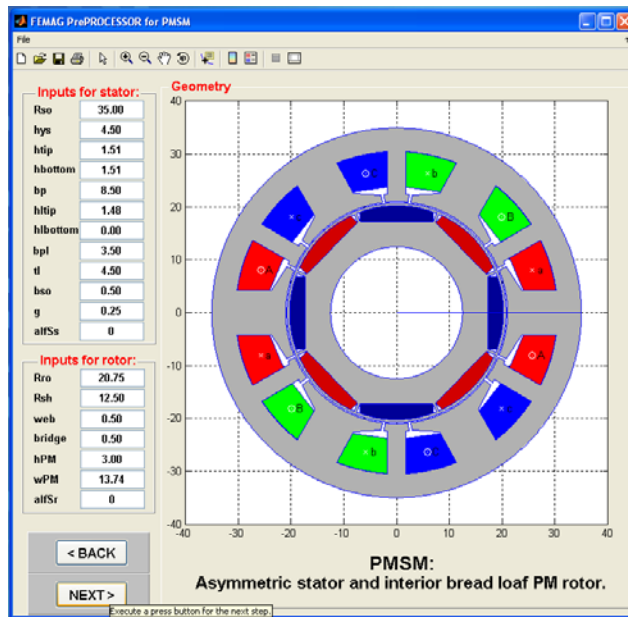


Fig. 3.47. FPreP PMSM – dimensions selection page. PMSM: Asymmetric stator and interior bread loaf PM rotor.

Fig. 3.49 presents the postprocessor page result, including: cogging torque variation, phase back-EMFs and line-to-line back-EMFs, phase currents and load torque computation, for the PMSM with asymmetric stator and interior bread loaf PM rotor. The FEM solver used to obtain these calculations was the 2-D FEMAG software.

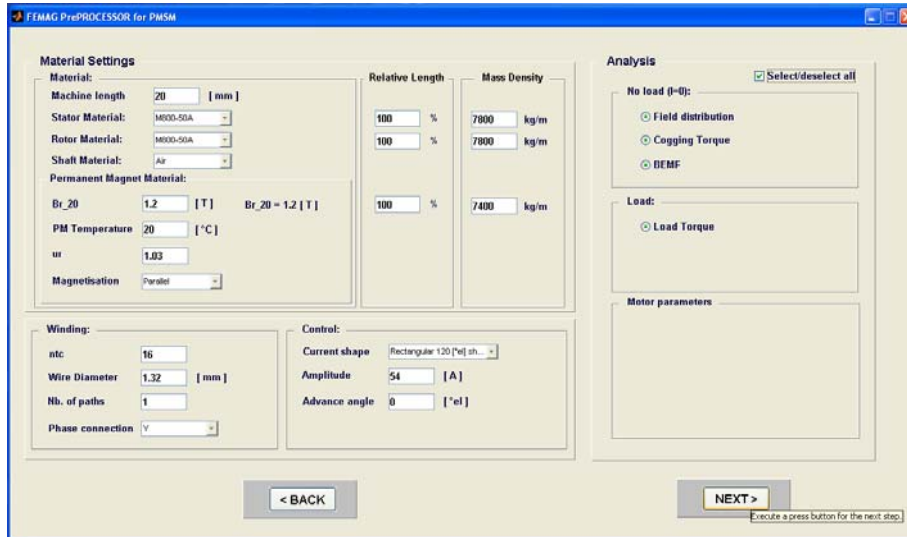


Fig. 3.48. FPreP PMSM – FEM dialog page: material selection, winding definition, control specifications and postprocessor requirements.

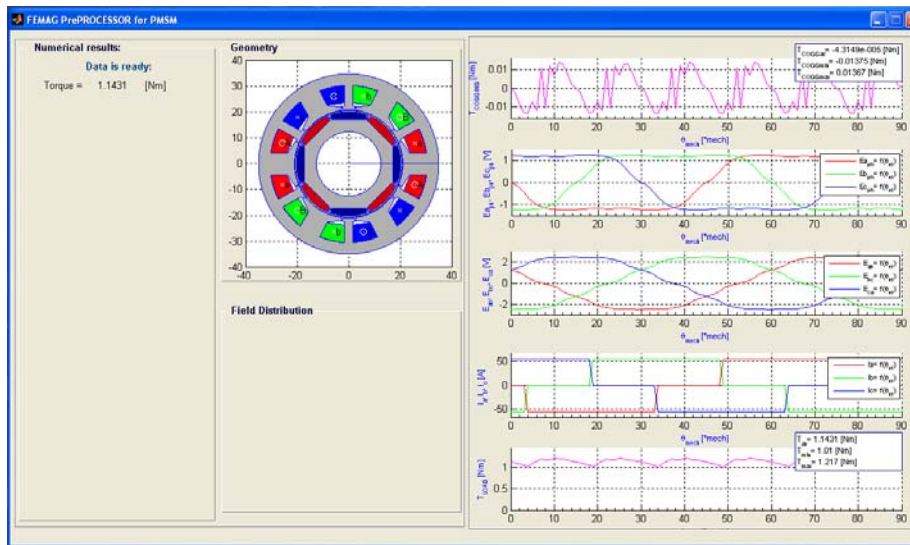


Fig. 3.49. FPreP PMSM – Postprocessor page result.

3.5. Conclusion

An investigation of an interior permanent magnet synchronous motor with 8 rotor poles and (6+6) nonuniform stator slots and concentrated windings fed with trapezoidal currents, was done in this chapter.

This chapter has presented a comparison between FEM-calculated and measured parameters of an interior permanent magnet BLDC motor. This comparison was done in order to validate the FEM-calculated parameters of the motor.

The proposed topology of IPMSM has the general advantages of machines with concentrated coils, such as: lower copper losses, due to the minimization of copper volume, in particular if the axial length of the machine is small, and lower manufacturing costs, due to the possibility to produce the stator in several pieces. It also has a few advantages resulting from the chosen topology, such as: a very low cogging torque ($T_{cogg} < 0.7\% \cdot T_{ab}$) obtained directly without skewing the slots, a simplified production of the rotor in comparison with PMSM with concentrated coils and surface mounted permanent magnets [8], due to the simple shape and fixture of the permanent magnets, and the extended trapezoidal shape of no-load back-EMF calculated for our IPMSM via FEM, makes it suitable for trapezoidal (block) current control drives.

The FE analysis of the calculated total torque emphasizes the idea that for this type of IPMSM the total torque pulsations will be reduced by decreasing the reluctance and commutation torque. Applying the torque ripple reduction method using shifted PM segments (using 2 axial segments, shifted one from each other with 7.5 mechanical degrees) the total torque ripple has been reduced to 7.7% from average torque for 2 axial segments.

For the normal and transient inductances, one obtains analytical expressions that will be used in the dynamic model of the motor.

A measurement procedure was described and the measured results were presented and discussed, confirming satisfactorily FEM calculations. The tests carried out within the measurement procedure had the purpose to deliver machine parameters necessary for further system simulations and control tasks.

References

- [1] D. Iles-Klumpner, *Automotive Permanent Magnet Brushless Actuation Technologies*, PhD Thesis, University Politehnica Timisoara, Romania, 2005.
- [2] N. Bianchi, S. Bolognini, F. Luise, "Analysis and design of a brushless motor for high speed operation", *IEEE Trans. on Energy Conversion*, Vol. 1, pp. 44-51, June 2003.
- [3] D. Iles-Klumpner, I. Şerban, M. Risticvic, I. Boldea, "High-Speed Automotive Permanent Magnet Synchronous Motors", *Proceedings of PCIM*, Nürnberg, Germany, 2005.
- [4] S.-O. Kwon, S.-II. Kim, P. Zhang, J.-P. Hong, "Performance comparison of IPMSM with distributed and concentrated windings", *IEEE Trans. on Industry Application*, Vol. 4, pp. 1984-1988, Oct. 2006.
- [5] M.S. Islam, S. Mir, T. Sebastian, "Paralleling the Stator Coils in Permanent Magnet Machines", *IEMDC*, pp. 1479-1486, May 2005.
- [6] T. Noguchi, "Trends of Permanent-magnet Synchronous Machine Drives", *IEEJ Trans. on Electrical and Electronic Engineering*, pp. 125-142, 2007.
- [7] H. Jussila, P. Salminen, M. Niemelä, J. Pyrhönen, "Comparing Different Slot-Pole Combinations of a Concentrated-Winding Fractional-Slot Permanent-Magnet Machine", *Norpie*, Lund, Sweden, 2006.
- [8] J. Cros and P. Viarouge, "Synthesis of high performance PM motors with concentrated windings", *IEEE Trans. on Energy Conversion*, Vol. 17, No. 2, pp. 248-253, June 2002.
- [9] D. Iles-Klumpner, M. Risticvic, I. Serban, I. Boldea, "Sinusoidal and trapezoidal PMSM drives for automotive applications: a comparative characterization", *PCIM Europe*, 2006.

- [10] C. Grabner, "Idea, realization and characteristics of a novel permanent magnet motor topology with higher harmonic air-gap waves in the BLDC mode", *ISIE*, pp. 1056-1061, June 2007.
- [11] A. Știrban, L. Tutelea, D. Iles-Klumpner, I. Boldea, "FEM analysis of concentrated coils nonuniform slot (6+6/8) IPMSM fed with trapezoidal current", *OPTIM*, pp. 45-52, 2008.
- [12] J.-H. Choi, S.-H. You, J. Hur, H.-G. Sung, "The Design and Fabrication of BLDC Motor and Drive for 42V Automotive Applications", *ISIE*, pp. 1086-1091, June 2007.
- [13] S. Waikar, T. Gopalarathnam, H.A. Toliyat, J.C. Moreira, "Evaluation Of Multiphase Brushless Permanent Magnet (BPM) Motors Using Finite Element Method (FEM) and Experiments", *APEC*, Vol. 1, pp. 396-402, March 1999.
- [14] S.F. Gorman, C. Chen, J.J. Cathey, "Determination of Permanent Magnet Synchronous Motor Parameters for Use in Brushless DC Motor Drive Analysis", *IEEE Trans. on Energy Conversion*, Vol. 3, No. 3, pp.674-681, Sept. 1988.
- [15] K.M. Rahman and S. Hiti, "Identification of Machine Parameters of a Synchronous Motor", *IAS*, Vol. 1, pp. 409-415, Oct. 2003.
- [16] T. Sun, S.-O Kwon, J.-J. Lee, J.-P. Hong, "An Improved AC Standstill Method for Testing Inductances of Interior PM Synchronous Motor Considering Cross-magnetizing Effect", *IEEE-ECCE 2009*, pp. 2415-2422, Sept. 2009.
- [17] M. Kondo, "Parameter Measurements for Permanent Magnet Synchronous Machines", *IEEJ Trans. on Electrical and Electronic Engineering*, pp. 109-117, 2007.
- [18] T.J.E. Miller, M. Popescu, C. Cossar, M. McGilp, "Performance Estimation of Interior Permanent-Magnet Brushless Motors Using the Voltage-Driven Flux-MMF Diagram", *IEEE Trans. On Magnetics*, Vol. 42, No. 7, pp. 1867-1872, July 2006.
- [19] A. Știrban, D. Iles-Klumpner, M. Risticovic, I. Boldea, "(6+6) Slot/8 Pole 3 Phase IPM Brushless DC Automotive Actuator: Torque, EMF, and Inductance Characterization by FEM vs. Experiments", *IEEE-IEMDC 2009*, May 2009.
- [20] D. Meeker, "Finite Element Method Magnetics-FEMM, Version 4.2, User's Manual", May 2009.
- [21] I. Boldea and L.N. Tutelea, "Electric Machines: Steady State, Transients, and Design with MATLAB", CRC Press, Taylor and Francis Group, Boca Raton, FL, 2010.
- [22] J.F. Gieras, "Permanent Magnet Motor Technology, Design and Applications", 3rd ed., CRC Press, Taylor and Francis Group, Boca Raton, FL, 2010.
- [23] V. Grădinaru, L. Tutelea, I. Boldea, "25 kW, 15 krpm, 6/4 PMSM: Optimal Design and Torque Pulsation Reduction via FEM", *OPTIM*, pp. 249-256, 2008.
- [24] B. Zhang, X. Wang, R. Zhang, X. Mao, "Cogging Torque Reduction by Combining Teeth Notching and Rotor Magnets Skewing in PM BLDC with Concentrated Windings", *International Conference on Electrical Machines and Systems (ICEMS) 2008*, pp. 3189-3192, 2008.
- [25] G.-H. Kang, Y.-D. Son, G.-T. Kim, "A Novel Cogging Torque Reduction Method for Interior Type Permanent Magnet Motor", *IAS*, pp. 199-125, Sept. 2007.

Chapter 4

Dynamic circuit model with FEM extracted parameters

Abstract

This chapter presents an accurate and efficient model of brushless DC motor drives considering the phase commutation phenomenon. The torque characteristic of BLDC motor is a very important factor in the design of motor drive system, so it is necessary to predict the precise value of torque, which is determined by the waveform of the back-EMF. The conventional simulation model of BLDC motor is obtained by approximation of real back-EMF waveform to ideal trapezoidal waveform. As a result, when using the ideal trapezoidal waveform, differences occur between simulated BLDC model and real machine. In consequence, in order to reduce these differences, the model of BLDC motor with real back-EMF is needed instead of its approximation model.

The developed model of BLDC motor, considering phase commutation phenomenon, with real back-EMF waveform and adjustable inductance component (to account for the dependence of inductances with rotor position – for interior permanent magnet rotor) is verified through numerical simulations, showing its practical effectiveness.

4.1. Introduction

Brushless DC (BLDC) motor drives are becoming widely used in various consumer and industrial applications, such as servo motor drives, home appliances, computer peripherals, and automotive applications. Simulation models for BLDC motor drives are essential for the fast prediction of the motor drive system during the evaluation of different BLDC motors and designing control algorithms [1].

In general, the overall system consists of three parts [2]: (1) PWM inverter, (2) BLDC motor and load, and (3) speed, torque, and current controllers. An exact understanding of each part is mandatory for analysis and prediction of the overall system operation.

Several simulation models have been proposed for the analysis of BLDC motor drives. These models are based on state-space equations, Fourier series, and the d - q axis model [3-5]. In [5], the authors proposed a model by means of state array matrices to simulate the drive system along with the PWM inverter. However, in addition to its inherent complexity, detailed investigation of the inverter is not included in this work. For large- and small-signal analysis of BLDC motor drive systems, the so-called average-value models (AVMs) are indispensable [6].

Because of the nonsinusoidal nature of the back-EMF and current waveforms, transformation of the machine equations to the d - q model is cumbersome, and it is easier to use the phase-variable approach for modeling and

simulation [7]. The commonly used abc model assumes that the self and mutual inductances are constant [3, 8]. But due to the physical rotation of the rotor and the nonlinear magnetization property of stator iron, the inductance varies with rotor position and winding current [9]. The dependence of inductances versus rotor position can be accurately evaluated through nonlinear FE analysis. The torque of the BLDC motor is mainly influenced by the waveform of the back-EMF and hence it is needed to predict its precise back-EMF [10]. In a similar way as for inductances, the rotor position dependence of the back-EMF and the cogging torque can be calculated. Using these rotor position dependent parameters, the physical phase variable model of BLDC is developed. For dynamic performance studies, the circuit equations and the FE motor equations are strongly coupled and solved simultaneously [11]. This gives accurate results but is time consuming. Using the abc phase variable model the drive system simulation behaves much faster with the same level of accuracy.

Ref. [2] proposes a simulation model for an entire BLDC motor drive. In this model the trapezoidal back EMF waveforms are modeled as a function of rotor position, so that position can be actively calculated according to the operating speeds. Moreover, the switching function concept is adopted to model the PWM inverter. However, the model does not reflect the electronically commutation phenomenon and the waveform of back-EMF is trapezoidal. Hence it is needed to compensate the existing model's precise commutation phenomenon and back-EMF [4, 10].

The BLDC model developed in this chapter takes into account the phase commutation phenomenon, the real waveforms of back-EMF and inductances which are modeled through Fourier series, and respectively through look-up tables, based on FEM calculations from previous chapter. Therefore, it can be expected that the developed simulation model can be an easy-to-design tool for the design and analysis of BLDC motor drives including control algorithms.

4.2. Mathematical model of BLDC motor drive system

Fig. 4.1 shows the overall system configuration of the three-phase BLDC motor drive. The PWM inverter topology is a six-switch voltage-source configuration with constant DC-link voltage (V_{DC}).

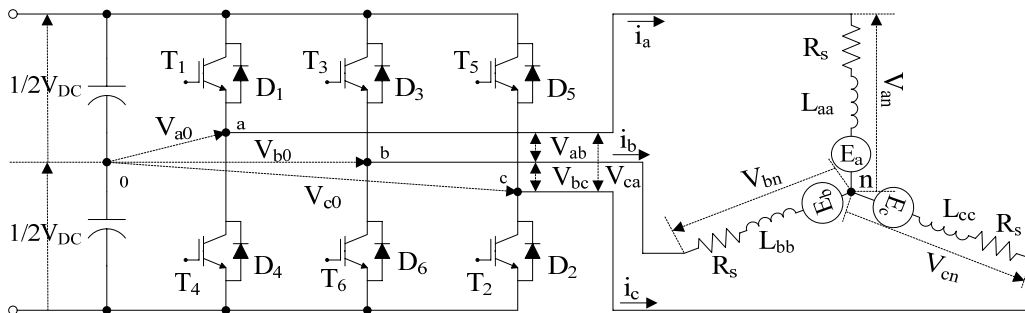


Fig. 4.1. Configuration of BLDC motor drive system.

The analysis is based on the following assumption for simplification [8]:

1. Stator resistances of all windings are equal.
2. Power semiconductor devices in the inverter are ideal.

3. Iron losses are negligible.

BLDC motor drives require variable-frequency, variable-amplitude excitation that is usually provided by a three-phase, full-bridge inverter as shown in Fig. 4.1. Each phase is conducting 120° electrical degrees. Therefore, for this kind of machine, each commutation sequence has one winding that is energized to positive power (current enters into the winding), one winding is deenergized (current exists the winding) and the third winding is in a nonenergized condition. Maximum torque can be obtained, if the inverter is commutated every 60° so that the current is in phase with the back-EMF (Fig. 4.2).

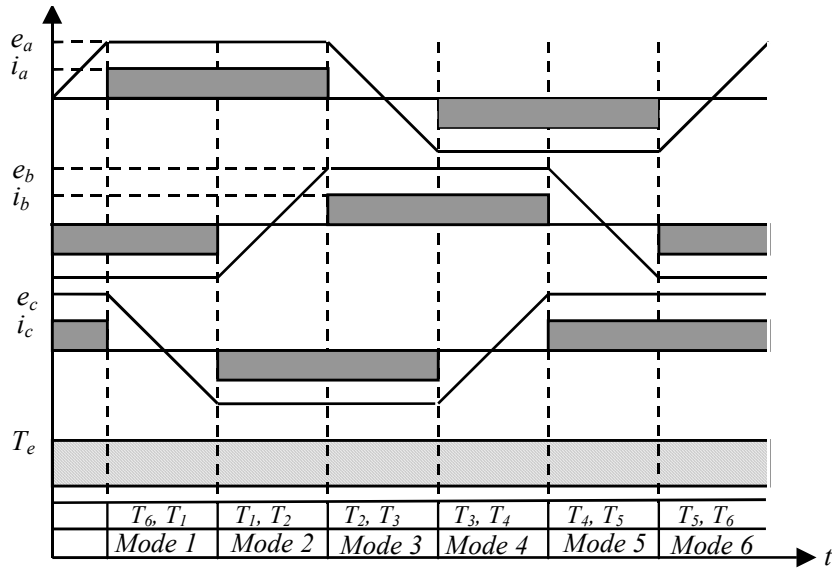


Fig. 4.2. Ideal currents, phase back-EMFs, and electromagnetic torque of a three-phase BLDC Y-connected motor with 120° bipolar currents.

BLDC motor model is composed of two parts. One is an electrical part which calculates electromagnetic torque and current of the motor. The other is a mechanical part which generates revolution of the rotor.

Each phase in an AC motor can be described by a first order differential equation. The circuit equations of the three windings in phase variables can be represented in the matrix form as

$$\begin{bmatrix} V_{a0} \\ V_{b0} \\ V_{c0} \end{bmatrix} = \begin{bmatrix} R_s & 0 & 0 \\ 0 & R_s & 0 \\ 0 & 0 & R_s \end{bmatrix} \begin{bmatrix} i_a \\ i_b \\ i_c \end{bmatrix} + \frac{d}{dt} \begin{bmatrix} \Psi_A(\theta_m, i_a, i_b, i_c) \\ \Psi_B(\theta_m, i_a, i_b, i_c) \\ \Psi_C(\theta_m, i_a, i_b, i_c) \end{bmatrix} + \begin{bmatrix} V_{n0} \\ V_{n0} \\ V_{n0} \end{bmatrix} \quad (4.1)$$

where V_{a0} , V_{b0} , V_{c0} are the phase voltages, i_a , i_b , i_c are the phase currents, R_s is the phase resistance, θ_m is the rotor position, Ψ_A , Ψ_B , Ψ_C are the total flux linkages of the windings, and V_{n0} is the voltage between motor and inverter neutral points.

The total flux linkage in a phase includes both self and mutual flux linkages, and may be defined in the following form:

$$\begin{bmatrix} \Psi_A \\ \Psi_B \\ \Psi_C \end{bmatrix} = \begin{bmatrix} L_{aa}(\theta_m, i_a) & L_{ab}(\theta_m, i_b) & L_{ac}(\theta_m, i_c) \\ L_{ba}(\theta_m, i_a) & L_{bb}(\theta_m, i_b) & L_{bc}(\theta_m, i_c) \\ L_{ca}(\theta_m, i_a) & L_{cb}(\theta_m, i_b) & L_{cc}(\theta_m, i_c) \end{bmatrix} \begin{bmatrix} i_a \\ i_b \\ i_c \end{bmatrix} + \begin{bmatrix} \lambda_{PMa}(\theta_m) \\ \lambda_{PMb}(\theta_m) \\ \lambda_{PMc}(\theta_m) \end{bmatrix} \quad (4.2)$$

where, the term $L_{xx}(\theta_m, i_x) \cdot i_x$ represents the self flux linkage of phase x ; the term $L_{xy}(\theta_m, i_y) \cdot i_y$ stands for the mutual flux linkage between phases x and y ; and the terms λ_{PMa} , λ_{PMb} , λ_{PMc} are the phase flux linkages due to the permanent magnets.

The back-EMF equation is given by Faraday's law

$$e = -\frac{d\lambda_{PM}}{dt} = \frac{d\lambda_{PM}}{d\theta_m} \cdot \frac{d\theta_m}{dt} = k_E \cdot \omega_m \quad (4.3)$$

where k_E stands for back-EMF constant, ω_m is the mechanical speed.

Substituting (4.2) and (4.3) into (4.1), the phase voltage equations become:

$$\begin{bmatrix} V_{a0} \\ V_{b0} \\ V_{c0} \end{bmatrix} = \begin{bmatrix} R_s & 0 & 0 \\ 0 & R_s & 0 \\ 0 & 0 & R_s \end{bmatrix} \begin{bmatrix} i_a \\ i_b \\ i_c \end{bmatrix} + \frac{d}{dt} \left(\begin{bmatrix} L_{aa} & L_{ab} & L_{ac} \\ L_{ba} & L_{bb} & L_{bc} \\ L_{ca} & L_{cb} & L_{cc} \end{bmatrix} \begin{bmatrix} i_a \\ i_b \\ i_c \end{bmatrix} \right) + \begin{bmatrix} e_a \\ e_b \\ e_c \end{bmatrix} + \begin{bmatrix} V_{n0} \\ V_{n0} \\ V_{n0} \end{bmatrix} \quad (4.4)$$

Since the neutral point of the motor is not available for the most commercial motors, the line-to-line voltage equations can be used as follows:

$$\begin{bmatrix} V_{ab} \\ V_{bc} \\ V_{ca} \end{bmatrix} = K \cdot \begin{bmatrix} R_s & 0 & 0 \\ 0 & R_s & 0 \\ 0 & 0 & R_s \end{bmatrix} \begin{bmatrix} i_a \\ i_b \\ i_c \end{bmatrix} + \frac{d}{dt} \left(K \cdot \begin{bmatrix} L_{aa} & L_{ab} & L_{ac} \\ L_{ba} & L_{bb} & L_{bc} \\ L_{ca} & L_{cb} & L_{cc} \end{bmatrix} \begin{bmatrix} i_a \\ i_b \\ i_c \end{bmatrix} \right) + \begin{bmatrix} e_{ab} \\ e_{bc} \\ e_{ca} \end{bmatrix} \quad (4.5)$$

where K is the matrix transformation from phase quantities to line-to-line quantities, and it has the following form

$$K = \begin{bmatrix} 1 & -1 & 0 \\ 0 & 1 & -1 \\ -1 & 0 & 1 \end{bmatrix} \quad (4.6)$$

The electromagnetic torque is given by

$$T_e = \frac{(e_a \cdot i_a + e_b \cdot i_b + e_c \cdot i_c)}{\omega_m} \quad (4.7)$$

The mechanical part of BLDC motor is

$$J \cdot \frac{d\omega_m}{dt} + B_m \cdot \omega_m = T_e - T_L \quad (4.8)$$

where T_L is the load torque, B_m is the damping constant, and J is the moment of inertia of the drive.

The electrical frequency is related to the mechanical speed by

$$\omega_e = p_1 \cdot \omega_m \quad (4.9)$$

where p_1 is the number of rotor pole pairs.

4.3. Commutation of BLDC motors

4.3.1. Bipolar excitation, two phases on

For BLDC motor the currents are commutated into the appropriate phases in synchronism with the rotation of the rotor. The inverter is usually responsible for both the electronic commutation and current regulation. The position information obtained from the position sensors is used to open and close the six inverter switches. For three-phase sinewave drives it is often the practice to have three transistors conducting at any time, but with squarewave drives normally only two transistors are conducting: one upper and one lower transistor in the inverter bridge [12], Fig. 4.1. If the motor windings are star-connected and the star point is isolated, the inverter input current flows through two of the three phases in series at all time [7]. Hysteresis or pulse-width-modulated (PWM) current controllers are typically used to regulate the actual machine currents to the rectangular current reference waveforms shown in Fig. 4.2. Either soft chopping or hard chopping could be employed for this purpose. The flow of currents during one 60° interval when switches T_1 and T_6 are active is shown in Fig. 4.3a for soft chopping and Fig. 4.3b for hard chopping. When T_1 and T_6 are in their on state, the current builds up in the path shown by the solid lines. In soft chopping, the current regulator commands the turn-off of switch T_1 once the current crosses the threshold. The current then decays through diode D_4 and switch T_6 as shown by the dashed lines. Alternatively, T_6 could be turned-off, and the current would then decay in the loop formed by T_1 and D_3 . The fall time of the current can be made smaller by hard chopping, in which both switches are turned off. The current then freewheels through D_4 , D_3 , and the DC link capacitor, feeding energy back to source. The freewheeling diodes thus provide important paths for the currents to circulate when the switches are turned off and during the commutation intervals.

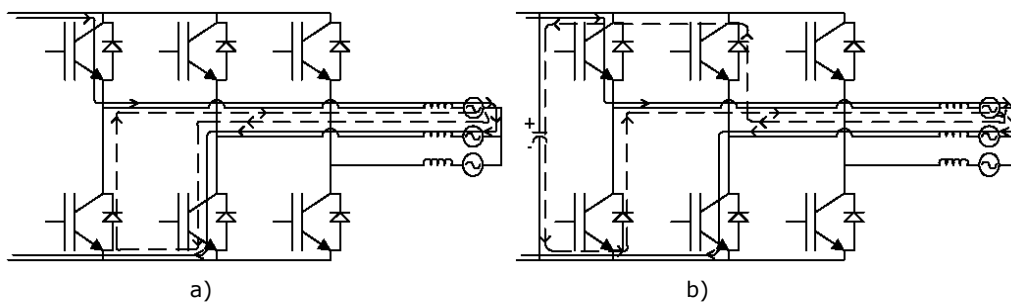


Fig. 4.3. Illustration of soft chopping a) and hard chopping b) for current regulation [7].

The above discussion has concentrated on the operation of the BLDC machine as a motor. The BLDC machine can, however, operate equally as a generator. The polarity of the torque can be reversed by simply reversing the

polarity of the phase current waveforms with respect to the back-EMFs. This situation can be used for regenerative braking operation, in vehicle propulsion, for example [7]. Special arrangements may be made in the power converter to accept energy from the machine, as conventional bridge rectifiers are not able to feed energy back to the AC supply. The situation is considerably simplified if the source is a battery, as in automotive applications.

4.3.2. Bipolar excitation, three phases on

In six-step mode operation only one upper and one lower solid state switch are turned on at a time (120° conduction). With more than two switches on at a time, a 180° current conduction can be achieved, as shown in Fig. 4.4. If the full current flows, say, through one upper leg, two lower legs conduct half of the current [13].

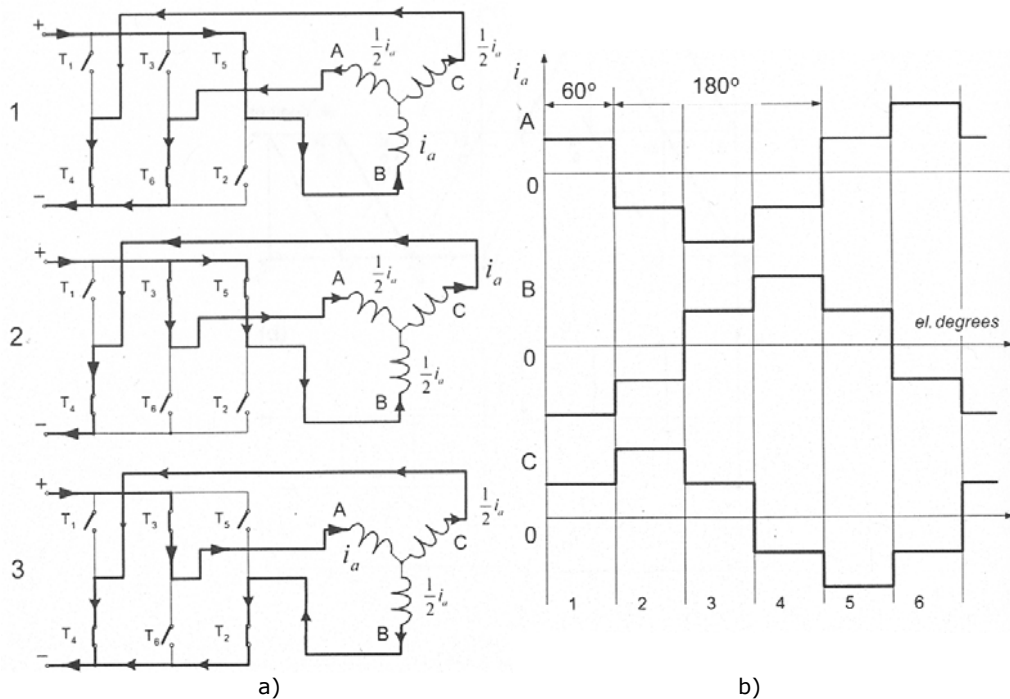


Fig. 4.4. Three-phase bipolar-driven star-connected PM brushless DC motor with three phases on at a time: a) commutation, b) current waveforms.

4.3.3. Unipolar excitation

Unipolar current conduction limits the phases to only one direction of current, and the commutation frequency is half that of a bipolar or full-wave drive. The unipolar motor needs fewer electronic parts and uses a simpler circuit than bipolar motor. For these reasons, unipolar-driven motors are widely used in low-cost applications [7]. Unipolar excitation results in an inefficient winding utilization compared with bipolar excitation, but they have the following advantages over bipolar circuits [7]:

1. There is only one device in series with each phase, minimizing conduction losses.
2. The risk of shoot-through faults is eliminated.
3. Switching of devices connected to the supply rails, which generally requires some isolation circuitry, can be avoided.

The unipolar or half-wave operation of BLDC motors is explained in Fig. 4.5. The three phase winding is star-connected and the motor neutral point has to be available because the phase currents are no longer balanced. The DC voltage V_{DC} is switched across phase-to-neutral terminals with the aid of one solid state switch per phase. Each phase terminal receives positive voltage and the neutral wire is of negative polarity.

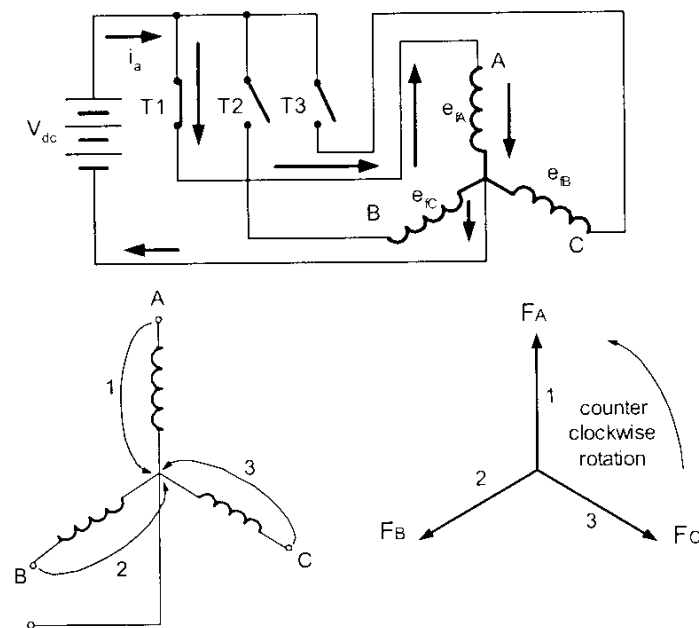


Fig. 4.5. Switching sequence and MMF phasors for three-phase unipolar-driven star-connected PM brushless DC motor [13].

For the current sequence i_a, i_b, i_c the MMF phasors F_A, F_B, F_C rotate counterclockwise. If the switching sequence is reversed, i.e. i_a, i_c, i_b , the direction of rotation of MMF phasors will be clockwise [13]. This type of operation (commutation) is called *half-wave operation* because conduction occurs only during the positive half of the EMF waveform.

The main issue in unipolar BLDC motor drives is high torque ripple, not acceptable in some PM brushless motor applications. By exciting a 12-slot motor with 120° bipolar currents gives a torque ripple of 13% [7]. This value represents the ripple component caused by the nonideal back-EMF alone, without considering the inverter effects. Exciting the same motor with 120° unipolar currents, for example, would produce a torque ripple of 23.7%. However, by exciting the motor with 180° unipolar current waveforms shown in Fig. 4.6, the torque ripple is significantly reduced [7]. It is important to correlate the motor characteristics to those of the inverter. Increasing the number of phases can reduce the torque

pulsation, but the cost of the drive increases. The simplest unipolar converter has a single switch in series with each motor winding, and a reverse-parallel diode provides a freewheeling path at turn-off. This drive has no regenerative control, but four-quadrant operation is possible by using topologies with more than one switch per phase but fewer than two switches per phase. One such topology that has been used for switched reluctance drives is the C-dump converter shown in Fig. 4.7 [7].

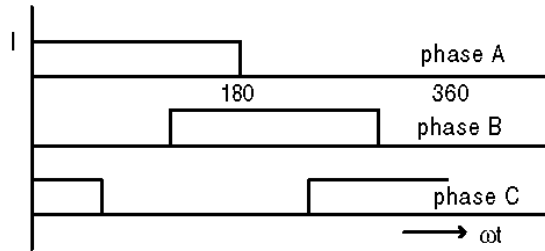


Fig. 4.6. 180° unipolar current waveform.

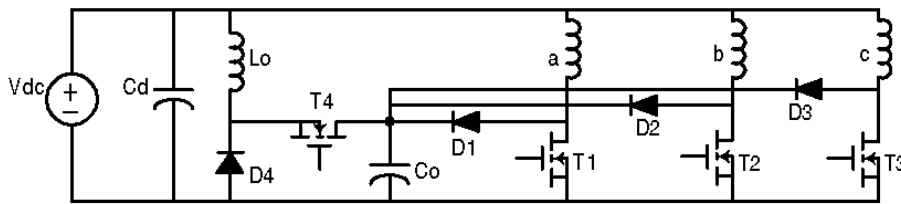


Fig. 4.7. Schematic of C-dump topology for unipolar three-phase BLDC motor.

4.4. Voltage Source Inverter for bipolar-driven BLDC motor

The inverter operation can be divided into six sectors according to the current conduction states as shown in Fig. 4.8 [1].

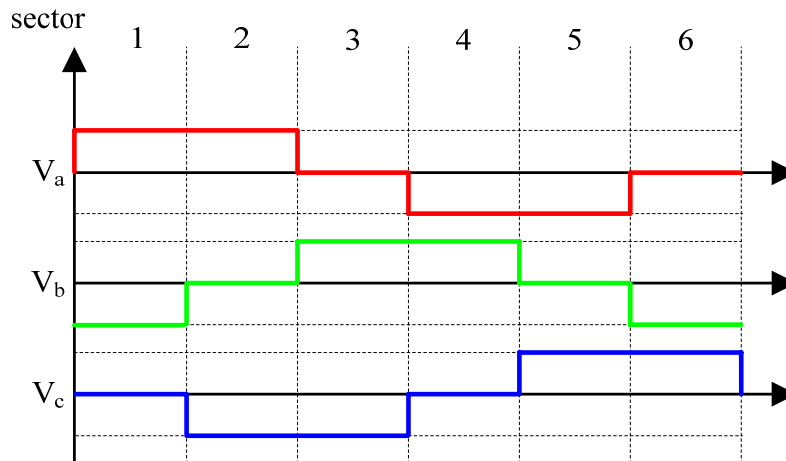


Fig. 4.8. Sectors of BLDC 120° conduction mode.

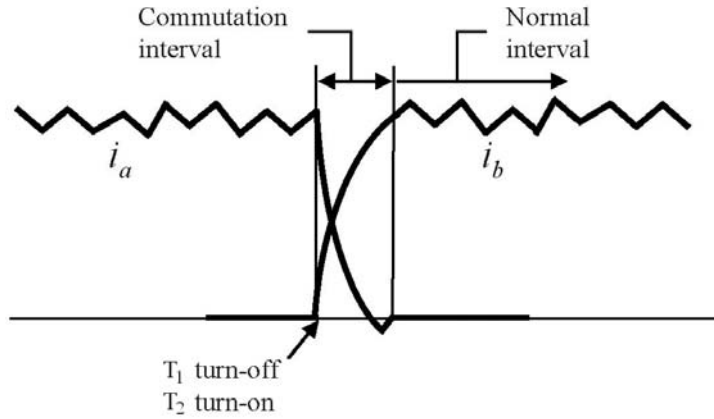
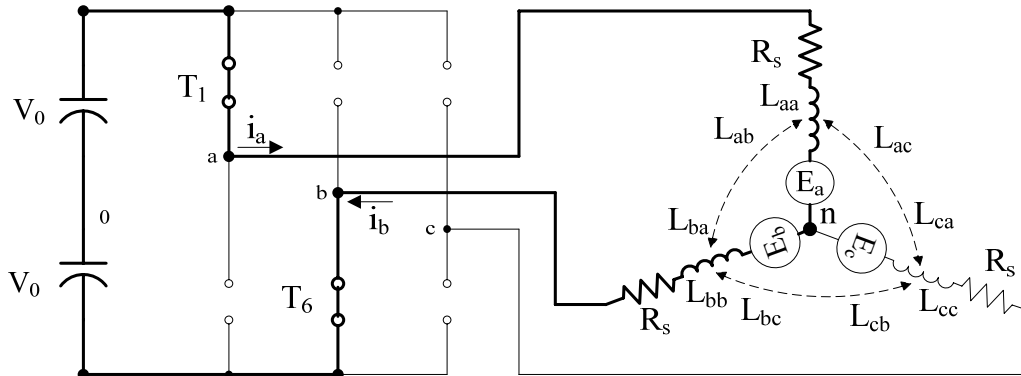


Fig. 4.9. Typical current waveform during commutation between phase A and phase B.

Every sector is divided into two parts, commutation and normal interval. The commutation interval is the initial freewheeling interval, just after the switching, when both mesh currents are non-zero. During commutation interval, all three lines are conducting [1]. The next interval when only phase B and phase C are conducting is called normal interval. Normal interval begins when the freewheeling mesh current extinguishes. During commutation interval, i_a is falling to zero and i_b is increasing. Ideally $di_b/dt = -di_a/dt$ so that i_c remains constant.

The freewheeling or commutation interval is shown in Fig 4.9. Each line-to-line voltage is calculated depending on the interval. The switching states and a conduction sequence are described in Fig. 4.10.

Fig. 4.10 describes the situation when the sector is changing from 1 to 2. In the normal interval of sector 1 the top switch of phase A and bottom switch of phase B are turned-on. There is only one way for the current to flow, i.e., the loop through phases A and B as shown in Fig. 4.10a.



a) Current flow during normal interval of the sector 1

Fig. 4.10. (continued).

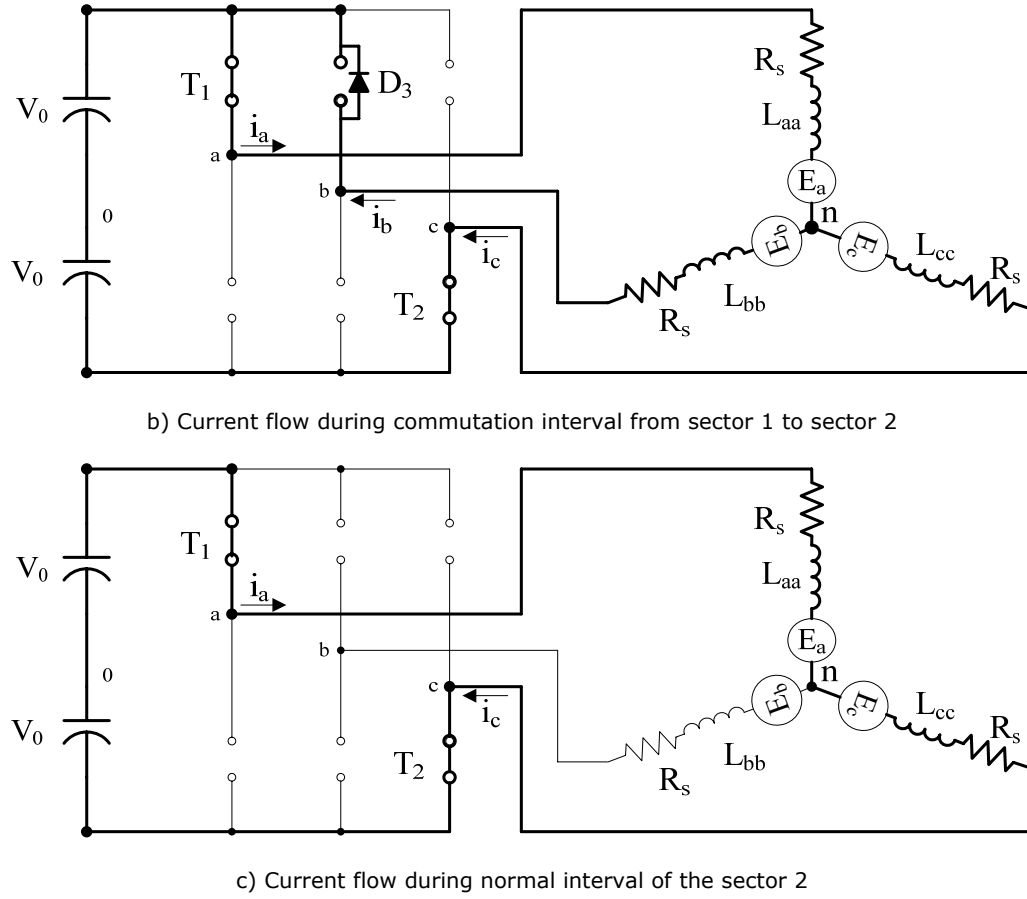


Fig. 4.10. A sequence of commutation in the three-phase BLDC star-connected motor.

For the situation in Fig. 4.10a the phase voltages can be written as

$$V_{a0} = V_0 = R_s \cdot i_a + \frac{d}{dt} (L_{aa} \cdot i_a + L_{ab} \cdot i_b + L_{ac} \cdot i_c) + e_a + V_{n0} \quad (4.10)$$

$$V_{b0} = -V_0 = R_s \cdot i_b + \frac{d}{dt} (L_{ba} \cdot i_a + L_{bb} \cdot i_b + L_{bc} \cdot i_c) + e_b + V_{n0} \quad (4.11)$$

$$V_{c0} = e_c + V_{n0} \quad (\text{when, } i_c = 0) \quad (4.12)$$

$$V_{n0} = \frac{1}{2} \cdot (-e_a - e_b) \quad (4.13)$$

$$V_0 = \frac{1}{2} \cdot V_{DC} \quad (4.14)$$

For a balanced star-connected BLDC motors, the three phase currents always meet the following equation:

$$i_a + i_b + i_c = 0 \quad (4.15)$$

Using (4.15), with $i_c = 0$, and the transient inductances instead of the normal inductances the phase voltages are

$$V_{a0} = V_0 = R_s \cdot i_a + (L_{aat} - L_{abt}) \cdot \frac{di_a}{dt} + e_a + V_{n0} \quad (4.16)$$

$$V_{b0} = -V_0 = R_s \cdot i_b + (L_{bbt} - L_{bat}) \cdot \frac{di_b}{dt} + e_b + V_{n0} \quad (4.17)$$

$$V_{c0} = e_c + V_{n0} \quad (4.18)$$

$$V_{an} = V_0 - V_{n0} = R_s \cdot i_a + (L_{aat} - L_{abt}) \cdot \frac{di_a}{dt} + e_a \quad (4.19)$$

$$V_{bn} = -V_0 - V_{n0} = R_s \cdot i_b + (L_{bbt} - L_{bat}) \cdot \frac{di_b}{dt} + e_b \quad (4.20)$$

$$V_{cn} = e_c \quad (4.21)$$

Corresponding rotor position sector is changing from 1 to 2. The bottom switch of phase B is turned-off and the bottom switch of phase C simultaneously is turned-on. Ideally the current in phase A should remain constant, while the phase B current falls to zero and the phase C current builds up to the reference value. There are two paths for current to flow as shown in Fig. 4.10b. The phase voltages can be represented as

$$V_{a0} = V_0 = R_s \cdot i_a + L_{aat} \cdot \frac{di_a}{dt} + L_{abt} \cdot \frac{di_b}{dt} + L_{act} \cdot \frac{di_c}{dt} + e_a + V_{n0} \quad (4.22)$$

$$V_{b0} = V_0 = R_s \cdot i_b + L_{bat} \cdot \frac{di_a}{dt} + L_{bbt} \cdot \frac{di_b}{dt} + L_{bct} \cdot \frac{di_c}{dt} + e_b + V_{n0} \quad (4.23)$$

$$V_{c0} = -V_0 = R_s \cdot i_c + L_{cat} \cdot \frac{di_a}{dt} + L_{cbt} \cdot \frac{di_b}{dt} + L_{cct} \cdot \frac{di_c}{dt} + e_c + V_{n0} \quad (4.24)$$

$$V_{n0} = \frac{1}{3} \cdot (V_0 - E) \quad (4.25)$$

where, $E = e_a + e_b + e_c$.

$$V_{an} = V_0 - V_{n0} = R_s \cdot i_a + L_{aat} \cdot \frac{di_a}{dt} + L_{abt} \cdot \frac{di_b}{dt} + L_{act} \cdot \frac{di_c}{dt} + e_a \quad (4.26)$$

$$V_{bn} = V_0 - V_{n0} = R_s \cdot i_b + L_{bat} \cdot \frac{di_a}{dt} + L_{bbt} \cdot \frac{di_b}{dt} + L_{bct} \cdot \frac{di_c}{dt} + e_b \quad (4.27)$$

$$V_{cn} = -V_0 - V_{n0} = R_s \cdot i_c + L_{cat} \cdot \frac{di_a}{dt} + L_{cbt} \cdot \frac{di_b}{dt} + L_{cct} \cdot \frac{di_c}{dt} + e_c \quad (4.28)$$

In a similar way, the commutation phenomenon of other sectors can be analyzed.

4.5. Modeling and implementation of BLDC motor drive system

The development and analysis of BLDC motor drives has been the subject of many papers and academic theses [14-37]. The simulation can be done under Matlab/Simulink environment, which is a standard tool in control and system engineering.

In this section the modeling process is explained and the actual implementation using Matlab/Simulink is described. Fig. 4.11 shows the overall block diagram of the developed model for BLDC motor drive. The proposed model consists of six functional blocks: BLDC motor model block which includes the back-EMF block, inductance block, Voltage Source Inverter, current control block, and speed controller block.

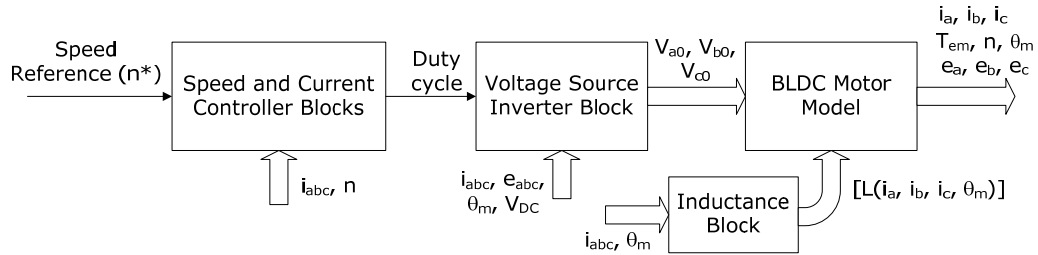


Fig. 4.11. Overall block diagram of the developed model for BLDC motor drive system.

4.5.1. BLDC motor model block

Fig. 4.12 shows the detailed implementation of the BLDC motor model under Matlab/Simulink environment. The phase voltage equations and motion equation used to model the BLDC motor were presented in section 4.2.

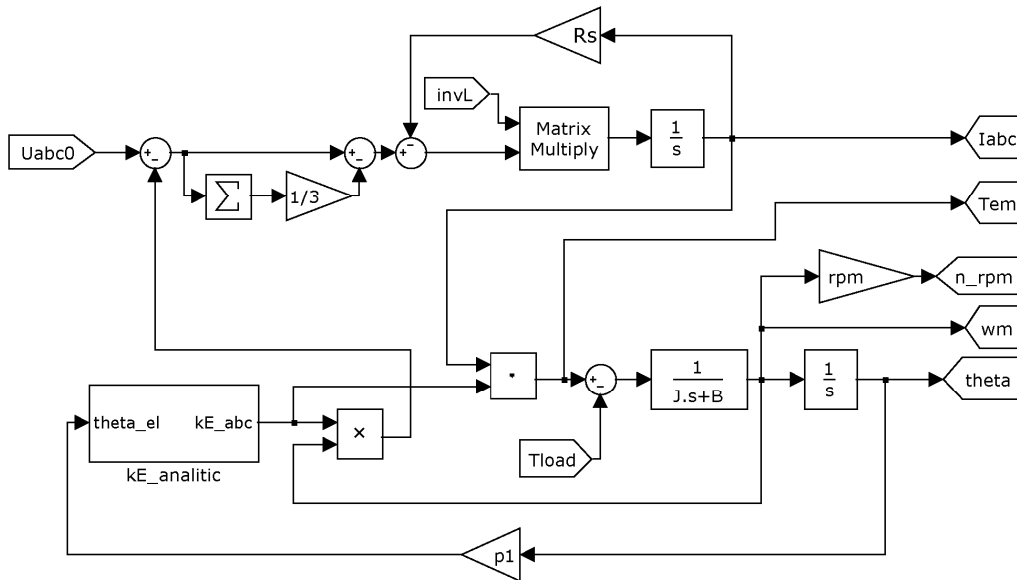


Fig. 4.12. Simulink BLDC motor model.

The back-EMF is a function of rotor electrical position ($\theta_e = p_1 \cdot \theta_m$) and has the amplitude

$$E = k_E \cdot \omega_m \tag{4.29}$$

where k_E is the back-EMF constant.

In this chapter the modeling of the back-EMF is performed first curve-fitting the FEM calculated expressions of the phase PM flux linkages (from Chapter 3). Knowing the fact that the back-EMF constant is the phase PM flux linkage derivative versus rotor position, analytical expressions for the back-EMF constants are obtained.

$$\lambda_{PMa}(\theta_m) = \sum_{k=1,3,5} A_k \cdot \cos(k \cdot p_1 \cdot \theta_m) \tag{4.30}$$

$$\lambda_{PMb}(\theta_m) = \sum_{k=1,3,5} A_k \cdot \cos\left(k \cdot \left(p_1 \cdot \theta_m - \frac{2 \cdot \pi}{3}\right)\right) \tag{4.31}$$

$$\lambda_{PMc}(\theta_m) = \sum_{k=1,3,5} A_k \cdot \cos\left(k \cdot \left(p_1 \cdot \theta_m + \frac{2 \cdot \pi}{3}\right)\right) \tag{4.32}$$

$$k_{Ea}(\theta_m) = -\frac{d\lambda_{PMa}(\theta_m)}{d\theta_m} = p_1 \cdot \sum_{k=1,3,5} k \cdot A_k \cdot \sin(k \cdot p_1 \cdot \theta_m) \tag{4.33}$$

$$k_{Eb}(\theta_m) = -\frac{d\lambda_{PMb}(\theta_m)}{d\theta_m} = p_1 \cdot \sum_{k=1,3,5} k \cdot A_k \cdot \sin\left(k \cdot \left(p_1 \cdot \theta_m - \frac{2 \cdot \pi}{3}\right)\right) \tag{4.34}$$

$$k_{Ec}(\theta_m) = -\frac{d\lambda_{PMc}(\theta_m)}{d\theta_m} = p_1 \cdot \sum_{k=1,3,5} k \cdot A_k \cdot \sin\left(k \cdot \left(p_1 \cdot \theta_m + \frac{2 \cdot \pi}{3}\right)\right) \tag{4.35}$$

where the terms A_k are the first three coefficients of Fourier series, listed in Table 4.1.

Table 4.1. Fourier series coefficients for the back-EMFs analytical expressions

A_1	$3.1671 \cdot 10^{-3}$ [Vs/rad]
A_3	$0.2226 \cdot 10^{-3}$ [Vs/rad]
A_5	$0.0246 \cdot 10^{-3}$ [Vs/rad]

Based on the rotor position the numerical expressions of the back-EMF constants can be obtained using equations (4.33), (4.34), and (4.35), and it is implemented as shown in Fig. 4.13. Therefore, with the speed and rotor position, the three-phase back-EMF waveforms can be generated at every operating speed.

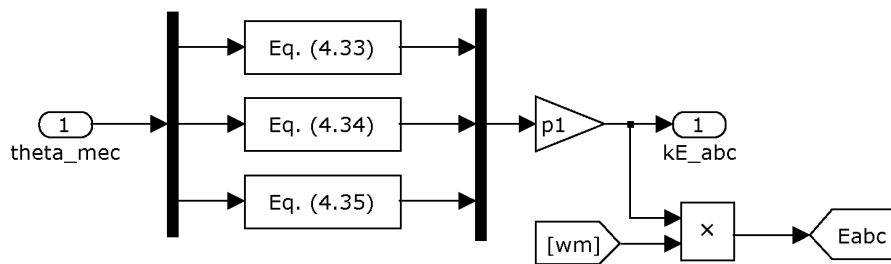


Fig. 4.13. Back-EMF generating block from rotor position and speed.

4.5.2. Inductance block

The modeling of the inductances variation versus position and phase current amplitude was performed through look-up tables, based on the FEM calculation of the three-phase BLDC motor from Chapter 3. The implementation is shown in Fig. 4.14. The inverse and the determinant of the matrix inductance were calculated using dedicated Simulink blocks from Aerospace Blockset/Utilities/Math Operations library.

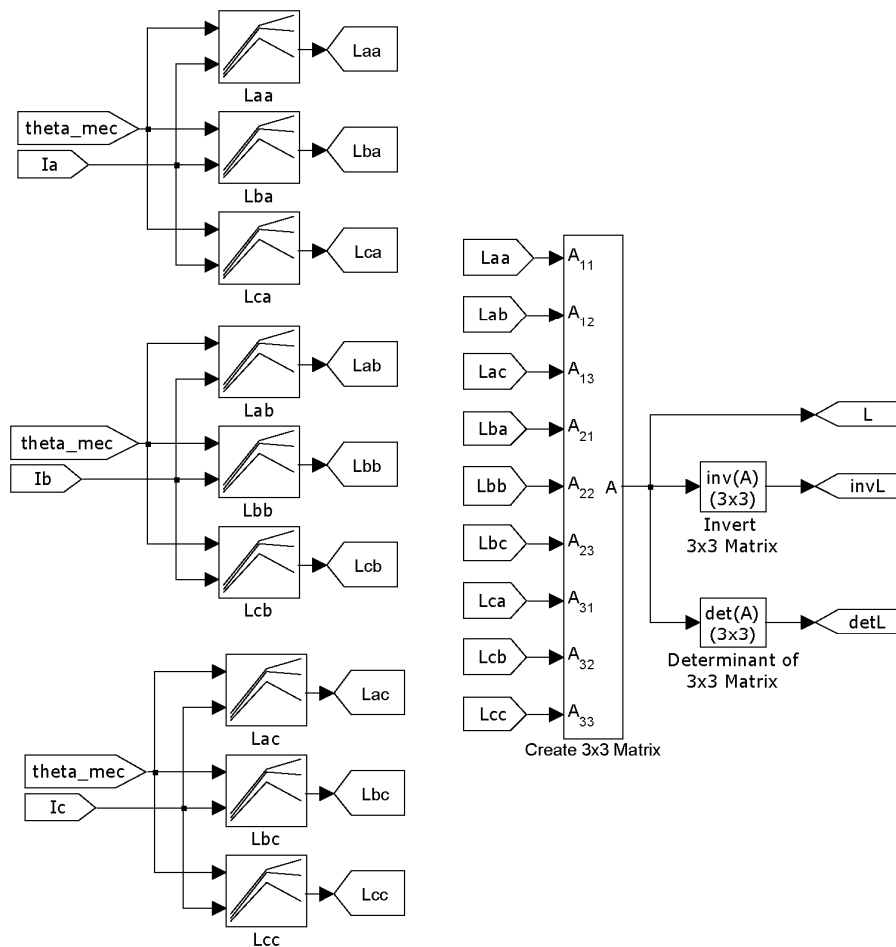


Fig. 4.14. The inductance block.

4.5.3. Voltage Source Inverter

The VSI was implemented in Matlab/Simulink for the bipolar-driven three-phase BLDC star-connected motor drive, 120° conduction mode, taking into account the phase commutation phenomenon detailed in section 4.4. The inverter takes DC bus voltage, back-EMFs, rotor position sectors (Fig. 4.15), commutation interval

condition (Fig. 4.16), and voltage between motor and the inverter neutral points V_{n0} (Fig. 4.17) and then calculates each phase voltage, as in Fig. 4.18.

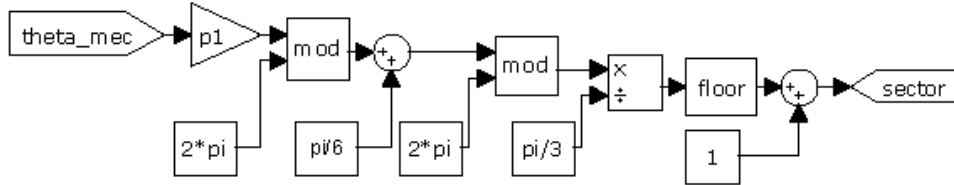


Fig. 4.15. Rotor position sectors.

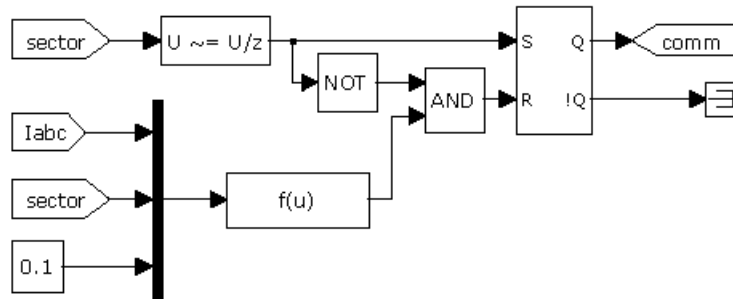


Fig. 4.16. Commutation interval signal.

Every sector is divided into two parts, commutation interval ($comm = 1$) and normal interval ($comm = 0$). Commutation interval condition is met every time the sector is changing and lasts until the freewheeling mesh current extinguishes, when the normal interval starts.

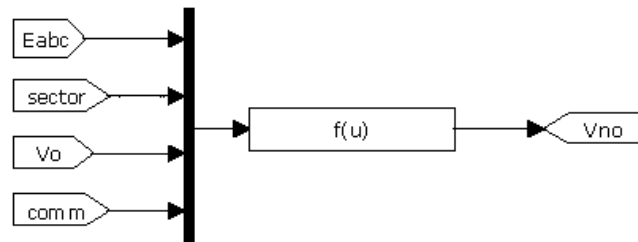


Fig. 4.17. Voltage between motor and the inverter neutral points V_{n0} .

Voltage V_{n0} is calculated using expression (4.13) for commutation interval and expression (4.25) for normal interval, with proper terms for each sector.

4.5.4. Speed and current controller blocks

The speed control circuit is implemented using a proportional-integral controller as shown in Fig. 4.19. The main current control strategies in the BLDC motor drive are duty-cycle controlled voltage PWM technique and hysteresis current

control [34]. In this section duty-cycle controlled voltage PWM technique is used (Fig. 4.19).

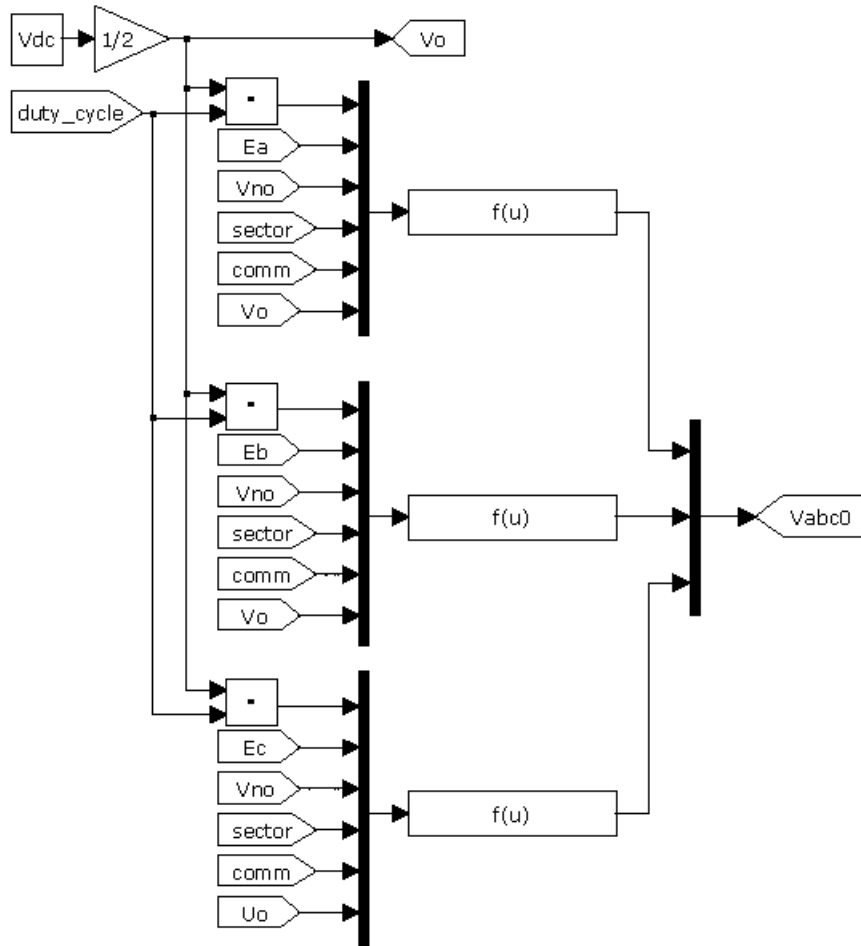


Fig. 4.18. Simulink diagram of Inverter for BLDC motor.

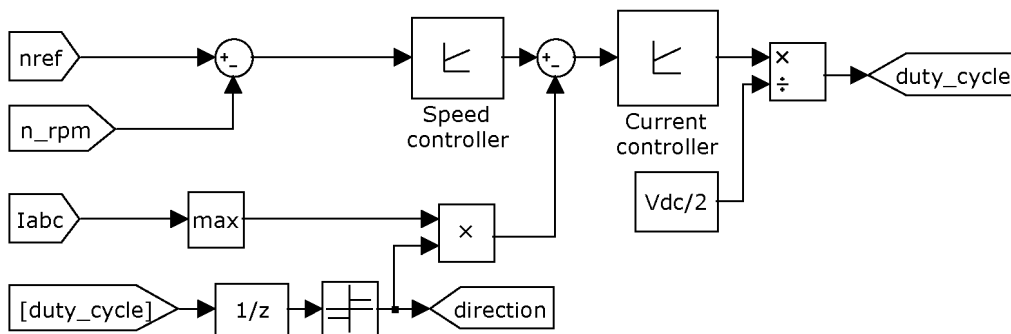


Fig. 4.19. Speed and current control blocks.

Fig. 4.20 shows the PI speed controller with anti-windup used in simulation. The PI gains are tuned using Ziegler-Nichols method, and they have the following values: $K_{p_w} = 0.3$ [A/rpm], $K_{i_w} = 15$ [1/s], $K_{aw} = 10$. The anti-windup compensator has the role to reduce the overshootings in the speed response caused by the saturation of the PI output. The output of the speed controller is limited between $-I_{max}$ and $+I_{max}$, where $I_{max} = k_{overload} \cdot I_n$. The overload factor in this case is $k_{overload} = 2$.

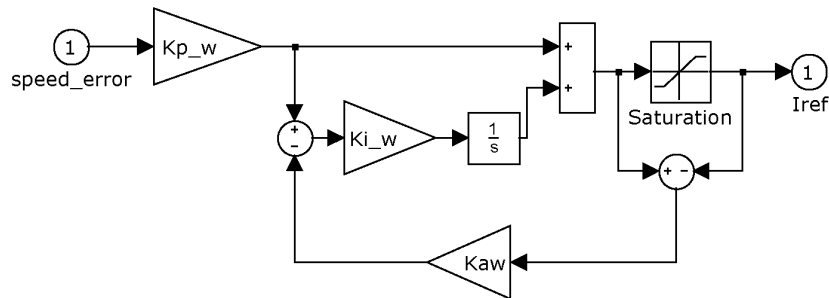


Fig. 4.20. PI speed controller.

Fig. 4.21 shows the PI current controller used in simulation. The PI gains are tuned with Ziegler-Nichols method, with the following values: $K_{p_{is}} = 0.5$ [V/A], $K_{i_{is}} = 200$ [1/s]. The output of the current controller is limited between $-V_{DC}/2$ and $+V_{DC}/2$.

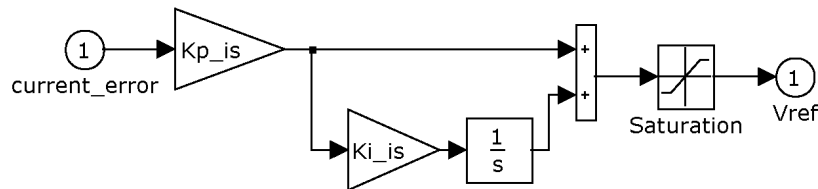


Fig. 4.21. PI current controller.

4.6. Simulation results and discussions

The BLDC parameters, used in the Simulink implementation, are listed in Table 4.2.

Table 4.2. BLDC motor specification

Parameter	Symbol	Value	Unit
Number of pole pairs	p_l	4	-
Rated torque	T_{eb}	1.14	Nm
Rated current	I_n	56	A
Rated speed	n_n	1000	rpm
DC bus voltage	V_{DC}	12	V
Stator phase resistance	R_s	11	m Ω
Moment of inertia of the drive	J	$3.066 \cdot 10^{-4}$	kg·m ²
Damping constant	B_m	$1 \cdot 10^{-4}$	Nm/(rad/s)

Fig. 4.22 shows the generated back-EMF from the rotor position and the phase-current waveforms at 1000 rpm and 0.3 Nm (a duty cycle of 0.263). The phase current in this experiment is not controlled. This experiment is to examine the implementation of functions which models the commutation phenomenon and waveform of back-EMF.

Fig. 4.23 shows the dynamic response of the speed and current controllers, which are designed using PI regulators as shown in Fig. 4.19, Fig. 4.20 and Fig. 4.21. The reference speed is 1000 rpm, and the load torque is 0.3 Nm. From the zoomed waveform in Fig. 4.23b, the torque pulsation due to the commutation can be measured.

Fig. 4.24 presents the simulation results for speed acceleration from 500 to 1000 rpm, proving the reliability of the proposed BLDC motor drive system model. Fig. 4.25 shows the simulation results for a load change from 1.14 Nm to 0.3 Nm at 0.4 s and back to 1.14 Nm at 0.8 s, proving that the BLDC model is satisfactory under load transients also.

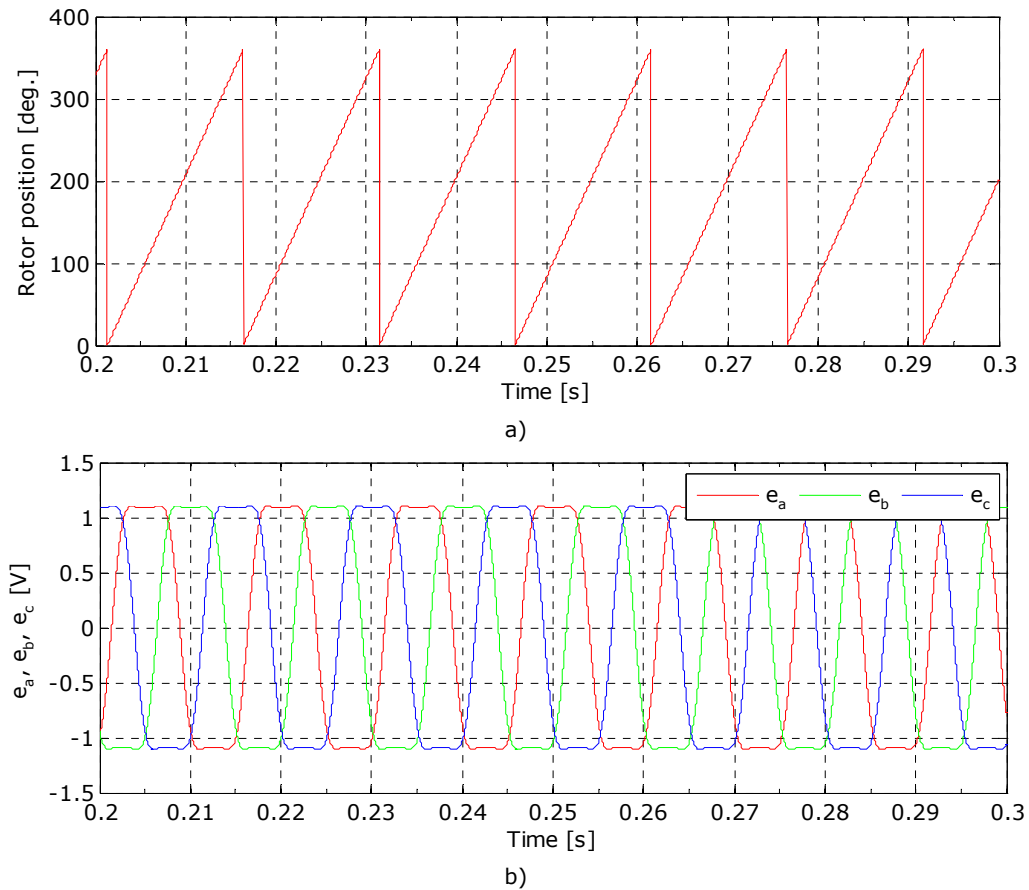
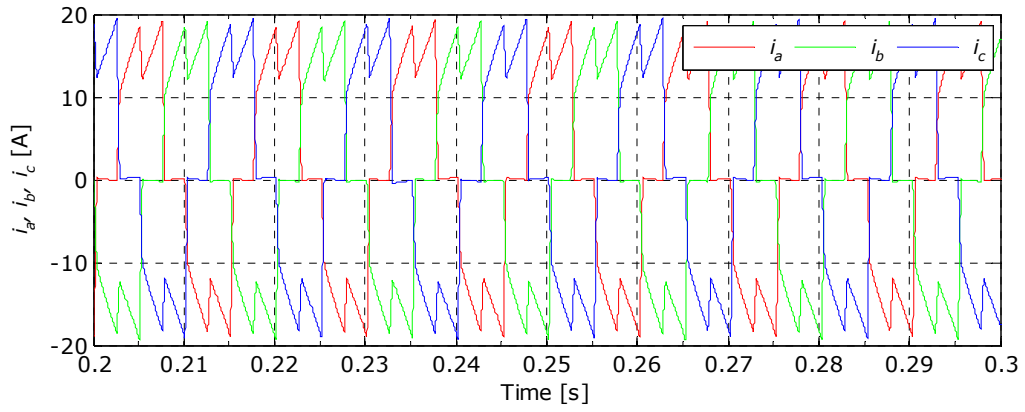
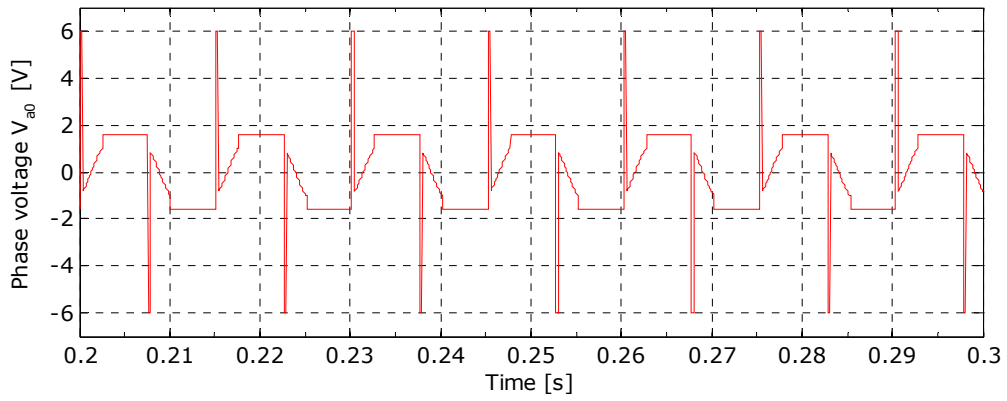


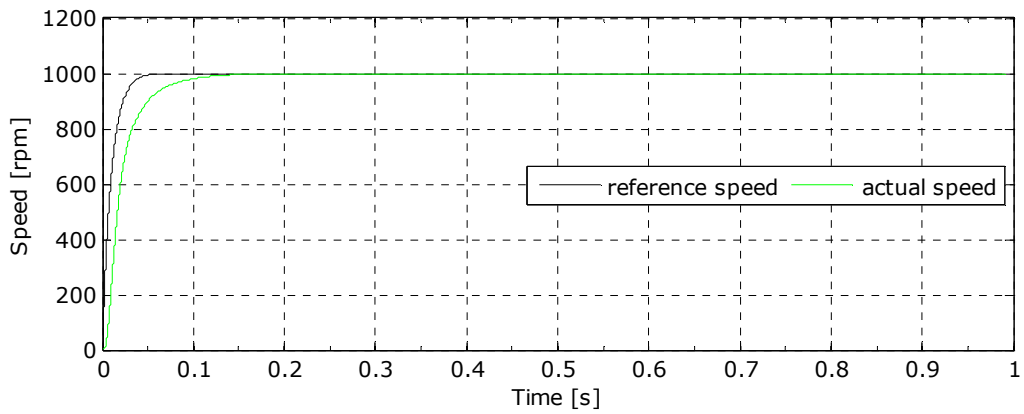
Fig. 4.22. (continued).



c)



d)



e)

Fig. 4.22. 1000 rpm and 0.3 Nm, with open-loop control: a) rotor position, b) phase back-EMFs, c) phase currents, d) phase voltage V_{a0} , e) actual speed.

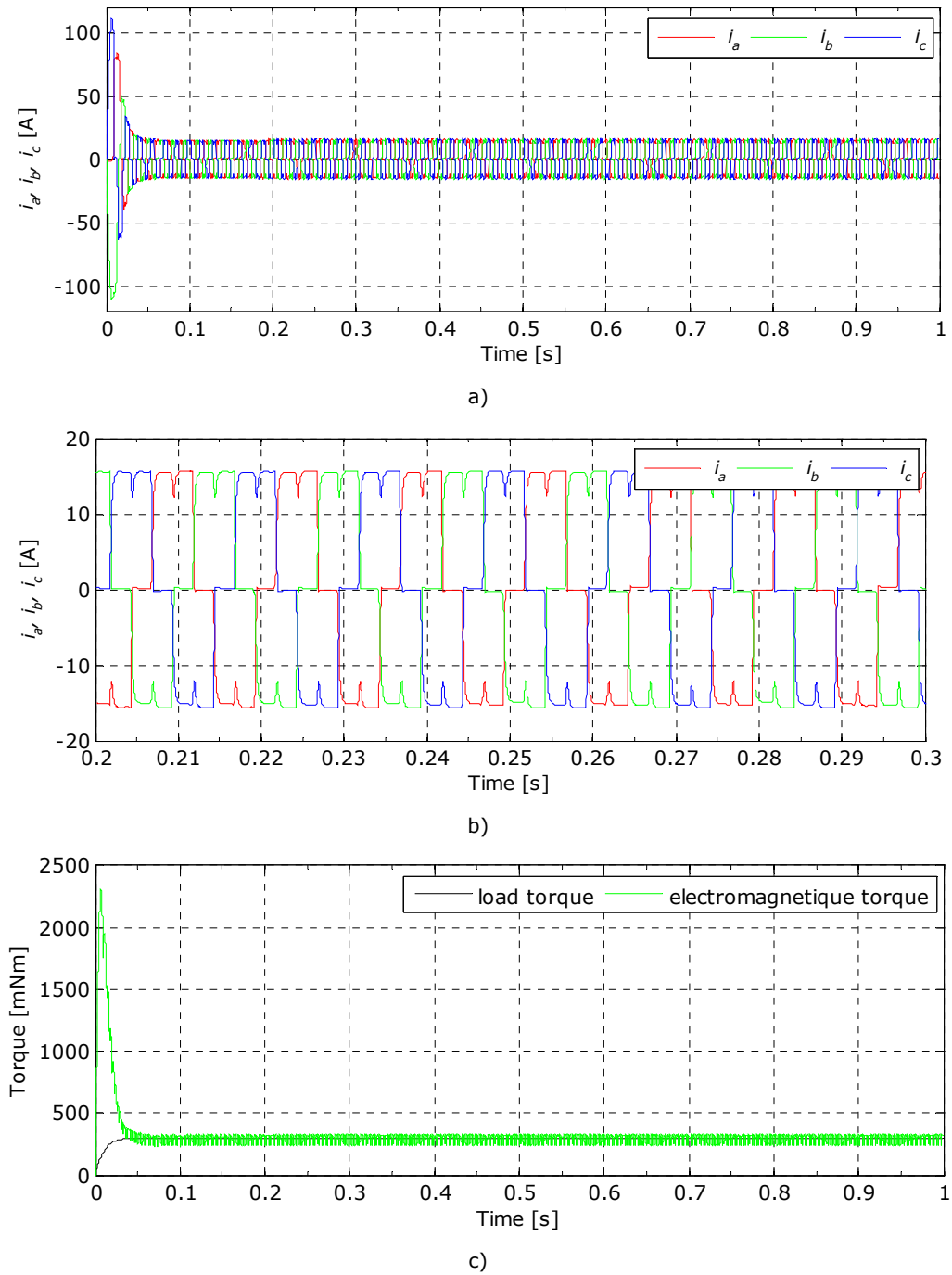


Fig. 4.23. (continued).

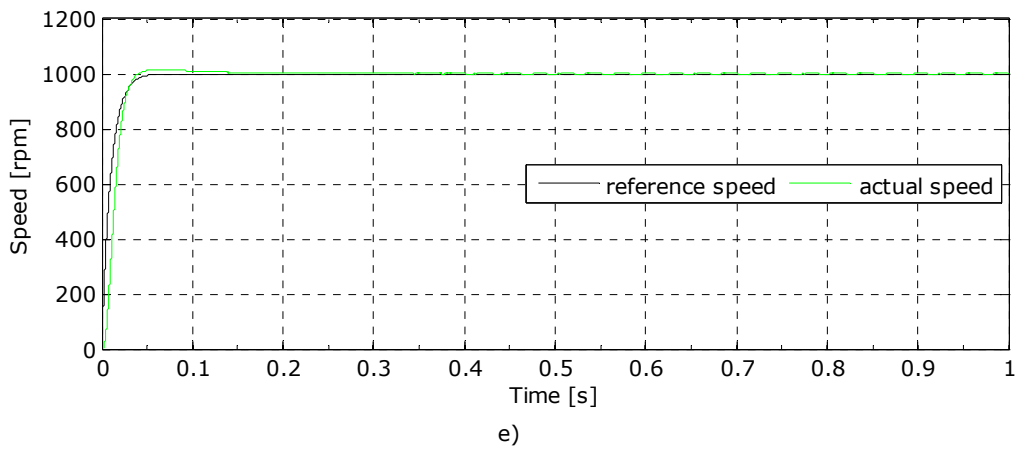
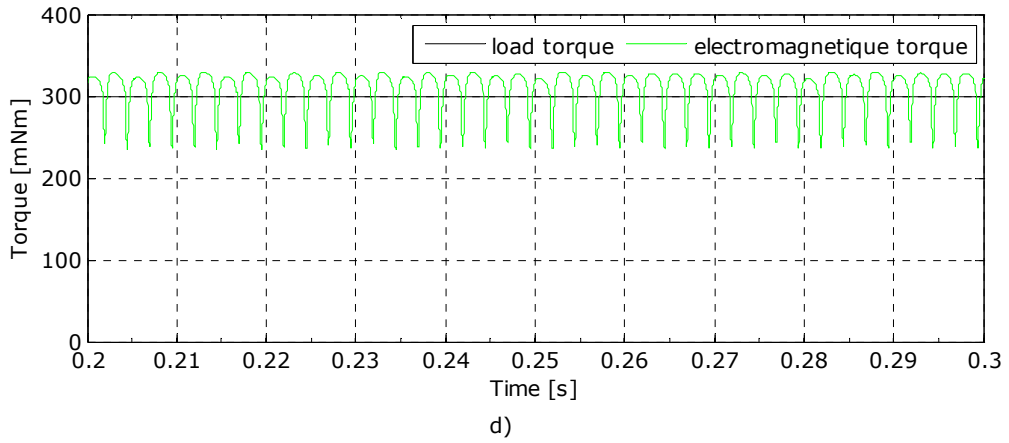


Fig. 4.23. 1000 rpm and 0.3 Nm, with closed-loop control: a) phase currents, b) phase currents (zoom in), c) torque, d) torque (zoom in), e) actual speed.

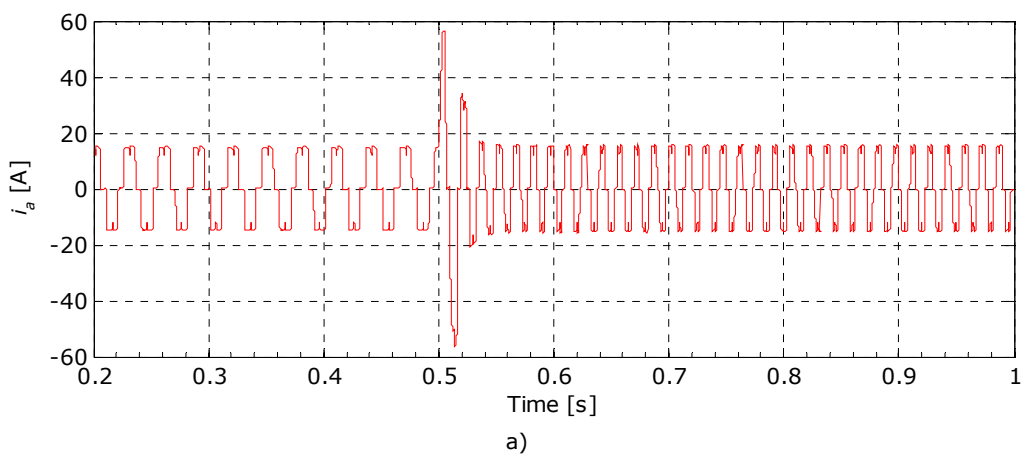


Fig. 4.24. (continued).

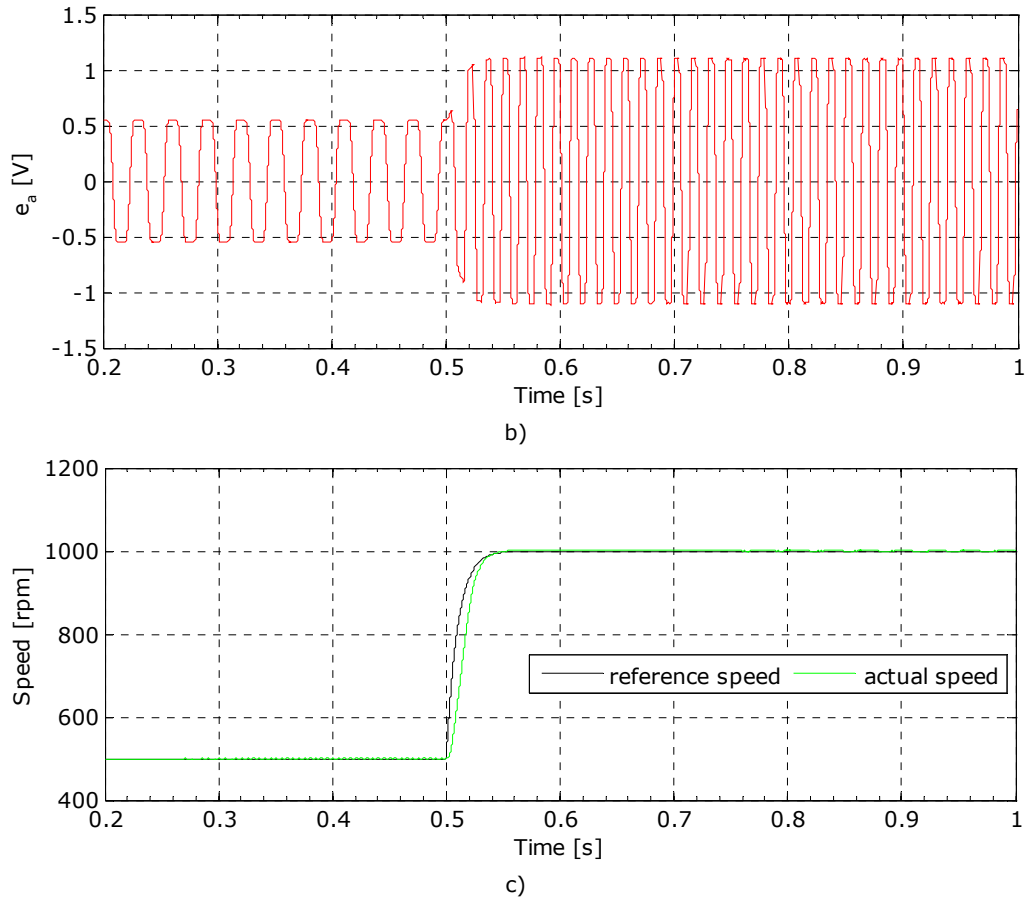


Fig. 4.24. Acceleration from 500 to 1000 rpm, and 0.3 Nm: a) phase A current, b) phase A back-EMF, c) actual speed.

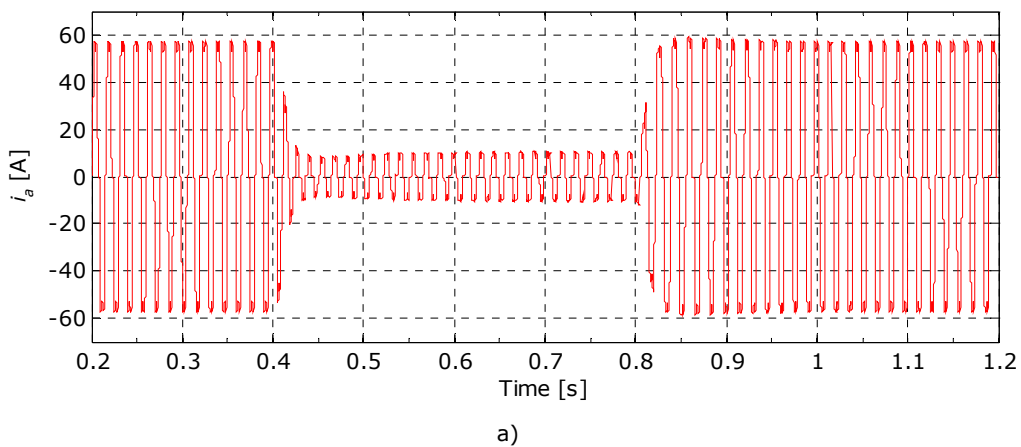
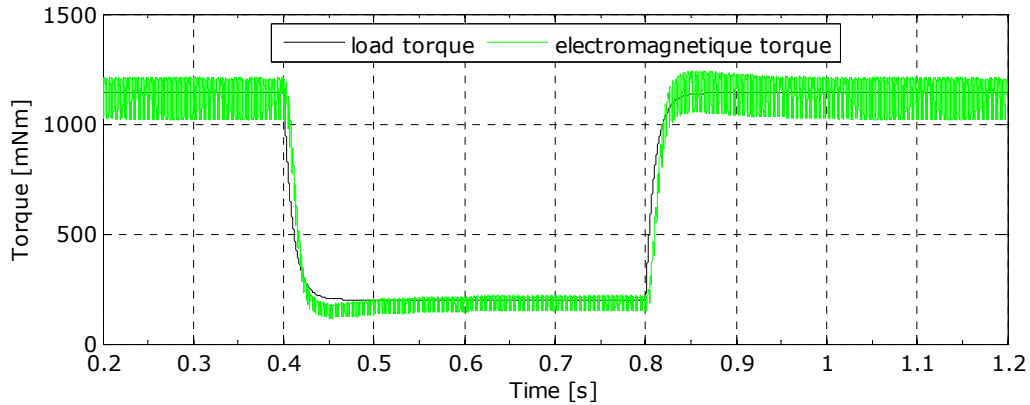
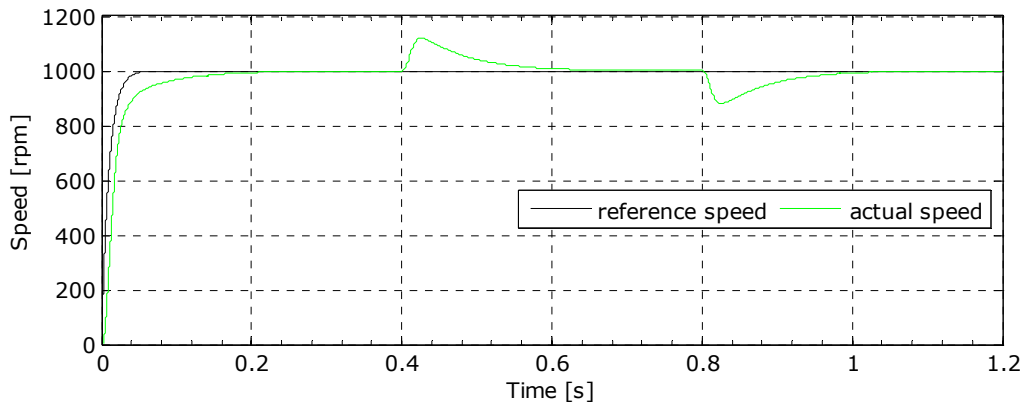


Fig. 4.25. (continued).



b)



c)

Fig. 4.25. Load change from 1.14 Nm to 0.3 Nm at 0.4 s and back to 1.14 Nm at 0.8 s: a) phase A current, b) torque, c) actual speed.

4.7. Conclusion

In this chapter an advanced simulation model for BLDC motor drives is presented, and the performance and feasibilities have been examined by simulation verification. From the investigation of the developed simulation model, it is expected that the dynamic characteristics as well as the steady state can be effectively monitored and predicted. This model was implemented under Simulink environment. In order to maintain the accuracy of the proposed model the back-EMF and the inductances were modeled through Fourier series, and respectively through look-up table, based on FEM calculations of the BLDC IPM motor from Chapter 3. The proposed model can be used effectively in analysis and design of control algorithms of the BLDC motor drive system.

References

- [1] W. Hong, W. Lee, B.-K. Lee, "Dynamic Simulation of Brushless DC Motor Drives Considering Phase Commutation for Automotive Applications", *IEMDC'07*, Vol. 2, pp. 1377-1383, May 2007.
- [2] B.-K. Lee and M. Ehsani, "Advanced Simulation Model for Brushless DC Motor Drives", *EMP 31(9), Electric Power Components and Systems*, Taylor and Francis Group, 2003.
- [3] P. Pillay and R. Krishnan, "Modeling, Simulation, and Analysis of Permanent-Magnet Motor Drives, Part II: The Brushless DC Motor Drive", *IEEE Trans. on Industry Applications*, Vol. 25, No. 2, pp. 274-279, March/April 1989.
- [4] R. Carlson, M. Lajoie-Mazenc, C. dos S. Fagundes, "Analysis of Torque Ripple Due to Phase Commutation in Brushless DC Machines", *IEEE Trans. On Industry Applications*, Vol. 28, No. 3, pp. 632-638, May/June 1992.
- [5] P.D. Evans and D. Brown, "Simulation of Brushless DC Drives", *Proc. of the IEE*, Vol. 137, No. 5, pp. 299-308, September 1990.
- [6] Q. Han, N. Samoylenko, J. Jatskevich, "Average-Value Modeling of Brushless DC Motors With 120° Voltage Source Inverter", *IEEE Trans. on Energy Conversion*, Vol. 23, No. 2, pp. 423-432, June 2008.
- [7] H.A. Toliyat and T. Gopalarathnam, "AC Machines Controlled as DC Machines (Brushless DC Machines/Electronics)", Chapter 10 in "The Power Electronics Handbook", J.D. Irwin, CRC Press LLC, Boca Raton, FL, 2002.
- [8] S.K. Safi, P.P. Acarnley, A.G. Jack, "Analysis and Simulation of the High-Speed Torque Performance of Brushless DC Motor Drives", *IEE Proceedings Electric Power Applications*, Vol. 142, No. 3, pp. 191-200, May 1995.
- [9] O.A. Mohammed, S. Liu, Z. Liu, "A Phase Variable Model of Brushless DC Motors Based on Finite Element Analysis and Its Coupling With External Circuits", *IEEE Trans. on Magnetics*, Vol. 41, No. 5, pp. 1576-1579, May 2005.
- [10] Y.S. Jeon, H.S. Mok, G.H. Choe, D.K. Kim, J.S. Ryu, "A New Simulation Model of BLDC Motor With Real Back EMF Waveform", *IEEE CNF. on Computers in Power Electronics, COMPEL 2000*, pp. 217-220, July 2000.
- [11] G.H. Jang, J.H. Chang, D.P. Hong, K.S. Kim, "Finite-Element Analysis of an Electromechanical Field of a BLDC Motor Considering Speed Control and Mechanical Flexibility", *IEEE Trans. on Magnetics*, Vol. 38, No. 2, pp. 945-948, March 2002.
- [12] T.J.E. Miller, "SPEED's Electric Motors", Glasgow, 2002.
- [13] J.F. Gieras, "Permanent Magnet Motor Technology, Design and Applications", 3rd ed., CRC Press, Taylor and Francis Group, Boca Raton, FL, 2010.
- [14] M.A. Alhamadi and N.A. Demerdash, "Modeling and Experimental Verification of the Performance of a Skew Mounted Permanent Magnet Brushless DC Motor Drive with Parameters Computed From 3D-FE Magnetic Field Solutions", *IEEE Trans. on Energy Conversion*, Vol. 9, No. 1, pp. 26-35, March 1994.

-
- [15] I. Boldea and S.A. Nasar, "Electric Drives", 2nd ed., CRC Press, Taylor and Francis Group, Boca Raton, FL, 2006.
- [16] A. Ştirban, I. Boldea, G.-D. Andreescu, D. Iles, F. Blaabjerg, "FEM Assisted Position and Speed Observer for BLDC PM Motor Drive Sensorless Control, With Experiments", *EPE-PEMC 2010*, September 2010.
- [17] H. Zeroug, B. Boukais, H. Sahraoui, "Analysis of Torque Ripple in a BDCM", *IEEE Trans. on Magnetics*, Vol. 38, No. 2, pp. 1293-1296, March 2002.
- [18] S. Baldursson, "BLDC Motor Modeling and Control – A Matlab®/Simulink® Implementation", Master Thesis, Göteborg, Sweden, May 2005.
- [19] H. Lu, L. Zhang, W. Qu, "A New Torque Control Method for Torque Ripple Minimization of BLDC Motors With Un-Ideal Back EMF", *IEEE Trans. on Power Electronics*, Vol. 23, No. 2, pp. 950-958, March 2008.
- [20] P.C. Desai and A. Emadi, "A Novel Digital Control Technique for Brushless DC Motor Drives: Current Control", *IEMDC 2005*, pp. 326-331, 2005.
- [21] Z. Li, S. Cheng, Y. Qin, K. Cai, "A Novel Line-to-line Back EMF Calculation for Sensorless Brushless DC Motor Drives", *ICEMS 2008*, pp. 1406-1411, 2008.
- [22] J.S. Mayer and O. Wasynczuk, "Analysis and Modeling of A Single-Phase Brushless DC Motor Drive System", *IEEE Trans. on Energy Conversion*, Vol. 4, No. 3, pp. 473-479, Sept. 1989.
- [23] K.A. Corzine and H.J. Hegner, "Analysis of a Current-Regulated Brushless DC Drive", *IEEE Trans. on Energy Conversion*, Vol. 10, No. 3, pp. 438-445, Sept. 1995.
- [24] L. Hao and H.A. Toliyat, "BLDC Motor Full Speed Range Operation Including the Flux-Weakening Region", *38th IAS Annual Meeting*, Vol. 1, pp. 618-624, 2003.
- [25] C.-H. Won, J.-H. Song, I. Choy, "Commutation Torque Ripple Reduction in Brushless DC Motor Drives Using a Single DC Current Sensor", *IEEE Trans. on Power Electronics*, Vol. 19, No. 2, pp. 312-319, March 2004.
- [26] C.C. Chan, J.Z. Jiang, G.H. Chen, K.T. Chau, "Computer Simulation and Analysis of a New Polyphase Multipole Motor Drive", *IEEE Trans. on Industrial Electronics*, Vol. 40, No. 6, pp. 570-576, Dec. 1993.
- [27] O. Wallmark, "Control of Permanent-Magnet Synchronous Machines in Automotive Applications", PhD Thesis, Göteborg, Sweden, 2006.
- [28] J. Wiberg, "Controlling a Brushless DC Motor in a Shift-by-Wire System", Master Thesis, Linköpings University, Dec. 2003.
- [29] S.B. Ozturk and H.A. Toliyat, "Direct Torque Control of Brushless DC Motor with Non-Sinusoidal Back-EMF", *IEMDC'07*, pp. 165-171, 2007.
- [30] T.-Y. Kim, B.-K. Lee, C.-Y. Won, "Modeling and Simulation of Multiphase BLDC Motor Drive Systems for Autonomous Underwater Vehicles", *IEMDC'07*, pp. 1366-1371, 2007.
- [31] A.S.O. Al-Mashakbeh, "Proportional Integral and Derivative Control of Brushless DC Motor", *European Journal of Scientific Research*, Vol. 35, No. 2, pp. 198-203, 2009.

- [32] H. Guo, B. Zhou, J. Li, F. Cheng, L. Zhang, "Real-Time Simulation of BLDC-based Wind Turbine Emulator Using RT-LAB", *ICEMS 2009*, pp. 1-6, 2009.
- [33] K.-Y. Nam, W.-T. Lee, C.-M. Lee, J.-P. Hong, "Reducing Torque Ripple of Brushless DC Motor by Varying Input Voltage", *IEEE Trans. on Magnetics*, Vol. 42, No. 4, pp. 1307-1310, April 2006.
- [34] J. Faiz, M.R. Azizian, M. Aboulghasemian-Azami, "Simulation and Analysis of Brushless DC Motor Drives Using Hysteresis, Ramp Comparison and Predictive Current Control Techniques", *Simulation Practice and Theory*, Vol. 3, No. 6, pp. 347-363, Jan. 1996.
- [35] L. Deng, P. Liu, Q. Fu, Q. Zheng, H. Liu, "Study on Commutation for Permanent Magnet Brushless DC Motor", *WAC 2008*, pp. 1-4, 2008.
- [36] A. Lidozzi, L. Solero, F. Crescimbeni, R. Burgos, "Vector Control of Trapezoidal Back-EMF PM Machines Using Pseudo-Park Transformation", *PESC 2008*, pp. 2167-2171, 2008.
- [37] L. Ying and N. Ertugrul, "The Dynamic Simulation of the Three-Phase Brushless Permanent Magnet AC Motor Drives with LabVIEW", *AUPEC/ECON*, Darwin, Australia, Sept. 1999.

Chapter 5

Observers for sensorless control of BLDC PM motor drive, with experiments

Abstract

This chapter proposes and investigates a FEM assisted position and speed observer for brushless DC PM motor drive sensorless control, based on the line-to-line PM flux linkage estimation. The line-to-line PM flux may be estimated using measured currents and line-to-line voltages. The zero-crossing of the line-to-line PM flux linkage occurs right in the middle of two commutation points. The time period from one commutation point to zero-crossing is equal with the time period from zero-crossing to the next commutation point, at constant or slowly varying speed. This is used as a basis for the position and speed observer. For performance applications, the position between commutation points is obtained by comparing the estimated line-to-line PM flux with a look-up table, which contains the position versus FEM calculated line-to-line PM flux. A simulation model and experimental results are shown, demonstrating the reliability of FEM assisted position and speed observer for BLDC PM motor.

5.1. Introduction

Brushless DC permanent magnet (BLDC PM) motors are often considered proper candidates in various industrial applications. This motor requires rectangular stator currents to produce rather constant (low ripple) torque. The rotor position is used to manage the switching of the supply voltage to the phases of the stator, in correct sequence by a control circuit. The control system requires position information from a rotor position sensor or Hall sensors [1], to perform the commutation process. However, sensing the position of the rotor is a drawback for this type of machine, because the presence of the sensor is increasing the system cost and machine size. These disadvantages can be eliminated or reduced with shaft position sensorless operation.

For BLDC PM motors various methods for obtaining rotor position and speed have been proposed in the literature [2-12]. One method, the back-EMF sensing technique (1) [4-8], is a scheme estimating the rotor position indirectly by using the zero-crossing point detection of open phase's terminal voltage. It is the most commonly used sensorless control method for this type of machine, and has been improved for a wide range speed [7]. Other sensorless methods are: back-EMF integration techniques (2); flux linkage-based technique (3) [9]; and freewheeling diode conduction (4) [10]. All mentioned methods have advantages (easy implementation and low computational burden) as well as disadvantages (need of an external hardware circuitry (1, 2, and 4), error accumulation problem at low speeds (2, and 3), position error in transient state (1, and 4)).

Ref. [11], with improvements [12], introduces a sensorless position detection technique based on a speed-independent position function for BLDC motors, which proves good reliability in a wide speed range. Ref. [13] proposes the calculation of the commutation instants based on the slope variations of the common dc current I_{MAX} , which is obtained taking the absolute values of two of the three phase currents. This last technique introduces unavoidable delay in the switching status at higher frequencies.

This chapter proposes and investigates a FEM assisted position and speed observer for brushless DC PM motor drive sensorless control, based on the line-to-line PM flux linkage. Using measured phase currents and line-to-line voltages that are calculated by multiplication of the DC bus voltage by switching status, which are known in the controller, the line-to-line PM flux linkage can be estimated. The zero-crossing of the line-to-line PM flux linkage occurs right in the middle of two commutations points. At constant or slowly varying speed, the time period from one commutation point to zero-crossing and the time period from zero-crossing to the next commutation point are equal to each other. This is used as a basis for the position and speed observer.

Since the shape of line-to-line PM flux is identical at all speeds, it provides rather precise commutation points. The proposed method doesn't need external hardware circuitry for sensing terminal voltages. For BLDC PM motors, where the objective is to achieve quasi-square current waveforms, it is only required to know the position of commutation points. But, for special purpose control strategies (e.g. advance angle control for the field weakening operation), the position between commutation points is obtained by comparing the estimated line-to-line PM flux linkage with a look-up table, which contains the position versus line-to-line PM flux linkage, calculated for a BLDC PM motor using a 2D Finite Element Method (FEM). A simulation model for the FEM assisted position and speed observer for BLDC PM motor sensorless control has been developed for validation, and experimental results are shown, demonstrating the reliability of this observer.

5.2. Commutation strategy and FEM assisted position observer

The general line-to-line voltage equations are used as follows

$$\begin{bmatrix} V_{ab} \\ V_{bc} \\ V_{ca} \end{bmatrix} = K \cdot \begin{bmatrix} R_s & 0 & 0 \\ 0 & R_s & 0 \\ 0 & 0 & R_s \end{bmatrix} \begin{bmatrix} i_a \\ i_b \\ i_c \end{bmatrix} + \frac{d}{dt} \left(K \cdot \begin{bmatrix} L_{aa} & L_{ab} & L_{ac} \\ L_{ba} & L_{bb} & L_{bc} \\ L_{ca} & L_{cb} & L_{cc} \end{bmatrix} \begin{bmatrix} i_a \\ i_b \\ i_c \end{bmatrix} \right) + \begin{bmatrix} e_{ab} \\ e_{bc} \\ e_{ca} \end{bmatrix} \quad (5.1)$$

where K is the matrix transformation from phase quantities to line-to-line quantities, and it has the following form

$$K = \begin{bmatrix} 1 & -1 & 0 \\ 0 & 1 & -1 \\ -1 & 0 & 1 \end{bmatrix} \quad (5.2)$$

From (5.1) and knowing the fact that the line-to-line back EMF is the line-to-line PM flux linkage derivative, the line-to-line PM flux linkages can be evaluated in the following form:

$$\begin{bmatrix} \lambda_{PMab} \\ \lambda_{PMbc} \\ \lambda_{PMca} \end{bmatrix} = -\int_0^t \left\{ \begin{bmatrix} V_{ab} \\ V_{bc} \\ V_{ca} \end{bmatrix} - K \cdot \begin{bmatrix} R_s & 0 & 0 \\ 0 & R_s & 0 \\ 0 & 0 & R_s \end{bmatrix} \begin{bmatrix} i_a \\ i_b \\ i_c \end{bmatrix} \right\} d\tau + K \cdot \begin{bmatrix} L_{aa} & L_{ab} & L_{ac} \\ L_{ba} & L_{bb} & L_{bc} \\ L_{ca} & L_{cb} & L_{cc} \end{bmatrix} \begin{bmatrix} i_a \\ i_b \\ i_c \end{bmatrix} \quad (5.3)$$

The dependence of machine inductances on currents has been thoroughly treated in Chapter 3; here, however, for control design, approximated constant values are considered.

Direct measurement of the phase currents and calculation of the line-to-line voltages, by multiplication of the DC bus voltage and switching status, can allow the estimation of the line-to-line PM flux linkages. From these line-to-line PM flux linkages, the position of the rotor can be estimated, as explained in what follows.

Fig. 5.1 shows the back-EMFs, phase currents, line-to-line PM flux linkages of the BLDC PM motor from [14], and the detection of the zero crossings of the PM line-to-line flux linkages.

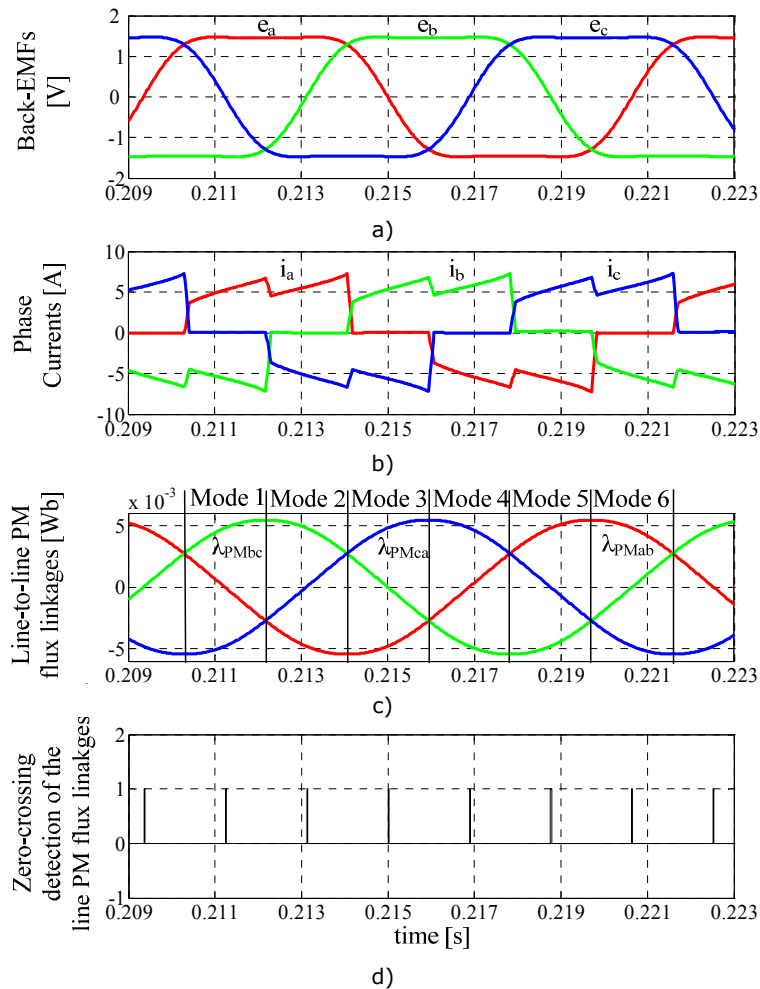


Fig. 5.1. Basis of the sensorless operation of the BLDC PM: a) back-EMFs; b) phase currents; c) line-to-line PM flux linkages; d) zero-crossing detection of the line-to-line PM flux linkages.

As can be seen from Fig. 5.1, the zero-crossings of the line-to-line PM flux linkages occur right in the middle of two commutations points. At constant or slowly varying speed, the time period from one commutation point to zero-crossing and the time period from zero-crossing to the next commutation point are equal to each other. This is used as a basis for the implementation of the position and speed sensorless observer.

In each mode (sector) only two of the three phases are conducting at any time, leaving the third floating phase open. The phase voltage in the floating phase is unknown by the controller, being equal with the back-EMF. From Eq. (5.3), it is obvious that only one line-to-line PM flux linkage can be estimated correctly in each mode: this is the PM flux linkage between the two active phases. Based on this idea, in each mode the proper estimated line-to-line PM flux linkage can be used to detect the zero-crossing, and then a delay of 30° is applied to switch-on the current in the corresponding phases (next commutation point). After commutation is produced, a new couple of phases will be conducting, and the corresponding line-to-line PM flux linkage will give the information for the next commutation.

Table I shows the proper line-to-line PM flux linkage at each mode.

Table 5.1. Line-to-line PM flux linkages at each mode

	Positive speed
Mode 1 and 4	λ_{PMab}
Mode 2 and 5	λ_{PMca}
Mode 3 and 6	λ_{PMbc}

The line-to-line PM flux linkage estimator (Fig. 5.2) based on the voltage model in stator reference frame, employs an equivalent integrator in close-loop, with a speed-adaptive proportional controller to compensate the dc offset and phase-delay. The transfer function of this equivalent integrator is:

$$H(s) = \frac{T_i}{1+s \cdot T_i}; \quad T_i = \frac{1}{\omega_0} \tag{5.4}$$

where ω_0 is the corner frequency.

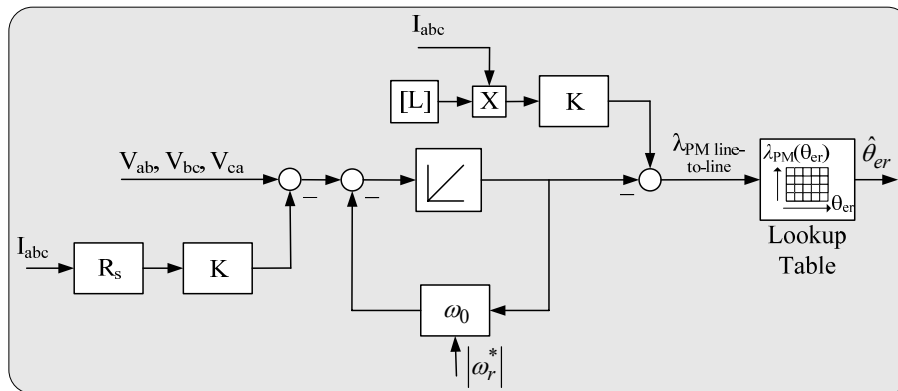


Fig. 5.2. Line-to-line PM flux estimator (K is from Eq. (5.2)).

For BLDC PM motor general drives, where the objective is just to achieve quasi-square current waveforms, knowing of the position of commutation points suffices. But, for special purpose drives, with advance angle control for the field weakening operation, the position between commutation points can be obtained by comparing the estimated line-to-line PM flux linkage with a look-up table, which contains the position versus characterized line-to-line PM flux linkage. This PM flux linkage can be calculated by using FEM-method [14], if the motor was designed using this method, or measured by running the machine as a generator with opened phases at constant speed. The line voltage signals are recorded and by integrating these voltages, the line-to-line PM flux linkages can be calculated. The position between commutation points can be estimated because the corresponding line-to-line PM flux linkage at each mode is either increasing or decreasing.

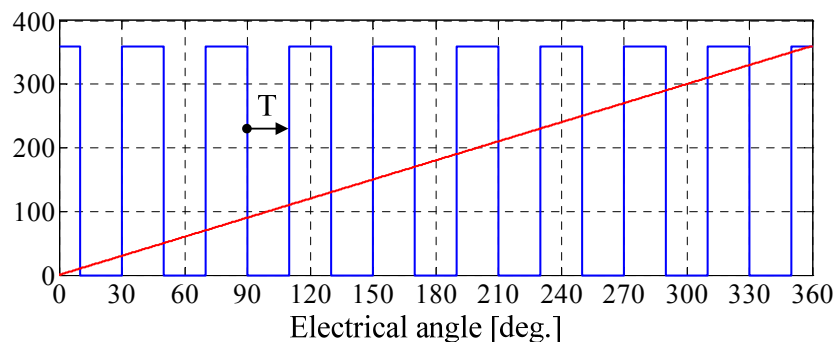
5.3. Speed observers

With no sensors available, the speed must be calculated (for speed feedback) using information from the commutation controller. From the estimated position, pulses can be generated (e.g.: at every 20° electrical angles) (Fig. 5.3a). The time between two edges of the pulse is used to calculate the rotational speed. At every edge, a new speed measurement is available, and between two edges the speed is kept at the old value. The speed has the expression:

$$\omega = \frac{2 \cdot \pi}{T \cdot nb_{edges}} \quad (5.5)$$

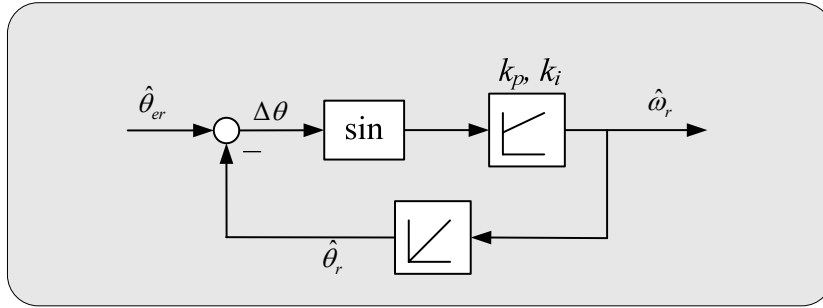
where nb_{edges} is the number of edges (from Fig. 5.3a were pulses are generated at every 20° , $nb_{edges} = 18$).

Another solution to estimate the speed is to use a PLL structure (Fig. 5.3b), having the estimated position as input (the PI gains have the following values: $K_p = 110$ [rpm/rad], $K_i = 3025$ [1/s]).



a)

Fig. 5.3. (continued).



b)

Fig. 5.3. Proposed speed observers: a) speed observer based on pulse edges, b) equivalent PLL state-observer structure.

From the mechanical model an observer can be constructed [15, 16]. The mechanical model of the drive is approximated as:

$$\frac{d}{dt} \begin{bmatrix} \theta_e \\ \omega_e \\ T_L \end{bmatrix} = \begin{bmatrix} 0 & 1 & 0 \\ 0 & 0 & -p_1/J \\ 0 & 0 & 0 \end{bmatrix} \cdot \begin{bmatrix} \theta_e \\ \omega_e \\ T_L \end{bmatrix} + \begin{bmatrix} 0 \\ p_1/J \\ 0 \end{bmatrix} \cdot T_e \quad (5.6)$$

where θ_e is the rotor position, ω_e is the rotor electrical speed and the load torque T_L was assumed constant.

The electromagnetic torque T_e is regarded as known input and is calculated by the following equation:

$$T_e = \frac{e_a \cdot i_a + e_b \cdot i_b + e_c \cdot i_c}{\omega_m} = k_{Ea} \cdot i_a + k_{Eb} \cdot i_b + k_{Ec} \cdot i_c \quad (5.7)$$

The observer is:

$$\frac{d}{dt} \begin{bmatrix} \hat{\theta}_{er} \\ \hat{\omega}_r \\ \hat{T}_L \end{bmatrix} = \begin{bmatrix} 0 & 1 & 0 \\ 0 & 0 & -p_1/J \\ 0 & 0 & 0 \end{bmatrix} \cdot \begin{bmatrix} \hat{\theta}_{er} \\ \hat{\omega}_r \\ \hat{T}_L \end{bmatrix} + \begin{bmatrix} 0 \\ p_1/J \\ 0 \end{bmatrix} \cdot \hat{T}_e + \begin{bmatrix} k_1 \\ k_2 \\ k_3 \end{bmatrix} \cdot \varepsilon \quad (5.8)$$

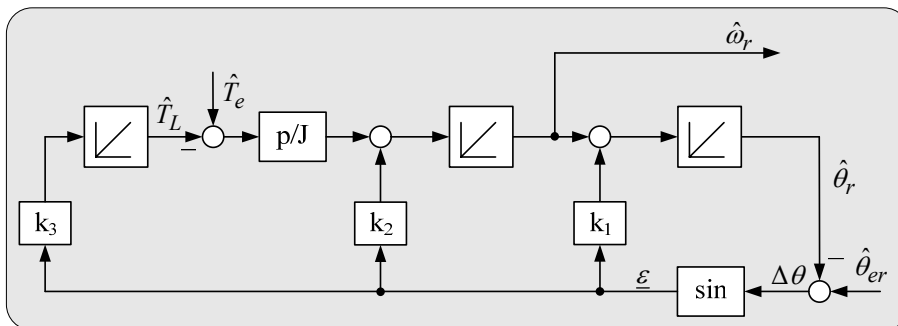


Fig. 5.4. Equivalent PLL state-observer structure.

The PLL observer error is:

$$\varepsilon = \sin(\hat{\theta}_{er} - \hat{\theta}_r) = \sin(\hat{\theta}_{er}) \cdot \cos(\hat{\theta}_r) - \cos(\hat{\theta}_{er}) \cdot \sin(\hat{\theta}_r) \quad (5.9)$$

The PLL speed observer block diagram is shown in Fig. 5.4. This observer estimates the rotor speed and the load torque. However, the load torque estimation is poor [15].

The observer gains are determined by pole placement method [15]. Let p_1 , p_2 , and p_3 be the observer poles, allocated such that the observer is fast and stable. In this case, the observer gains are:

$$k_1 = -S, \quad k_2 = SP_2, \quad k_3 = \frac{J}{p_1} \cdot P \quad (5.10)$$

where: $S = p_1 + p_2 + p_3$, $SP_2 = p_1 \cdot p_2 + p_2 \cdot p_3 + p_3 \cdot p_1$, $P = p_1 \cdot p_2 \cdot p_3$.

Gain values are limited only by noise consideration. If the noise level is small, it is possible to select all three poles real, negative. However, for better dynamics, two of them can be selected complex conjugates with not too large imaginary parts (the observer gains have the following values: $K_1 = 120$ [rpm], $K_2 = 4400$ [rpm/s], $K_3 = -3.68$ [N/s]).

All three speed estimation techniques were implemented. Sample results are shown in the next sections only with the first speed estimator.

5.4. Simulation results

The FEM assisted position and speed observer, for brushless DC PM motor drive sensorless control, have been verified through digital simulation. A BLDC PM motor model was implemented in Matlab/Simulink, using the general equations of a brushless DC PM motor (Chapter 4). In the implementation the phase commutation phenomenon was considered [17].

Fig. 5.5 illustrates the performance of the proposed FEM assisted position and speed observer at 500 rpm, loaded at 0.1 Nm. The phase currents are controlled by a PI controller. The commutation points, from Fig. 5.5b, represent in fact, the zero-crossing detection of the line-to-line PM flux linkages, delayed with 30°.

In order to obtain accurate and efficient simulation [18], the back-EMF and the inductances (IPM rotor) were modeled through Fourier series, and respectively through look-up tables, based on FEM calculation of the BLDC IPM motor.

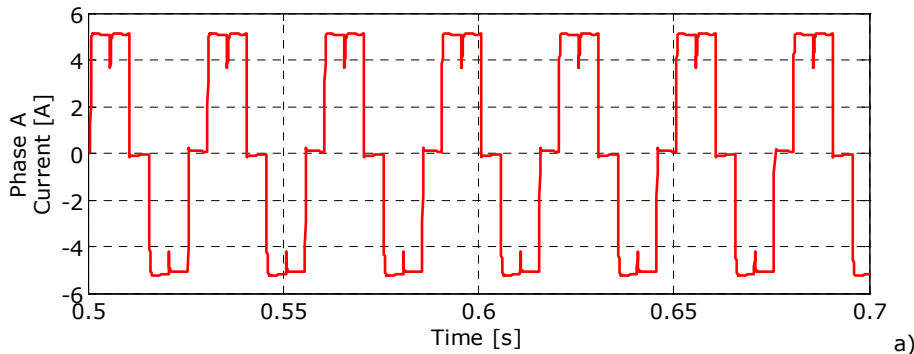


Fig. 5.5. (continued).

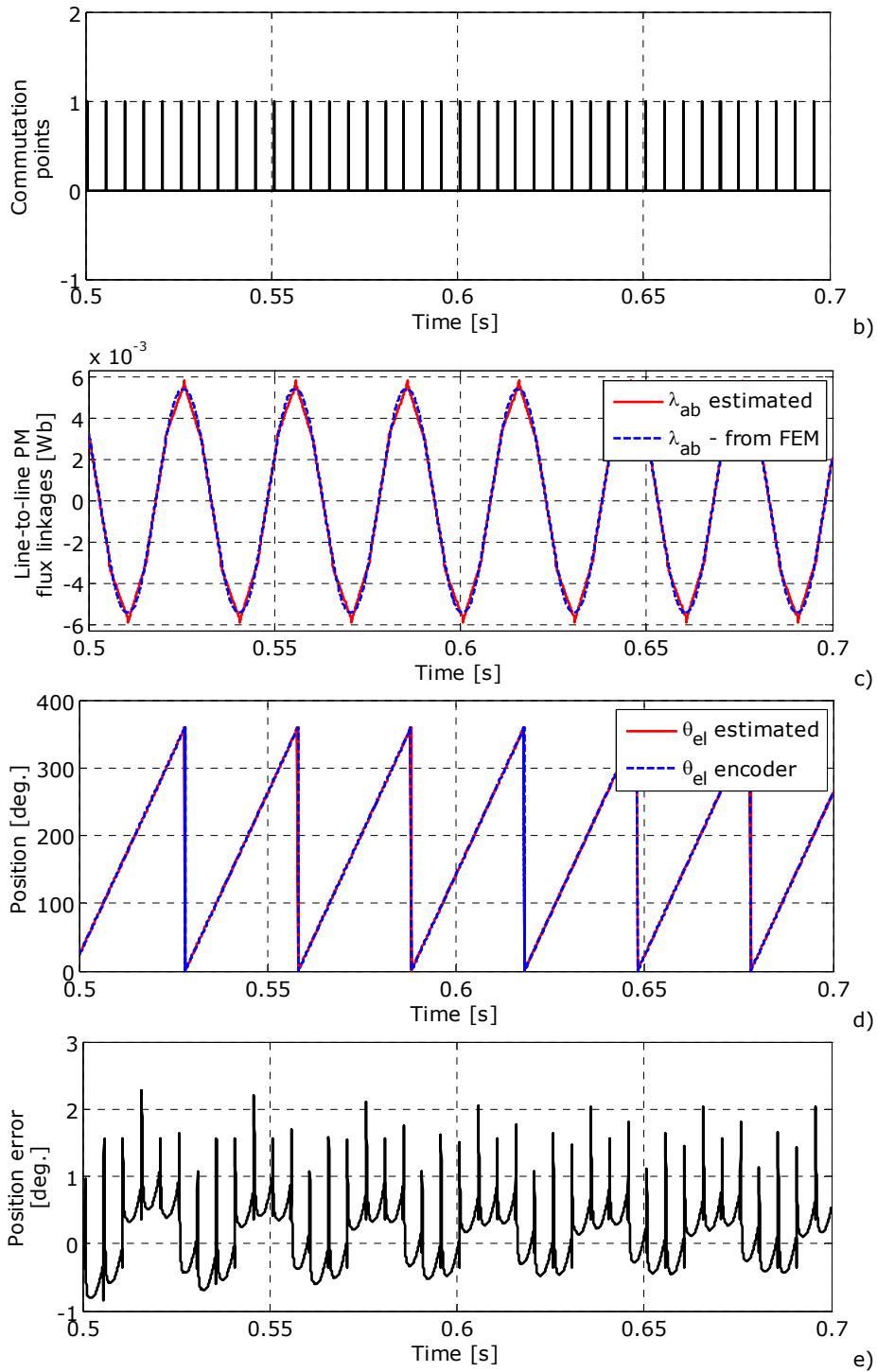


Fig. 5.5. (continued).

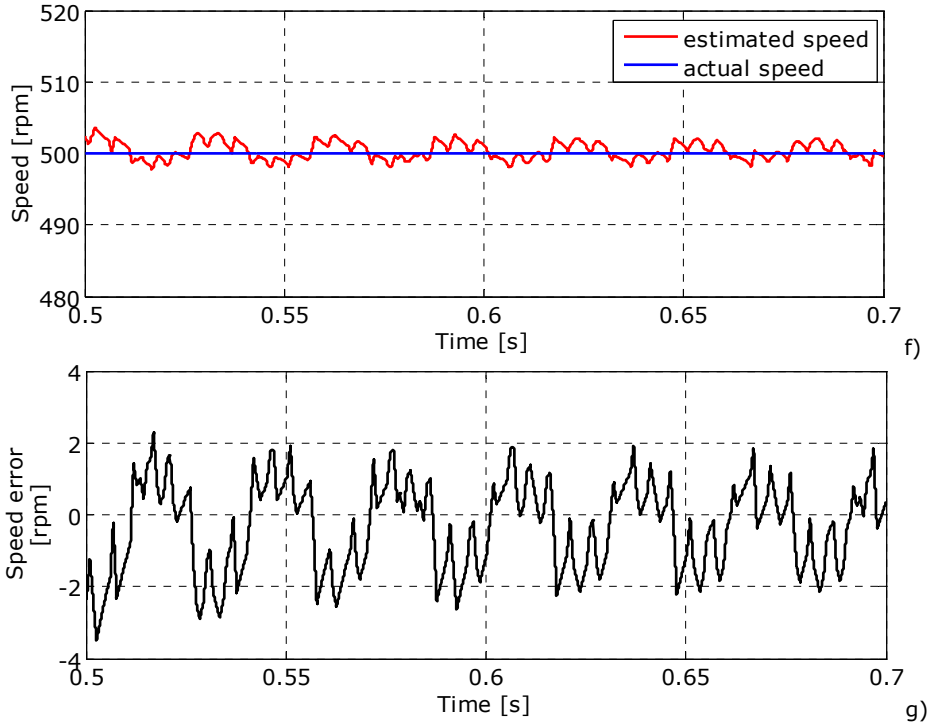


Fig. 5.5. Simulation results of the proposed position and speed FEM assisted observer at 500 rpm and 0.1 Nm load: a) phase A current; b) observer commutation points; c) line-to-line PM flux linkage; d) position; e) position error; f) speed; and g) speed error.

Fig. 5.6 shows the performance of the FEM assisted observer at 1000 rpm, loaded at 0.15 Nm. The numerical simulations demonstrate the reliability of this observer. Next, experimental results are presented, in order to validate the FEM assisted position and speed observer in real-time applications.

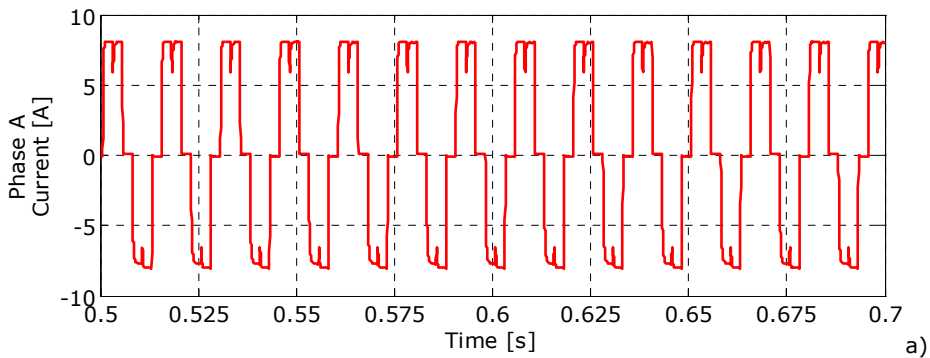


Fig. 5.6. (continued).

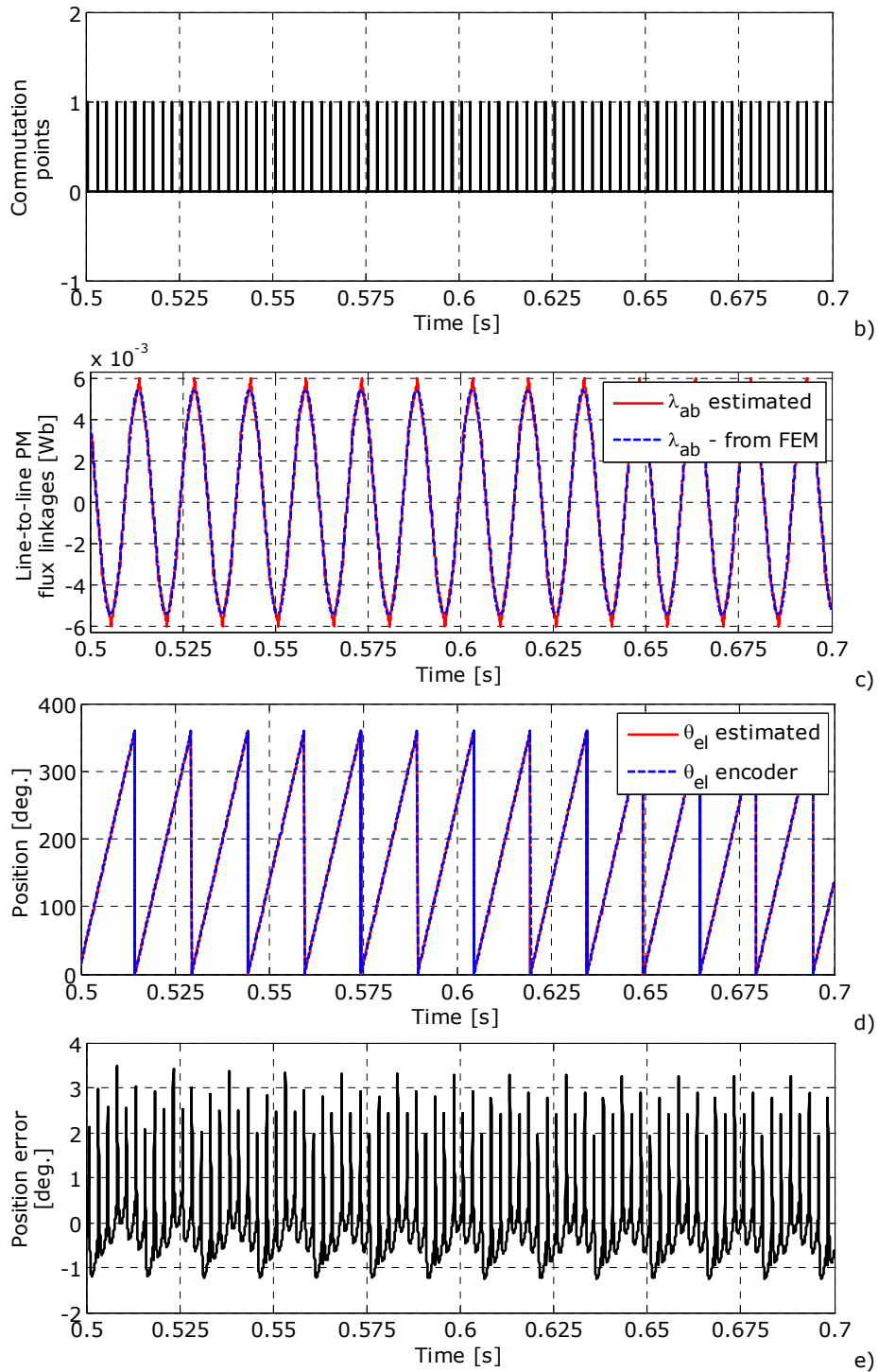


Fig. 5.6. (continued).

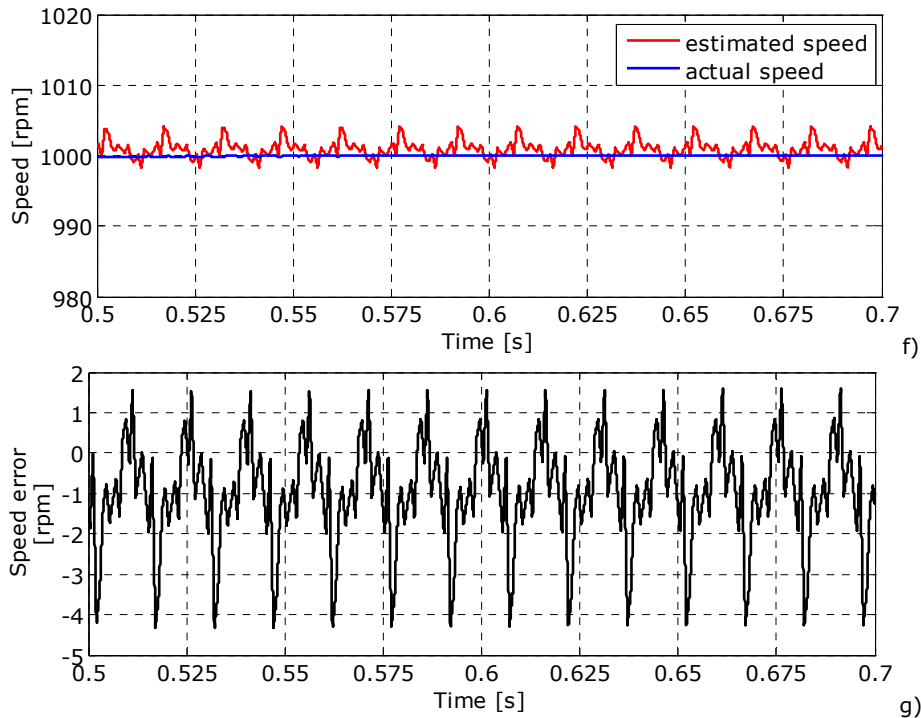


Fig. 5.6. Simulation results of the proposed position and speed FEM assisted observer at 1000 rpm and 0.15 Nm load: a) phase A current; b) observer commutation points; c) line-to-line PM flux linkage; d) position; e) position error; f) speed; and g) speed error.

5.5. Experimental results

The experimental setup consists of BLDC IPM motor, with the parameters as in the simulations, loaded with an interior permanent magnet synchronous generator. The dSpace CLP1103 platform is used to control the entire drive system.

Fig. 5.7 shows an overall system block diagram of the proposed sensorless drive. In this experiment, the line-to-line voltages are calculated by multiplication of the DC bus voltage by switching status, which are known in the controller. The proportional-integral (PI) speed and current controllers employed in the real-time control are tuned using Ziegler-Nichols method, with the following gains: $K_{p_w} = 0.008$ [A/rpm], $K_{i_w} = 1.5$ [1/s], $K_{a_w} = 10$, $K_{p_{is}} = 0.2$ [V/A], $K_{i_{is}} = 90$ [1/s]. These gains are close to those used in the simulation model (in Chapter 4). The small differences are caused by some inexactitudes between the parameters used in the simulation model and the real motor parameters.

Experimental results include: constant speed operation (Fig. 5.8), acceleration (Fig. 5.9), deceleration (Fig. 5.10), and step change of load (Fig. 5.11) [19].

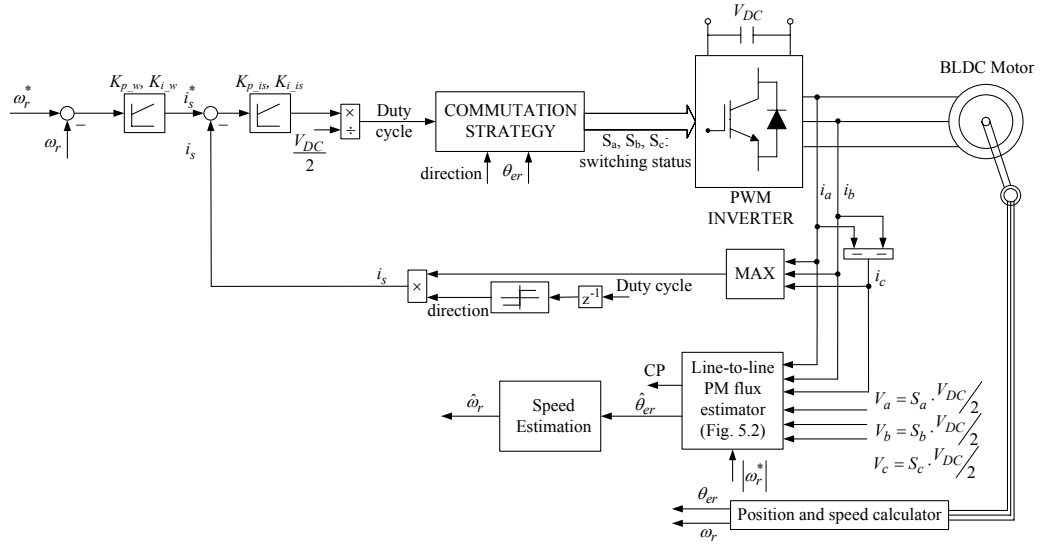


Fig. 5.7. Overall system block diagram used for testing FEM assisted position and speed observer for BLDC PM drive sensorless control.

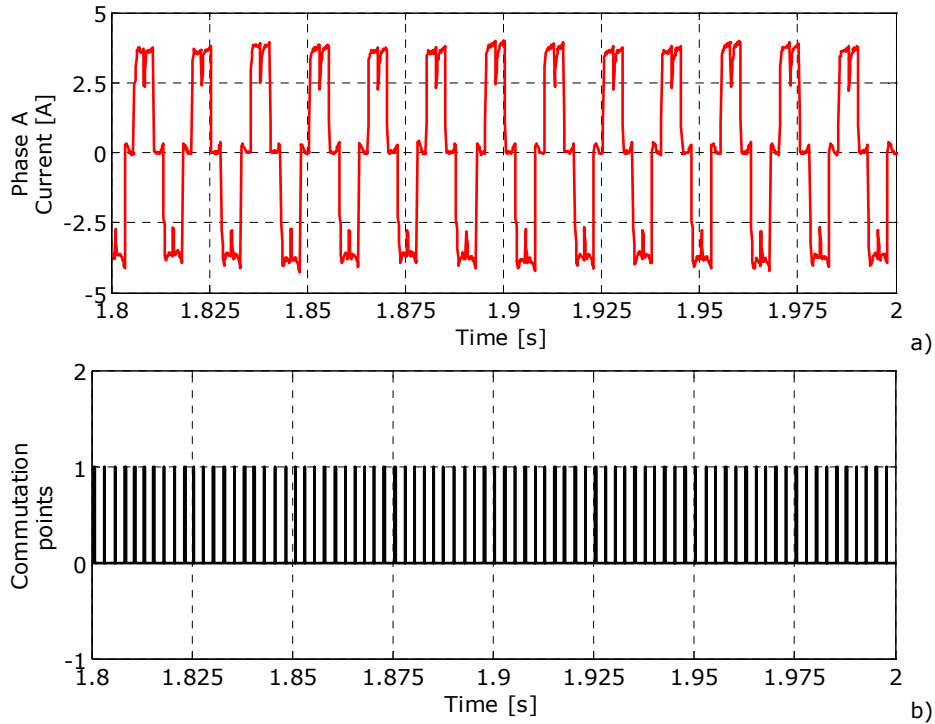


Fig. 5.8. (continued).

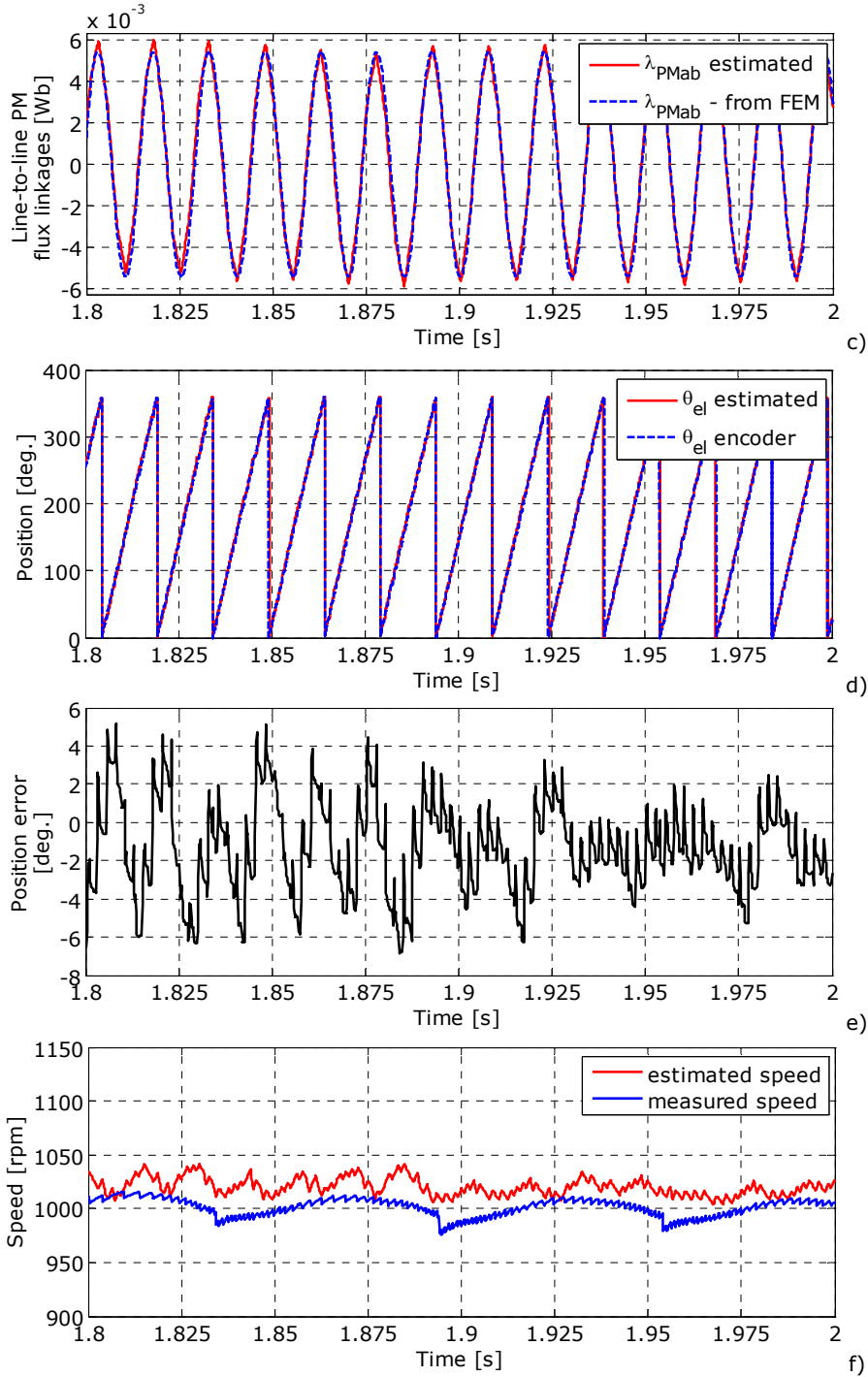


Fig. 5.8. Experimental results of the proposed position and speed FEM assisted observer at 1000 rpm, no-load: a) phase A current; b) observer commutation points; c) line-to-line PM flux linkage; d) position; e) position error; and f) speed.

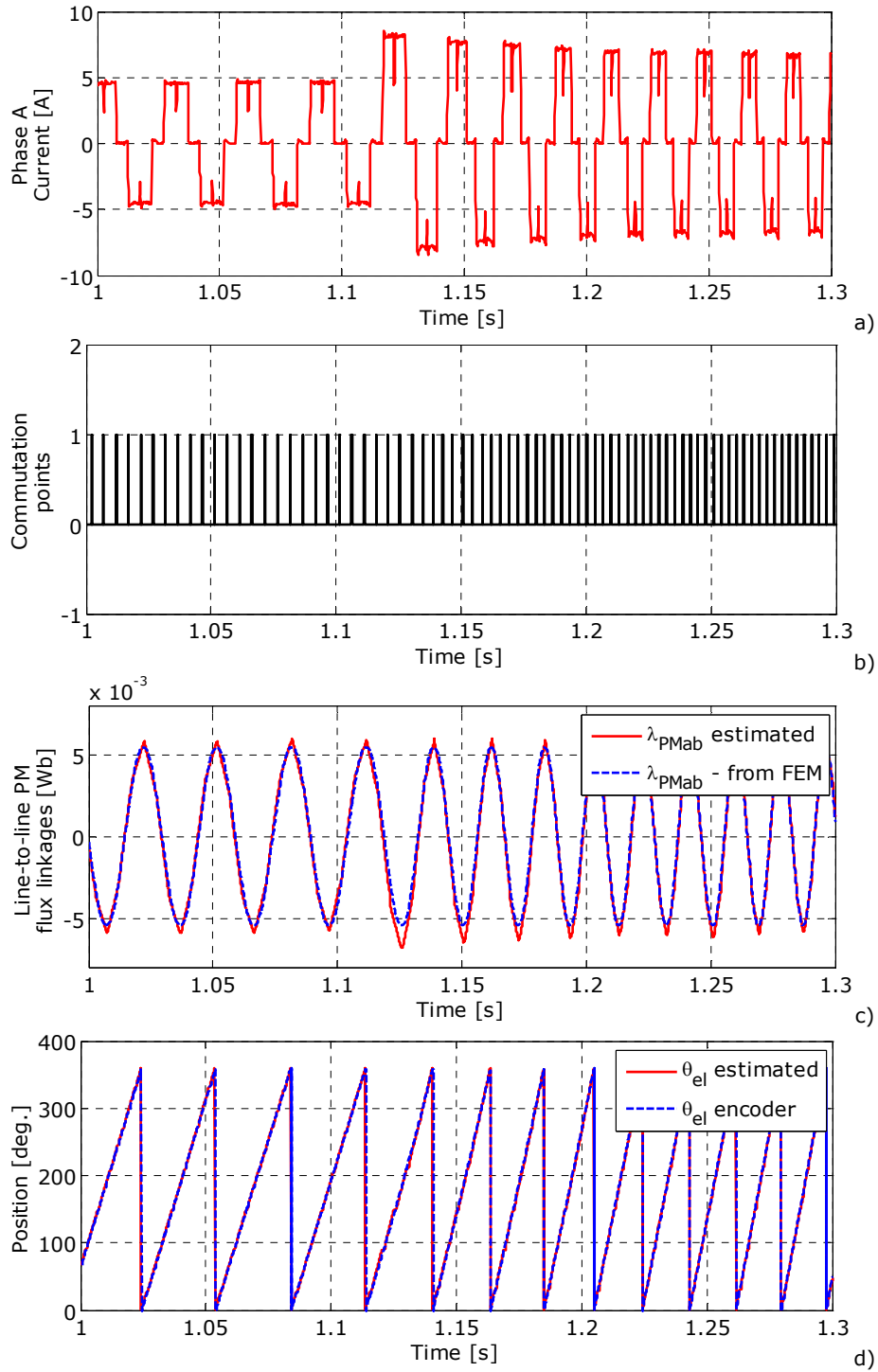


Fig. 5.9. (continued).

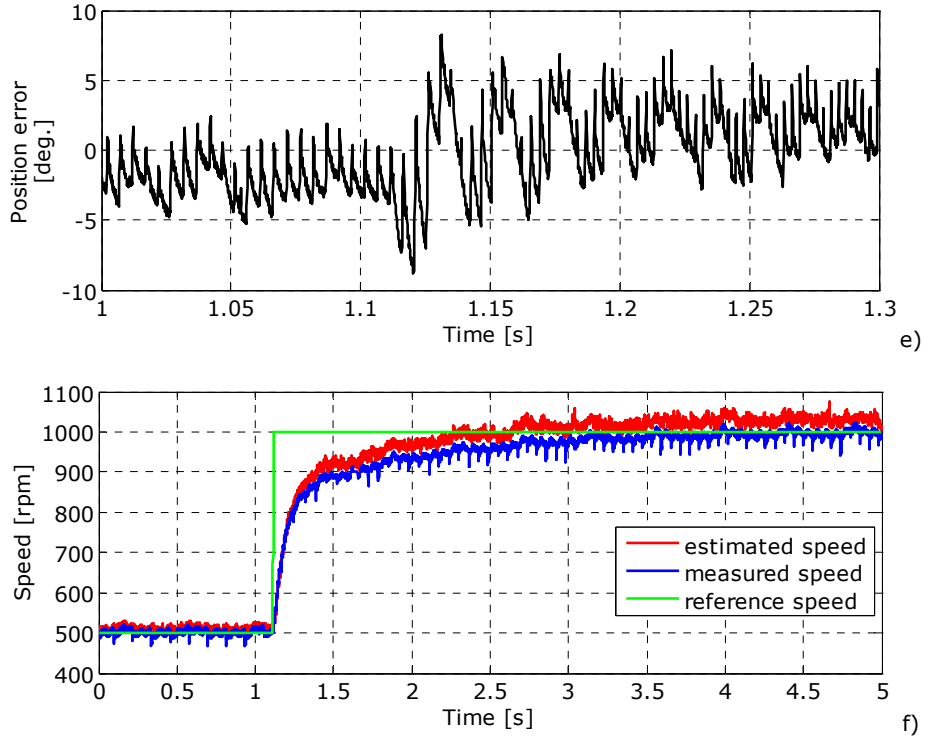


Fig. 5.9. Experimental results of the proposed position and speed FEM assisted observer for acceleration from 500 rpm to 1000 rpm: a) phase A current (zoom in); b) observer commutation points (zoom in); c) line-to-line PM flux linkage (zoom in); d) position (zoom in); e) position error (zoom in); and f) speed.

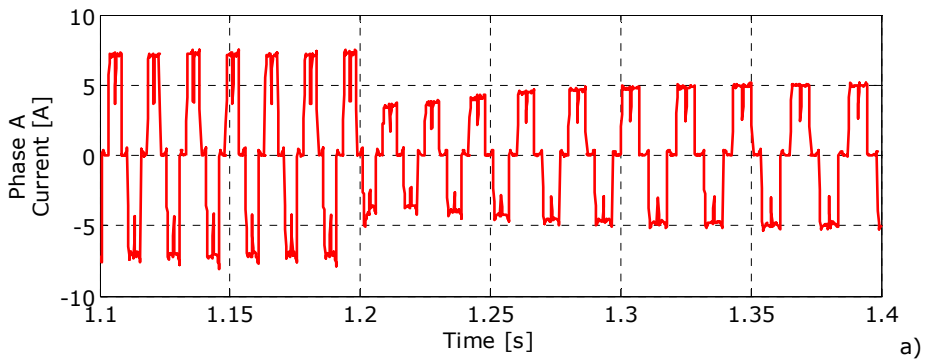


Fig. 5.10. (continued).

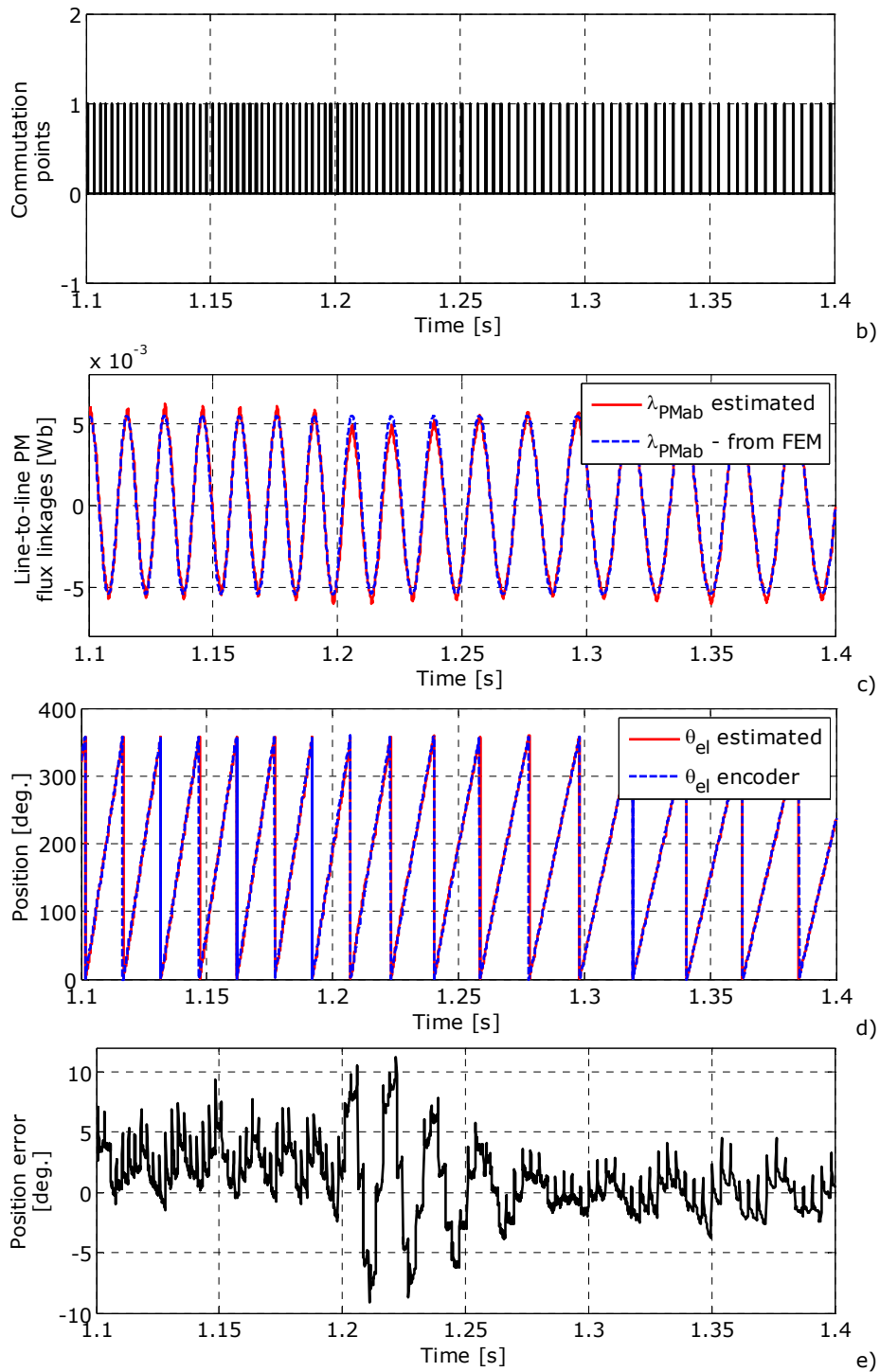


Fig. 5.10. (continued).

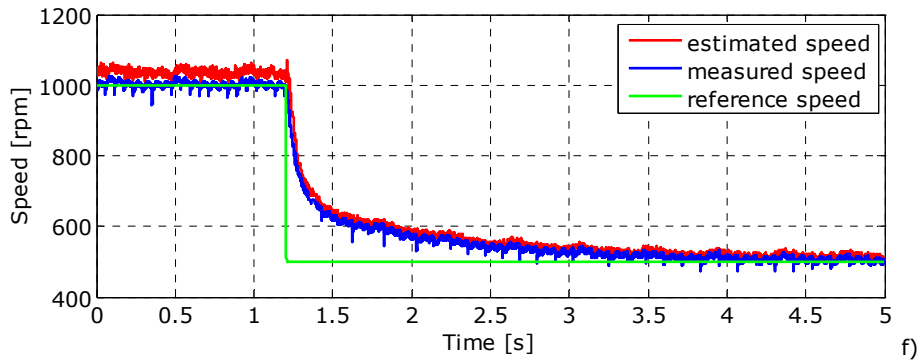


Fig. 5.10. Experimental results of the proposed position and speed FEM assisted observer for deceleration from 1000 rpm to 500 rpm: a) phase A current (zoom in); b) observer commutation points (zoom in); c) line-to-line PM flux linkage (zoom in); d) position (zoom in); e) position error (zoom in); and f) speed.

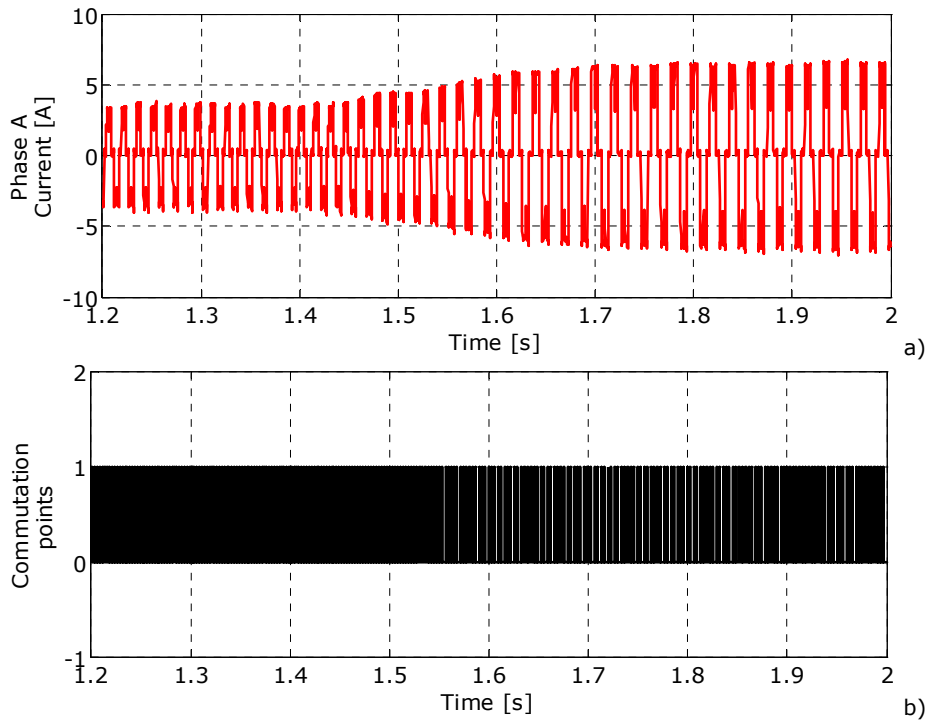


Fig. 5.11. (continued).

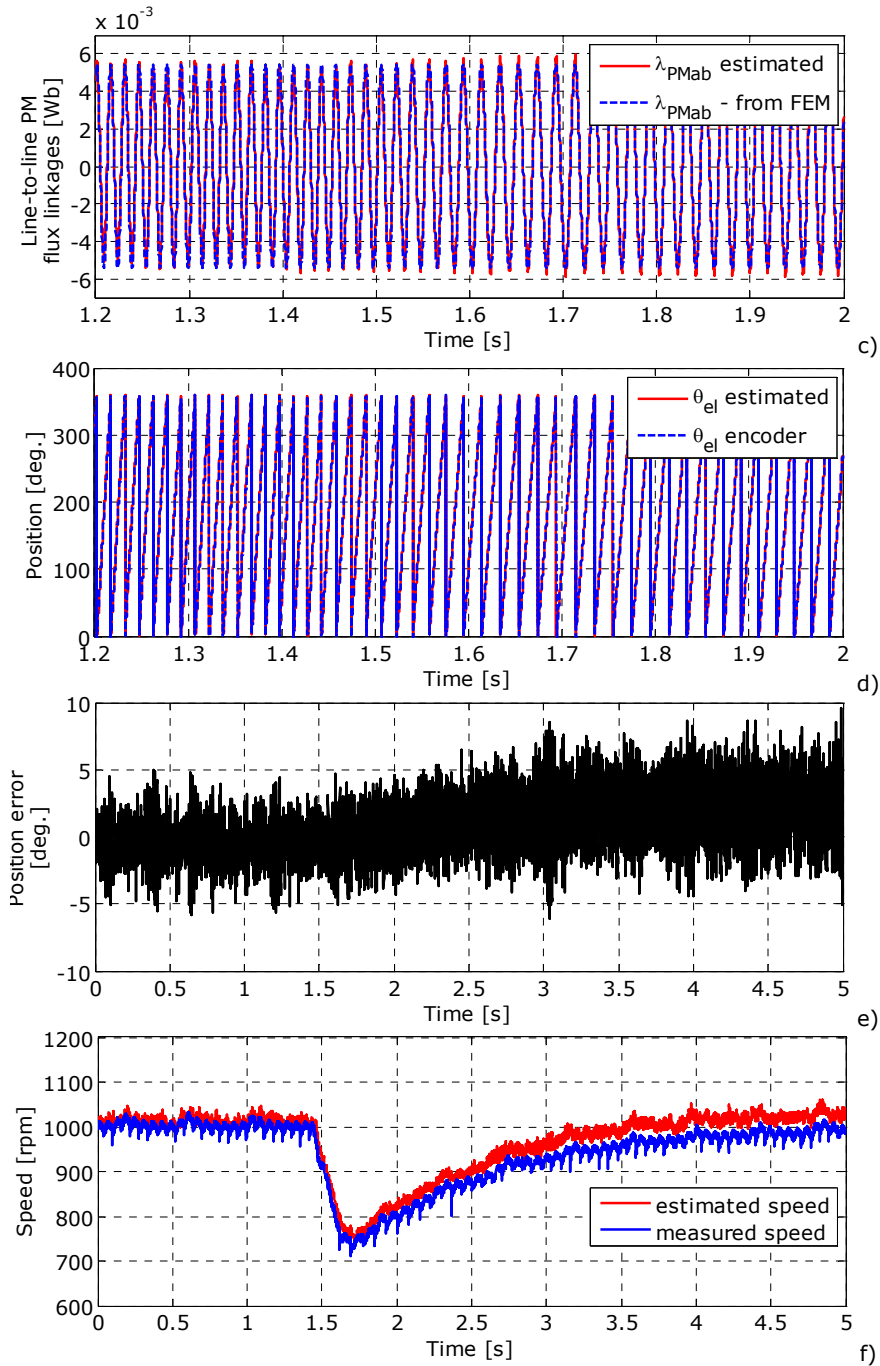


Fig. 5.11. Experimental results of the proposed position and speed FEM assisted observer for loading at 0.15 Nm at 1.5 s: a) phase A current (zoom in); b) observer commutation points (zoom in); c) line-to-line PM flux linkage (zoom in); d) position (zoom in); e) position error; and f) speed.

During the speed transient tests (acceleration and deceleration) the load is proportional to speed

All these experimental results show a rather satisfactory agreement between encoder position and estimated position, proving that the position and speed obtained from the FEM assisted observer can be used in a sensorless operation of a BLDC PM motor.

5.6. Conclusions

The chapter has introduced a FEM assisted position and speed observer for brushless DC PM motor drive sensorless control, based on the line-to-line PM flux linkage. The line-to-line PM flux linkage can be estimated from measured phase currents and calculated line-to-line voltages. The zero-crossing of the line-to-line PM flux occurs right in the middle of two commutations points. This is used as a basis for the position and speed observer. Simulation results and experimental results demonstrate that the FEM assisted position and speed observer for BLDC PM motor provides rather precise commutation points even during speed or load transient states.

As even the proposed observer relies on the machine fundamental model, a safe starting strategy under heavy load torque (with seamless transition to the proposed method) is still needed; such an investigation and sensorless control operation will be presented in the next chapter.

References

- [1] N. Samoylenko, Q. Han, and J. Jatskevich, "Dynamic Performance of Brushless DC Motors With Unbalanced Hall Sensors", *IEEE Trans. on Energy Conversion*, vol. 23, no. 3, September 2008.
- [2] J.P. Johnson, M. Ehsani, and Y. Güzelgünler, "Review of Sensorless Methods for Brushless DC", *IAS Annual Meeting 1999*, vol. 1, pp.143-150, October 1999.
- [3] I. Boldea and S.A. Nasar, *Electric Drives*, 2nd ed., CRC Press, Taylor & Francis, New York, 2005.
- [4] AVR444: "Sensorless Control of 3-Phase Brushless DC Motors", 2005.
- [5] J. Shao, D. Nalon, and T. Hopkins, "A Novel Direct Back EMF Detection for Sensorless Brushless DC (BLDC) Motor Drives", *Proc. of IEEE APEC*, pp.33-37, 2002.
- [6] Y.-S. Lai and Y.-K. Lin, "A Unified Approach to Back-EMF Detection for Brushless DC Motor Drives without Current and Hall Sensors", *IECON 2006*, pp.1293-1298, November 2006.
- [7] Y.-S. Lai and Y.-K. Lin, "Back-EMF Detection Technique of Brushless DC Motor Drive for Wide Range Control", *IECON 2006*, pp.1006-1011, November 2006.
- [8] L. Mingyao, Z. Zhiyao, and L. Keman, "A Novel and Easy-Realizing Initial Rotor Position Detection Method and Speedup Algorithm for Sensorless BLDC Motor Drives", *ICEMS 2008*, pp.2860-2865, October 2008.

- [9] N. Ertugrul and P. Acarnely, "A New Algorithm for Sensorless Operation of Permanent Magnets Motors", *IEEE Trans. on Industry Applications*, vol. 30, no. 1, pp.126-133, January/February 1994.
- [10] S. Ogasawara and H. Akagi, "An Approach to Position Sensorless Drive for Brushless DC Motors", *IEEE Trans. on Ind. Applications*, vol. 27, pp.928-933, September/October 1991.
- [11] T.-H. Kim and M. Ehsani, "Sensorless Control of the BLDC Motors from Near-Zero to High Speeds", *IEEE Trans. on Power Electronics*, vol. 19, no. 6, pp.1635-1645, November 2004.
- [12] T.-S. Kim, B.-G. Park, D.-M. Lee, J.-S. Ryu, and D.-S. Hyun, "A New Approach to Sensorless Control Method for Brushless DC Motors", *International Journal of Control, Automation, and Systems*, vol. 6, no. 4, pp.477-487, August 2008.
- [13] J. Dixon, M. Rodriguez, and R. Huerta, "Position Estimator and Simplified Current Control Strategy for Brushless-DC Motors, Using DSP Technology", *IECON 02*, vol. 1, pp.590-596, November 2002.
- [14] A. Ştirban, D. Iles-Klumpner, M. Risticvic, and I. Boldea, "(6+6) Slot / 8 Pole 3 Phase IPM Brushless D.C. Automotive Actuator: Torque, EMF and Inductances Characterization by FEM vs. Experiments", *IEEE-IEMDC 2009*, May 2009.
- [15] C. Lasu, "Direct Torque Control of Sensorless Induction Machine Drives", PhD Thesis, University Politehnica of Timisoara, Timisoara, 2002.
- [16] A. Ştirban, I. Boldea, G.-D. Andreescu, D. Iles, F. Blaabjerg, "Motion Sensorless Control of BLDC PM Motor with Offline FEM Info Assisted State Observer", *OPTIM 2010*, May 2010.
- [17] W. Hong, W. Lee, and B.-K. Lee, "Dynamic Simulation of Brushless DC Motor Drives Considering Phase Commutation for Automotive Applications", *IEMDC'07*, vol. 2, pp.1377-1383, May 2007.
- [18] O.A. Mohammed, S. Liu, and Z. Liu, "A Phase Variable Model of Brushless DC Motors Based on Finite Element Analysis and Its Coupling with External Circuits", *IEEE Trans. on Magnetics*, vol. 41, no. 5, pp.1576-1579, May 2005.
- [19] A. Ştirban, I. Boldea, G.-D. Andreescu, D. Iles, F. Blaabjerg, "FEM Assisted Position and Speed Observer for BLDC PM Motor Drive Sensorless Control, With Experiments", *EPE-PEMC 2010*, September 2010.

Chapter 6

Sensorless control implementation and performance, with experiments

Abstract

This chapter presents the brushless DC (BLDC) PM motor drive sensorless control with the offline FEM assisted position and speed observer, based on the line-to-line PM flux linkage estimation, presented in detail in Chapter 5. The zero-crossing of the line-to-line PM flux linkage occurs right in the middle of two commutation points, which is used as a basis for the position and speed observer. For performance applications, the position between commutation points is obtained by comparing the estimated line-to-line PM flux linkage with the FEM calculated line-to-line PM flux linkage. Even if the proposed observer relies on the fundamental model of the machine, a safe starting strategy under heavy load torque, called *I-f* control, is used, with seamless transition to the proposed sensorless control. The *I-f* starting method allows low-speed sensorless control, without knowing the initial position, and without machine parameters identification. Digital simulations and experimental results are shown, demonstrating the reliability of the FEM assisted position and speed observer for BLDC PM motor sensorless control operation.

6.1. Introduction

For brushless dc permanent magnet (BLDCPM) motors, many sensorless control strategies for obtaining the rotor position and speed have been proposed in the literature [1-16]. One category, the back-EMF sensing technique (1) [3-8], is a scheme estimating the rotor position indirectly, by using the zero-crossing point detection from the terminal voltage of the unenergized phase winding. It is the most popular sensorless control method, and has been improved for wide range speed control [6]. Other sensorless methods are: back-EMF integration techniques (2); flux linkage-based technique (3) [9]; and freewheeling diode conduction (4) [11]. All mentioned methods have advantages (easy implementation and low computational burden) as well as disadvantages (need of an external hardware circuitry (1, 2) and (4), error accumulation problem at low speeds (2) and (3), and position error in transient state (1) and (4)).

This chapter presents the brushless DC (BLDC) PM motor drive sensorless control with the offline FEM assisted position and speed observer, based on the line-to-line PM flux linkage. Using measured phase currents and line-to-line voltages that can be measured or calculated (by multiplication of the dc bus voltage by switching status, which are known in the controller), the line-to-line PM flux linkage can be estimated. The zero-crossing of the line-to-line PM flux occurs right in the middle of two commutations points. At constant or slowly varying speed,

the time period from one commutation point to zero-crossing, and the time period from zero-crossing to the next commutation point are equal to each other. This is used as a basis for the position and speed observer.

As the proposed observer relies on the fundamental model of the machine, a safe starting strategy under heavy load torque is still needed. For the starting method from standstill to a certain low speed, various methods were proposed: inductance variation method [15] or the "align and go" method with the peak currents limited during the starting period [16]. In this paper, a safe, robust sensorless start-up method, called "*I-f* control" [17], without initial position detection, is used. Seamless transition from *I-f* control to the proposed sensorless control, based on the line-to-line PM flux linkage is achieved. Digital simulations and experimental results demonstrate the reliability of the offline FEM assisted position and speed observer for BLDC PM motor sensorless control operation.

6.2. I-F control starting method

I-f control method consists in ramping the stator current frequency while the current reference is kept constant by the current controller [17]. During the experiments, in order to have a finite acceleration during start-up, the frequency time-variation form was chosen as:

$$f^* = \begin{cases} \frac{f_{\max}^*}{2} \cdot (1 - \cos(\omega_f \cdot t)), & \omega_f \cdot t \leq \pi \\ f_{\max}^*, & \omega_f \cdot t > \pi \end{cases} \quad (6.1)$$

$$\omega_f \cdot t_f = \pi \Rightarrow 2 \cdot \pi \cdot f_f \cdot t_f = \pi \Rightarrow f_f = \frac{1}{2 \cdot t_f} \quad (6.2)$$

where t_f is the time period of the reference frequency ramp ($t_f = 0.2$ [sec], in our case).

The frequency is used to calculate a current reference angle θ_{er}^i , which is the feedforward position-angle corresponding to the imposed synchronous reference frame:

$$\theta_{er}^i = \int 2 \cdot \pi \cdot f^* dt \quad (6.3)$$

6.3. Transition strategies

6.3.1. Transition from I-f Control to FEM Assisted Position and Speed Observer

I-f control method is used only for start-up and low speeds. When the reference frequency exceeds a certain level (f_{min}), the system automatically initiates the transition to the sensorless control operation of the BLDC, based on FEM assisted position and speed observer (Fig. 6.1a). In order to achieve a smooth transition, the angle used for control has to go smoothly from θ_{er}^i to $\hat{\theta}_{er}$:

$$\theta = (1-k) \cdot \theta_{er}^i + k \cdot \hat{\theta}_{er} \quad (6.4)$$

where:

$$k = \begin{cases} 0; & \text{for } |f^*| < f_{\min} \\ \frac{|f^*| - f_{\min}}{f_{\max} - f_{\min}}; & \text{for } f_{\min} \leq |f^*| \leq f_{\max} \\ 1; & \text{for } |f^*| > f_{\max} \end{cases} \quad (6.5)$$

When the reference frequency reaches f_{\max} , the control switches to FEM assisted position and speed observer motion sensorless control ($k = 1$). Because the I - f feedforward position-angle and the estimated position are kept between 0 and $2 \cdot \pi$, based on the fact that $\Delta\theta \cong \sin(\Delta\theta)$ for small $\Delta\theta$, (6.4) is implemented in the following form:

$$\theta = \begin{cases} \theta_{er}^i; & \text{for } |f^*| < f_{\min} \\ \theta_{er}^i + k \cdot \sin(\hat{\theta}_{er} - \theta_{er}^i); & \text{for } f_{\min} \leq |f^*| \leq f_{\max} \\ \hat{\theta}_{er}; & \text{for } |f^*| > f_{\max} \end{cases} \quad (6.6)$$

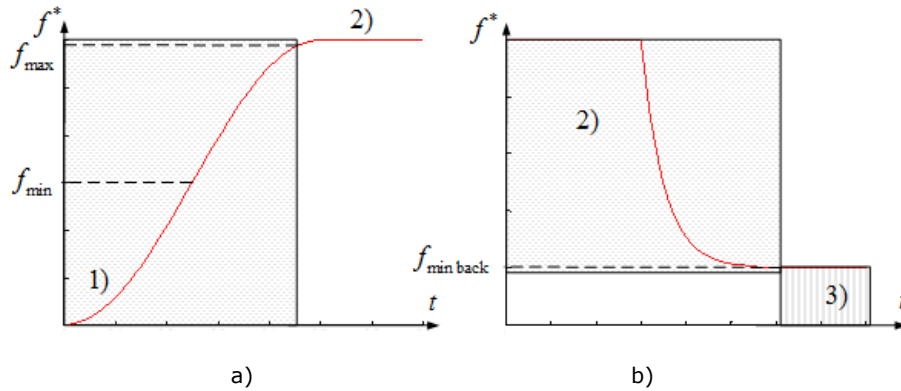


Fig. 6.1. Control strategy: 1) I - f control; 2) FEM assisted position and speed observer motion sensorless control; 3) I - f control.

6.3.2. Transition from FEM Assisted Position and Speed Observer to I - f Control

The transition from FEM assisted position and speed observer motion sensorless control, to I - f control, is done automatically by the system when the reference speed is below a certain level (Fig. 6.1b). When the above condition is met, the control system generates an angle (θ_{er1}^i - feedforward position angle):

$$\theta_{er1}^i = \int \omega^* dt = \int 2 \cdot \pi \cdot f^* dt \quad (6.7)$$

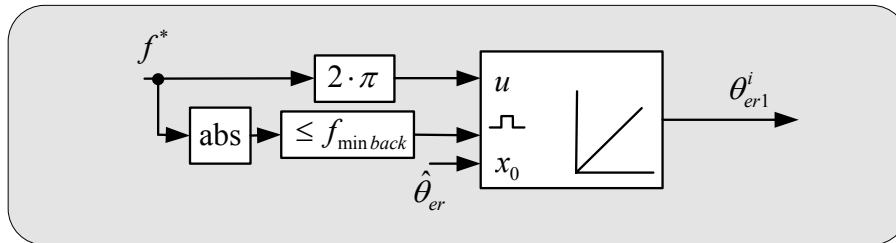


Fig. 6.2. Transition strategy from FEM assisted position and speed observer motion sensorless control to I - f method.

The transition to I - f control is performed by setting the initial condition of the feedforward position angle θ_{er1}^i , equal to the last value of the estimated rotor position $\hat{\theta}_{er}$ (Fig. 6.2).

6.4. Simulation Results

The brushless DC (BLDC) PM motor drive sensorless control with the offline FEM assisted position and speed observer have been first verified through digital simulation. A BLDC PM motor model was implemented in Matlab/Simulink, using the general equations of a brushless DC PM motor. The speed estimator with PLL structure constructed from the mechanical model (Chapter 5, Fig. 5.4), was used both in simulation and experiments.

Fig. 6.3 illustrates the performance of the proposed FEM assisted position and speed observer BLDC motor drive motion sensorless control at 1000 rpm, loaded at 0.15 Nm. The phase currents are controlled by a PI controller. The commutation points from Fig. 6.3b, represent in fact, the zero-crossing detection of the line-to-line PM flux linkages, delayed with 30° .

The numerical simulations demonstrate the reliability of this observer. Next, experimental results are presented, in order to validate the FEM assisted position and speed observer motion sensorless control in real-time applications.

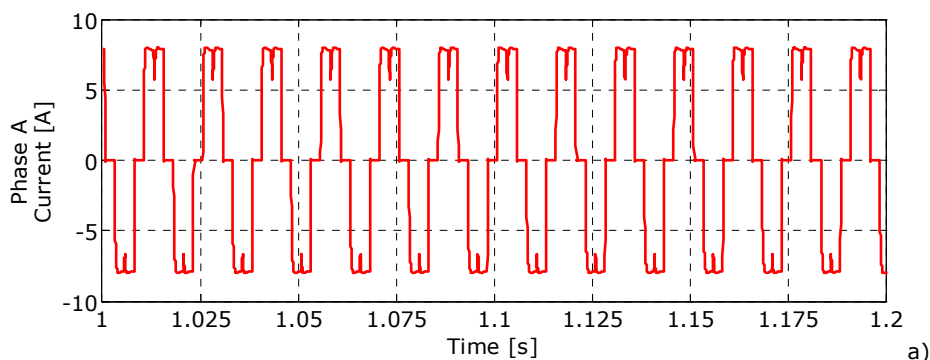


Fig. 6.3. (continued).

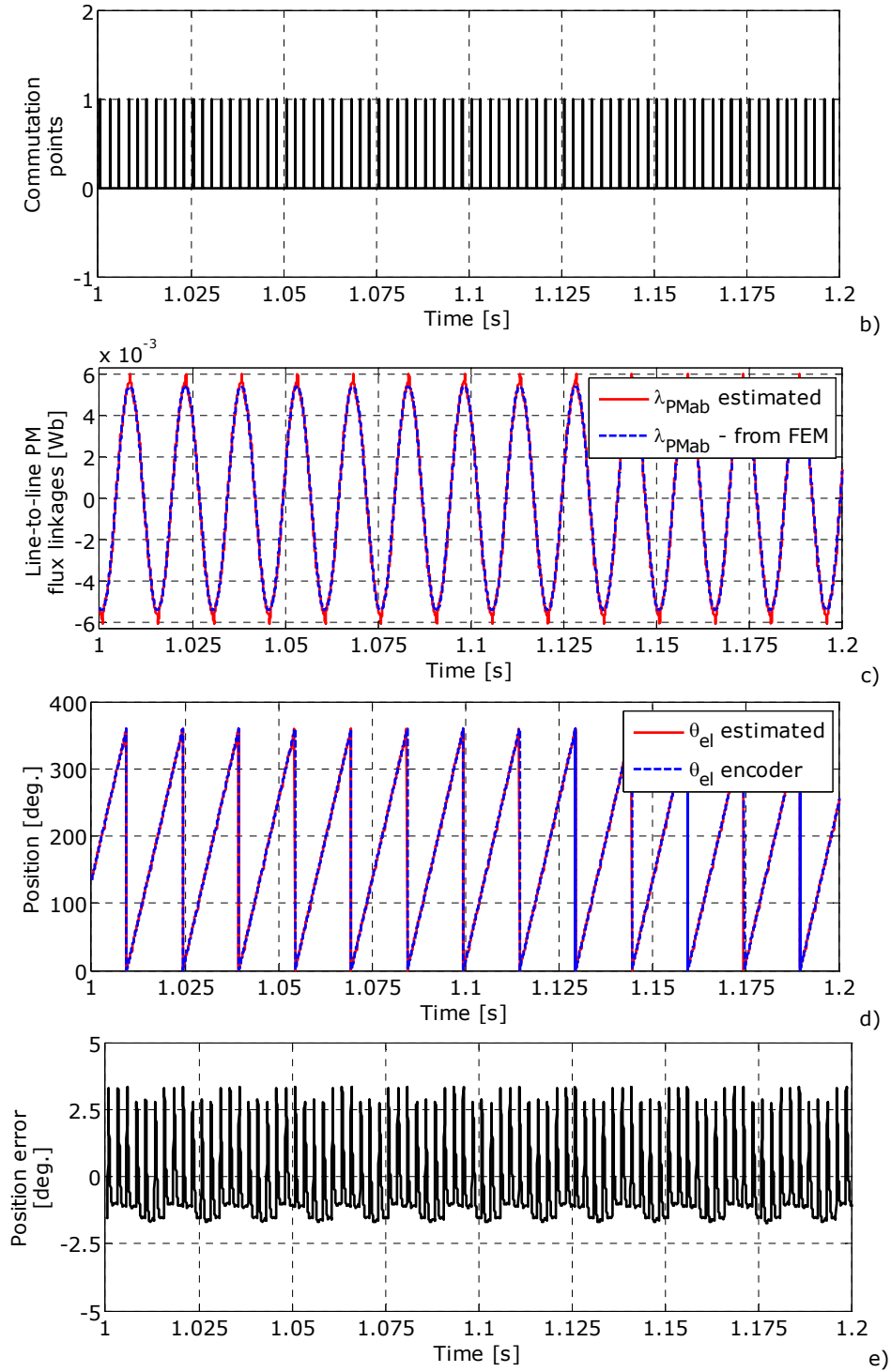


Fig. 6.3. (continued).

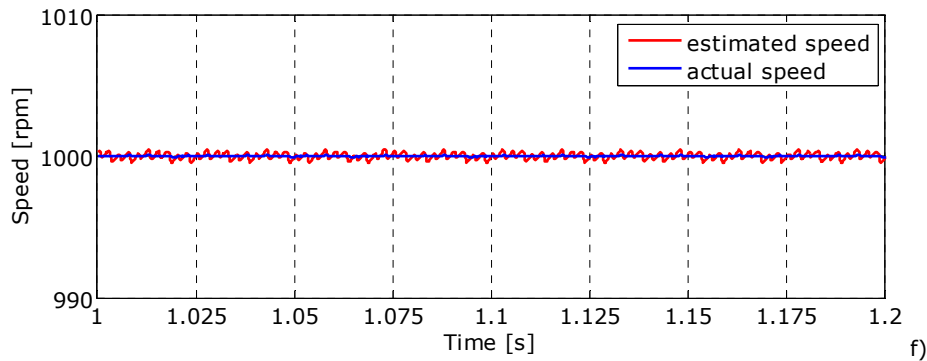


Fig. 6.3. Simulation results of motion-sensorless control of BLDC PM motor with the proposed position and speed FEM assisted observer at 1000 rpm and 0.15 Nm load: a) phase A current; b) commutation points; c) line-to-line PM flux linkage; d) electrical position; e) position error; f) speed.

6.5. Experimental Results

Fig. 6.4 shows an overall system block diagram of the proposed sensorless drive. In this experiment, the line-to-line voltages are measured, but they also can be calculated by multiplication of the DC bus voltage by switching status, which are known in the controller. The use of the measured line-to-line voltages instead of the calculated ones was done in order to achieve better stability and dynamic responses during the sensorless operation.

The performance of the proposed motion sensorless control system is investigated in four cases: constant speed, speed variations, start-up with $I-f$ method and transition to the FEM assisted position and speed observer, and back when the reference speed is below a certain level [18].

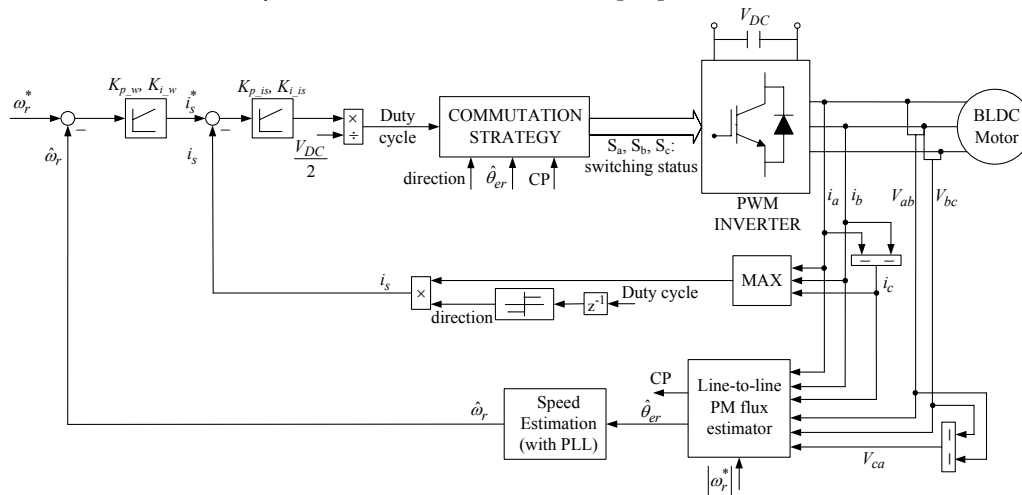


Fig. 6.4. Block diagram of the proposed sensorless drive (CP - commutation points).

6.5.1. Constant Speed Operation

The sensorless operation of the BLDC motor with the proposed FEM assisted position and speed observer at constant speed (Fig. 6.5 – 1000 rpm, loaded at 0.15 Nm), shows a rather satisfactory agreement between encoder position and estimated position, certifying good estimation results. In both cases there are some differences between the estimated and measured speeds.

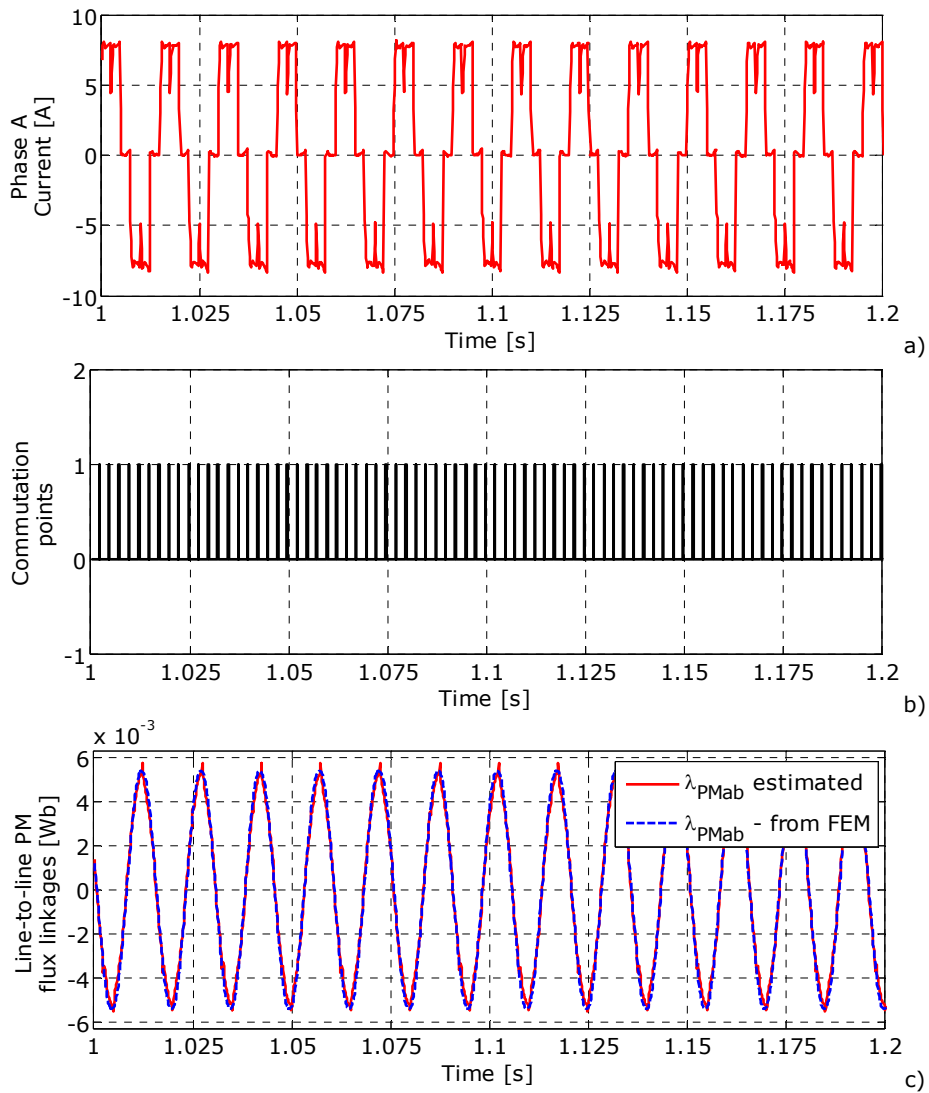


Fig. 6.5. (continued).

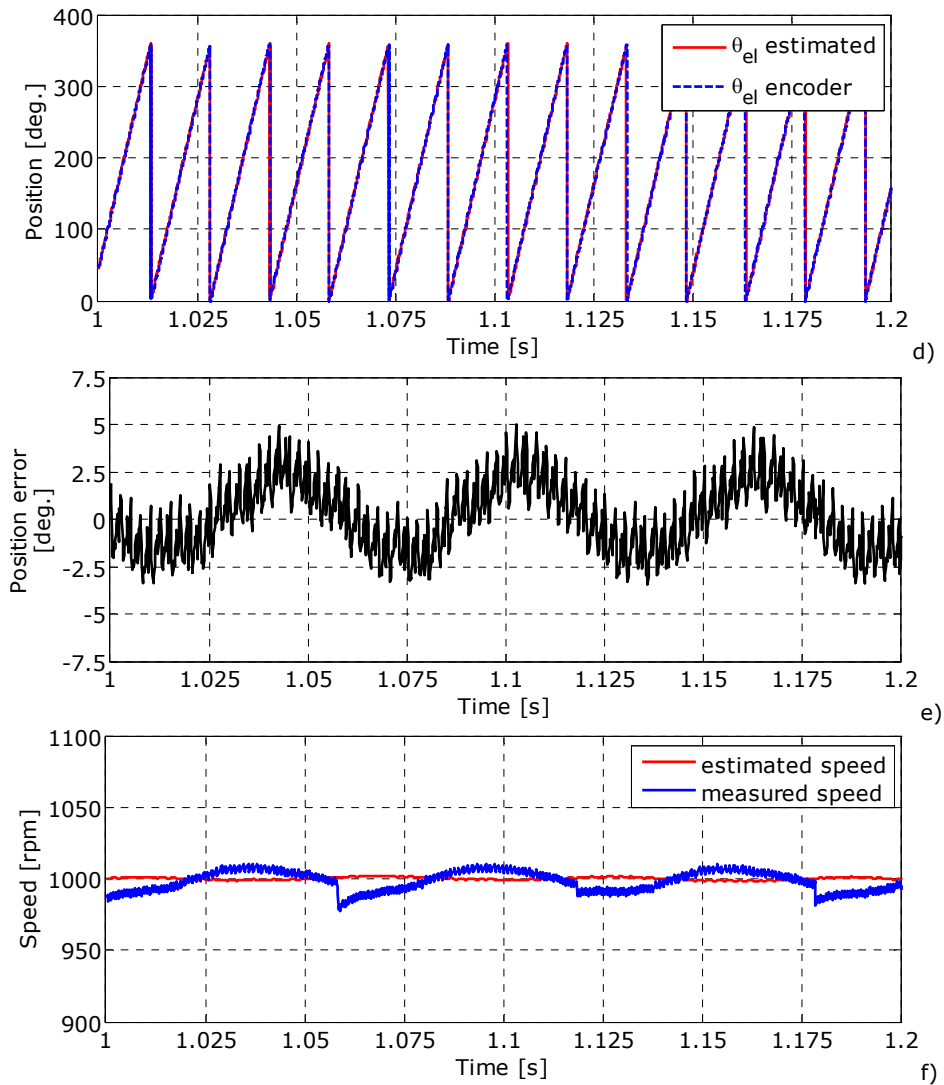


Fig. 6.5. Experimental results of motion-sensorless control of BLDC PM motor with the proposed position and speed FEM assisted observer at 1000 rpm and 0.15 Nm load: a) phase A current; b) commutation points; c) line-to-line PM flux linkage; d) electrical position; e) position error; f) speed).

6.5.2. Dynamics

Fig. 6.6 shows if the FEM assisted position and speed observer is reliable under acceleration and deceleration, and that the load is proportional to speed. During these transient tests, the agreement between encoder position and estimated position is rather satisfactory. The error between these two positions may be minimized by a more carefully tuning of the position and speed observer.

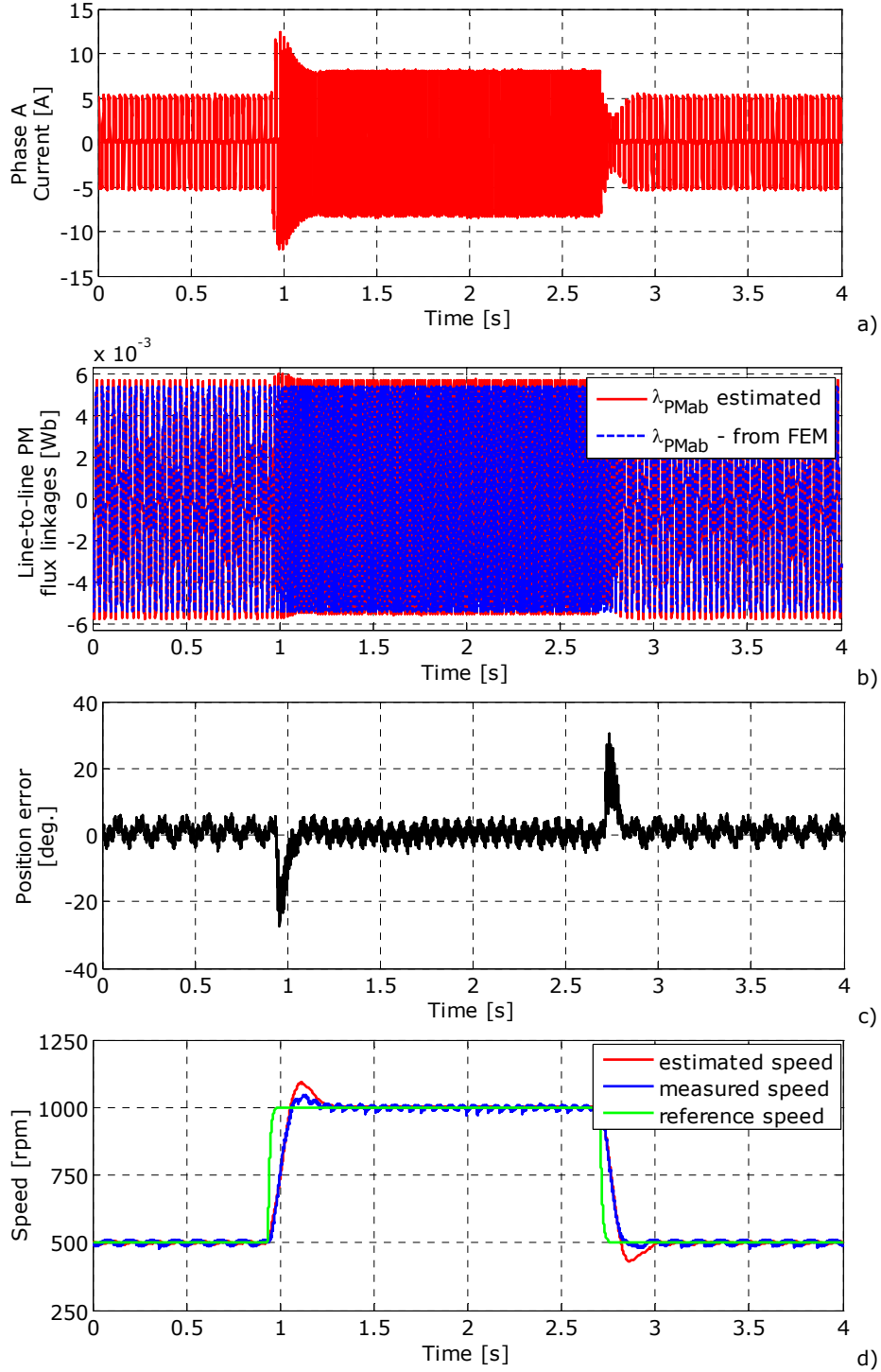


Fig. 6.6. (continued).

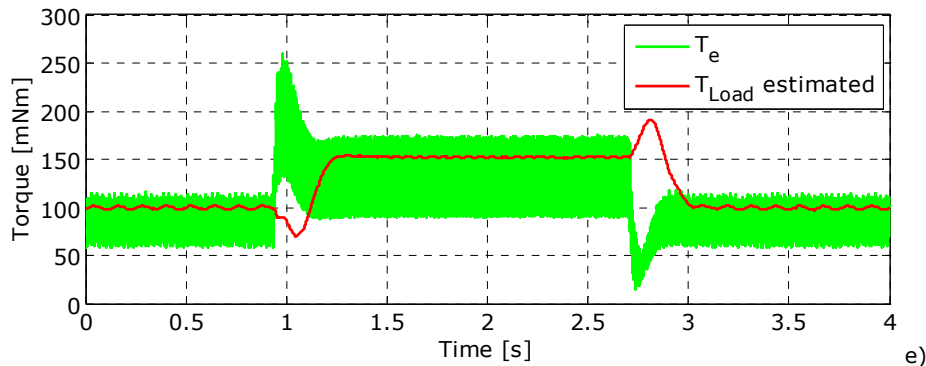


Fig. 6.6. Experimental results of motion-sensorless control of BLDC PM motor with the proposed position and speed FEM assisted observer for acceleration from 500 to 1000 RPM and deceleration from 1000 to 500 RPM: a) phase A current; b) line-to-line PM flux linkage; c) position error; d) speed; e) torque.

From Fig. 6.6d it is obvious that the speed estimated with the PLL observer is in agreement with the measured speed, in both steady state and transients. However, the load torque estimation is poor in transients (Fig. 6.6e).

6.5.3. Transition from I-F Control to FEM Assisted Position and Speed Observer BLDC PM Motion-Sensorless Control

For a smooth start-up, the frequency time-variation form was chosen as in (6.1), up to 66.66 Hz (1000 rpm). The control strategy automatically switches from *I-f* control method to the FEM assisted position and speed observer motion sensorless control, when the reference frequency is between 7 and 10 Hz (Fig. 6.7).

It is obvious from Fig. 6.8 that when the system automatically switches between the two control methods, the angle used for control switches smoothly (Eq. (6.6)) from *I-f* feedforward position to estimated position

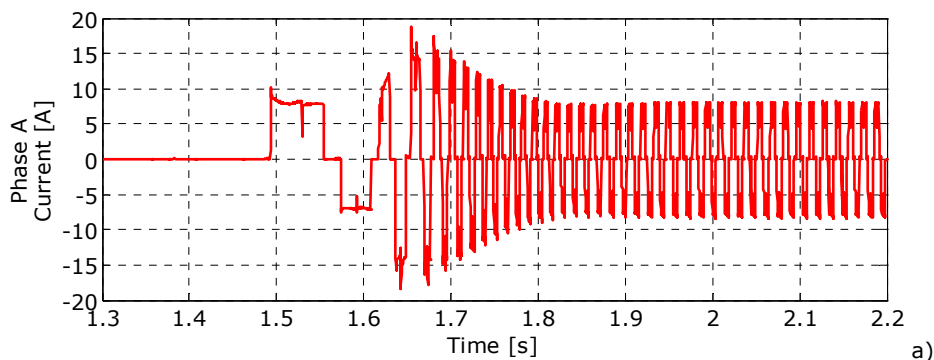


Fig. 6.7. (continued).

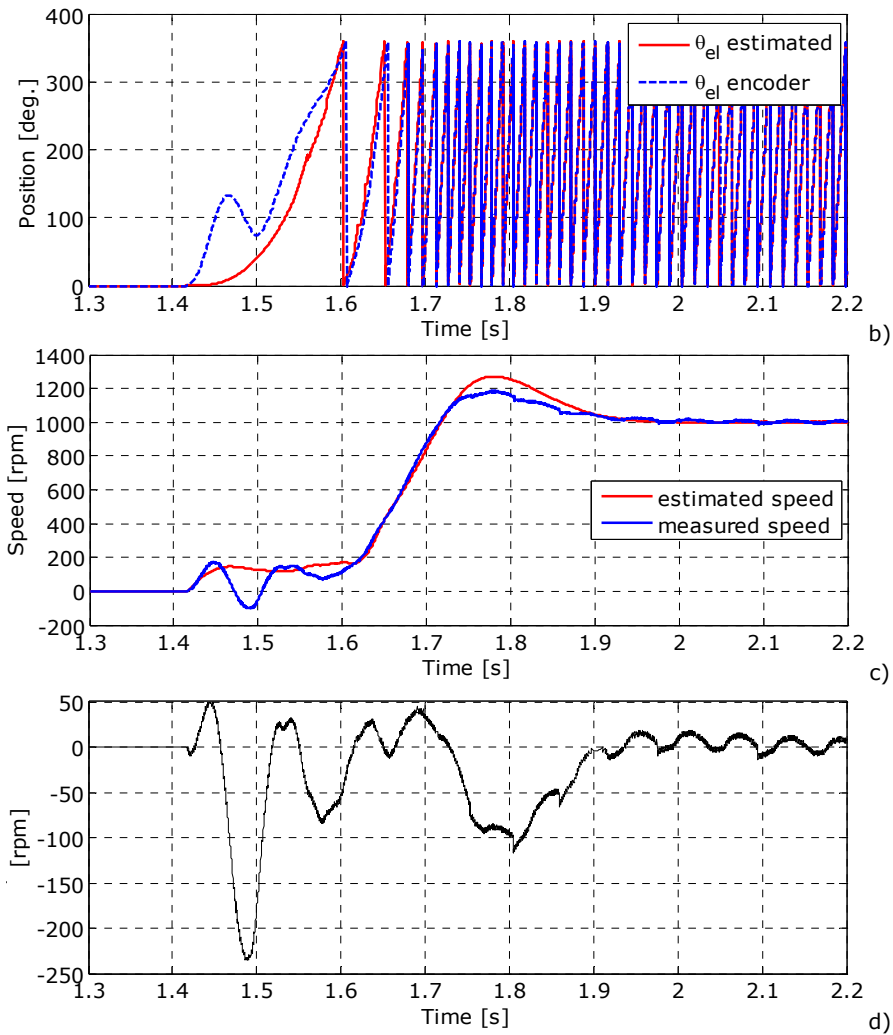


Fig. 6.7. Transition from I-f control method to FEM assisted position and speed observer: a) phase A current; b) position; c) speed; and d) speed error.

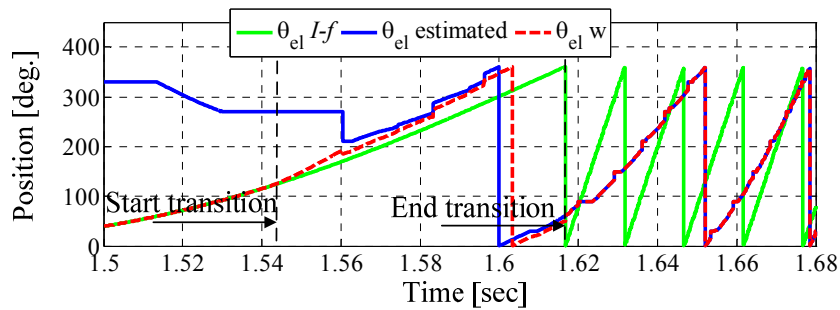


Fig. 6.8. I-f position, estimated rotor position, and the angle used for control [deg.], in transition to FEM assisted position and speed observer.

6.5.4. Transition from FEM Assisted Position and Speed Observer BLDC PM Motion-Sensorless Control to I-F Control

When the reference frequency is below a certain level (12 Hz), the control strategy automatically switches from FEM assisted position and speed observer motion sensorless control, to *I-f* control (Fig. 6.9) with currents frequency equal with the reference frequency. A seamless transition from the estimated position to *I-f* feedforward position is visible in Fig. 6.10, using the solution from Fig. 6.2.

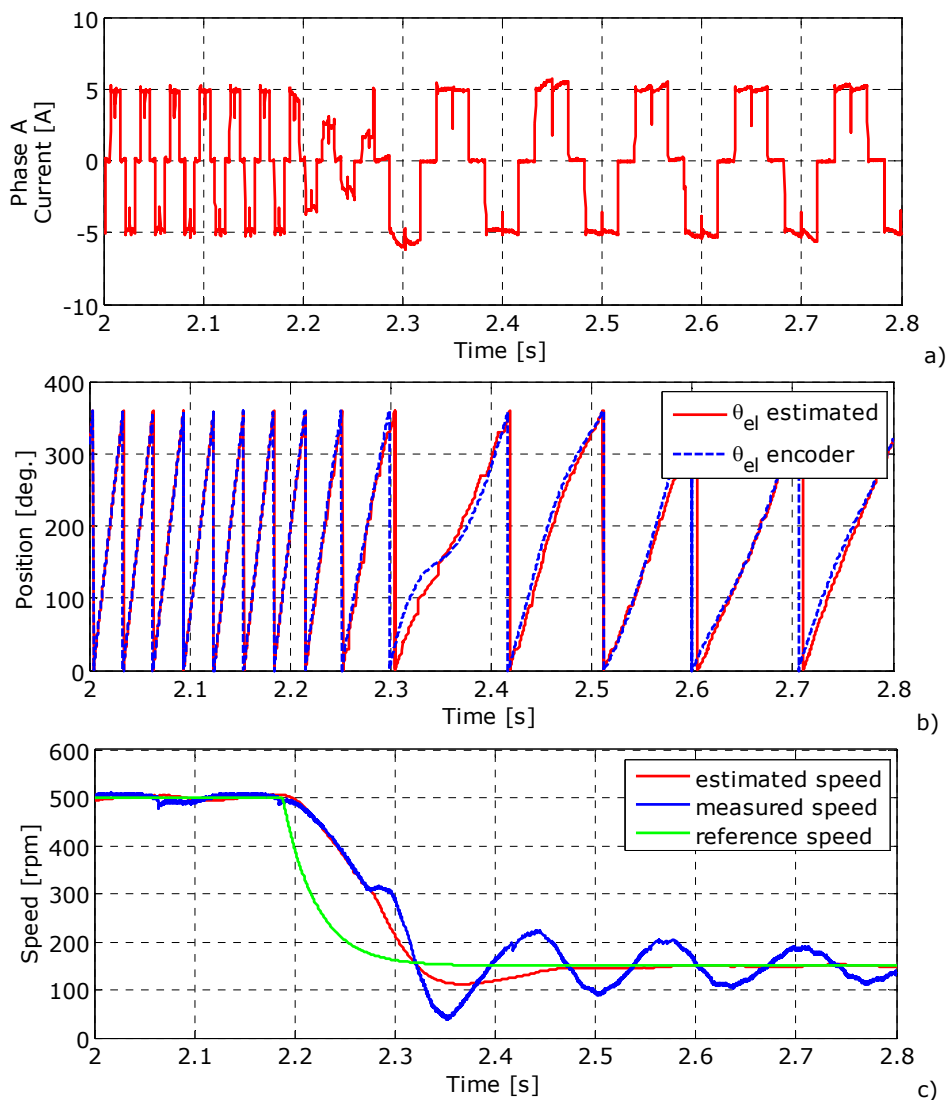


Fig. 6.9. Transition FEM assisted position and speed observer to I-f control method: a) phase A current; b) position; and c) speed.

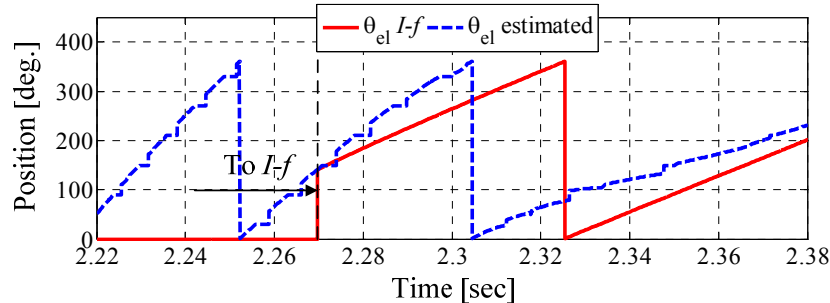


Fig. 6.10. I - f position and estimated rotor position [deg.] in transition to I - f control.

6.6. Conclusion

The chapter has presented the brushless DC (BLDC) PM motor drive sensorless control with the offline FEM assisted position and speed observer, based on the line-to-line PM flux linkage estimation, presented in detail in Chapter 5.

This sensorless control method is used together with the I - f sensorless control, for start-up and for low speed control, with seamless transitions between them.

Digital simulations and experimental results demonstrate that the FEM assisted position and speed observer for BLDC PM motor sensorless control operation, provides rather precise commutation points, even during speed or load transient states.

References

- [1] J.P. Johnson, M. Ehsani, and Y. Güzelgünler, "Review of Sensorless Methods for Brushless DC", *IAS Annual Meeting 1999*, vol. 1, pp.143-150, October 1999.
- [2] I. Boldea and S.A. Nasar, *Electric Drives*, 2nd ed., CRC Press, Taylor & Francis, New York, 2005.
- [3] AVR444: "Sensorless Control of 3-Phase Brushless DC Motors", 2005.
- [4] J. Shao, D. Nalon, and T. Hopkins, "A Novel Direct Back EMF Detection for Sensorless Brushless DC (BLDC) Motor Drives", *Proc. of IEEE APEC*, pp.33-37, 2002.
- [5] Y.-S. Lai and Y.-K. Lin, "A Unified Approach to Back-EMF Detection for Brushless DC Motor Drives without Current and Hall Sensors", *IECON 2006*, pp.1293-1298, November 2006.
- [6] Y.-S. Lai and Y.-K. Lin, "Back-EMF Detection Technique of Brushless DC Motor Drive for Wide Range Control", *IECON 2006*, pp.1006-1011, November 2006.
- [7] L. Mingyao, Z. Zhiyao, and L. Keman, "A Novel and Easy-Realizing Initial Rotor Position Detection Method and Speedup Algorithm for Sensorless BLDC Motor Drives", *ICEMS 2008*, pp.2860-2865, October 2008.

- [8] C.-T. Lin, C.-W. Hung, and C.-W. Liu, "Sensorless Control for Four-Switch Three-Phase Brushless DC Motor Drive", *Conference Record of the IEEE on Industry Applications*, vol. 4, pp.2048-2053, October 2006.
- [9] J. X. Shen and S. Iwasaki, "Sensorless Control of Ultrahigh-Speed PM Brushless Motor Using PLL and Third Harmonic Back EMF", *IEEE Trans. on Industrial Electronics*, vol. 53, no. 2, pp.421-428, April 2006.
- [10] N. Ertugrul and P. Acarnely, "A New Algorithm for Sensorless Operation of Permanent Magnets Motors", *IEEE Trans. on Industry Applications*, vol. 30, no. 1, pp.126-133, January/February 1994.
- [11] S. Ogasawara and H. Akagi, "An Approach to Position Sensorless Drive for Brushless DC Motors", *IEEE Trans. Ind. Applications*, vol. 27, pp.928-933, September/October 1991.
- [12] T.-H. Kim and M. Ehsani, "Sensorless Control of the BLDC Motors from Near-Zero to High Speeds", *IEEE Trans. on Power Electronics*, vol. 19, no. 6, pp.1635-1645, November 2004.
- [13] T.-S. Kim, B.-G. Park, D.-M. Lee, J.-S. Ryu, and D.-S. Hyun, "A New Approach to Sensorless Control Method for Brushless DC Motors", *International Journal of Control, Automation, and Systems*, vol. 6, no. 4, pp.477-487, August 2008.
- [14] J. Dixon, M. Rodriguez, and R. Huerta, "Position Estimator and Simplified Current Control Strategy for Brushless-DC Motors, Using DSP Technology", *IECON 02*, vol. 1, pp.590-596, November 2002.
- [15] K.-W. Lee, D.-K. Kim, B.-T. Kim, and B.-I. Kwon, "A Novel Starting Method of the Surface Permanent-Magnet BLDC Motors Without Position Sensor for Reciprocating Compressor", *IEEE Trans. on Industry Applications*, vol. 44, no. 1, pp.85-92, January/February 2008.
- [16] W.-J. Lee and S.-K. Sul, "A New Starting Method of BLDC Motors Without Position Sensor", *IEEE Trans. on Industry Applications*, vol. 42, no. 6, pp.1532-1538, November/December 2006.
- [17] M. Fătu, R. Teodorescu, I. Boldea, G.-D. Andreescu, and F. Blaabjerg, "I-F Starting Method with Smooth Transition to EMF Based Motion-Sensorless Vector Control of PM Synchronous Motor/Generator", *PESC 2008*, pp.1481-1487, June 2008.
- [18] A. Știrban, I. Boldea, G.-D. Andreescu, D. Iles, F. Blaabjerg, "Motion Sensorless Control of BLDC PM Motor with Offline FEM Info Assisted State Observer", *OPTIM 2010*, May 2010.

Chapter 7

The experimental test platform

Abstract

This chapter presents the laboratory setup used for the carried out tests. The first part of the setup, used for the experiments presented in Chapter 3, was realized in the R&D Lab, ebm papst, Saint Georgen, Germany, with intended purpose to measure electric machines parameters. The second part of the setup used for the experiments presented in Chapters 5 and 6, was realized in the Intelligent Motion Control Lab, Faculty of Electrical Engineering Timisoara,

7.1. Laboratory setup for Chapter 3

The test setup includes the BLDC motor, voltage source inverter, motor controller, and test rig.

7.1.1. BLDC motor

In the following the case study BLDC motor used for the experimental analysis will be presented. Table 7.1 presents the specification data of the motor.

Table 7.1. BLDC motor specification data

Parameter	Symbol	Value	Unit
Number of pole pairs	p_l	4	-
Rated torque	T_{eb}	1.14	Nm
Very low cogging torque	$T_{cogg} < 1\% \cdot T_{eb}$		
Rated current	I_n	56	A
Rated speed	n_n	1000	rpm
DC bus voltage	V_{DC}	12	V
Stator phase resistance	R_s	11	m Ω
Moment of inertia of the drive	J	$3.066 \cdot 10^{-4}$	kg·m ²
Damping constant	B_m	$1 \cdot 10^{-4}$	Nm/(rad/s)
Constant values for inductances			
Phase self inductance	L_s	51	μ H
Mutual inductance	M	7.5	μ H

In Fig. 7.1 shows the stator with concentrated windings and the rotor with permanent magnets before assembling.



Fig. 7.1. Stator and rotor before assembling.

7.1.2. Laboratory precise dynamometer

Most of the tests were on the precision dynamometer with the configuration presented in Fig. 7.2.

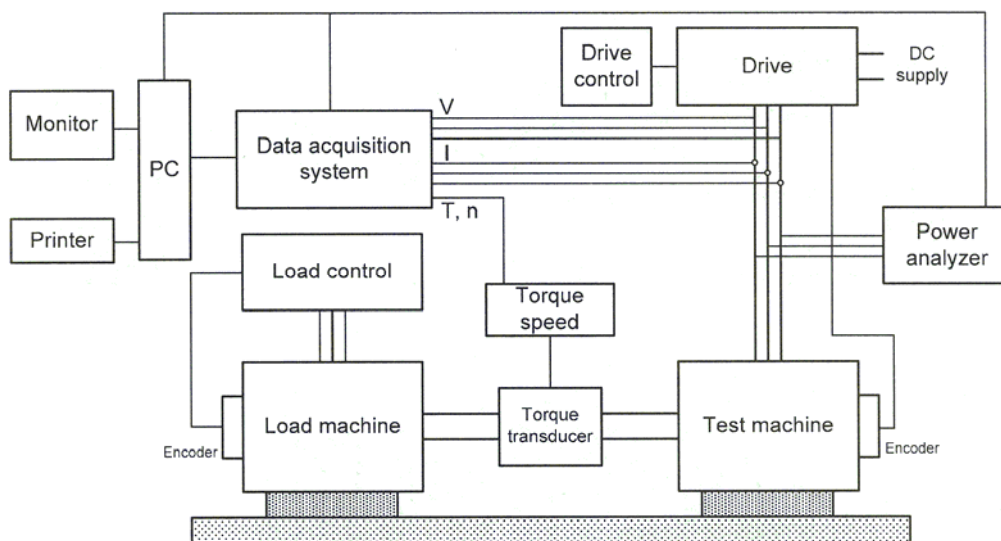


Fig. 7.2. Precision dynamometer configuration [1].

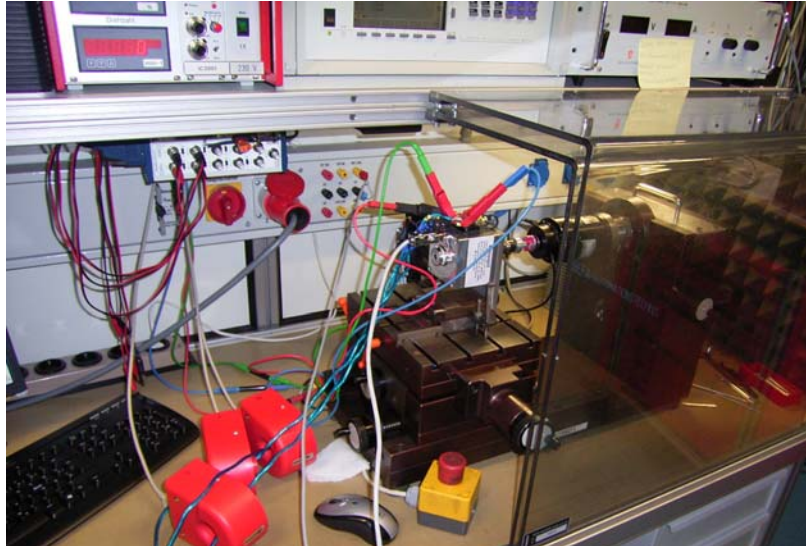


Fig. 7.3. Laboratory test rig.

Fig. 7.4 presents the rotor positioning device used for the measurements of phase inductance in dependence with rotor position.

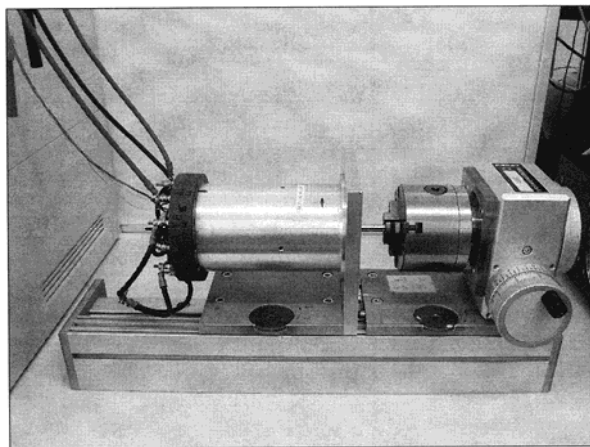


Fig. 7.4. Rotor positioning device used for inductance measurements [1].

The standstill torque measurements were done using the rotor positioning device presented in Fig. 7.5.

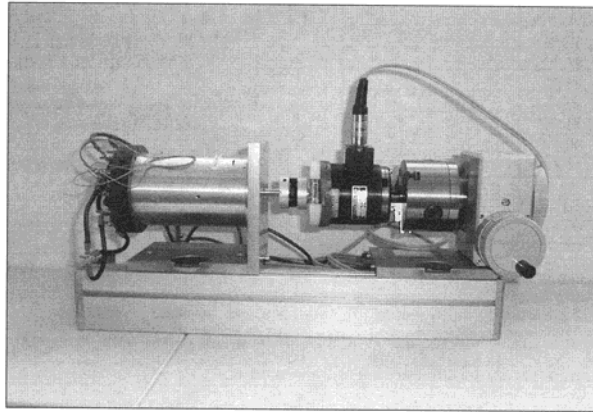


Fig. 7.5. Standstill torque measurement setup (rotor positioning device with torque sensor) [1].

7.2. Laboratory setup for Chapters 5 and 6

The experimental setup contains two back-to-back twins three-phase BLDC IPM machines – one operating as a motor and one as a generator, loaded with a three-phase resistance ($R_{ph}=0.45 \Omega$), a high current MOSFET three-phase inverter, the phase measurement device. dSpace CLP1103 platform is used to control the entire drive system (Fig. 7.6).

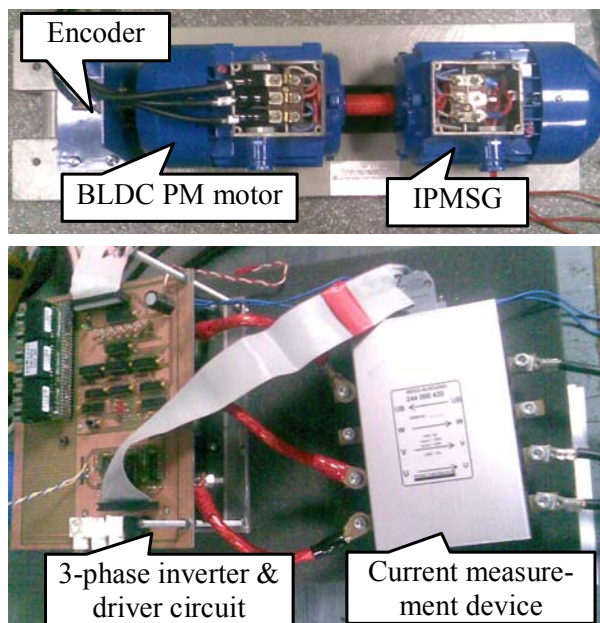


Fig. 7.6. Experimental setup.

7.2.1. dSpace DS1103

The DS1103 PPC is a very flexible and powerful system featuring both high computational capability and comprehensive I/O periphery [2, 3]. Additionally, it features a software SIMULINK interface that allows all applications to be developed in the MATLAB®/Simulink friendly environment. All compiling and downloading processes are carried out automatically in the background. Experimenting software, called Control Desk, allows real-time management of the running process by providing a virtual control panel with instruments and scopes (Fig. 7.7). The DS1103 is a single board system based on the Motorola PowerPC 604e/333MHz processor (PPC), which forms the main processing unit.

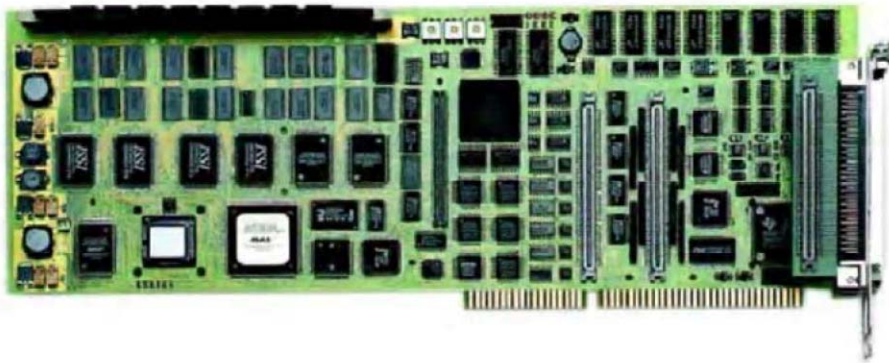


Fig. 7.7. The single board control system dSpace DS1103 [4].

7.2.2. Position sensor

The BLDC motor was equipped with an incremental encoder to prove the sensorless position estimation techniques. The encoder has 500 pulses-per-revolution (ppr) and provides the real rotor position and speed (Fig. 7.8).

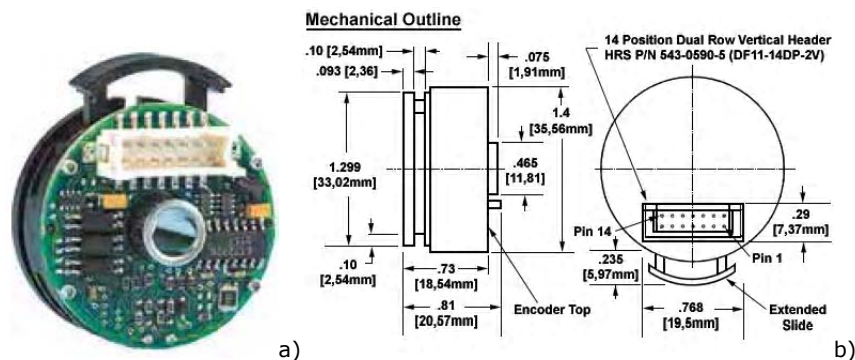


Fig. 7.8. Commutation RENCO encoder attached to the BLDC motor: a) Encoder 3D Model, b) Mechanical outline [5].

The device was a RENCO encoder type RCM15. The features of this encoder are:

- 2 data channels in quadrature
- Once around index marker pulse.
- 3 commutation channels optically & electrically isolated.
- RS-422 interface (data & comm.).
- Self aligning.
- Self centering.
- Self gapping.
- Frequency response to 300 KHz.
- Differential Index, commutation, and data channels.
- PC Board connector for easy installation.

7.3. Software

The control algorithms were implemented in Simulink environment, compiled automatically using Microtec C compiler for Motorola Power PC and Texas Instruments C compiler and built/downloaded automatically using the dSpace system specialized MLIB/MTRACE mechanism (Fig.7.9).

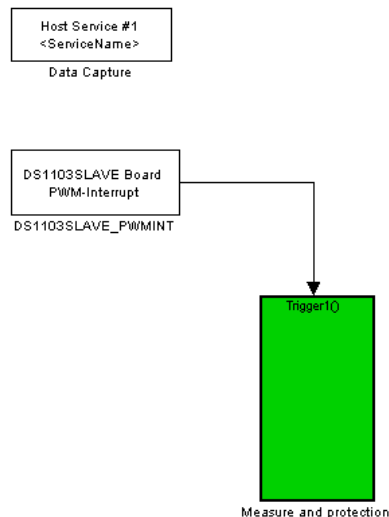


Fig. 7.9. Simulink software.

From the encoder interface (Fig. 7.10) the position of the rotor and its speed are computed. This could be obtained by counting the pulses coming on the dedicated hardware interface and knowing the encoder resolution (number of the pulses for one revolution) and the system sampling time.

The software includes a control algorithm which can be built taking account into the user rules.

The algorithm uses the inputs (currents, voltages, position, speed etc.) and computes the applied command voltage. The duty cycle is calculated from the command voltage. Then, this duty cycle is introduced in dSpace special blocks which will provide the PWM command signals for the upper and lower transistors (Fig. 7.11).

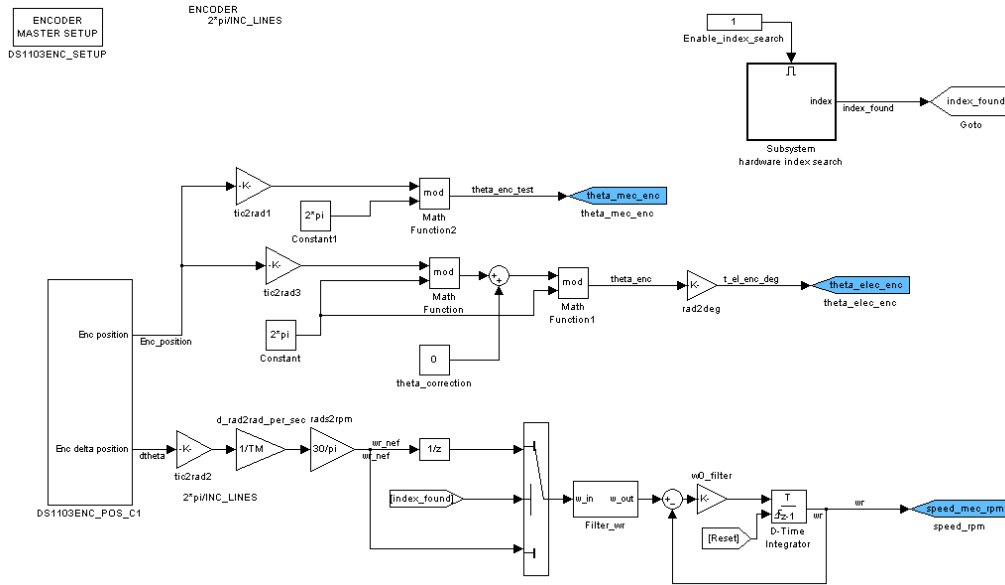


Fig. 7.10. Blocks for incremental encoder.

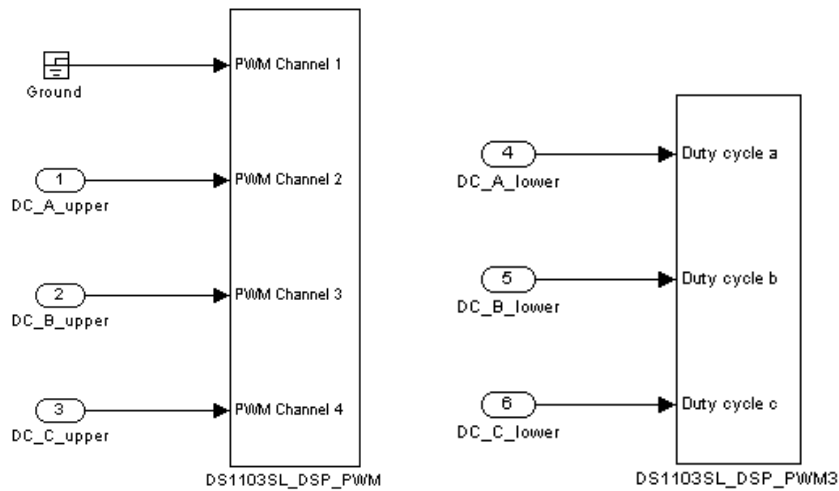


Fig. 7.11. Inverter command.

When the soft is ready and there are no errors, it can be compiled in dSpace. After the compilation, the soft is loaded in the interface called Control Desk (Fig. 7.12). This interface contains all system parameters and allows their visualization, acquisition and changing. Thus at first, the system starts having all its variables and constants loaded from the soft developed in Matlab/Simulink, and latter, if it is desired, these variables can be modified in real time from the Control Desk Developer.

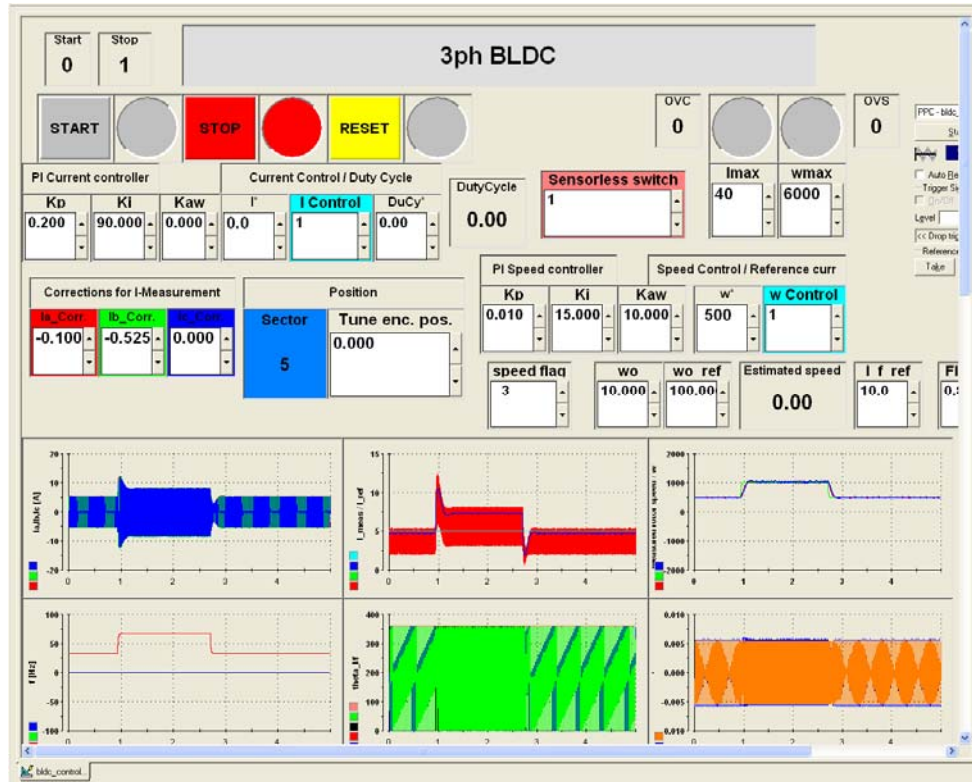


Fig. 7.12. Control Desk environment.

7.4. Conclusion

The experimental test platforms used during the parameter measurements and the tests of state observers and sensorless control of a BLDC motor drive system were presented in this chapter.

The hardware components of the system were presented, discussed and analyzed. The software developed in Matlab Simulink and the interface "Control Desk" Developer from the dSpace platform and the way these two interact was also presented.

References

- [1] D. Iles, "Automotive Permanent Magnet Actuation Technologies", PhD Thesis, Timisoara, 2005.
- [2] R. Teodorescu, "Getting Started with dSpace System", Flexible Drives System Laboratory (FDSL) Reference Manual, Version 1.0, Institute of Energy Technology, Aalborg University, Denmark.
- [3] www.dspace.com.
- [4] R. Ancuți, "Fast Dynamics Response of Sensorless Control of High Speed Surface Permanent Magnet Synchronous Motor Drives", PhD Thesis, Timisoara, 2008.
- [5] www.renco.com.

Chapter 8

Conclusion and Contributions

8.1. Conclusion

The present work is dedicated to three phase brushless DC actuator with interior permanent magnets design, control and applications

The thesis focused on the following major topics:

- operation principle of brushless DC motor;
- main application areas of brushless DC motors;
- synthesis of fractional slot concentrated winding permanent magnet synchronous machines, emphasizing the PMSM structures with concentrated windings and irregular distribution of stator slots;
- electromagnetic design for a fractional slot concentrated winding permanent magnet synchronous machine;
- a comparison between FEM-calculated and measured parameters of an interior permanent magnet BLDC motor;
- total torque ripple reduction;
- simulation model for BLDC motor drives;
- new solution for brushless DC PM motor drive sensorless control;

Based on the presented topics the main conclusions are:

- For a brushless DC motor, the air-gap flux density waveform is essentially a square wave, but fringing causes the corners to be somewhat rounded. As the rotor rotates, the waveform of the voltage induced in each phase with respect to time is an exact replica of the air-gap flux density waveform with respect to rotor position. The shape of the back-EMF waveform distinguishes the BLDC motor from the permanent magnet synchronous motor (PMSM), which has a sinusoidal back-EMF waveform. This has given rise to the terminology "trapezoidal motor" and "sinusoidal motor" for describing these two permanent magnet AC (PMAC) machines.
- The advantages of BLDC motors and their rapidly decreasing cost, have led to their widespread application in many variable-speed drives. Their high power density makes them ideal candidates for applications such as robotic actuators, computer disk drives, and office equipment. With their high efficiency, high power factor, and maintenance-free operation, domestic appliances and heating, ventilating, and air conditioning (HVAC) equipments are now increasingly employing BLDC motors in preference to DC and induction motors. They are also being developed for automotive applications such as electric power steering, power accessories, and active suspension, in addition to vehicle propulsion.
- The use of windings concentrated around the teeth, offer obvious advantages for the electric machines with radial air-gap. With concentrated windings, the volume of copper used in the end-windings can be reduced significantly, particularly if the axial length of the machine

is small. There is minimization of both copper volume and Joule losses, reduction in the manufacturing cost, and improvement in the output characteristics for these machines, when compared to more traditional structures with one slot/pole/phase. This winding structure is also easier to realize than a lap winding and the number of coils is reduced.

- Based on the general aspects regarding the sizing of electric machines the selection of the key design quantities, and the dimensioning procedure for the actual case study IPMSM can be defined algorithmically.
- The finite element method (FEM) is a very useful tool for predicting and estimating the effect of different design parameters on motor performance.
- Because of the nonsinusoidal nature of the back-EMF and current waveforms, transformation of the machine equations to the d - q model is cumbersome, and it is easier to use the phase-variable approach for modeling and simulation. The commonly used abc model assumes that the self and mutual inductances are constant. But due to the physical rotation of the rotor and the nonlinear magnetization property of stator iron, the inductance varies with rotor position and winding current. The dependence of inductances versus rotor position can be accurately evaluated through nonlinear FE analysis. The torque of the BLDC motor is mainly influenced by the waveform of the back-EMF and hence it is needed to predict its precise back-EMF.
- The line-to-line PM flux linkage can be estimated from measured phase currents and calculated line-to-line voltages. The zero-crossing of the line-to-line PM flux occurs right in the middle of two commutations points. This is used as a basis for the position and speed observer.
- As even the proposed observer relies on the machine fundamental model, a safe starting strategy under heavy load torque is still needed. The I - f sensorless control is used for start-up and for low speed control, with seamless transition to the proposed method.
- Digital simulations and experimental results demonstrate that the FEM assisted position and speed observer for BLDC PM motor sensorless control operation, provides rather precise commutation points, even during speed or load transient states.

8.2. Original contributions

The present thesis includes, from the author point of view, the following original contributions:

- An overview of brushless permanent magnet synchronous machines and their control, focusing on BLDC machines;
- The electromagnetic design for a fractional slot concentrated winding permanent magnet synchronous machine case study: an interior permanent magnet synchronous motor with 8 rotor poles and nonuniform (6+6) stator slots and concentrated windings fed with trapezoidal currents;
- A numerical calculation of the magnetic field distribution, using a 2D Finite Element Method (FEM), was used. FEM is used to validate and to analyze the topology, determining all relevant characteristics of the machine: field distribution at no-load and at load, back-EMF at no-load, cogging torque (zero current), load torque pulsations, reluctance torque

- pulsations, torque-rotor angular position characteristics for different trapezoidal-current shapes, torque-rotor angular position characteristics for different current amplitudes, and saturated synchronous inductances.
- To reduce the total torque pulsations at rated torque the skewing technique is applied ($<10\% \cdot T_{eb}$)
 - A measurement procedure was described and the measured results were presented and discussed, confirming satisfactorily FEM calculations;
 - An advanced simulation model for BLDC motor drives is presented, and the performance and feasibilities have been examined by simulation verification.
 - The back-EMF and inductances were modeled through Fourier series, and respectively through look-up table, based on FEM calculations of the BLDC IPM motor from Chapter 3, in order to maintain the accuracy of the proposed model.
 - A FEM assisted position and speed observer for brushless DC PM motor drive sensorless control, based on the line-to-line PM flux linkage (can be estimated from measured phase currents and calculated or measured line-to-line voltages);
 - The development of three speed observers: the first based on pulses generated from the estimated position (e.g.: at every 20° electrical angles), the second, a PLL structure having the estimated position as input and the third one, a PLL structure constructed from the mechanical model of the motor;
 - The proposed sensorless control method is used together with the $I-f$ sensorless control, for start-up and for low speed control, with seamless transitions between them;
 - Implementation of all necessary setup using dSpace 1103 system to perform all presented experiments.

8.3. Future work

Even though several topics have been addressed in this thesis, there are some other, which are interesting for future research:

- Distributed electromagnetic FEA: implementation of different computations (field distribution, cogging torque, back-EMF, torque pulsations, parameters-inductances, iron losses) to be started on several cores and/or other server PC in the cluster.
- Optimal electromagnetic design (optimization tool, computer networking and distributed computing): start FEM software using parallel computing, check if the job-processing is ready, get the results back for post processing inside the optimizer/selection of best solution, graphics and stop for grid-search or run optimization algorithms/start new jobs on servers if other optimization algorithms
- Testing the BLDC motor drive sensorless control performance at nominal speed and torque.
- Extend the speed range for the proposed BLDC motor drive sensorless control, especially at low speed.
- Stability study of the proposed FEM assisted position and speed observer and investigation of the observer's performance, due to the parameters variation (stator resistance, inductances, DC link voltage).

Author's papers related to the Ph.D. thesis

- [1] A. Ştirban, L. Tutelea, D. Iles-Klumpner, I. Boldea, "FEM analysis of concentrated coils nonuniform slot (6+6/8) IPMSM fed with trapezoidal current", *OPTIM 2008*, pp. 45-52, 2008 (ISI Proceedings, IEEEExplore, Inspec, Compendex).
- [2] A. Ştirban, D. Iles-Klumpner, M. Risticvic, I. Boldea, "(6+6) Slot/8 Pole 3 Phase IPM Brushless DC Automotive Actuator: Torque, EMF, and Inductance Characterization by FEM vs. Experiments", *on the CD-ROM of IEEE-IEMDC 2009 Proceedings*, IEEE Catalog Number: CFP09EMD, ISBN: 978-1-4244-4252-2, pp. 1528-1534, May 2009.
- [3] A. Ştirban, I. Boldea, G.-D. Andreescu, D. Iles, F. Blaabjerg, "Motion Sensorless Control of BLDC PM Motor with Offline FEM Info Assisted State Observer", *OPTIM 2010*, pp. 321-328, May 2010 (ISI Proceedings, IEEEExplore, Inspec, Compendex).
- [4] A. Ştirban, I. Boldea, G.-D. Andreescu, D. Iles, F. Blaabjerg, "FEM Assisted Position and Speed Observer for BLDC PM Motor Drive Sensorless Control, With Experiments", *EPE-PEMC 2010*, pp. 34-40, September 2010 (ISI Proceedings, IEEEExplore, Engineering Index).

Author's CV

Alin Nicușor Știrban

Office: University Politehnica of Timisoara, Romania

Blvd. Vasile Parvan, no. 2, room D108

Tel: +40 256403463

Email: stirban.alin@gmail.com

Home Address: Aleea Teilor, no. 9

Tecuci, Galati, Romania

Mobile: +40 746906683

EDUCATION

- 2007-2010 Ph.D. student at University "Politehnica" of Timisoara,
Faculty of Electrical and Power Engineering,
Dept. of Electrical Machines and Drives, Timisoara, Romania
- 2007 Dipl. degree in Electrical Engineering
- 2002-2007 University "Politehnica" of Timisoara, Timisoara, Romania
Faculty of Electrical Engineering
- 1998-2002 High School "Spiru Haret", Tecuci, Romania

PERSONAL EXPERIENCE

- July-Oct. 2009 Guest Researcher at Institute of Energy Technology, Aalborg
University Denmark,
- July-Sep. 2008 Guest Researcher at EBM-Papst St. Georgen GmbH&Co. KG., St.
Georgen, Germany,
- Mar.-Oct. 2007 Project manager/(Electrical engineer) at S.C. ELTrex SRL,
Timisoara, Romania.

PERSONAL INFORMATION

Born: November 22nd, 1982

Family: Unmarried